Doctoral theses at NTNU, 2022:196

Andres Soler

Low-density EEG Source Reconstruction: Towards an Automated Framework for Minimizing Electrode Count While Retaining High Accuracy

Doctoral thesis

NTNU
Norwegian University of Science and Technology
Thesis for the Degree of Philosophiae Doctor
Faculty of Information Technology and Electrical Engineering
Department of Engineering Cybernetics

NTNU
Norwegian University of Science and Technology

Andres Soler

Low-density EEG Source Reconstruction: Towards an Automated Framework for Minimizing Electrode Count While Retaining High Accuracy

Thesis for the Degree of Philosophiae Doctor

Trondheim, July 2022

Norwegian University of Science and Technology
Faculty of Information Technology and Electrical Engineering
Department of Engineering Cybernetics

NTNU
Norwegian University of
Science and Technology

NTNU
Norwegian University of Science and Technology

Thesis for the Degree of Philosophiae Doctor

Faculty of Information Technology and Electrical Engineering
Department of Engineering Cybernetics

ISBN 978-82-326-5845-9 (printed ver.)
ISBN 978-82-326-5909-8 (electronic ver.)
ISSN 1503-8181 (printed ver.)
ISSN 2703-8084 (online ver.)

Doctoral theses at NTNU, 2022:196

Printed by NTNU Grafisk senter

Preface

This thesis is submitted in partial fulfillment of the requirements for the degree of Philosophiae Doctor (PhD) at the Norwegian University of Science and Technology (NTNU). This work was carried out at the Department of Engineering Cybernetics (ITK), with the supervision of Marta Molinas, Eduardo Giraldo, and Lars Lundheim. This work was supported by NTNU Biotechnology through the project "David versus Goliath: single-channel EEG unravels its power through adaptive signal analysis-FlexEEG".

Acknowledgements

First, I would like to express my deep gratitude to my main supervisor Professor Marta Molinas, for her outstanding supervision, guidance, and support during these years. I appreciate enormously her knowledge, dedication, and passion for this research. I would also like to thank my co-supervisors Professor Eduardo Giraldo and Professor Lars Lundheim for the thoughtful discussions and their insightful contributions to this work.

It is also important for me to thank my project colleagues Luis Moctezuma and Erwin Shad for the lively time at the office and for the stimulating discussions throughout this time. I also acknowledge Pablo Muñoz and Maximiliano Bueno for their valuable ideas and contributions to my work.

Very special thanks to my colleagues at the Departments of Engineering Cybernetics and the Faculty of Information Technology and Electrical Engineering for the friendly working environment, and the enjoyable talks during coffee breaks, lunches, and football afternoons. Also, to the administrative and technical staff at the faculty and department who have been very helpful during my PhD time.

Some additional words are dedicated again to Professor Eduardo Giraldo, who has been a mentor for me and has supervised me during my bachelor's, master's, and now during my PhD, whose support and expertise have been essential throughout my studies.

Finally, my family deserves endless gratitude: my wife Yenny and my son Nicolas for their support, love, and patience during this journey; my parents and brothers for their love and continuous support during my life; and my friends who from the distance supported and encouraged me.

Andres Soler

July 2022, Trondheim, Norway

Abstract

In this thesis, multiple approaches for electroencephalographic (EEG) source reconstruction using low-density electrode counts are introduced. Source reconstruction provides valuable information about the location and time-courses of the source activity in the brain cortical areas. For such estimation, the use of a high number of electrodes has been proven to provide the most accurate estimation of the underlying brain activity. However, high-density EEG (hdEEG) is not generalized for most EEG applications, thus neither is the use of the source estimated activity. Although source reconstruction can provide spatially segregated time courses and relevant information about the dynamical interaction of brain regions, most EEG applications still rely on analysis and feature extraction from the electrode space.

This thesis provides a link between source reconstruction and low-density EEG (ldEEG) systems. It presents a set of rigorous methodologies designed to identify EEG electrodes according to their contribution to localization accuracy and minimizes their numbers through optimization routines. hdEEG is taken as the reference for source imaging when mapping a particular brain activity or the activity of a region of interest (ROI). Previous works have studied the influence of the spatial sampling (number of electrodes) in brain generalized source reconstruction, where the positions of the electrodes were selected to attempt covering the entire head/scalp. In contrast, this work presents approaches to identify and select electrode locations based on their relevance to capture the underlying activity or their contribution to obtain accurate reconstructions of the activity of interest, while using the lowest number of electrodes possible.

Simplifying the number of electrodes while obtaining detailed information of the source activity can be beneficial for multiple EEG applications. It can serve to

improve portability, enabling recordings to be taken in more natural environments outside the lab; to design easy-to-use devices that can monitor the source activity for different neuroparadigms/applications; to reduce the accessibility boundaries to non-traditional EEG users; and to expand the research scope of EEG based source activity reconstruction. For these purposes, three methodologies are introduced in this work. The first study consists of constraining the estimation to a set of frequency modes extracted in the electrode space prior to source activity reconstruction. The method of Multivariate Empirical Mode Decomposition (MEMD) was applied to extract the frequency modes of the underlying source activity in ldEEG electrode configuration.

A second study consists of the use of spatial constraints, in which the estimation is conferred to a section of the brain, using *a priori* knowledge of the general location of the source activity. For this, a technique based on partial models of the brain is combined with relevance-based electrode selection using a Q-alpha ($Q - \alpha$) method for relevance feature selection, in order to determine the most relevant electrode positions that can be used to map a region of interest. In addition, when considering the full brain model, relevance selection is compared in multiple electrode scenarios to compare the accuracy of the reduced number of electrodes with denser systems. A third study consists of electrode selection based on its contribution to localization accuracy, and a methodology combining evolutionary optimization and source reconstruction is introduced. The non-dominated sorting genetic algorithm II (NSGA-II) is applied to identify optimal combinations of electrodes that offer the best source reconstruction accuracy.

The results show the feasibility of identifying reduced electrode counts that offer an equal or better reconstruction quality. In most cases, electrode counts between 6 and 12 electrodes are found to maintain the hdEEG accuracy of electrode counts with 128 electrodes. This represents an important reduction in the number of electrodes while maintaining high accuracy; demonstrating that a set of a few electrodes can be used to estimate the source activity in a particular scenario. The frameworks established here can serve to evaluate to what extent current systems with reduced electrode counts can be used for source reconstruction, and to identify the optimal electrode positions for different neuro-paradigms and applications.

Contents

List of Abbreviations

ACNS	American Electroencephalographic Society.
ADC	Analog-to-digital Converters.
AP	Action Potential.
BCI	Brain-Computer Interface.
BEM	Boundary Element Modelling.
BIDS	Brain Imaging Data Structure.
BMA	Bayesian Model Averaging.
BOLD	Blood Oxygenation Level Dependent.
BSS	Blind Source Separation.
CEEMD	Complete Ensemble Empirical Mode Decomposition.
CLARA	Classical LORETA Analysis Recursively Applied.
CSF	Cerebrospinal Fluid.
CT	Computed Tomography Scan.
dSPM	Dynamic Statistical Parametric Mapping.
ECD	Equivalent Current Dipoles.

ECG	Electrocardiography.
ECoG	Electrocorticography.
EEG	Electroencephalography.
EEMD	Ensemble Empirical Mode Decomposition.
EMD	Empirical Mode Decomposition.
EMG	Electromyography.
EOG	Electrooculogram.
EP	Evoked Potential.
EPI	Echo-planar Imaging.
EPSP	Excitatory Postsynaptic Potential.
ERP	Event Related Potential.
ESI	EEG Source Imaging.
FEM	Finite Element Modelling.
fMRI	Functional Magnetic Resonance Imaging.
GA	Genetic Algorithm.
GMNE	Generalized Minimum Norm Estimation.
hdEEG	High-density EEG.
HHT	Hilbert-Huang Transform.
ICA	Independent Component Analysis.
IFCN	International Federation of Clinical Neurophysiology.
IMF	Intrinsic Mode Function.
IPSP	Inhibitory Postsynaptic Potential.

ldEEG	Low-density EEG.
LFP	Local Field Potential.
LORETA	Low-resolution Electromagnetic Tomography.
LPA	Left pre-Auricular Point.
LS	Least Square.
MEG	Magnetoencephalography.
MEMD	Multivariate Empirical Mode Decomposition.
MFDM	Multivariate Fourier Decomposition Method.
MNE	Minimum Norm Estimation.
MoBI	Mobile Brain/Body Imaging.
MOOP	Multi-Objective Optimization Problems.
MRI	Magnetic Resonance Imaging.
MSP	Multiple Sparse Priors.
MUSIC	Multiple Signal Classification.
MVDM	Multivariate Variational Mode Decomposition.
NSGA	Non-dominated Sorting Genetic Algorithm.
PBM	Partial Brain Model.
PCA	Principal Component Analysis.
PET	Positron Emission Tomography.
PSD	Power Spectrum Density.
PSP	Postsynaptic Potential.
RAP-MUSIC	Recursively Applied and Projected Multiple Signal Classification.
ROI	Region of Interest.

RPA	Right pre-Auricular Point.
sEEG	Stereo-electroencephalography.
sLORETA	Standardized Low-resolution Electromagnetic Tomography.
SNR	Signal-to-noise Ratio.
SPM	Statistical Parametric Mapping.
SSVEP	Steady State Visual Evoked Potential.
TRAP-MUSIC	Truncated Recursively Applied and Projected Multiple Signal Classification.
VEP	Visual Evoked Potential.
WM	Wasserstein Metric.
wMNE	Weighted Minimum Norm Estimation.

List of Tables

List of Figures

Chapter 1

Introduction

This thesis presents multiple approaches for electroencephalographic (EEG) source reconstruction using low-density electrode counts. The objectives are to identify low-density EEG (ldEEG) subsets that can retain the reconstruction accuracy of high-density EEG (hdEEG) systems and validate the feasibility of using ldEEG source reconstruction to retrieve the source activity information in particular brain activities. Achieving these objectives paves the way for EEG systems based on a minimum number of electrodes with source reconstruction capabilities. This can contribute to the development of low-cost and portable systems that can extract and monitor the underlying activity for current applications, and to expand the research use of EEG source reconstruction in new applications.

This research work is part of the project ***David and Goliath: single-channel EEG unravels its power through adaptive signal analysis-FlexEEG****, which aims to identify an optimal minimum EEG electrode count for wearable EEG solutions for universal applications. This thesis contributes to this goal by achieving optimization-based electrode reduction for EEG source reconstruction.*

This chapter presents a brief background to put into context the motivations and knowledge gaps this work aims to address. The scope and research questions present the fundamental hypotheses that are the basis and set the direction for the research. This chapter continues by presenting the list of publications directly related to the thesis contributions based on their category: journal articles, conference papers, and conference abstracts. The publications non-directly related to the thesis but which

were written during the Ph.D are also presented according to their category. Finally, the outline of the rest of the thesis is presented.

1.1 Background and Motivations

Electroencephalography (EEG) is a non-invasive technique that allows for measurements of electrical brain activity. It is characterized by its high temporal resolution (milliseconds) compared with other techniques, like functional magnetic resonance imaging (fMRI), computed tomography scan (CT), and positron emission tomography (PET), which offer a lower temporal resolution (seconds). In contrast, EEG is characterized by its lower spatial resolution (centimeters) in comparison with the aforementioned techniques (millimeters). Similar to EEG, magnetoencephalography (MEG) is a non-invasive technique that measures the electrical brain activity from sensors close to scalp. Both EEG and MEG are indirect measurements of the current sources in cortical areas produced by postsynaptic activity. Particularly, EEG registers the voltage difference between electrodes at the scalp that result from the electrical field propagated from the cortical sources to the scalp, while MEG measures the magnetic field produced by such current sources. Although both have a millisecond temporal resolution, EEG has been more broadly adopted than MEG, due to its lower cost of equipment and setup.

Since the first report of measurements of human brain electrical activity was presented by Hans Berger in 1929 [1], the EEG technique has become an important tool to study the different dynamics of brain activity and the multiple processes that take place in this astonishing and complex organ. Among them, cognitive processes like memory, perception, attention [2–5]; brain diseases like epilepsy, Alzheimer's, and other neuro-degenerative diseases [6–8]; and the development of brain-computer-interfaces [9, 10].

As EEG provides important information about the neural activity, it can be used as a neuroimaging tool to estimate the properties of the underlying activity inside the brain. This process is often referred to as EEG source reconstruction, as well as EEG brain imaging or EEG source imaging [11]. EEG source reconstruction is the estimation of the properties of the current sources that originated the potentials recorded at the scalp. Generally, the properties to estimate are localization and time courses [12, 13]. However, the estimation is not a straightforward process.

The source activity is mixed in the brain before reaching the scalp. This is known as the volume conductor effect [14, 15]. The electrical field can be propagated from the current sources to the whole brain in a highly conductive medium (brain soft tissues), and must pass through a highly resistive medium (skull), before reaching the scalp to be measured by the electrodes [16, 17]. This results in non-linear, not-stationary, and debilitated brain signals that are hidden in surrounding noise, where pre-processing techniques are often required to attenuate the noise and enhance the underlying signals [18].

To provide an accurate estimation, it is required to solve the so-called forward and inverse problems. Briefly, the forward problem solution consists of modeling the interaction between a large population of neurons at the brain cortex and the electrical potential at scalp. Multiple methods, like Finite Element Modeling (FEM) and Boundary Element Modeling (BEM) based on Magnetic resonance imaging (MRI) head images, allow to obtain realistic representations of the brain and provide an accurate modeling of the source-electrode relationship [19]. This allows to alleviate the influence of the volume conduction problem. In contrast, the inverse problem solution makes use of the forward modeling and the registered EEG activity to estimate the properties of the current sources [13].

The inverse problem is characterized to be mathematically ill-posed and ill-conditioned [12, 20], which in practical terms means that infinite configurations of the source activity can lead to the same scalp recordings, and that the solution is highly sensitive to noise in the recordings. This is due to the number of sources, which are *unknowns* to estimate, being much higher than the number of electrodes or *knowns* of the problem. Generally, the sources are in the order of thousands, while the number of electrodes is in the order of a few hundreds [21]. To attenuate the effect of this characteristic and to mitigate against the lack of spatial resolution of the EEG, source reconstruction is typically done by using a high number of electrodes.

It is widely known that hdEEG offers the best accurate reconstruction and it is the standard for estimating the source activity [22–26]. EEG is considered hdEEG when the number of electrodes is around 60 or more, with common choice configurations being 64, 128 and 256 electrodes. However, hdEEG is not the standard nor required in all EEG applications. Clinically EEG is traditionally done

with 21 electrodes and majority of BCI systems and leisure applications are based on ldEEG systems, in which the the number of electrodes can be much lower. Unfortunately, hdEEG systems are still costly, and have reduced portability, and those disadvantages have made difficult for the hdEEG technique to be broadly adopted. In addition, inherent to an increase in the number of electrodes, the volume of information to store, process and analyze from the data also increases, posing challenges for online applications, while demanding more computing power. Moreover, the preparation time for recording increases, and in particular this time can be much higher compared to wearable EEG devices that have proliferated over the last few decades.

Currently, as hdEEG systems are typically found in research with few clinical applications, source reconstruction has been mostly applied in these environments. The source space resulting from source reconstruction analysis can offer useful information of the activation and interaction between regions, with a better region discrimination resolution than electrode space analysis [27], particularly for determining functional connectivity, identification of neural biomarkers, and determining the active brain regions [11, 27–30]. However, it is still unclear to what degree source reconstruction can be applied in low-density settings, and alternatives to alleviate the ill-posed and ill-conditioned characteristics of the inverse problem have been poorly explored. In that direction, the following knowledge gaps have been identified and serve as the principal motivations behind the research work of this thesis:

- **Knowledge gap 1:** Due to the non-linearity and non-stationary properties of the EEG signals, pre-processing is often required to extract the underlying brain activity and separate it from the noise. Frequency decomposition-based methods have been evaluated in the context of feature extraction in order to identify biomarkers that can represent a particular activity/disease of interest. However, very few studies have reported the application of such methods in the context of source reconstruction. Particularly, the use of frequency decomposition-based methods for source reconstruction in low-density settings is not currently available.

- **Knowledge gap 2:** A high number of electrodes are required in order

to improve the spatial resolution of EEG and alleviate the ill-posedness of the inverse problem. Often the electrodes are positioned to be equally distributed over the scalp to cover the whole brain. This has been proven effective to reconstruct the source activity of the entire brain, however, in some cases, it is required to identify the activation of a particular region rather than the whole brain. In that direction, solutions based on limiting the region to reconstruct and reduce the number of *unknowns* in the inverse problem have been scarcely reported.

- **Knowledge gap 3:** Multiple studies have compared hdEEG and ldEEG for source reconstruction, demonstrating how the number of electrodes influences the quality of the reconstruction. In those studies, the denser count of electrodes has been obtained by over-sampling standard electrode positioning systems by placing electrodes in intermediate positions; and the sparser electrode count by down-sampling the number of electrodes, omitting electrodes symmetrically from standard electrode positioning systems. Therefore, those combinations of electrodes were selected considering a coverage basis, thus, an approach to select subsets of electrodes according to their contribution to source reconstruction accuracy has not been analyzed.

These knowledge gaps are explained in more detail in the literature review and the state-of-the-art presented in the introductions of chapters 4, 5, and 6.

1.2 Scope and Research Questions

This thesis explores and presents alternatives to perform source reconstruction in ldEEG settings with the objective to identify and develop methodologies (algorithms and tools) to allow ldEEG electrode counts to maintain hdEEG source reconstruction accuracy, and to validate those tools, in particular source activity reconstruction tasks. Considering the knowledge gaps presented, the scope of this thesis is based on answering the following research questions:

- ***Research Question 1:*** **Frequency decomposition for extracting underlying source activity.** Can the extraction of the underlying source activity captured using ldEEG based on frequency decomposition improve

the accuracy of the inverse solution by attenuating the ill-condition of the source reconstruction?

- ***Research Question 2:*** **Include *a priori* information to reduce the number of unknowns in source reconstruction.** Can the number of *unknowns* be reduced by involving *a priori* information of the active brain regions of a particular task and constraining the source reconstruction to a brain region of interest (ROI)? Can the source activity of a Brain-ROI be accurately reconstructed using ldEEG electrode counts?

- ***Research Question 3:*** **Selection of EEG electrodes based on reconstruction accuracy.** Is it possible to identify a subset of ldEEG electrodes that can maintain the hdEEG reconstruction accuracy by selecting the electrodes by their contribution for reconstructing the source activity during a particular brain activity or task?

1.3 Thesis Contributions

This thesis investigates multiple approaches to perform source reconstruction using ldEEG electrode counts and provides understandable frameworks and methodologies to approach brain imaging under low-density electrode settings. A diagram summarizing the contributions of the thesis is presented in figure 1.1.

A first contribution is the inclusion of frequency decomposition using Multivariate Empirical Mode Decomposition (MEMD) to constrain the estimation to a set of frequency modes. The proposed methodology establishes a pipeline to extract the underlying frequency activity and the selection of the frequency modes in the electrode space prior to source activity reconstruction. This was validated using the ground-truth activity from synthetic EEG signals and EEG recordings from visual stimulation.

Another contribution of this thesis is the use of partial brain models (PBM) to constrain the inverse solution to a prior region of interest and alleviate the ill-posedness of the inverse problems. The theoretical formulation for this approach is presented and the methodology to involve *a priori* knowledge of the general location of the source activity is described. The selection of electrodes based on relevance was applied to identify subsets of electrodes based on their relevance

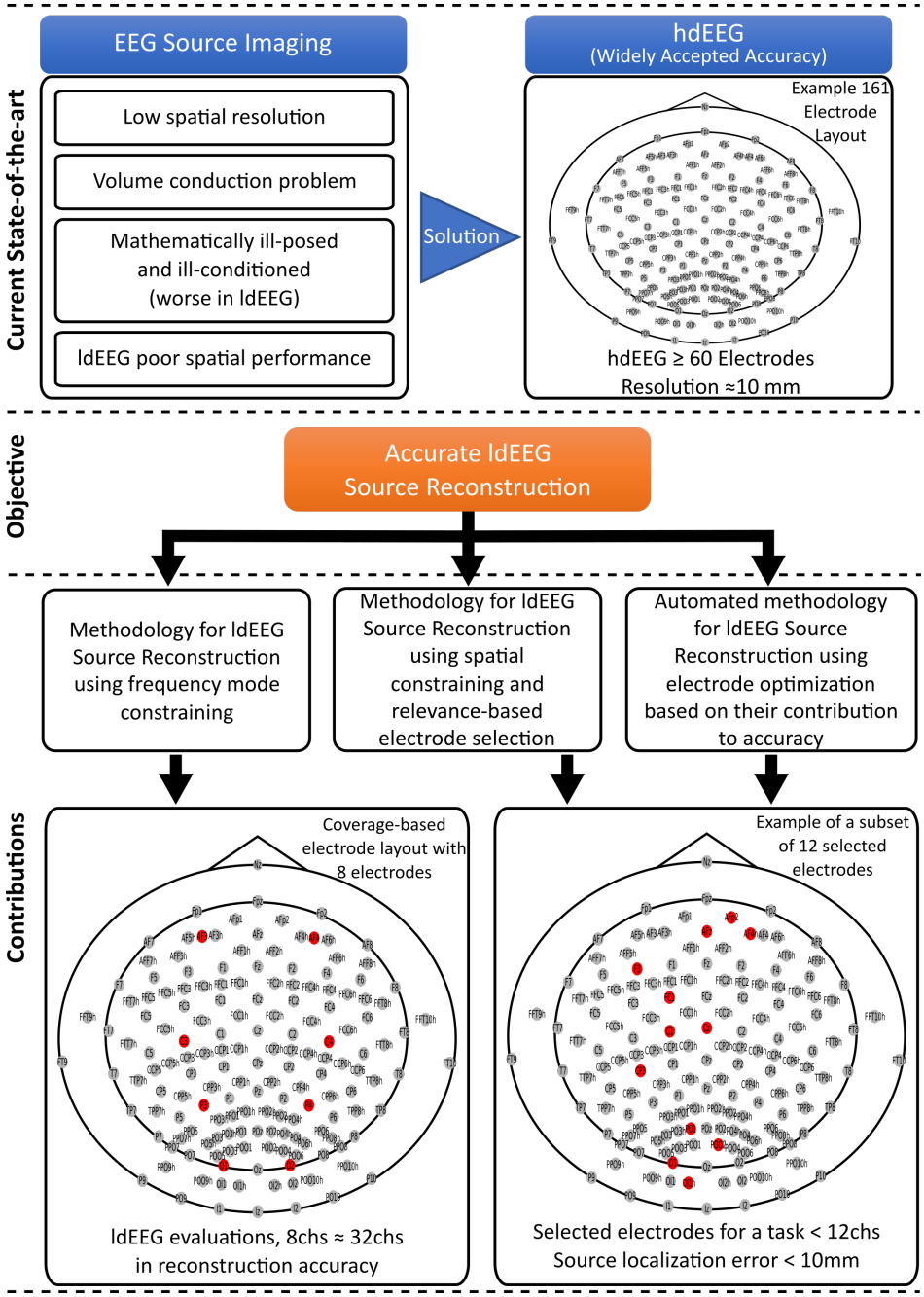

Figure 1.1: Summary of the thesis contributions

for capturing a particular brain activity. The methodology to include PBM and relevance-based electrode selection is described and evaluated under different electrode counts, and different electrode selection criteria.

Another important contributions of this thesis is to establish a methodology to identify reduced electrode counts that can offer an equal or better reconstruction accuracy than hdEEG while reconstructing a particular brain activity. Multiple source reconstruction algorithms were combined with a multi-objective optimization algorithm and, independently of the inverse estimation algorithm, it was possible to identify low-density subsets that retain the accuracy of high-density systems. To the best of the author's knowledge, this is the first work that investigates the electrode selection according to their contribution to reconstruction accuracy and minimizes their numbers through optimization routines. The non-dominated sorting genetic algorithm II (NSGA-II) was applied to identify optimal combinations of electrodes that offer the best source reconstruction accuracy.

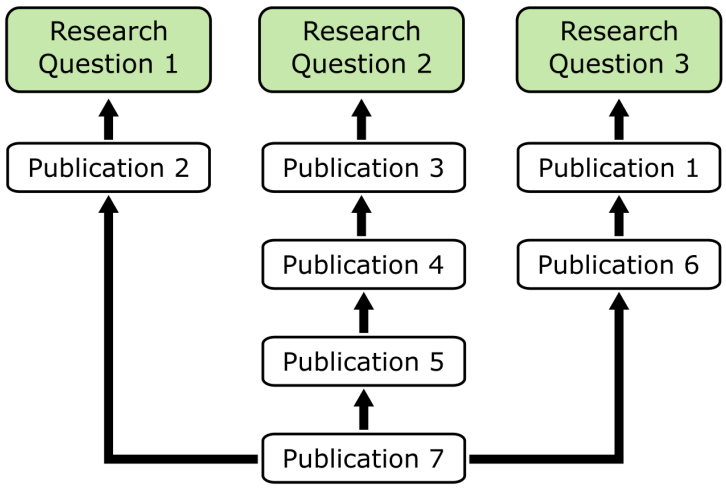

Figure 1.2: Contribution of publications to each research question.

Finally, this thesis offers multiple comparisons between high-density and low-density electrode counts, where the ldEEG electrodes were selected in a different manner to the traditional coverage criteria. When the electrodes are selected

based on their relevance to capture the underlying activity and their contribution accuracy, low-density subsets can be identified and are able to retain high accuracy. Figure 1.2 presents a flowchart of the relationship between the research questions and the contribution from the publications.

The following journal articles, conference papers and abstracts were published during the Ph.D. and are directly related to the thesis' contribution:

Journal Articles

1. **Andres Soler**, Luis Alfredo Moctezuma, Eduardo Giraldo, and Marta Molinas. "Automated methodology for optimal selection of the minimum electrode subset for accurate EEG source estimation based on Genetic Algorithm optimization". Scientific Reports [Under Review], 2022. DOI: 10.1101/2021.11.24.469917

2. **Andres Soler**, Pablo A. Muñoz-Gutiérrez, Maximiliano Bueno-López, Eduardo Giraldo, and Marta Molinas. "Low-Density EEG for Neural Activity Reconstruction Using Multivariate Empirical Mode Decomposition". Frontiers in Neuroscience, 2020. DOI:10.3389/fnins.2020.00175/full

Peer-reviewed Conferences

3. **Andres Soler**, Eduardo Giraldo, Lars Lundheim, and Marta Molinas. "Relevance-based Channel Selection for EEG Source Reconstruction: An Approach to Identify Low-density Channel Subsets". The 15th International Joint Conference on Biomedical Engineering Systems and Technologies, 2022.

4. **Andres Soler**, Eduardo Giraldo, and Marta Molinas. "Low-Density EEG for Source Activity Reconstruction using Partial Brain Models". The 13th International Joint Conference on Biomedical Engineering Systems and Technologies, 2020. DOI:10.5220/0008972500540063

5. **Andres Soler**, Eduardo Giraldo, and Marta Molinas. "Partial brain model for real-time classification of RGB visual stimuli: A brain mapping approach to BCI". The 8th Graz Brain Computer Interface Conference, 2019. DOI:10.3217/978-3-85125-682-6-54

Peer-reviewed Abstracts

6. **Andres Soler**, Luis Alfredo Moctezuma, Eduardo Giraldo, and Marta Molinas. “EEG channel-selection method based on NSGA-II for source localization”. The 4th HBP Student Conference on Interdisciplinary Brain Research, 2020.
7. Luis Alfredo Moctezuma, **Andres Soler**, Erwin H. T.Shad, Marta Molinas, and Alejandro A. Torres-Garcia. “David versus Goliath: Low-density EEG unravels its power through adaptive signal analysis - FlexEEG”. The 4th HBP Student Conference on Interdisciplinary Brain Research, 2020.

Other Contributions

The following conference papers and abstracts were published during the Ph.D. but are not directly related to the thesis’ contribution.

Peer-reviewed Conferences

8. Sara L. Ludvigsen, Emma H. Buoen, **Andres Soler**, and Marta Molinas. "Searching for Unique Neural Descriptors of Primary Colours in EEG Signals: A Classification Study”. The 14th International Conference on Brain Informatics, 2021. DOI:10.1007/978-3-030-86993-9_26
9. **Andres Soler**, Ole Drange, Junya Furuki, Takashi Abe and Marta Molinas."Automatic Onset Detection of Rapid Eye Movements in REM Sleep EEG Data”. The 11th IFAC Symposium on Biological and Medical Systems BMS, 2021. DOI:10.1016/j.ifacol.2021.10.265
10. **Andres Soler**, Eduardo Giraldo, and Marta Molinas. "DYNLO: Enhancing non-linear regularized state observer brain mapping technique by parameter estimation with extended kalman filter”. The 7th International Work-Conference on Bioinformatics and Biomedical Engineering, 2019. DOI:10.1007/978-3-030-17935-9_36

Peer-reviewed Abstracts

11. Junya Furuki, Ole Drange, **Andres Soler**, Marta Molinas, and Takashi Abe."Estimating the source of the negative potential that occurs before rapid eye movement during REM sleep: Analysis of recordings using a

high-density electroencephalography (EEG)". The 39th Annual Meeting of the Japanese Society for Physiological Psychology and Psychophysiology (JSPP), 2021. DOI:10.13140/RG.2.2.28938.80323

12. Junya Furuki, Ole Drange, **Andres Soler**, Yoko Suzuki, Marta Molinas, and Takashi Abe. "Current sources of brain potentials before rapid eye movements during human REM sleep: A high-density electroencephalography study". Tsukuba Conference, 2021.
13. Junya Furuki, Ole Drange, **Andres Soler**, Yoko Suzuki, Marta Molinas, and Takashi Abe. "Decision making in uncertain situations: Effects on brain activity during REM sleep". The 82nd Annual Meeting of the Japan Society of Physiological Anthropology, 2021.

1.4 Thesis Outline

The rest of this thesis is organized in the following order:

Chapter 2 introduces the theoretical and fundamental knowledge of EEG brain imaging that serves as the basis for this thesis. The chapter starts by presenting the basics of brain anatomy and brain physiology, and includes an explanation of the generation of EEG potentials and where they come from. This is followed by a description of the generalities of EEG signals and its recording process. The chapter continues by presenting the electrode placement system, and offers a brief history of standard montage systems and other derivations. Finally, source reconstruction is introduced. This includes an explanation of the forward modeling and inverse problem, the general pipeline for brain imaging, and a review of how the spatial sampling is influential for this task. The chapter concludes with a comparison between EEG and other brain imaging techniques.

Chapter 3 focuses on the key material and methods to perform source reconstruction, and the methods to analyze and extract underlying activity from EEG signals. It starts by presenting the algorithms for solving the inverse problem that are used in the thesis, as well as the measurements of performance. The chapter continues by introducing a simulation framework for source activity and EEG signals, and presents the typical pipeline from raw EEG signals to event-related potentials. Then, a description of relevant frequency decomposition methods based on the Hilbert-Huang Transform (HHT) is presented, which

includes the empirical mode decomposition (EMD) method and its multivariate version MEMD, which are the basis for chapter 4. It continues with a description of relevance analysis and its computation algorithm that is used for the analysis in chapter 5. Then, the concept of multi-objective optimization is presented and the description of the algorithm to perform it is described. This is the basis for the contribution in chapter 6. Subsequently, the EEG datasets used for source reconstruction evaluations and the description of the ground-truth activity for further comparisons are provided. The chapter concludes by mentioning the software and hardware used for signal analysis, processing and source reconstruction.

Chapter 4 presents a proposed methodology for applying frequency decomposition and constraint the source reconstruction to a set of frequency modes. In particular, the implementation of MEMD to extract the underlying brain activity, and the influence on the source reconstruction accuracy in the context of low-density electrode counts, are detailed.

Chapter 5 introduces the concept of PBM as a method to constrain the spatial solution involving *a priori* knowledge of the regions activated during a particular brain activity. Subsequently, it presents the first approach for electrode selection based on their relevance, and proposes methodologies to use relevance analysis for selection and the pipeline to combine PBM and relevance-based electrode selection. The chapter concludes by presenting multiple comparisons of hdEEG coverage-based electrode counts and ldEEG relevance-based selected electrode counts.

Chapter 6 introduces and describes the process to identify the minimum number of electrode counts while maintaining hdEEG accuracy. A methodology for electrode selection based on their contribution to accurate source localization is introduced, where multiple source reconstruction algorithms are combined with a multi-objective optimization process based on the NSGA-II algorithm.

In Chapter 7 the findings and contributions of the thesis are summarized. Finally, the conclusions of the investigation and the opportunities for future work are presented.

Chapter 2

Fundamentals of EEG Brain Imaging

This chapter reviews the fundamental aspects of EEG as a technique for neuroimaging, starting from the brain structure and generation of EEG signals, and finishing with the typical steps taken to perform source reconstruction and generate brain activation images or maps. Important principles and elements of the EEG signals and source reconstruction are presented in this chapter: how the EEG signals are recorded and what the different noise artifacts are; the effect of the volume conduction from the EEG generators to the electrodes in the scalp; the brain rhythms and their frequencies; the electrode placement and the evolution of the number of electrodes; realistic modeling of brain structures; the mathematical framework of source reconstruction; the influence of the electrode number or spatial sampling in source reconstruction accuracy; and a comparison with other brain imaging methods.

2.1 Brain Anatomy and Physiology

2.1.1 Brain Anatomy

The brain is considered to be the most complex organ of the human body. It is the largest part of the central nervous systems (CNS), and it is in charge of multiple functionalities of the human being. The major parts of the brain are the brain stem, the cerebellum and the cerebrum. The brain stem is the structure that connects the two hemispheres of the cerebrum and the cerebellum. It has fibers and cells

and serves as an information bridge from the cerebrum to the spinal cord and cerebellum, and vice versa. The brain stem is vital for human beings: it regulates breathing, heart rate, consciousness, the control of body temperature and other autonomic processes that are independent of conscious brain functions [31]. The cerebellum is located behind the cerebrum and even though it is small compared to the cerebrum, it contains just as many neurons. The cerebellum is the movement control center and is responsible for the coordination of movement, balance and posture of the body. Figure 2.1 shows the three main structures of the human brain.

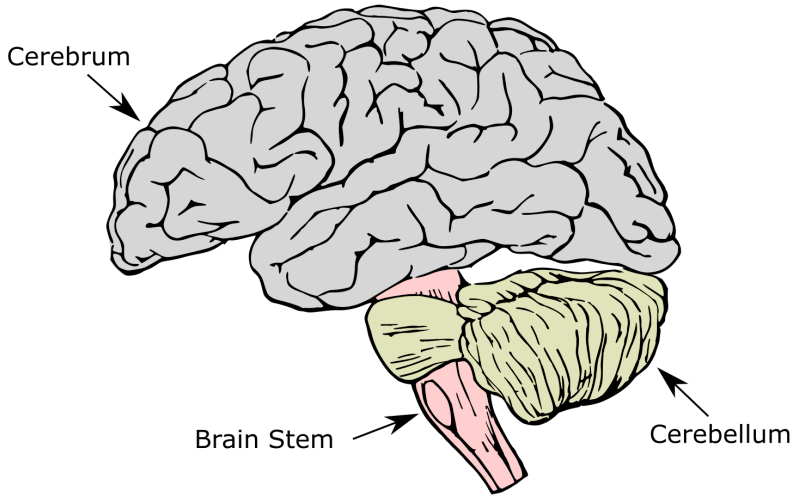

Figure 2.1: CNS structure: cerebellum, cerebrum and brain stem. (Based on the content of [31]).

The cerebrum is made of soft tissue, gray and white matter; those tissues contain the nerve cells and non-neuronal cells. The gray matter is the outer most layer of the brain and contains a large number of neuronal cell bodies. It is the reason behind its gray tone. The gray matter that surrounds the cerebrum is know as the brain cortex. Due to the high concentration of neurons bodies, most of the brain information processing takes place in this layer, and it is transmitted through the neuron axons that form the white matter [32]. The cerebral cortex is heavily folded, which increases the surface area. The complex patters of ridges, convolutions or *gyri* and grooves or *sulci* can vary between individuals, however

all brains have basic similarities [33].

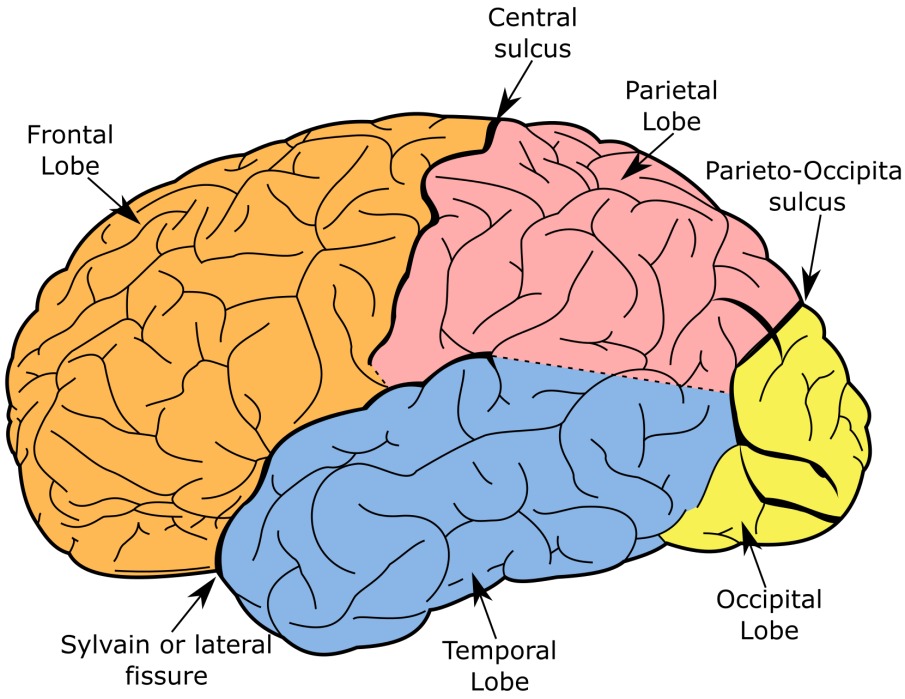

Figure 2.2: Hemisphere distribution. (Based on the content of [31, 33]).

The cerebrum is split into two hemispheres by the sagittal fissure, the right and left hemispheres. In general, the somatosensory and motor control functions are coordinated by the contralateral hemisphere of the brain. The functions of the left side of the body are coordinated by the right hemisphere and the right functions of the body by the left hemisphere [31]. Each hemisphere consist of four lobes: frontal lobe, parietal lobe, temporal lobe, and occipital lobe. Their location (depicted in figure 2.2) and general functions are described as follows:

- **Frontal lobe:** It is located in front of the central sulcus and above the lateral fissure (also called Sylvian fissure) and represents about a quarter of the entire cerebral cortex in the human brain. The frontal lobe is considered responsible for motor planning and execution. It controls many aspects of the personality and mental faculties.

- **Temporal lobe:** The temporal lobe is located below the Silvian fissure. It houses receiving ares for the auditory and olfactory systems. It is responsible for processing auditory information and is essential for the comprehension of spoken language. It serves as gateways for information from the neocortex areas. e.g., the amygdala and hippocampus. Therefore, it plays an important role in memory and learning.

- **Parietal lobe:** It is located between the central sulcus and the parieto-occipital sulcus, and over the temporal lobe. It integrates multiple sensory information and contains the largest regions of reception and processing of somatosensory impulses. It also houses important pathways of the visual system.

- **Occipital lobe:** The occipital lobe is the smallest lobe of the cerebral cortex and is located in the posterior part of the brain, below the parieto-occipital sulcus and next to the temporal lobe. It is primarily related to visual function and the processing of visual information.

2.1.2 Generation of Electroencephalographic signals

The cerebral cortex is the most relevant tissue for EEG and MEG recordings. The interactions (synapses) between pyramidal neurons in the cerebral cortex are responsible for producing the currents that generate a magnetic field measurable by MEG systems and a secondary electrical field that propagates until the scalp where it can be measured by EEG electrodes [18]

The cerebral cortex contains between 21-26 billion neurons [34, 35]. The neurons are the basic units of the CNS. Each nerve cell is formed by cell bodies, dendrites and axons, and its structure is presented in figure 2.3. The axons are long cylinders and transmit the electrical impulses from the cell body. Dendrites are connected to axons and dendrites of other neurons and receive the impulses from them. The junctions between dendrites or dendrites-axons are called synapses. In a rest state, the neuron membrane has a negative potential of 60-70 mV, however it changes due to the impulses that the neuron receive. The synapses can increase (polarize) or decrease (depolarize) the membrane potential. If the neuron receives an impulse through an excitatory synapse, a depolarization process of

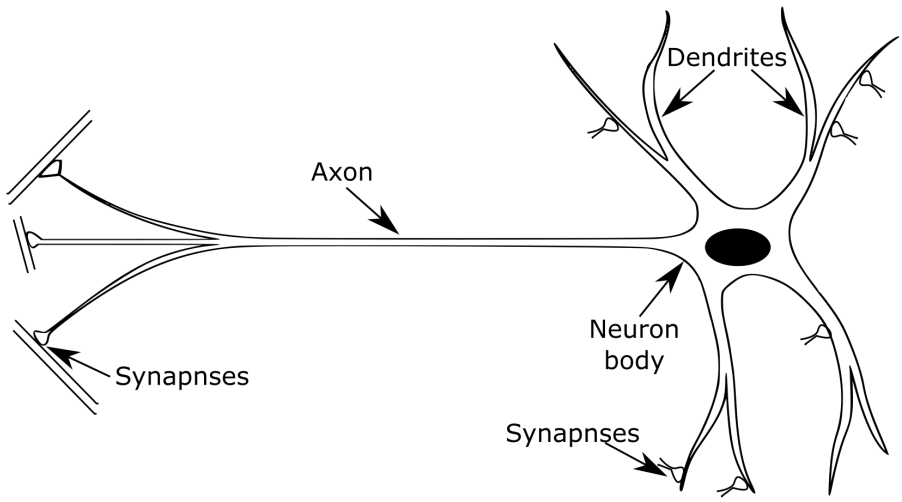

Figure 2.3: Structure of a neuron. (Adapted from [18]).

the membrane will take place, this is known as excitatory postsynaptic potential (EPSP). In contrast, if the impulse is received through an inhibitory synapse, hyperpolarization will occur, this is known as inhibitory postsynaptic potential (IPSP). These changes in the potential of the membrane produce a primary current that flows along the intra-cellular space. However, part of the intra-cellular primary current leaks continuously out of the cell to the extracellular space, and as consequence of this current, the field potentials are generated. The extracellular field potentials are called EEGs and usually have less than 100 Hz frequency [16, 18].

In the brain, all neurons can contribute to the local field potential (LFP), but their contribution can depend on the cell shape and organization. In the cerebral cortex the most populous neurons are the pyramidal cells. The dendrites of this cells lie parallel to each other and perpendicular to the cortex surface (see figure 2.4). This organization plays a key role in generating a strong extracellular field. This geometry allows for the superposition of synchronously active dipoles, which potential can be registered by electrodes at scalp. Pyramidal cells have long and thicker dendrites and they can generate strong currents. Such dipoles generate an open field, as there is considerable spatial separation of the active sink from the return currents. Thus, as the pyramidal cells generate open fields they can

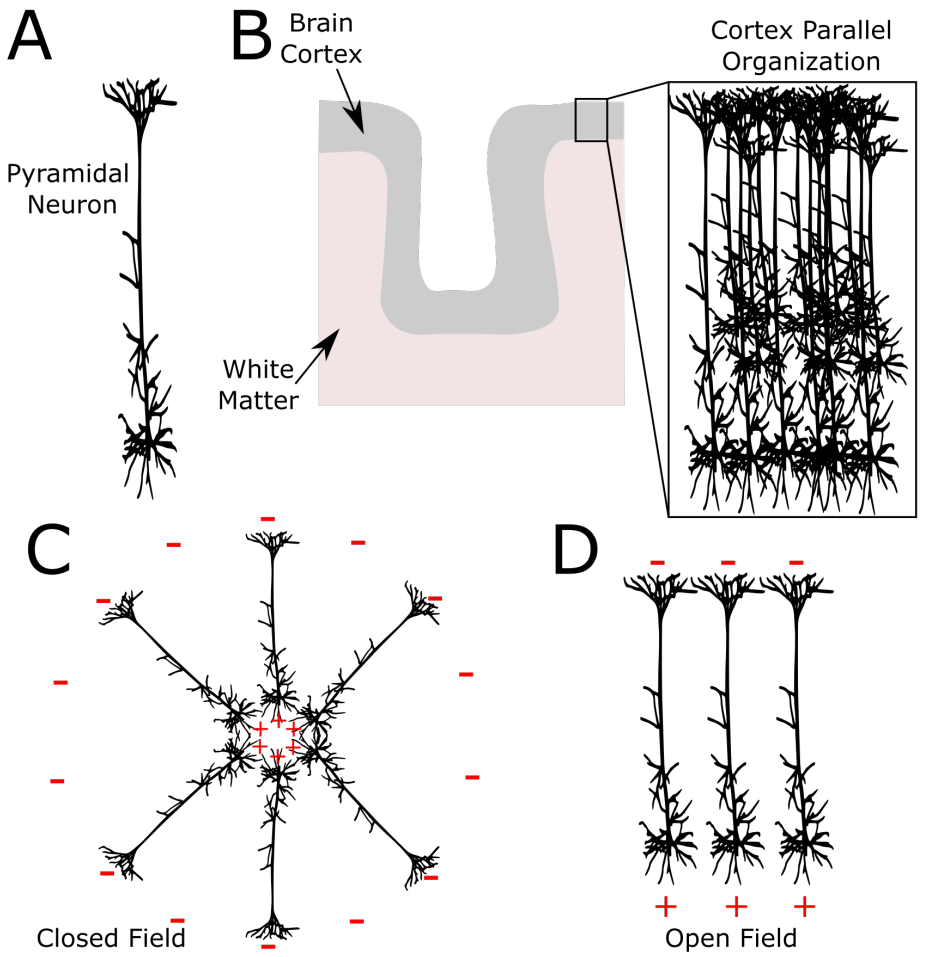

Figure 2.4: **(A)** Pyramidal neuron, **(B)** Parallel organization of the pyramidal neurons in the cerebral cortex, **(C)** Closed field due to spherical organization, **(D)** Open field due to parallel organization. (**(A)** and **(B)** are based on the content of [36], **(C)** and **(D)** were adapted from [16]).

contribute to the extracellular field [16, 36]. In contrast, spherically symmetric neurons, e.g. thalamocortical cells, emanate dendrites in multiple directions. This can lead to a closed field. Only if all dendrites receive impulses at the same time will a strictly closed field be generated, but when a single or few number of dendrites are activated, this can produce a small dipole that is difficult to measure from distance [37]. An example of an open field and a closed field is shown in figure 2.4.

Action Potentials

The action potentials (AP) are pulses that are transmitted along the axons. These are generated by the exchange of ions across the neuron membrane. This temporary pulse in the membrane potential is initiated in the cell body and travels in one direction. An AP is initiated when the neuron receives an excitatory impulse from other neurons, which will open the Na^+ channels. The neuron will continue receiving excitatory impulses and opening the Na^+ channels until the voltage of the membrane changes from -70 mV to -55 mV. At this point additional channels of Na^+ open, and the depolarization continues until it reaches levels around +30 mV, then the Na^+ channels close and the K^+ channels open. The cell host Na^+ and K^+ during a short period, and having the K^+ channels open will repolarize the cell back to the rest potential. However, this repolarization typically overshoots the rest potential, usually to -90 mV. This effect is called hyperpolarization and prevents the neuron from triggering another AP in the opposite direction. After hyperpolarization the membrane will come back to the resting potential. An AP lasts for around 1 to 2 ms and the neuron requires approximately 2 ms before another stimulus is presented [16, 18]. The phases of polarization, depolarization and hyperpolarization are presented over the action potential behavior in figure 2.5.

Postsynaptic Potentials

The arrival of an action potential via synapses triggers the transmission of the signal to a postsynaptic cell, leading to postsynaptic potentials (PSP) that can be either EPSP or IPSP. The PSP are considered the main generators of the source currents. The electrical field and magnetic field associated with those currents are the phenomena that can be measured from outside the head using EEG and MEG techniques, respectively. In the case of the EEG technique by electrodes at scalp; and for the MEG technique by magnetometers and gradiometers close to the scalp. [38].

2.1.3 EEG Volume Conduction Problem

The term volume conduction problem refers to the multiple effects that arise when measuring electrical potentials a distance from their generation [39], in this particular case the volume conduction problem in EEG technique is introduced.

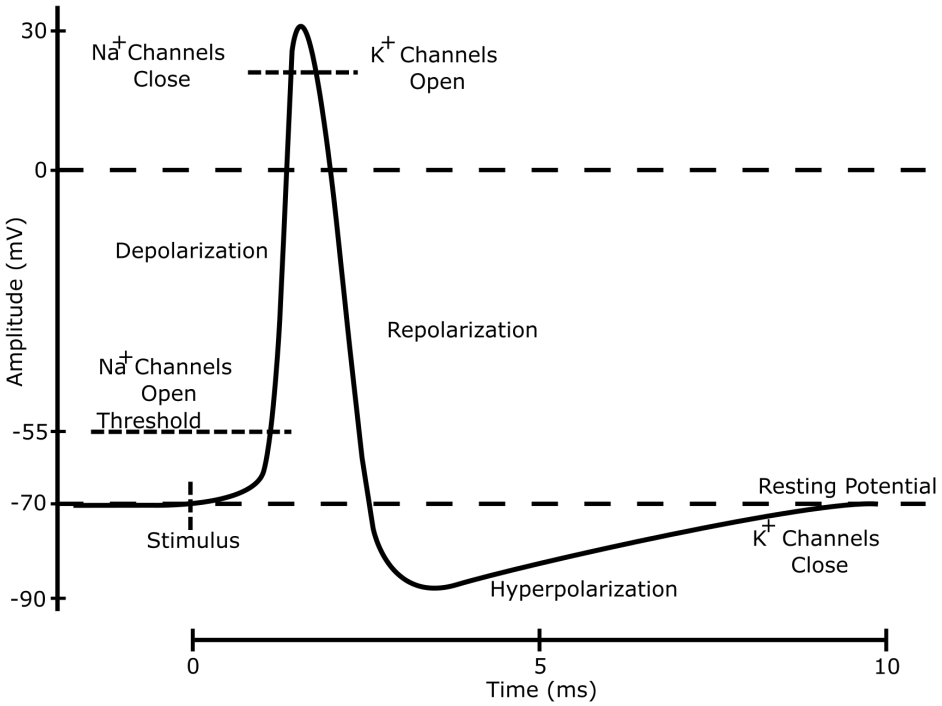

Figure 2.5: An action potential. (Adapted from [18]).

The postsynaptic activity and its associated electrical field takes place in the cortical areas of the brain. From there, the electrical field can theoretically propagate to all directions due to the high conductivity of the soft brain tissue. The human body acts as a passive volume conductor due to its high content of salt water. This explains the reason electrocardiograph (ECG) activity can be recorded not just from electrodes on the chest but also from distant locations like hands or even scalp.

The human head has several layers, including, brain matter (gray and white), skull, scalp, cerebrospinal fluid (CSF) and other thin layers in between. Therefore, the field must pass through the different head layers before reaching the scalp where the electrodes are placed. Those layers vary in thickness and conductivity levels. The cortex is a layer between 1 to 3 mm and posses a conductivity around 0.33 S/m. The skull has a thickness between 3 to 7 mm and a conductivity of 0.012 S/m. It possesses a much lower conductivity when compared with the cortex and

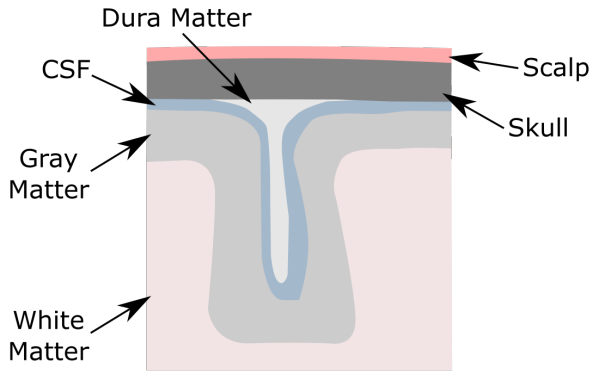

Figure 2.6: Head Layers, the path of EEG from gray matter to scalp. (Based on the content of [40]).

scalp. The scalp has a conductivity of 0.33 S/m and a thickness of approximately 2 to 5 mm. The CFS thickness varies, but its conductivity level is much higher than the scalp with a level around 1.79 S/m [18, 41]. The different layers of the head are displayed in figure 2.6. In general, any electrical field is attenuated when the current travels through a resistive medium. This attenuation is a function of the conductivity and the distance where it is measured from. In the case of EEG signals, the low conductivity of the skull has a significant impact as it can attenuate the signals approximately a hundred times more than the soft tissue. The EEG signals are considered a nonlinear sum of brain sources because the layers have different electrical properties. Another effect of the volume conduction is that the EEG signals can be easily hidden in noise from EEG systems and other electrical signals from the body, e.g. the EEG signals registered at scalp are smaller in amplitude when compared with the electromyography (EMG) muscular signals. Those signals different to EEG are considered artifacts. Finally, because of volume conduction, only a large population of active neurons firing synchronously can generate enough potential to pass through head layers and be detected at the scalp.[42]

2.1.4 Brain Rhythms

In the EEG it is possible to identify rhythmic activity. The brain rhythms, also known as brain waves, are a consequence of neural oscillations, which are

fluctuations in the excitability of neuron groups [43]. The EEG signals can contain simultaneously multiple brain rhythms and as consequence multiple frequencies that can vary in power level. The general brain rhythms are classified in five categories and they can be found during different neural functions, brain processes and states. The categories are described as follows:

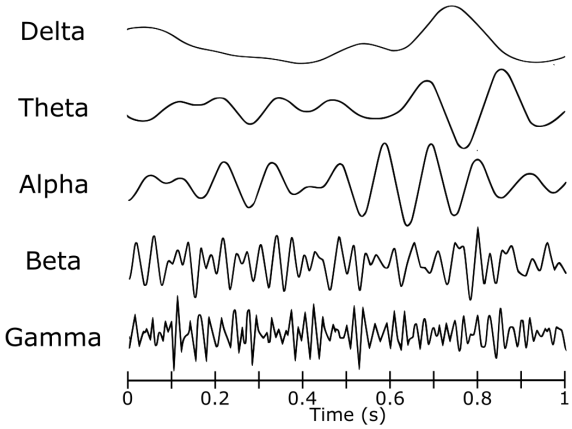

Figure 2.7: EEG brain rhythms. (Adapted from [44]).

- **Delta (δ)**: Delta waves are the slowest brain frequencies (see figure 2.7, where an example of the brain rhythms is depicted). Its frequency range lies between 0.5 and 4 Hz. They are associated with deep and healing sleep. Delta can be seen in brain injuries and in people with learning disabilities during awake state [44].

- **Theta (θ)**: Theta waves represent consciousness toward drowsiness. They are also associated with deep meditation, intuition, and relaxation. They are known to be the creative brain rhythm because of their association with creative inspiration. This frequency band can also be seen during sleep. The suppression of theta waves can lead to anxiety, stress and depression. The theta wave plays an important role in infancy and childhood [2]. Its range of frequency is from 4 to 8 Hz.

- **Alpha (α)**: This brain wave lies in the range between 8 to 13 Hz. In awake state, it is related to a relaxed state with consciousness. In sleep, it is related

with drowsiness associated with sleep onset [2, 45]. Its origin is mainly established in the occipital lobe, and it can be enhanced when a subject closes their eyes and it can be attenuated by attention processes and mental concentration. This brain rhythm was first observed and reported by Hans Berger, who also observed the beta rhythm. [1, 46].

- **Beta (β)**: Its range of frequency is between 14 to 30 Hz. This rhythm is usually presented in low-amplitude (usually less than 20 μV) and is commonly observed in awake state. It is involved in logical thinking, active attention, and concentration. It can be found in several locations of the brain, but frontal and central regions are the most common areas [47]. The frontal beta rhythm is a consistent pattern in a healthy subject. Sub classifications of beta rhythms are presented ambiguously in the literature, while the most common classification is into two sub bands, low beta (13–21 Hz) and high beta (21–30 Hz) [48, 49]. Low beta is associated with concentration, focus, increased energy and performance, while high beta is associated with high arousal and high energy states, as well with high levels of stress and anxiety.

- **Gamma (γ)**: The EEG signals with a frequency greater than 30 Hz are considered to lie in the gamma frequency band. As a continuous rhythm its occurrence is rare, however induced oscillations have been found in the frequency band around 40 Hz, related to visual stimulation and movement tasks. It is considered that they are related to the binding of sensory information and sensorimotor integration [50]. On the other hand, the gamma frequency band is also associated with brain diseases, particularly related to epilepsy [51].

A summary of the main brain rhythms is presented in table 2.1. Other rhythms like the mu rhythm (8-12 Hz) and the beta Rolandic (20 Hz) rhythm are found to be relevant and are associated with processing somatosensory information, and for motion planning and control, respectively. [48, 52]

2.2 EEG Generalities

EEG is an electrophysiological measurement of the electrical activity produced by current sources at the cerebral cortex. Richard Caton was the first to register brain

Wave	Frequency	Brain States
Delta (δ)	0.5-4 Hz	Sleep
Theta (θ)	4-8 Hz	Deeply relaxed, creativity
Alpha (α)	8-13 Hz	Very relaxed, passive attention
Beta (β)	14-30 Hz	Active, external attention
Gamma (γ)	>30 Hz	Concentration

Table 2.1: Frequency bands and brain states of brain waves. (Adapted from [44]).

activity using intracranial electrodes in animals, and reported his findings in 1875 [53]. The first EEG activity was registered using galvanometers that used a mirror to project the signals onto a wall. Later on, the string galvanometer was introduced and signals were registered on photographic paper [18]. Human EEG was first recorded by Hans Berger in the 1920s, using Siemens' double coil galvanometer. He reported a series of 14 reports [54], from which can be highlighted information about the alpha rhythm and how it was affected when opening the eyes and through mental effort. The EEG kept evolving and an important step was done by the introduction of multi-channels systems that used a set of differential amplifiers and pen type registers plotted on plain paper or paper with a grid. Soon, the need of having the recordings in digital form was identified, particularly after the introduction of the first computers in the 1960s. By the 1980s the paperless systems became common and new amplifiers were developed to be more sensitive and to work with high input impedance [16, 18].

2.2.1 EEG Measurement and Recording

EEG technique is the measurement of brain electrical activity from electrodes on the scalp. There are other techniques that also measure the electrical brain activity like electrocorticography (ECoG) by placing electrodes directly over the cortical sheet [55, 56], and LFP technique that measures the LFPs and spikes of a few hundred to a few thousand neurons by using microelectrodes that penetrate the brain cortex [56, 57]. A comparison of these techniques and their recording location, signal amplitude, and frequency is presented in figure 2.8.

In general, a basic digital EEG system consists roughly of electrodes, amplifiers, filters, Analog-to-digital converters (ADC) and a signal storage system (usually a

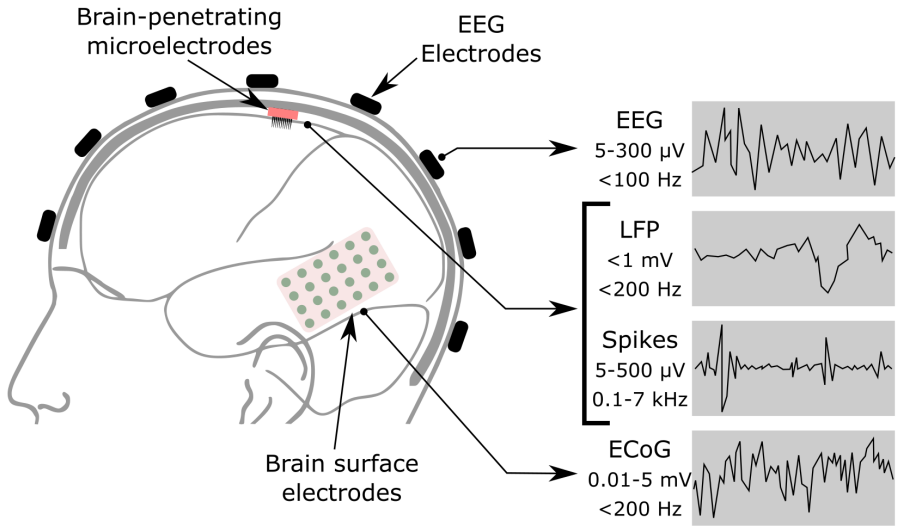

Figure 2.8: Recording location for EEG, ECoG and LFP, and their signal amplitude and frequency. (Adapted from [56]).

computer). Other elements for stimulation and to record inputs for participants are also common.

In general the electrodes can be categorized into two big categories, wet and dry electrodes, and between them there are multiple variations, in size, materials, disposition, and method of capturing the signals. The most used electrodes are the wet electrodes. They are characterized to use conductive gel or saline solutions to decrease the scalp impedance [58]. Usually, they are not in direct contact with the scalp skin, rather they use the gel or saline medium to capture the EEG signals. Although wet electrodes exhibit the best signal-to-noise ratio (SNR), they present some disadvantages. The conductive medium dries over time resulting in a signal quality decrease, therefore they are not recommended to be used over prolonged periods of time. In addition, the setup is relative long, particularly with gel-based electrodes, where a system with 60 electrodes can take between 30-60 min to be properly adjusted. On other hand, the dry electrodes are usually in contact with the scalp and do not require conductive gels. This represents an advantage because they can be used for prolonged recordings and do not require skin preparation, however, they have a series of disadvantages that have delayed its broad use as an

alternative to wet electrodes. In terms of signal quality, they exhibit lower SNR and high sensibility to environment noise. Moreover, they have a rapid deterioration of electrode impedance with use, and continuous contact with the scalp and skin sweat deteriorates its properties. Another disadvantage is related with the conform. As it pressures the scalp, it can lead to prickling and uncomfortable sensations [59]. Despite these issues, dry electrodes are a potential alternative to wet electrodes that can favor portability and the development of more wearable systems, yet they have not been broadly adopted. A recent study suggests that there is a small difference in signal quality and comfort between new dry-based EEG systems and wet, confirming their usefulness in mobile applications [60].

EEG systems use differential amplifiers. They measure the electrical activity of one electrode relative to another, therefore, at least two electrodes are required. The differential amplifiers allow for the removal of the common activity between a pair of electrodes. This is known as common mode rejection. EEG can use two techniques of recordings, monopolar and bipolar. Their central difference is the location of the electrodes. In the case of monopolar recordings, one electrode is located on the scalp or area of interest to register, and the second on a "neutral" area, serving as reference for the scalp electrode. In bipolar recordings, both electrodes are located on the scalp and can capture brain EEG activity. This can lead to a potential attenuation of the general brain activity assuming that both electrodes can potentially register similar activity due to volume conduction. However, it will depend on the areas and distance between the electrodes. In some cases, bipolar are preferred, in order to attenuate the general brain activity and to enhance small potentials that come from a particular area, e.g. Steady State Visual Evoked Potential (SSVEP) [61]. The monopolar is the most common choice, although the reference position can affect the distribution of the potential. In the monopolar case, it is possible to change the reference with simple arithmetic operations, therefore it can be done easily offline, and set up to multiple references [62, 63].

2.2.2 EEG Artifacts

It would be ideal if EEG electrodes record only EEG signals at scalp, however, in practice this is not possible. There are several signals that are generally registered by the electrodes and do not concern EEG signals from the cortex. They are

called artifacts. The undesirable potentials that contaminate the EEG can come from non-physiological sources, external to the participant, and physiological sources, from other physiological activities of the person being recorded. The most common artifacts from external sources are power line noise and changes in the electrodes' impedance, i.e. due to conductive gels that become dry during recordings. The noise related to the power line is easy identifiable because it is always present in frequencies around 50Hz or 60Hz, and their harmonics at 100 or 120 Hz. This noise is often attenuated by notch filtering and their influence has not been found to be significant [62, 64].

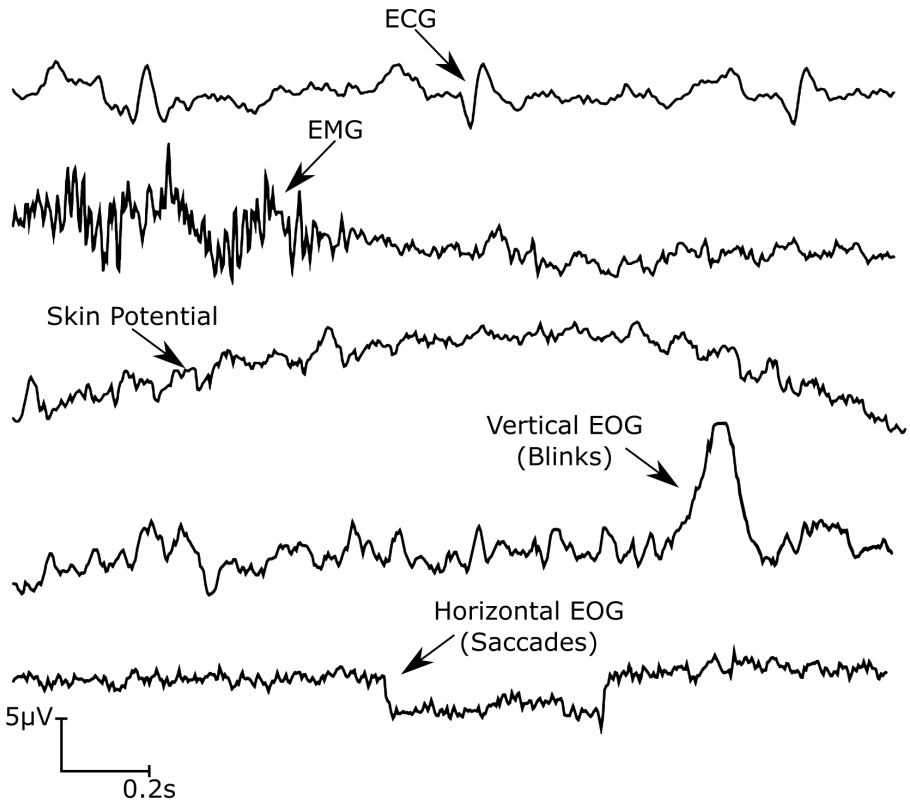

Figure 2.9: Physiological artifacts in EEG signals. (Adapted from [43]).

Physiological artifacts are the main concern during EEG recordings, as it might be difficult to correct and attenuate its effects. The most common sources are skin potentials, eye movements, muscular activity and heart activity. Figure 2.9

presents the effects of physiological artifacts over EEG signals. The skin potentials are slow drifts in the signals, that are produced because of changes of impedance in the skin due to sweating. The eye movements potentials Electrooculogram (EOG) during blinks and saccades produce an important disturbance in the signal and they are always present in the recordings. The eye blink produces a strong deflection, while the saccades effect is similar to a step function that lasts for a few hundred milliseconds. EMG activity is produced for muscular activity. The most typical found in EEG are from face muscles due to changes in facial expressions, chewing and swallowing, and from the neck due to head movements. The EMGs are usually bursts of high frequency activity presented in the EEG. In some cases, strong head movement can lead to a loss of electrode contact, thus, it is usual to ask the participants to remain still during recordings. The ECG artifacts are small positive and negative deflections that are presented periodically with a similar pattern on heart activity.

2.2.3 Event Related Potentials

The event related potentials (ERP) are the brain responses related to specific events, usually due to a stimulus exposure, but also due to internal events. They are small electrical potentials that are time-locked to an event. The have been extensively used to study responses associated with cognitive, sensory and motor events [65–69]. These valuable and tiny brain potentials are hidden in noise, and in order to obtain them a process of averaging is often performed. As the responses are time-locked, averaging multiple trials of the same event improves the SNR and allows to enhance the time-locked brain activity while attenuating the noise and background brain activity or non time-locked activity. The ERPs are differentiated by components based on their peak latency and positive or negative amplitude. These peaks have been named according to their occurrence after the stimuli. e.g. the first positive peak is P1; or according to their latency, e.g, negative peak around 170 ms is N170. Figure 2.10 shows an example of ERP components labeled by their appearance order.

The interpretation of the ERP cannot be generalized, it will depend on the stimuli attributes, e.g. intensity, modality, presentation rate, and the brain activity it is intend to trigger, e.g. visual, auditory, memory. In a visual activity context, these components can represent different processes: C1 can be either a positive or

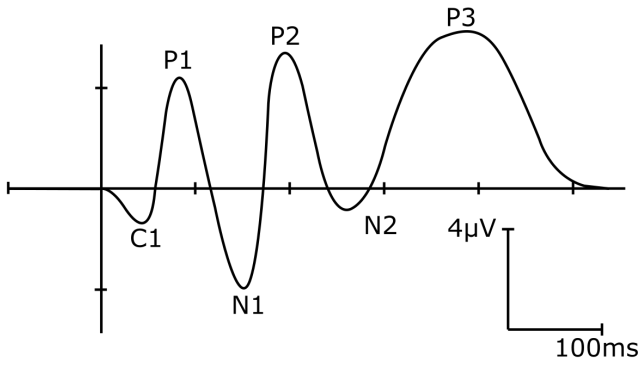

Figure 2.10: Example of idealized ERP components of a visual study. (Adapted from [62]).

a negative peak around 50-70 ms, representing sensory processing. P1 is the first positive peak after C1, with a latency of 90-100 ms. It is found to represent sensory and perceptual processing. N1 is the first negative peak around 170-200 ms, and is often related to visual discrimination and expert recognition. e.g. humans are experts in face recognition [3, 70]. P2 is not well understood and is often difficult to distinguish from the overlapping between N1 and N2. N2 has a latency around 225-250 ms and is related to object recognition, categorization and detection of novelty [71]. P3 after 300 ms is related to stimulus evaluation, working memory, cognitive load and categorization [72, 73].

2.3 Electrode Placement Systems

The first EEG studies presented findings based on few number of electrodes. After the first report from Hans Berger, other researchers followed by studying electrical brain signals and presented their findings. Laboratories and hospitals developed their own systems of electrode placement, and during the first congress of the International Federation of Societies for Electroencephalography and Clinical Neurophysiology in 1947, the need was identified for the establishment of a standard placement of electrodes to standardize EEG measurements and to facilitate comparisons of findings and communications of results in the literature [74]. Four principles were the basis for establishing an international standard.

These principles are quoted from [74]:

1. *Position of electrodes should be determined by measurements from standard landmarks on the skull. Measurements should be proportional to skull size and shape, insofar as possible.*

2. *Adequate coverage of all parts of the head should be provided with standard designated positions even though all would not be used in a given examination.*

3. *Designations of positions should be in terms of brain areas (Frontal, Parietal, etc.) rather than only in numbers so that communications would become more meaningful to the non-specialist.*

4. *Anatomical studies should be carried out to determine the cortical areas most likely to be found beneath each of the standard electrode positions in the average subject.*

Dr. Jasper was designated to perform a study of the current systems and established recommendations based on those principles that, years later, resulted in the first standard electrode placement system, denominated "The Ten Twenty Electrode System" [75, 76].

2.3.1 Standard Placement Systems

There are two standard systems that have been broadly adopted: the international 10-20 and 10-10 electrode systems. They were accepted as standards by the International Federation of Clinical Neurophysiology (IFCN) and the American Electroencephalographic Society (ACNS) [77, 78].

The 10-20 system, presented by Jasper in 1958, established a distribution of the electrodes on the scalp based on percentages of the distance between head landmarks nasion and inion (A-P line), and the naming nomenclature. Figure 2.11 presents a lateral, frontal and top view of the 10-20 system. First frontal (Fp) and occipital (O) electrodes, were located at 10% of the A-P distance, above the nasion and inion, respectively. In between three more electrodes were placed with a 20% distance: Frontal (F), Central (C), and Parietal (P). A central line was established between the left and right pre-auricular points where electrodes were distributed at 10% over the landmarks located over the temporal lobes (T), and other central

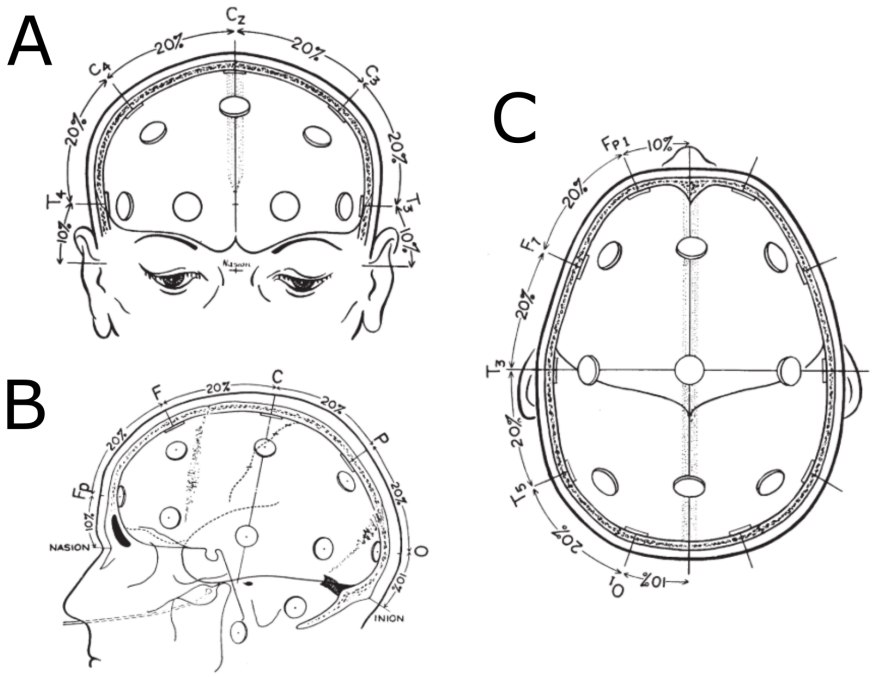

Figure 2.11: **(A)** Frontal, **(B)** Lateral, and **(C)** Top view of the distribution of the electrodes over the scalp according to the 10% and 20% of the A-P line. (Adapted from [76]).

electrodes each at 20% in between. Finally, using the A-P line between Fp and O electrodes, two electrodes at each direction were distributed at 10% of the distance and more electrodes in between at 20% of the distance. In order to differentiate the electrodes at right and left hemisphere, a number next to the letter was included. The electrodes at the left hemisphere use even numbers, and odd numbers are used for the right hemisphere. This resulted in a set 21 standard electrodes. Their names and locations are presented in figure 2.12.

The 10-10 (previously called 10% electrode position) presented in 1985 [79] introduced 60 auxiliary electrodes using a 10% distribution: four were placed over regions close to the cerebellum, four more on the face to measure eye activity, and two on the mastoids (to provide alternatives to the earlobe leads of the 10-20 system). The initial nomenclature of the new electrodes used prime and double prime to designate the electrodes in intermediate positions of the original 10-

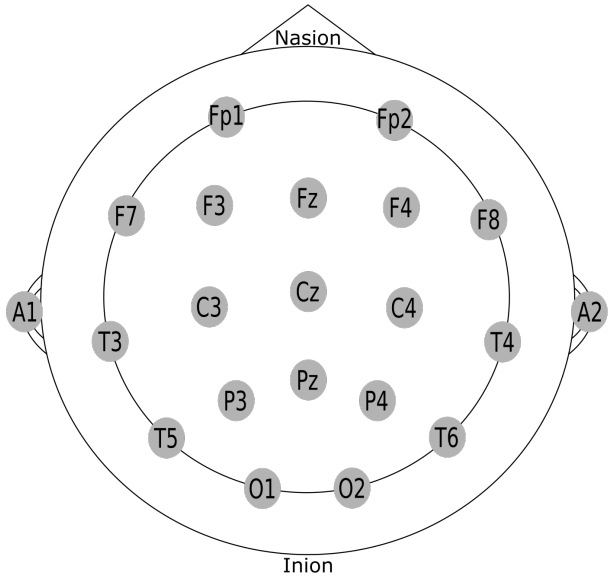

Figure 2.12: Original 10-20 electrode positioning system and names by Jasper in 1958. (Adapted from [75]).

20. e.g. (F') or (F"). Just a year after its introduction it was strongly criticized and the nomenclature was considered confusing [80], resulting in an improved nomenclature [81]. It was again modified to the nomenclature used nowadays by the ACNS [78] and confirmed as standard by the IFCN [77]. The ACNS modified the terminology inconsistencies and adopted two letters for the intermediate electrodes between brain areas, frontotemporal (FT), frontocentral (FC), temporal-posterior (TP), centroparietal (CP), parieto-occipital (PO) and anterior frontal (AF), and presented a set of 75 electrodes in its guidelines [78]. Years later IFNC confirmed this as a standard and established procedures for recording and documenting the recordings. In its guidelines a set of 64 electrodes was presented [77]. The electrode distribution in these two guidelines are presented in figure 2.13.

The main motivation of those standard systems were to facilitate the communications and exchange of findings in the literature, creating a positioning electrode framework for ERP studies to be used in laboratories around the world. The extension to the 10% system added more electrodes with the objective of

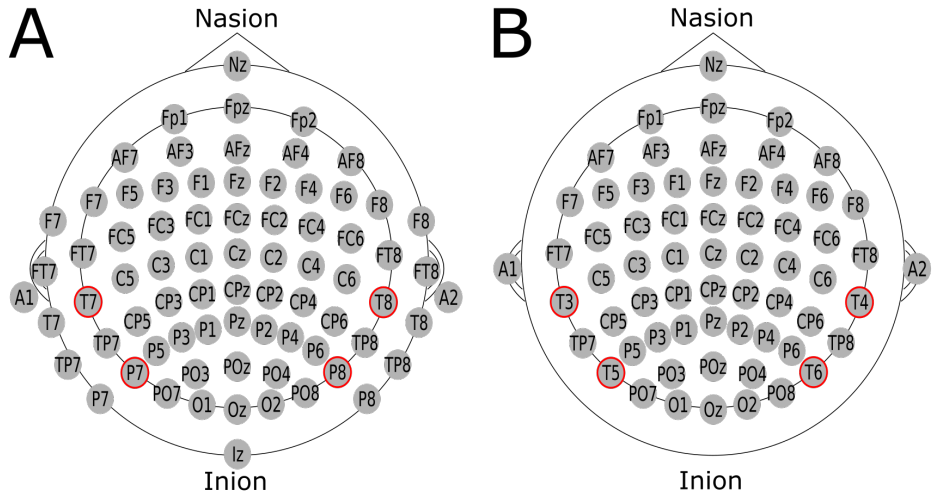

Figure 2.13: **(A)** ACNS [78], **(B)** IFCN [77], Standards 10-10 system made from the original 10-20 system and its 10% extension. Red circles denote the electrode positions that change names between the ACNS and IFCN standards. (Adapted from [77, 78]).

providing full coverage of the head to be used in topographic studies. Here is a quote from [79] about the 10% system: *"The l0% electrode system described in this paper provides full coverage of the head by closely and evenly spaced electrodes applied in readily measurable standardized locations. Although as many as 81 electrode positions are provided by this method, certain studies may require the use of only some of these leads such as those placed on the left, the right. the anterior or the posterior halves of the head or over even more limited areas of the scalp. The utilization of this system in topographic studies of spontaneous and evoked EEG activities is advocated to facilitate communications among laboratories by promoting standardization."*

The 10-20 system is considered the standard in clinical practice. To improve coverage of the temporal lobe, the IFCN presented and a new standard electrode array of 25 electrodes as the minimum number for standardized recordings in clinical practice [82]. This is presented in figure 2.14

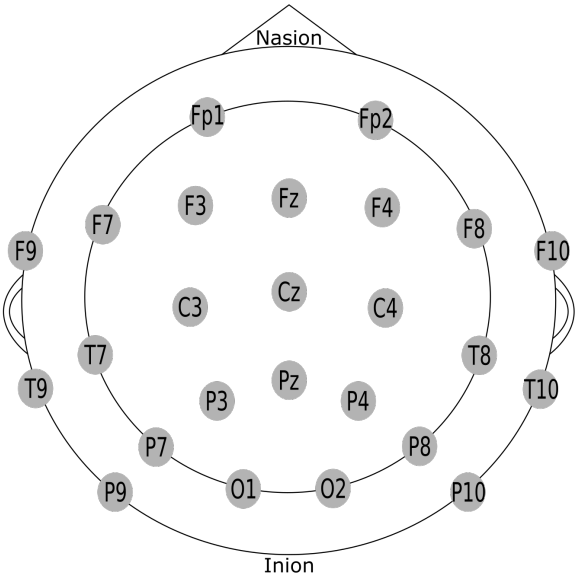

Figure 2.14: The IFCN array for EEG measurements. (Adapted from [82]).

2.3.2 Derivations from Standard Montage Systems

The five percent electrode system, or 10-5, was proposed to extend the international 10-20 and 10-10 systems up to 345 electrode locations, for studies on ERP topography and source analysis of EEG signals, and to promote standardization in hdEEG studies [83]. Similarly to the first extension of the 10-20 system to the 10-10 system; the 10-5 system included a more dense cover of the head, up to 345 positions, by adding electrodes in the intermediate areas of the 10-10 standard, and introducing the designation of those new position. A subset of 128 electrodes was recommended for high-density studies and development of EEG caps.

2.3.3 Other Montage Systems

Other montage systems provide high-density recordings up to 256 electrode positions, however the use of different electrode distributions are mostly associated to certain companies that produce them. Three examples of distributions that can reach such a number of electrodes are presented here: geodesic distribution, electrode distribution over a curve space (Electrical Geodesics, Inc; Oregon, USA) with a designation based on number. This distributes the electrodes over the head,

and includes electrodes on the lower part of the brain and face [84]. Equidistant ANT/DUKE layout in which all electrodes have the same distance with their neighbors, uses designations starting with letters standing up for left (L), right (R) and central (Z) and numbers to aside (ANT Neuro, Inc; Hengelo, Netherlands). A circular distribution considering the head as concentric circles, labels the electrodes using a combination of letter and numbers (BioSemi, Inc; Amsterdam, Netherlands).

2.4 EEG Source Reconstruction

Source reconstruction is the estimation of source activity from the information registered by electrodes at the scalp. In this process, the parameters of the current sources or dipoles are estimated. In the static case, when a single time sample or the averaged time courses of EEG activity are considered, the parameters to estimate are location, orientation, and intensity (amplitude) and where all the parameters can be described with three components (x,y,z), referring to a 3D space. When considering the dynamic case, a time series of EEG is the input, therefore, the intensity can vary over time. Therefore the time-courses of the source activity can also be estimated.

EEG Source reconstruction is often called EEG source imaging (ESI) in the literature, and less often brain mapping. In this work, the term source reconstruction is referred to as the estimation using EEG as the recording technique and input for the estimation process. Source reconstruction is a broad and extensively studied neuroimaging technique. Multiple approaches and methods have been proposed to estimate current source activity and there are multiple elements that are involved in this estimation. In this section, some generalities and elements required for source reconstruction are introduced.

The applications of source reconstruction are diverse, with localization of epileptic foci one of the most widely known and researched applications. In this clinical application, source reconstruction serves as pre-surgical tool, with the objective of identifying and locating the epileptic zone in drug-resistant focal epilepsy [23, 85–88]. In addition to its clinical significance in epilepsy, it has been an important tool for cognitive neuroscience in order to identify neural markers within source activity [89–91]. Source reconstruction allows researchers

to create activity maps that can be used to identify active regions and patterns in the cortical sheet. This has been demonstrated in experimental studies involving motor, sensory, and cognitive functions [92–96], in which source reconstructions have been applied. Due to the high temporal resolution, the reconstructed source space can serve to decode dynamics and interactions of brain regions in functional connectivity studies [97–100]. It has been applied to identify networks in healthy brain activity and during diseases [27], and to monitor cognitive states [101], using connectivity in the source space. The source activity maps offer a better discrimination between brain regions, resulting in a higher discrimination and interpretability of connectivity networks, while connectivity at electrode space is considered difficult to interpret due to the volume conduction problem [28, 102]. Other applications involve the use of cortical space for BCI systems for motor imagery classification and biomarker identification [103–108].

The source reconstruction technique can be summarized intro three closely related elements: source activity, volume conductor and scalp recordings. Modeling the relationship from source activity to electrode recordings is called forward modeling, while using the electrode space to estimate the source activity is called inverse modeling. While the forward model estimates the module conductor, the inverse modeling estimates the source activity that produces the recordings at scalp. Figure 2.15 shows the three elements involved in source reconstruction and their relation with forward and inverse modeling.

The relationship between the current sources and electrodes can be represented using the following equation, called the forward equation:

$$\boldsymbol{y} = \boldsymbol{M}\boldsymbol{x} + \varepsilon \tag{2.1}$$

The data matrix $\boldsymbol{y}$ represents the EEG signals registered at scalp. $\boldsymbol{x}$ represents the amplitude time courses of the current source activity, which is unknown. $\boldsymbol{M}$ is the volume conductor model, also called the lead field matrix, that contains the linear relationship between the cortical current sources and the registered signals by electrodes; and ε is the noise matrix. The data matrix $\boldsymbol{y} \in \mathbb{R}^{N_{ch} \times N_t}$ where its rows are formed with elements y_{it}, being $i = 1, 2, ..., N_{ch}$ and $t = 1, 2, ..., N_t$, in other words, the signal recorded by the ith sensor at time t. The matrix of the current source activity $\boldsymbol{x} \in \mathbb{R}^{N_s \times N_t}$ contains the source time courses of the

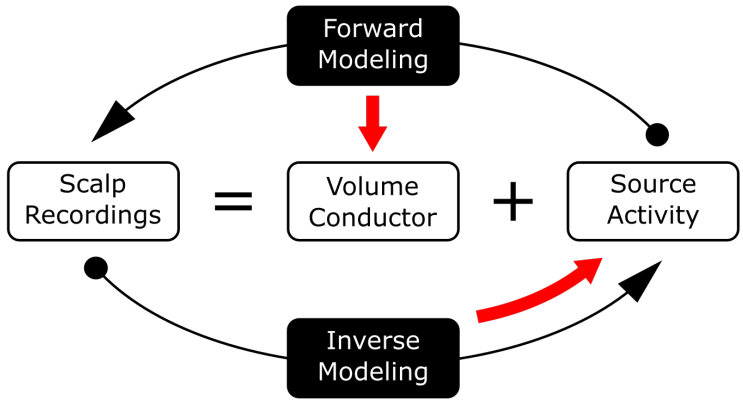

Figure 2.15: Elements of source reconstruction: source activity, volume conductor and scalp recordings. The red arrows point to the elements that each modeling estimates.

sources x_{st} produced by sources $s = 1, 2, ..., N_s$ at the time t. The lead field matrix $\boldsymbol{M} \in \mathbb{R}^{N_{ch} \times N_s}$ establishes how is the potential for each electrode due to the sources, particularly, the element M_{is} of $\boldsymbol{M}$ relates the ith sensor with the sth source. Therefore, each electrode registered potential y_{it} is a weighted sum of the electrical fields due to the source activity, represented as follows:

$$y_i(t) = M_{i1}x_1(t) + M_{i2}x_2(t) + ... + M_{iN_s}x_{N_s}(t) + \varepsilon_i(t) \tag{2.2}$$

expressed in matrix form in the forward equation (2.1).

In forward modeling the problem is centered on computing the lead field matrix $\boldsymbol{M}$, as it represents how the potentials are distributed in the scalp due to current sources in the cerebral cortex; while in the inverse modeling (solving the inverse problem), the problem is centered on estimating the amplitude time-courses of the unknown source activity $\boldsymbol{x}$

2.4.1 Forward Modeling

Forward modeling aims to identify the relationship of the current source activity with the electrodes at scalp. In summary, computing the lead field matrix M. The volume conductor model $\boldsymbol{M}$ is essential for solving the inverse problem

and estimating source activity, where the accuracy of the model can influence the quality of the estimation [109–111]. There are several methods to compute this model that can vary in complexity and accuracy to represent the complex cortex-electrodes relationship. To describe this, the forward model considers the conductivity properties of the different tissues that the electrical field passes through before arriving to the electrodes. Generally, the tissues considered are: scalp, skull, and gray matter (brain cortex). However, more complex models can include some additional tissues like the CSF, white matter, and air cavities. The CSF is key in the volume conduction problem and its influence in modeling has been found significant to perform source reconstruction accurately [110, 112].

The most widely used methods to compute the volume conductor are the spherical head model, the boundary element method (BEM), and the finite element method (FEM). Listed below are the generalities of each method:

- The spherical head model is a simplified representation of the brain. It uses concentric spheres to represent the conductivity effects of different tissues. Each sphere is related to the tissues to model, and the most common models involve 3 tissues (3-shell head model) and 4 tissues. Often brain, skull, scalp are modeled, with CSF in the 4-shell head model. This representation considers the different conductivities of each tissue, and also considers each tissue as an homogeneous medium and thus, the scalp voltage distribution is a result of series of source distributions in the homogeneous spheres [113].

- Similar to the spherical head models, BEM head models approximate each of the different tissues of the volume conductor as a isotropic and homogeneous conductive medium, but instead of using spheres it uses realistic shaped compartments [114]. The realistic shapes are derived from MRI segmented images that allow researchers to differentiate the tissues. The different layers (associated with each tissue) in BEM are represented by a triangle mesh in their boundaries with another tissue; and in each layer, the conductivity is considered homogeneous. Skull, scalp and brain are modeled in 3-layer models, while, CSF and white matter can be modeled in 4- and 5-layer models, respectively. Regarding its complexity, it is more complex than a spherical model, as the BEM layers calculation depends on segmented MRI

images. It requires more computing power. Years back this could take days, but nowadays a couple of hours are required.

- The FEM method uses polyhedrons (in general tetrahedrons or hexahedrons) to represent each one of the different head layers. As BEM, the FEM layers are also derived from MRI-segmented images, however FEM has the particularity that each polyhedron can have a different conductivity. It allows to model each tissue as an anisotropic and non-homogeneous tissue, approaching the forward model to a more realistic scenario, not only on shape, but also in conductivity modeling [111, 115, 116]. In particular, the influence of the skull anisotropy has been found relevant for the inverse solution [117].

It has been shown that, by using a realistic head model based on BEM or FEM, it is possible to achieve a better spatial discrimination of cortical sources in comparison with the spherical models [118]. The use of a spherical model instead of a realistic model can lead to larger errors in reconstruction of around a few centimeters [112, 119]. Additionally, BEM and FEM models rely on MRI images and its processing to segment the different tissues in the head, therefore a more realistic and accurate representation of the brain can be achieved, including its sulci and gyri structures [19]. The most commonly used model is the BEM head model, primarily due to its low computational requirements. However BEM models cannot represent inhomogeneities, e.g. skull holes, while FEM models can deal with such inhomogeneities and mediums that have anisotropic conductivity. FEM implementation is more complex than BEM due to the volume of meshes required in the FEM modeling, while BEM uses meshes of boundaries that are more simple [117].

During forward modeling using realistic brain representations, the center of the current dipoles or sources are fixed *a priori* by sampling the cerebral cortex. Usually a number higher than 3000 source centers are selected to constitute the source space. They are distributed to cover all the gray matter, usually maintaining the same amount between hemispheres, and trying to represent the whole gray matter without missing points in the thinner parts[13]. The number of sources N_s influences the spatial resolution of the cortex: a higher number of sources

represents the cortex better and might yield more spatial accuracy, while to process higher numbers involves the use of larger matrices, which can lead to numerical precision issues, the use of more computing complexity and memory for processing and displaying. The number of sources also influences the size of the lead field matrix $\boldsymbol{M}$, that lately influence the inverse modeling. In contrast, a lower number of sources can lead to less spatial sampling resolution and less spatial accuracy, while faster computations due to the smaller size of the matrices. Therefore, a balance of a number of sources is required; typically models contain between 3000 to 6000 sources [13]. Figure 2.16 presents the cortical sheet represented by 5000 sources.

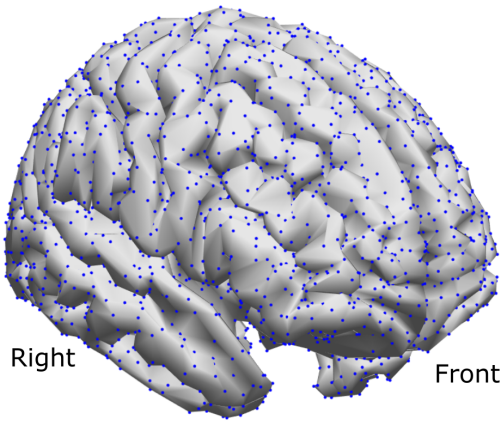

Figure 2.16: 3D view of the distributed sources representing the cortical sheet with 5000 sources. The centers of the distributed sources are represented by the blue points.

Before calculating the lead field matrix, the electrode positions must be co-registered with the MRI head [120]. The electrode positions can have a important impact on source reconstruction [121], and it is important that they correspond to reality; at the end of the process, the lead field matrix is a representation of how the electrodes capture source activity at that specific location.

Individual models to be used during source reconstruction offer better accuracy and enhance the reconstruction quality [122], therefore it is always recommended to use an individual MRI and co-register it with electrode positions. In the cases where an individual model is not available or not possible to obtain, template

models based on multiple subjects averaged MRIs can be used, however, they should be warped using multiple head points and co-registering of electrode positions must be performed [111].

2.4.2 Inverse Modeling

Inverse modeling is the estimation of source activity, as referred in this thesis as source reconstruction. Since the 1960s, the concept of estimating source activity using the information registered by the electrodes began to be developed. The first approaches involved the use of spherical models to attempt to explain the relationship between sources and scalp potentials [123, 124].

In general, two approaches can be used to estimate the source activity, using equivalent current dipoles (ECD) or distributed dipoles [12]. Both methods are based on the plausible concept that the current source activity is produced at the cerebral cortex by a large population of pyramidal neurons that fire in temporal synchrony 2.1.2.

The ECD approach works under the assumption that the registered electrical activity is the consequence of a few equivalent dipoles. This assumption is fairly realistic, as populations of neurons and their vicinities are expected to have a strong coherence in time. Therefore, the process is centered around estimating the location and orientation of a few dipoles that can represent each one of those closed neuronal populations [125]. This is done under a process called dipole fitting, where a pre-established number of dipoles is assumed to be active, then the dipoles are moved and rotated around the cortical areas and placed into positions that fit best with the EEG data. This approach uses multiple linear and non-linear methods to determine the positions of the dipoles, their orientation and magnitude, where the solution is accepted if the dipole locations lie in the whole volume within a certain radius of the sphere model [126]. Determining the number of dipoles to locate is not a straightforward process, *a priori* knowledge of the number and locations is required as inputs for the process [127]. The ECD approach can estimate the location center of the source activity, but it cannot describe the volume of cortex involved in the activity [125], therefore, general conclusions that a particular brain area or region is involved in the activity of interest can be made [128].

The distributed approach consists of estimating the amplitude of a predefined

number of sources; independently of the method for forward modeling, for distributed models the center of the current sources are fixed *a priori*, and depending on the inverse solution method, the orientation can also be fixed, e.g. using the plausible assumption that the currents flow perpendicularly to the cortex surface (see section 2.1.2), therefore the orientations can be set orthogonal to the cortex surface. The distributed approach estimates of the current density distribution, the amplitude of each source, can be found using the linear relationship electrodes-sources established by the lead field matrix. However, as the inverse solution focuses on estimating the moments of all the sources, the number of undermined elements of variables increases [125, 129]. Then, the inverse problem of estimating the amplitude of the N_s number of sources using the voltage recorded by N_{ch} number of channels is ill-posed and ill-conditioned, since $N_s >> N_{ch}$ the solution is non-unique and unstable. Infinite amplitude configuration in the sources can lead to the same electrode recordings; in addition, the solution becomes unstable, where the estimation is highly sensible to small changes in the EEG data [12].

To overcome such characteristics of inverse modeling, multiple algorithms have been proposed. The literature is vast in that sense. In attempts to summarize the algorithms and their properties, multiple comparisons and reviews in distributed source reconstruction have been written [130–135]. In multiple cases the algorithms have similarities, or are based on the same principles, and in other cases the algorithms are a hybrid between traditional algorithms. In the context of this thesis three types of algorithms are considered using a similar categorization as proposed in [129]: algorithms based on minimum norm, algorithms based on a Bayesian framework, and algorithms based on scanning methods.

- **Based on Minimum norm:** This family of algorithms offers a solution to the distributed inverse modeling by combining regularization with the least square (LS) problem solution. The inverse solution can be approached as a minimization problem as follows:

$$\boldsymbol{J} = argmin_{(\boldsymbol{x})}\{||\boldsymbol{M}\boldsymbol{x} - \boldsymbol{y}_k||_2^2\} \tag{2.3}$$

  To estimate the source activity distribution $\boldsymbol{x}$ using the LS approach, the

solution can be found by finding the derivative of the function $\boldsymbol{J}$ respect to $\boldsymbol{x}$ and making it equal to zero, resulting in the LS formula for $\boldsymbol{x}$:

$$\hat{\boldsymbol{x}} = (\boldsymbol{M}^T\boldsymbol{M})^{-1}\boldsymbol{M}^T\boldsymbol{y} \tag{2.4}$$

where the terms $\boldsymbol{M}^T$ refers to the transpose of the lead field matrix $\boldsymbol{M}$. From (2.4) the term $(\boldsymbol{M}^T\boldsymbol{M})^{-1}\boldsymbol{M}^T$ is known as $M^\dagger$ the Moore-Penrose pseudoinverse of $\boldsymbol{M}$ [136]. However, due to the ill-posedness and ill-conditioned characteristics of the inverse modeling, infinite solutions for the source activity $\boldsymbol{x}$ can be found to minimize $\boldsymbol{J}$ and fit with the EEG data $\boldsymbol{y}$, thus a solution that considers the noise is required. Using Tikhonov-Phillips regularization [137, 138], the optimization problem in equation 2.3 can be rewritten as:

$$\boldsymbol{J} = argmin_{(\boldsymbol{x},\lambda)}\{||\boldsymbol{M}\boldsymbol{x} - \boldsymbol{y}||_2^2 + \lambda^2||\boldsymbol{x}||_2^2\} \tag{2.5}$$

where λ is a regularization parameter that weights the norm of the estimated solution. Adding regularization to the minimization problem forces the estimation $\boldsymbol{x}$ to have the minimum norm and still fit the data. The solution to the optimization problem can be estimated as follows:

$$\hat{\boldsymbol{x}} = (\boldsymbol{M}^T\boldsymbol{M} + \lambda\boldsymbol{I})^{-1}\boldsymbol{M}^T\boldsymbol{y} \tag{2.6}$$

where I is an identity matrix $in\mathbb{R}^{N_s \times N_s}$. The method minimum norm estimation (MNE) uses this approach to estimate the current source activity [12, 139]. The MNE solution concentrates the active sources in the cortical surface closer to the scalp. It considers that small currents near to the the scalp can produce electric fields with a similar amplitude than higher currents in deep zones, therefore, the MNE solution biases the solution to superficial sources, and is therefore not appropriate for deep source reconstruction [140].

Variants of MNE, such as weighted minimum norm estimation (wMNE or WMN), introduces a weighting matrix in the regularization term in

order to attenuate the bias effect and compensate deep source activity [140, 141]. Another variation is the low-resolution electromagnetic tomography (LORETA), which introduces a Laplacian matrix in the MNE regularization term to ensure spatial coherence, assuming that the neighboring sources are simultaneously and synchronously activated. This results in an improvement of the spatial accuracy of source reconstruction [142]. The Dynamical Statistical Parametric Mapping (dSPM) [143] is also a variation of the minimum norm that imposes a normalization of the rows of the inverse operator using the covariance matrix of the noise [144]. Another variation is the standardized LORETA (sLORETA). It imposes a nonlinear normalization of the variance of the inverse estimation, this allows to guarantee zero errors in localizing the source activity in the absence of noise [142].

The minimum norm approach and the aforementioned variations are some of the most known and used algorithms for source estimation. However, their solutions are recognized to be smooth, extended over a high cortical area. Methods less recognized, like generalized MNE (GMNE) [145] and penalized LS [146], implement the use of the L1-norm in the regularization to obtain more focalized solutions. Other methods like Classical LORETA Analysis Recursively Applied (CLARA) [147] implements iterations of LORETA while reducing the source space in order to separate closely neighboring sources.

- **Based on a Bayesian framework:** This technique consists of estimating the prior probability of the source activity $p(\boldsymbol{x})$, and correcting it using the probability of the given measurements $p(\boldsymbol{y}|\boldsymbol{x})$ to estimate the posterior source activity distribution $p(\boldsymbol{x}|\boldsymbol{y})$ recorded by the electrodes [148]. In that sense, the posterior source activity $p(\boldsymbol{x}|\boldsymbol{y})$ can be expressed using the Bayes' theorem as:

$$p(\boldsymbol{x}|\boldsymbol{y}) = \frac{p(\boldsymbol{y}|\boldsymbol{x})p(\boldsymbol{x})}{p(\boldsymbol{y})} \tag{2.7}$$

where the noise $p(\varepsilon)$ is assumed as a Gaussian process with zero mean and covariance C_ε; and the probability of the measurements $p(\boldsymbol{y})$ in the denominator of 2.7 is considered 1 as the recordings do not vary. Based

on these considerations and applying the expectation operator, the source activity $\hat{\boldsymbol{x}}$ is the expected value of $p(\boldsymbol{x}|\boldsymbol{y})$, and can be expressed as:

$$\hat{\boldsymbol{x}} = E[p(\boldsymbol{x}|\boldsymbol{y})] \tag{2.8}$$

when the source activity $\boldsymbol{x}$ is assumed to follow a Gaussian distribution with covariance $\boldsymbol{C}_x$ and zero mean, the estimation can be described as:

$$\hat{\boldsymbol{x}} = C_x M^T (C_\varepsilon + M C_x M^T)^{-1} Y \tag{2.9}$$

Then the reconstruction quality depends on the estimation of the covariance matrices C_ε and C_x. Several methods uses this Bayesian framework as a basis and have established approaches to estimation of the covariance matrices e.g using informative priors. The methods multiple sparse priors (MSP) and Bayesian model averaging (BMA) are based on this framework. In the case of the first method MSP, it involves a set of spatial distributed priors called patches, and a minimization of a free energy cost function to estimate the parameters of the source covariance C_x and noise covariance C_ε [149–151]. In the case of the BMA method, a set of anatomical constraints can be included assuming that a particular functional space was the generator of the EEG recordings [152].

- **Based on Scanning methods:** These methods are focused on source localization instead of providing the source activity estimation for the cortical grid. This methods performs a scanning source by source, evaluating their possible contribution to the registered EEG activity. In this approach each source is evaluated and classified into two subspaces, noise subspace or signal subspace, assuming that both subspaces are orthogonal to each other. The multiple signal classification (MUSIC) and its variation Recursively Applied and Projected (RAP-MUSIC) and truncated RAP-MUSIC (TRAP-MUSIC) can be applied for estimating the number of sources and their location [38, 153, 154].

2.4.3 A General EEG Source Reconstruction Pipeline

The general steps for performing source reconstruction are summarized here. An overview of the steps is shown in figure 2.17, which presents an example of the typical source reconstruction pipeline. Accurate source reconstruction requires several processing steps that are based on two main elements: EEG recordings and structural MRI. Both EEG and MRI require pre-processing before being used as inputs for the source reconstruction algorithms. The MRI is the basis of the head model, and its processing consists of volume segmentation and the creation of 3D meshes to represent the tissues in the model, usually, scalp, skull, CSF, gray matter and white matter. As forward modeling establishes the relationship between sources and electrodes at scalp, the location of the 3D electrodes is required. A co-registration process using the fiducials (nasion and pre-auricular points) marked in the MRI and the fiducials registered with the electrode positions is applied to establish the correct electrode positions in the 3D volume[13]. The output of the forward model is then the lead field matrix $\boldsymbol{M}$ and a 3D mesh of the gray matter, including the position of the distributed sources.

Before starting the EEG recording, the electrode positions and the fiducial points are usually registered to be used for the MRI co-registration. After recording, the raw data needs to be processed in order to extract the brain activity of interest and reduce the noise level. Some common steps in pre-processing are filtering, artifact correction and rejection, electrode re-referencing, epoching and down-sampling. These pre-processing steps are reviewed in more detail in section 3.3.3. After pre-processing an averaging process of trials of the same condition is performed to obtain ERP responses. This constitutes the $\boldsymbol{y}$ signal to be reconstructed.

With the known values of $\boldsymbol{M}$ and $\boldsymbol{y}$, the inverse methods can be applied to estimate the source activity $\boldsymbol{x}$. A detailed description of the estimation algorithms used in this thesis is presented in section 3.1. Finally, by using the reconstructed source activity $\hat{\boldsymbol{x}}$ and the 3D mesh of the gray matter, brain activation maps can be generated and analyzed.

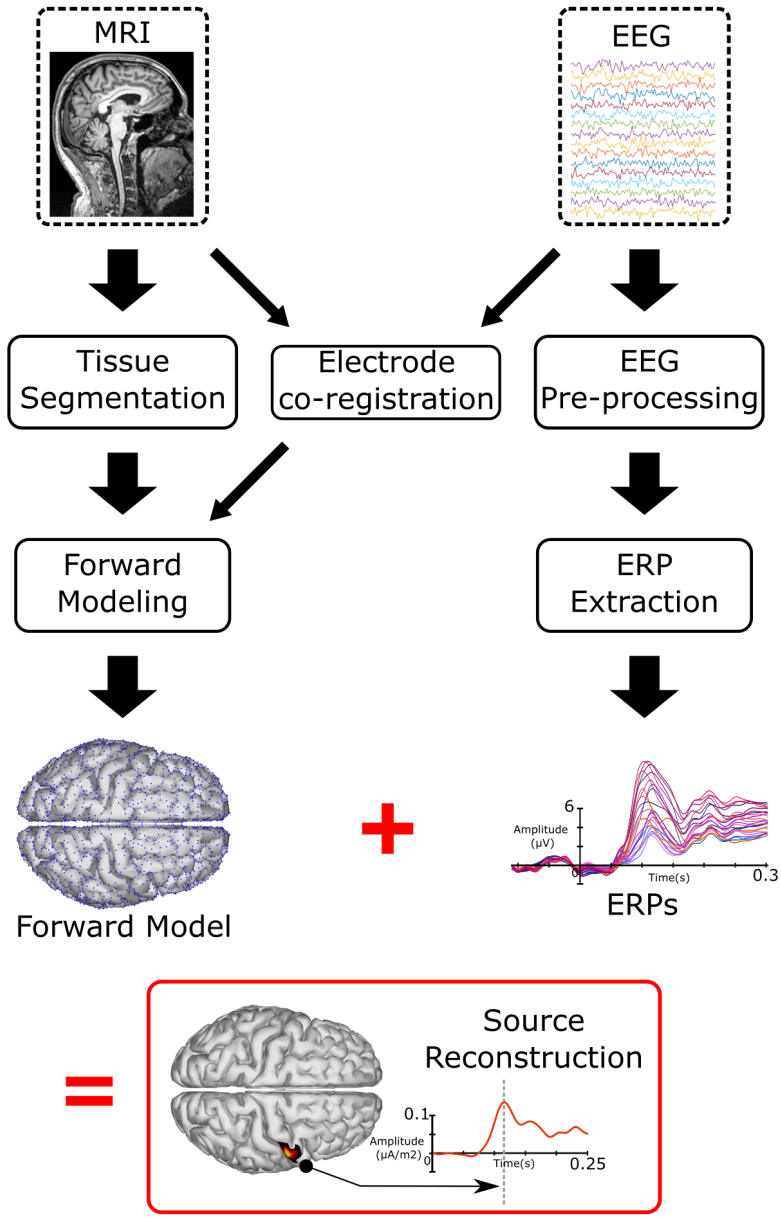

Figure 2.17: Typical Source reconstruction pipeline.

2.4.4 Influence of spatial sampling

The spatial sampling, number of electrodes on the scalp, has evolved since the first recording of Hans Berger with two electrodes[1]. It has gradually evolved towards

hdEEG. The introduction of the 10-20 system [75] established 21 electrodes that are still common practice in clinical settings, although the IFCN recently recommended a modified set of 25 electrodes that allow for a better covering of the temporal lobe [82]. The 10-10 system [81] expanded to 71 electrodes to cover the scalp; then, with the introduction of the geodesic electrode distribution, the number of electrodes was increased up to 256 electrodes [155], and with the introduction of the 10-5 system [83] the number of EEG electrode positions was set to 345 locations for scalp coverage, being the maximum number presented. Multiple ldEEG wearable devices have been developed in the last two decades, devices like Emotiv Epoch, OpenBCI, gNautilus (g.tec medical engineering GmbH, Austria) have been mostly used for BCI applications and cognitive neuroscience research while, NeuroSky and Muse have been used for neurofeedback and leisure activities [156]. As they are ldEEG its use is not intended for source reconstruction. A summary of the electrode number evolution is presented in figure 2.18. It includes an overview of the ldEEG wearables developed in the last two decades.

Accurate source reconstruction depends on multiple elements. Among them, the number of electrodes and their locations represent an important element [11, 13]. It is generally accepted that a higher number of electrodes yields higher source reconstruction accuracy [22, 23, 25]. Since the first studies on source reconstruction in the 1970s, it has been recognized that there is a need to use multiple electrodes covering the whole brain to extend the estimation to all sources in the brain [124]. Also, in [157], it was recognized that hdEEG with 128 electrodes appears to be sufficient to characterize the electrical potentials at scalp surface. Currently, systems with 128 and 256 electrodes are common commercial options. The IFCN recommends the use of hdEEG in brain imaging studies as it allows source reconstruction with sub-lobar precision [82], establishing that at least 64 channels of EEG should be used for source reconstruction. However, some hdEEG systems include a higher number of electrodes by adding electrodes to the scalp, but also locating some of them over the face, neck and cheeks. The effect of those electrodes away from the scalp have been found to be negative, and removing those electrodes allows to obtain a more accurate source reconstruction [158]. Therefore not only the number, but also the location of the electrodes, is relevant for spatial accuracy.

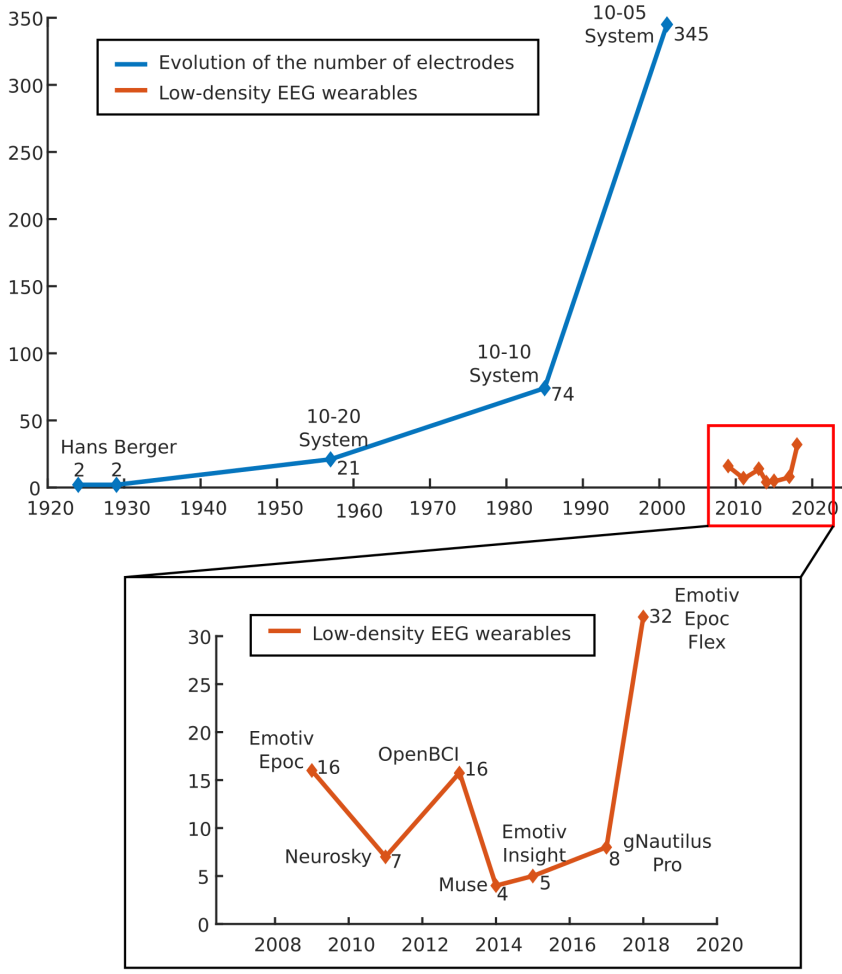

Figure 2.18: Evolution of the number of electrodes and comparison with recent developed ldEEG wearables.

Keeping adding electrodes does not represent a significant improvement of spatial accuracy. Plateaus in the localization error were found when increasing the electrode number from 96 to 128, when localizing epileptic sources in pediatric patients [24]; there is not a linear relationship between accuracy and the number of electrodes. Plateaus were also found when using more than 100 electrodes [127]. Recent studies have evaluated the use of ldEEG in epilepsy spikes localization, where non-significant differences were found when comparing source localization

using ldEEG with 25-40 with hdEEG with 204-257 electrodes [159]. In a similar line, the 25 electrodes recommended by the IFCN were used in 41 patients' EEG recordings, where the epilepsy foci localization was attempted. The results shows a satisfactory accuracy of 79% when compared with surgery outcomes [160]. Considering this, there is not a definitive consensus that only high-density can achieve high source reconstruction accuracy. In particular conditions low-density electrode configurations can obtain similar performances. In addition, electrode positioning has been found to be relevant. e.g. the recommended IFCN electrode array, by adding 4 electrodes to the 10-20 system, has had a important impact on epilepsy diagnosis and source reconstruction [159, 160].

2.4.5 Comparison of EEG with other Techniques for Brain Imaging

EEG and MEG are characterized by their high temporal resolution. As they measure the electrical and magnetic fields due to activity at the cerebral cortex, they are able to capture the complex dynamics of the brain regions' interactions with millisecond sampling, typically between 0.5 to 5 ms (2000 to 200 Hz frequency sampling). This is higher compared to other brain imaging techniques like fMRI, PET and CT, that obtain 1 or 2 samples per second. However, EEG and MEG have a poorer spatial resolution, EEG 7-10 mm and MEG 2-3 mm [161], when compared to fMRI, PET and CT. In particular, fMRI can determine the position of hemodynamic responses with millimeter resolution of 1 mm, and 0.5 mm in high-field fMRI [162]. It is important to consider that this techniques do not measure the electrical activity of the brain, they measure changes in metabolism, blood flow, regional chemical composition, and absorption. Thus, measuring these changes do not require sub sub-millisecond resolution: sampling once or twice per second is enough to capture this activity.

EEG and MEG are complementary measurements of the brain's electrical activity. The MEG technique is considered to offer a better spatial accuracy than EEG, due to the high number of sensors used in recordings and the fact that the brain's magnetic fields are not attenuated, neither are they mixed due to volume conduction. However, the brain's magnetic fields are very small: the evoked brain responses are in the order of 100 fT (10^{-15}T), while the steady earth magnetic field is in the order of 50 μT (10^{-6}T), making the brain's responses $5x10^{-8}$ times smaller than the earth's magnetic field [16]; therefore, the MEG recordings are performed

in a magnetically shielded room to isolate the brain signals from the magnetic noise around [16, 38]. As a consequence, MEG is a non-portable technique due to this special infrastructure. The same applies to fMRI, PET, and CT scans, due the volume of the systems and the infrastructure required. In the case of EEG, many measurement systems are still non-portable, however, recent advances in electrode types and wireless communication technologies have allowed for EEG recordings of 64 electrodes with portable devices that can be used for source reconstruction [101].

Chapter 3

Materials and Methods

This chapter presents the methods that are applied in the proposed methodologies. It describes in detail the source algorithms used for source reconstruction and evaluation of performance. It presents the EEG datasets that were used in multiple evaluations during the thesis, and introduces the simulation framework to generate ground-truth EEG source activity.

3.1 Algorithms for Source Reconstruction

Source reconstruction is one of the key elements of this work and has been briefly introduced in section 2.4. This section presents a more detailed approach of the algorithms that have been used in chapters 4, 5, and 6, to estimate the source activity and measure performance. As mentioned in section 2.4, multiple algorithms have been developed to solve the inverse problem, Here, only the algorithms applied in this work are detailed using the same algorithm categorization previously introduced: Based on minimum norm, based on a Bayesian framework, and based on scanning methods.

3.1.1 Based on Minimum Norm

MNE is one of the oldest algorithms for source reconstruction in distributed models. It was introduced in 1983 [139, 163, 164] and allows to estimate the current density distribution by using equation 2.6.

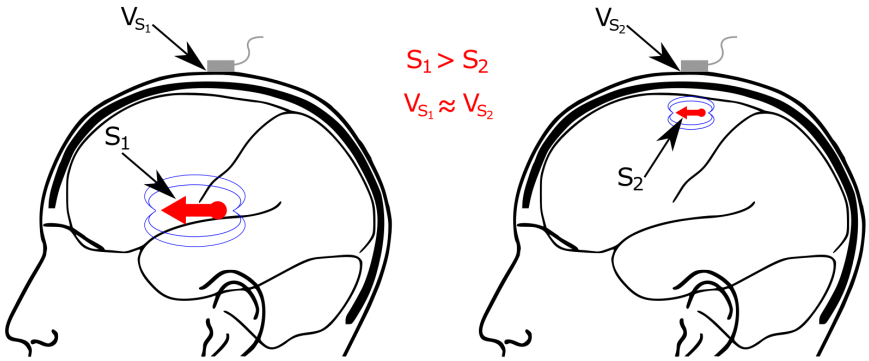

Figure 3.1: Deep source and superficial source with equal recorded potential but different strength.

This algorithm is known to produce current density distributions in the cortical areas close to the scalp. The electrical field produced close to the scalp can be similar to the one produced by a strong activation in a deeper area that is attenuated by volume conduction. To exemplify this effect, let's consider two independent sources in the brain $s1$ and $s2$ at different times. Source $s1$ is a superficial source close to the scalp, and $s2$ is a source in the cerebral cortex but located in a deep brain structure. Figure 3.1 presents a summary of the present example. Let's assume that electrode position measuring the scalp voltage produced by each source at Cz captures the same potential. The true current distribution in the deep source $s2$ has to be higher to be recorded at scalp with the same potential than the superficial source $s1$. Therefore, $\|\boldsymbol{x}_{s2}\|_2^2 > \|\boldsymbol{x}_{s1}\|_2^2$, the norm of the source activity due to the deep source $\boldsymbol{x}_{s2}$ is larger than the norm of the activity due to the superficial source $\boldsymbol{x}_{s1}$, as the inverse problem includes the minimization of source activity distribution (see equation 2.3), the source activity distribution due to source $\boldsymbol{x}_{s1}$ is preferred as it has a lower norm. To improve the MNE solution, a weighting matrix $\boldsymbol{W}$ can be included with the purpose to increase the accuracy of the method by compensating the deep sources effect on the scalp potentials. Several methods maintain the minimum norm structure while changing the calculation and structure of the weighting matrix, making this the main difference between them. Two of the most known and applied algorithms based on this structure are LORETA and wMNE [165–167].

3.1.1.1 wMNE

wMNE implements a weighting matrix $\boldsymbol{W}$ based on the topography, or contribution of each source to scalp voltage distribution. The inverse problem in wMNE can be rewritten as follows:

$$\boldsymbol{J} = argmin_{(\boldsymbol{x},\lambda)}\{\|\boldsymbol{M}\boldsymbol{x} - \boldsymbol{y}\|_2^2 + \lambda^2\|\boldsymbol{W}\boldsymbol{x}\|_2^2\} \tag{3.1}$$

and the estimation of the source activity can be computed using the following equation:

$$\hat{\boldsymbol{X}} = \boldsymbol{W}^{-1}\boldsymbol{M}^T(\boldsymbol{M}\boldsymbol{W}^{-1}\boldsymbol{M}^T + \lambda I)^{-1}\boldsymbol{y} \tag{3.2}$$

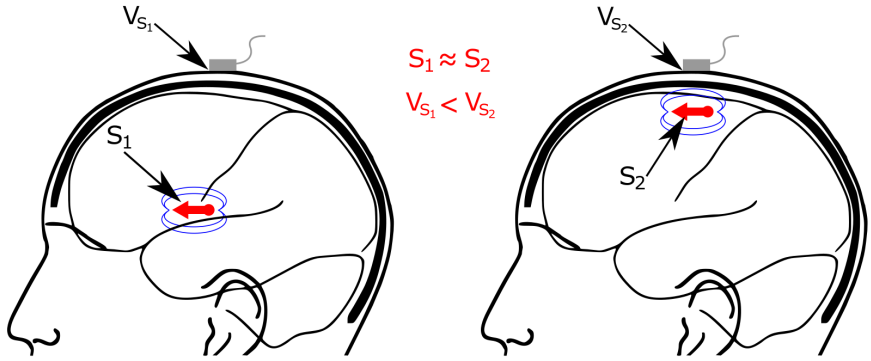

Figure 3.2: Deep source and superficial source with equal strength but different recorded potential.

Now consider the same two sources $s1$ and $s2$ with the same location as the previous example, but in this case, consider the sources with the same amplitude and producing the same source distribution$\|\boldsymbol{x}_{s2}\|_2^2 = \|\boldsymbol{x}_{s1}\|_2^2$ (see figure 3.2), and consider the structure of the lead field matrix as $\boldsymbol{M} = [l_1, ..., l_s]$, where the vector l_s is the contribution of the source s to the scalp voltage distribution. Thus, the contribution of the deeper source l_{s2} is smaller than the contribution of the source l_{s1} due to volume conduction. Considering this, wMNE uses the inverse of the norm of the topography $\|l_s\|_2$ to weight each source; where the deeper sources have a higher weight than the superficial sources. The weighting matrix can be

computed from the lead field matrix $\boldsymbol{M}$ as follows:

$$\boldsymbol{W}^{-1} = diag\left[\frac{1}{\|l_1\|_2}, \frac{1}{\|l_2\|_2}, ..., \frac{1}{\|l_s\|_2}\right] \tag{3.3}$$

where $\boldsymbol{W}$ is a diagonal matrix, and $\|l_s\|_2$ the Euclidean norm of the s-th column of $\boldsymbol{M}$. The weighting matrix works by influencing the deep sources to have a higher weight. This results in an improved localization of the source activity for deeper sources [140].

3.1.1.2 LORETA

LORETA is characterized by its low-resolution, as its estimations are blurry and widespread over large areas [142, 168]. Despite this undesired property, LORETA is one of the source reconstruction algorithms that performs better for source localization [130]. LORETA weights the source activity by using a Laplacian operator $\boldsymbol{L}$, where the weighing matrix can be defined as $\boldsymbol{W} = \boldsymbol{L}\boldsymbol{L}^2$. Through $\boldsymbol{L}$, the neighbor space of the active sources is weighted, considering the synchrony between close neuron populations. The selection of this operator directly affects the smoothness of the estimated source activity. In LORETA, the Laplacian operator is defined as follows:

$$\boldsymbol{L}_{ii} = -1 \; and \; \boldsymbol{L}_{ij} = (6/N_i)/(12N_i) \tag{3.4}$$

where $\boldsymbol{L} \in \mathbb{R}^{N_s \times N_s}$ is a matrix with values of -1 in its main diagonal ii, and values regarding the neighborhood in the ij-th locations. N_i is the number of direct neighbors of the source i, and it can be a maximum of six [140]. The estimation of the source activity in terms of the Laplacian can be expressed as:

$$\hat{\boldsymbol{X}} = (\boldsymbol{L}^T\boldsymbol{L})^{-1}\boldsymbol{M}^T(\boldsymbol{M}(\boldsymbol{L}^T\boldsymbol{L})^{-1}\boldsymbol{M}^T + \lambda^2\boldsymbol{I})^{-1}\boldsymbol{y} \tag{3.5}$$

3.1.1.3 sLORETA

sLORETA is a well-known method recognized by its zero localization errors in the absence of noise. This method is based on minimum norm, and improves the solution by applying a non-linear standardizing to the solution using the variance of the estimated activity [169]. This variance $\boldsymbol{S}_x$ is defined by:

$$\boldsymbol{S}_x = \boldsymbol{M}^T(\boldsymbol{M}\boldsymbol{M}^T + \lambda I)^{-1}\boldsymbol{M} \tag{3.6}$$

then, $\boldsymbol{S}_x$ is used to estimate the source activity as follows:

$$\hat{\boldsymbol{X}} = \sqrt{\frac{1}{[\boldsymbol{S}_x]_{ii}}}\boldsymbol{M}^T(\boldsymbol{M}\boldsymbol{M}^T + \lambda I)^{-1}\boldsymbol{y} \tag{3.7}$$

where $[\boldsymbol{S}_x]_{ii}$ represents the main diagonal of the variance. The solution of sLORETA is smooth as it is based on minimum norm, but its property of zero error localization is preferable for localizing the center of the source activity, where its position can be selected from the estimated source space by identifying the source with the highest power value.

3.1.2 Based on a Bayesian framework

The estimation of the source activity based on the Bayesian framework is given by:

$$\hat{\boldsymbol{x}} = C_x M^T(C_\varepsilon + MC_xM^T)^{-1}Y \tag{3.8}$$

where the focus of the methods is the estimation of the prior source covariance matrix C_x and the noise of the covariance matrix C_ε.

3.1.2.1 MSP

Using Empirical Bayes the source covariance C_x can be considered as a weighted sum of a number N_p of prior components $C = C_1, C_1, ..., C_{N_p}$ [150]:

$$C_x = \sum_{i=1}^{N_p} h_i C_i \tag{3.9}$$

where $h_i = h_1, h_2, ..., h_{N_p}$ are the hyperparamters (weights) of the prior components. MSP first establishes a set of distributed spatial priors or patches, where each one encodes the activity of a small brain region $C_i \in \mathbb{R}^{N_s \times N_s}$, and in a posterior process MSP optimize the hyperparamters using a cost function based on free energy.

The patches or spatial priors are formed from a column of a Green's function matrix $Q_G \in \mathbb{R}^{N_s \times N_s}$ that considers the inter-voxel distance and its connections. This matrix is defined by:

$$Q_G = e^{\sigma G_L} \tag{3.10}$$

in which $G_L \in \mathbb{R}^{N_s \times N_s}$ is a graph Laplacian that represents the inter-source connectivity information [170]; and σ is a positive value that determines the size of the patches. Therefore, each component forms a bell centered in the corresponding source. Ideally a component per each source should be considered, however due to the further optimizations to estimate the hyperparamters, in practical terms, the number of priors N_p is much less than the number of N_s.

A model based on the sample covariance matrix Σ_M can be written considering the lead field matrix:

$$\Sigma_M = C_\varepsilon + MC_xM^T \tag{3.11}$$

and considering the covariance matrices as a set of weighted sum of hyperparameters, this model covariance matrix Σ_M can be rewritten as:

$$\Sigma_M = e^{\lambda_0} C_\varepsilon + \sum_{i=1}^{N_p} e^{\lambda_i} MC_iM^T \tag{3.12}$$

where the change of variable $h_i = e^{\lambda_i}$ guarantees positive values and to apply Gaussian assumptions to the hyperparameters. MSP uses the negative variational free energy[171] as cost function for estimating the hyperparameters λ_i for the prior source covariance C_x and the hyperparameter λ_0 for the noise covariance matrix C_ε. Particularly, this hyperparameter λ_0 is considered as a regularization parameter, and MSP includes this in the hyperparameters' optimization. The free energy is used to fit the covariance of the sources to the covariance of the recorded data $C_y = \frac{1}{N_t} \boldsymbol{Y}\boldsymbol{Y}^T$, where the variational free energy cost function is defined as:

$$\begin{aligned} \boldsymbol{F} = -\frac{N_t}{2} tr(C_y \Sigma_M^{-1}) - \frac{N_t}{2} log|\Sigma_M| - \frac{N_t N_{ch}}{2} log 2\pi \\ -\frac{1}{2}(\hat{\lambda} - v)^T \Pi (\hat{\lambda} - v) + \frac{1}{2} log|\Sigma_\lambda \Pi| \end{aligned} \tag{3.13}$$

where the $|\cdot|$ represents the matrix determinant operator. $q(\lambda)$ is the prior hyperparameters and $p(\lambda)$ the approximate posterior. Both are considered Gaussian processes: $q(\lambda) = \mathcal{N}(\lambda; v, \Pi^{-1})$ and $p(\lambda) = \mathcal{N}(\lambda; \hat{\lambda}, \Sigma_\lambda)$. The meaning of each of the terms of the free energy equation 3.13 is expressed in words in table 3.1.

Free Energy Term	Meaning
$-\frac{N_t}{2} tr(C_y \Sigma_M^{-1})$	Model error
$-\frac{N_t}{2} log\|\Sigma_M\|$	Size of model covariance
$-\frac{N_t N_{ch}}{2} log 2\pi$	Number of data samples
$-\frac{1}{2}(\hat{\lambda} - v)^T \Pi (\hat{\lambda} - v)$	Error in hyperparameters
$\frac{1}{2} log\|\Sigma_\lambda \Pi\|$	Error in covariance of hyperparamters

Table 3.1: Explanation of the variational free energy equation terms [150]

The hyperparameter optimization is performed using variational Laplace, in which the objective is to identify the hyperparameters λ that maximize the free energy cost function [150]. Once the hyperparamters are found, the equation 3.8 can be solved to estimate the distributed source activity.

3.1.3 Based on Scanning Methods

MUSIC [153] algorithm is a source localization algorithm. It can estimate the localization of a source by projecting the contribution of each source to the sensor space, and evaluating whether its projection (topography) belongs to a signal-subspace or noise-subspace. This particular algorithm is useful to identify the number of active sources and locate them. However, the contribution is calculated using a localizer function, and it is often difficult to identify the true active sources due to the fact that neighbor sources of the true source can lead to a similar topography and similar value in the localizer function. Therefore, to avoid this problem the topography is out-projected and the sources can be calculated one

by one in the version RAP-MUSIC. However, the RAP version has an undesired property of leaving large values in the localizer function in the vicinity of already located sources, which produces an overestimation of the number of sources due to some false positive sources. This weakness was improved by applying a sequential dimension reduction of the estimated remaining signal space at each recursion step in TRAP-MUSIC [17, 154].

3.1.3.1 MUSIC

The objective of the algorithm is to estimate the location of the $\tilde{s}$ true sources $\boldsymbol{p}_1, ..., \boldsymbol{p}_{\tilde{s}}$ from the noisy EEG with the aid of spatial/physical information of the lead field matrix $\boldsymbol{M}$ and the temporal information of the measured signals $\boldsymbol{y}$.

The algorithm is based on the separation of data space $span(\boldsymbol{y})$ into two mutually orthogonal subspaces, the signal space $span(\boldsymbol{M})$ and the noisy space $span(\boldsymbol{M})^{\perp}$ [17, 153].

Let $\boldsymbol{P}_{sg} = \boldsymbol{M}\boldsymbol{M}^{\dagger}$ be the orthogonal projection from $\mathbb{R}^m$ data space onto $span(\boldsymbol{M})$, it is the projection to the signal space. Let's consider the structure of the volume conductor matrix as $\boldsymbol{M} = [l_1, ..., l_s]$, where l_s is the topography of the source s, and stores the weights to calculate the value of each sensor due to a possible activation of the source s.

The algorithm is based on the following property of the signal projection: for any $\boldsymbol{p}$, the norm $\|\boldsymbol{P}_{sg} l(\boldsymbol{p})\| = \|l(\boldsymbol{p})\|$ if $l(\boldsymbol{p})$ is one of the actual source topographies that contributed to the signal space. On the contrary, if $\|\boldsymbol{P}_{sg} l(\boldsymbol{p})\| < \|l(\boldsymbol{p})\|$ this is because $l(\boldsymbol{p})$ did not contribute. The localizer function $\boldsymbol{\mu}(\boldsymbol{p})$ can be computed as follows:

$$\boldsymbol{\mu}(\boldsymbol{p}) = \frac{\|\boldsymbol{P}_{sg} l(\boldsymbol{p})\|^2}{\|l(\boldsymbol{p})\|} \begin{cases} = 1, & \text{if } \boldsymbol{p} \in \{\boldsymbol{p}_1, ..., \boldsymbol{p}_{\tilde{s}}\} \\ < 1, & \text{otherwise} \end{cases} \tag{3.14}$$

To separate the signal and noise the eigenvalue decomposition of the covariance matrix $\boldsymbol{C}$ of the measurements is used, where the covariance is $\boldsymbol{C} = \boldsymbol{y}\boldsymbol{y}^T$ and is assumed to have the following structure:

$$\boldsymbol{C} = \boldsymbol{C_0} + \sigma^2 \boldsymbol{I} = \boldsymbol{U} diag(\boldsymbol{d_1} + \sigma^2, ..., \boldsymbol{d_k} + \sigma^2, \sigma^2, ..., \sigma^2) \boldsymbol{U}^T \tag{3.15}$$

Where $\boldsymbol{C_0} = \boldsymbol{U}\boldsymbol{D}\boldsymbol{U}^T$ is the covariance matrix of the noiseless data. Where

$\boldsymbol{d_1}, ..., \boldsymbol{d_{\tilde{s}}}$ are the eigenvalues related to the $\tilde{s}$ sources, and σ^2 the noise level. Then, the projection to the signal space $\boldsymbol{P_{sg}}$ can be calculated using the first $\tilde{s}$ eigenvectors, by:

$$\boldsymbol{P_{sg}} = \boldsymbol{U}(:, 1 : \tilde{s})\boldsymbol{U}(:, 1 : \tilde{s})^T \tag{3.16}$$

In practice, the number of true sources $\tilde{s}$ is not known. In theory it can be estimated from the eigenvalue decomposition of data covariance matrix $\boldsymbol{C}$, by determining the index j after which the eigenvalues $\boldsymbol{d}_j$ drop and stay flat. Figure 3.3 shows an example of the estimation of the number of sources using this approach. Another option is to use *a priori* knowledge of the number of sources based on the type of activity to analyze. However, this method can be prone to error, as the number of sources can be wrongly set, and the algorithm can estimate the locations of ghost sources, resulting from the volume conduction.

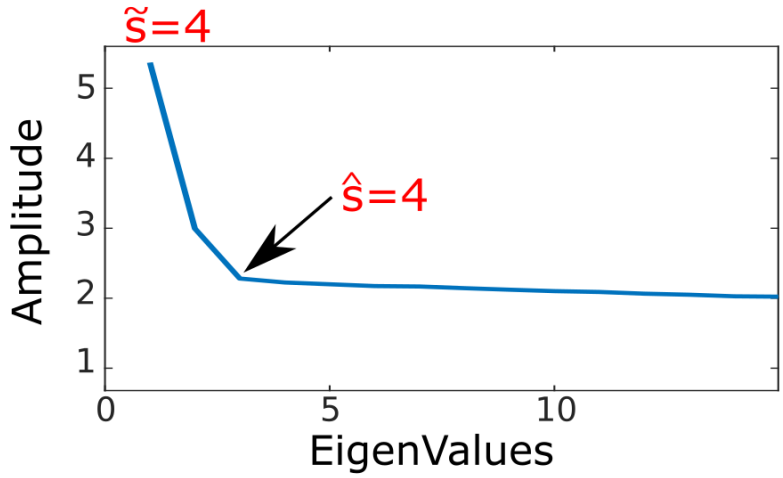

Figure 3.3: Estimation of the number of sources based on the eigenvalue decomposition of an EEG with four underlying sources.

In practice, due to the noise, the value of the localizer $\boldsymbol{\mu}(\boldsymbol{p}) \approx 1$ if $\boldsymbol{p}$ is one of the true sources $\boldsymbol{p}_1, ..., \boldsymbol{p}_{\tilde{s}}$, and $\boldsymbol{\mu}(\boldsymbol{p}) < 1$ if there is no source (or near) at the position $\boldsymbol{p}$. In the MUSIC algorithm, the $\tilde{s}$ true source positions are estimated by selecting the $\tilde{s}$ highest values of the localizer function.

3.1.3.2 RAP-MUSIC

In RAP-MUSIC, instead of finding $\tilde{s}$ local maximums of the localizer in one round, the algorithm finds a global maximum of the localizer in each sequential round. The RAP-MUSIC algorithm starts the first iteration with a plain MUSIC step in which the first location of $\boldsymbol{p}_1$ is estimated from the global maximum point of the localizer $\boldsymbol{\mu}(\boldsymbol{p})$ [17, 154].

To find $\boldsymbol{p}_k$ and $l_k(\boldsymbol{p}_k)$ with $k = 2, ..., \tilde{s}$. The process starts forming an orthogonal projection called the out-projector as $\boldsymbol{Q}_k = \boldsymbol{I} - \boldsymbol{B}_k \boldsymbol{B}_k^T$.

Where $\boldsymbol{B}_k = [l_1, ..., l_{k-1}]$ contains the topographies of the previously found sources

Now the transformed (approximated) signal space is $span(\boldsymbol{Q_k U_s})$, with $\boldsymbol{U_s} = U(:, 1 : \tilde{s})$. Its space can be decomposed as $\boldsymbol{Q}_k \boldsymbol{U}_s = \boldsymbol{U}_k \boldsymbol{D}_k \boldsymbol{U}_k^T$, where the new orthogonal projection $\boldsymbol{P}_k$ can be computed onto the transformed signal space $span(\boldsymbol{Q}_k \boldsymbol{U}_s)$ as follows:

$$\boldsymbol{P}_k = \boldsymbol{U}_k(:, 1 : \tilde{s}) \boldsymbol{U}_k(:, 1 : \tilde{s})^T \tag{3.17}$$

In the $k - th$ iteration, the location of $\boldsymbol{p}_k$ is now the global maximum point of the new localizer function $\boldsymbol{\mu}_k$ calculated as follows:

$$\boldsymbol{\mu}_k(\boldsymbol{p}) = \frac{\|\boldsymbol{P}_k \boldsymbol{Q}_k l(\boldsymbol{p})\|^2}{\|\boldsymbol{Q}_k l(\boldsymbol{p})\|} \tag{3.18}$$

RAP-MUSIC at each recursive step performs the same operation as the conventional MUSIC but applied to the transformed equation:

$$\boldsymbol{Q}_k \boldsymbol{y} = \boldsymbol{Q}_k \boldsymbol{M} \boldsymbol{x} + \boldsymbol{Q}_k \varepsilon \tag{3.19}$$

Which has the same form as the forward equation in 2.1, with the additional out-projector $\boldsymbol{Q}_k$ applied at both sides. RAP-MUSIC has the unwanted property in the recursive process, in which the algorithm leaves large residual values of the localizer $\boldsymbol{\mu}_k$ in the vicinity of already found sources, which may lead to a wrong choice of $\boldsymbol{p}_k$, this effect is known as the RAP-dilemma, and it prevents the algorithm from cleaning out the source information of previous recursion steps.

3.1.3.3 TRAP-MUSIC

To avoid the RAP-dilemma and attenuate the effect of the vicinity in the localizer function $\boldsymbol{\mu}_k$, a sequential dimension reduction of the estimated remaining signal space is calculated at each recursion step [17, 154]. The procedure is the same as in RAP-MUSIC, however, in TRAP-MUSIC at each recursion, one source is found and projected out, and hence in the following step there is one source less in the remaining signal space. This is done by calculating the out-projector $\boldsymbol{p}_k$ in the following way:

$$\boldsymbol{P}_{k(TRAP)} = \boldsymbol{U}_k(:, 1 : \tilde{s} - k + 1)\boldsymbol{U}_k(:, 1 : \tilde{s} - k + 1)^T \tag{3.20}$$

When the localization of the source is estimated by a MUSIC-based algorithm, the source time-course can be estimated using Tikhonov regularization or MNE method, by constraining the solution to the previous estimated locations.

3.1.4 Measurements of Performance

Several measurements of performance have been proposed in the literature over the years. They serve to quantify and compare the accuracy and performance of the source reconstruction algorithms. Some of the measurements of performance are meant to evaluate the spatial accuracy, which is particularly relevant for source localization and its applications e.g. localization of epileptic foci [12]. However, this is not the only source parameter that can be compared. The estimation of the source time courses is also relevant to determine the dynamics of a particular region or the dynamics of the brain networks in connectivity processes. Here, the performance measurements considered in this thesis are presented, some of which are relevant for localization, and others for time-course comparison.

The MUSIC-based methods provide a direct estimation of the source location $P_{\hat{x}}$, and if the time course is required at this position, it can be computed using MNE constrained to the estimated location. To compute the time course associated to $P_{\hat{x}}$ the MNE solution considers the column of the lead field matrix $l_{P_{\hat{x}}}$ and estimates the time course as follows:

$$\hat{\boldsymbol{x}} = l_{P_{\hat{x}}}(l_{P_{\hat{x}}}^T l_{P_{\hat{x}}} + \lambda \boldsymbol{I})^{-1} l_{P_{\hat{x}}}^T \boldsymbol{y} \tag{3.21}$$

In the case of MSP, sLORETA, and wMNE, the estimation $\hat{\boldsymbol{x}}$ is a distributed map with time-courses known. The location of the source is extracted by identifying the source with the highest power in a given sample or by averaging the power distributed map during a time of interest.

3.1.4.1 Localization Error

The localization error is computed using the euclidean distance between the position of the ground-truth source P_x and the estimated source position $P_{\hat{x}}$ using the following equation:

$$LocE = \|P_x - P_{\hat{x}}\|_2 \tag{3.22}$$

As the source space is represented in a 3D coordinated space, the euclidean distance is a direct measurement of the accuracy of the source localization.

3.1.4.2 Relative Error

The relative error, also known as a reconstruction error, is a measure that can be used for comparing both spatial and temporal accuracy.

$$RelE = \frac{\|\boldsymbol{x} - \hat{\boldsymbol{x}}\|_2}{\|\boldsymbol{x}\|_2} \tag{3.23}$$

When comparing the full matrix of the estimated source activity $\hat{\boldsymbol{x}}$ and the ground-truth $\boldsymbol{x}$, both time-courses and their locations are considered. The relative error can also be used for estimating the time-course fit between a pair-wise reconstructions computed from different numbers of electrodes. Consider the reconstruction $\boldsymbol{x}_A$ in which the position of the main source was found at P_i and its time-course $\boldsymbol{x}_{Ai}$ and the reconstruction $\boldsymbol{x}_B$ with the main source at P_j and time course $\boldsymbol{x}_{Bi}$. The relative error between the pair-wise of time-courses can be computed as:

$$RelE(pair - wise) = \frac{\|\boldsymbol{x}_{Ai} - \boldsymbol{x}_{Bj}\|_2}{\|\boldsymbol{x}_{Ai}\|_2} \tag{3.24}$$

where $\boldsymbol{x}_A$ is considered the reconstruction with the highest number of electrodes, or the reconstruction assumed to have better time-course reconstruction accuracy.

3.1.4.3 Pearson Correlation Coefficient

This performance metric measures the pair-wise correlation of the time courses of two reconstructions. Consider the same two time courses $\boldsymbol{x}_{Ai}$ and $\boldsymbol{x}_{Bi}$ from different reconstructions as in the pair-wise relative error. Then, the Pearson correlation coefficient r can be computed using the following expression:

$$r = \frac{\sum(\boldsymbol{x}_{Ai} - \overline{\boldsymbol{x}}_{Ai})(\boldsymbol{x}_{Bj} - \overline{\boldsymbol{x}}_{Bj})}{\sqrt{\sum(\boldsymbol{x}_{Ai} - \overline{\boldsymbol{x}}_{Ai})^2 \sum(\boldsymbol{x}_{Bj} - \overline{\boldsymbol{x}}_{Bj})^2}} \tag{3.25}$$

where $\overline{\boldsymbol{x}}_{Ai}$ represents the mean of the time course.

3.1.4.4 Wasserstein Metric

The Wasserstein Metric (WM), also known as earth mover's distance [172, 173], was proposed as a measurement of dissimilarity between two image histograms. In this case it can be used to evaluate the dissimilarity between an estimated reconstruction and a ground-truth [174, 175]. It measures the work required to transform the estimated power distribution of sources into the ground-truth power distribution by "transporting" the probability of mass [176].

To understand this measurement, the following example is introduced. Consider the two source distributions used previously, $\boldsymbol{x}_A$ and $\boldsymbol{x}_B$. The power of each one of the source distributions can be divided into small units with a fixed amplitude. Both distributions are divided in the same number of units. To transform the power distribution of sources $\boldsymbol{x}_A$ into $\boldsymbol{x}_B$, consider the power source distribution units of $\boldsymbol{x}_A$ as amounts of earth, and the power source distribution of units of $\boldsymbol{x}_B$ as an amount of holes. If the power distributions are equal $\boldsymbol{x}_A = \boldsymbol{x}_B$ the units of earth can directly fit in the holes. But when they are different, it will be necessary to move the earth in other directions to fill the holes. The average distance (work) between all units minimized over all possible transformations represents the WM. Considering this, a distribution of different types of distribution can be compared. e.g. the distribution resulting of a fMRI analysis can be compared with an EEG power source distribution in a meaningful way [174, 177]. This index provides a spatial comparison between the ground-truth and an estimated source activity, where a lower WM value represents a better spatial accuracy of the source reconstruction.

3.2 Simulation framework for source activity and EEG trials

The evaluation of source reconstruction methods requires a comparison with a ground-truth that accurately describes brain activity. The lack of ground-truth poses one major difficulty when evaluating the performance of source reconstruction algorithms and developing analysis methods. This problem arises when using scalp recorded EEG activity. Often there is no reference of the actual underlying source activity, only in some specific applications can ground-truth be available, e.g. epilepsy foci localization.

In this work, a technique based on sinusoidal Gaussian windowed activity has been applied to simulate the activation of a particular source. The simulation framework presented here has been used to generate EEG trials, including noise in the measurements to be of further use in evaluating the performance of source reconstruction algorithms.

The simulation framework starts with the simulation of a single or multiple source activity. By using the equation of a sinusoidal Gaussian windowed activity a source time-course s_i can be computed:

$$s_i(t) = a_i e^{-\frac{1}{2}(\frac{t-c_i}{\sigma})^2} sin(2\pi f_i t) \tag{3.26}$$

where i represents the source index and this source time-course s_i has several parameters associated with it: The window center c_i represents the time (s) in which the windowed source activity is centered. f_i determines the frequency (Hz) of the sinusoidal time-course source activity, and σ_i determines the shape of the Gaussian window by adjusting its width. An example of three source activities varying in center, frequency and width are presented in figure 3.4. The parameter a_i can be used to adjust the amplitude of the time-course, with a value of $a_i = 1$ the resulting maximum amplitude will be between -1 to 1, as the currents in source dipoles are defined in Amperes per area [16], typical values are in the order of $\mu A/mm^2$ or nA/mm^2, the parameter a_i can be adjusted to reach such levels. This simulation of source time-courses using sinusoidal Gaussian windowed activity has been applied in multiple studies to generate underlying source activity with similarities of ERP components [178].

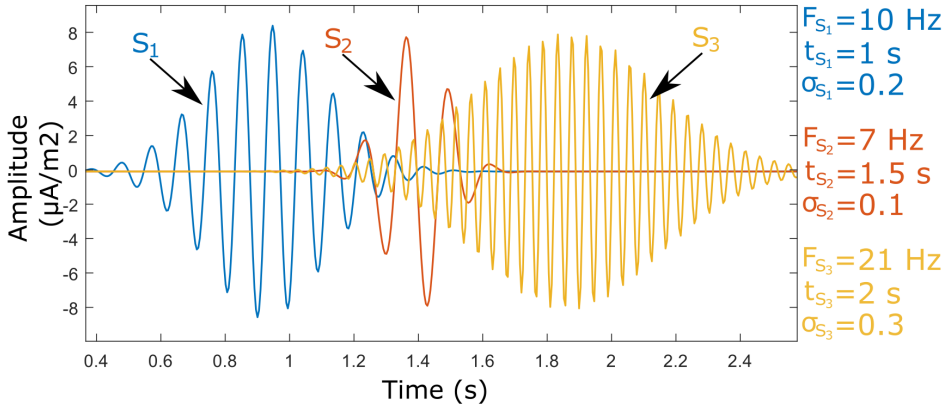

Figure 3.4: Source activity of three sources with different parameters.

The lead field matrix M has N_s columns, related to the N_s sources. Each one of the sources has an associated 3D location in the cortical sheet. After the source time-courses are simulated, a location parameter loc_{s_i} related with the column of the lead field matrix is assigned, where loc_{s_i} is the column index in which the source s_i is located. To include the neighboring synchronization, the Green's function matrix Q_G is used (equation 3.10. The time-course s_i vector is multiplied by each one of the elements of column loc_{s_i} of the Q_G matrix, producing a bell centered at loc_{s_i} source activity map x_{s_i}.

$$x_{s_i} = s_i \cdot Q_G(loc_{s_i}) \tag{3.27}$$

where $\cdot$ is the dot product, and $Q_G(loc_{s_i})$ the loc_{s_i}-th column of Q_G. Figure 3.5 shows the time-course of a single source, and the power density map at three times with and without the neighbor synchronization included.

A number n sources can be simulated, and the current source activity matrix$\boldsymbol{x}$ can be computed as a weighted sum of the n number of x_{s_i} current source maps, as follows:

$$\boldsymbol{x} = \sum_{i=1}^{n} k_i x_{s_i} \tag{3.28}$$

where k_i is a positive scalar factor that can be used to modulate the amplitude

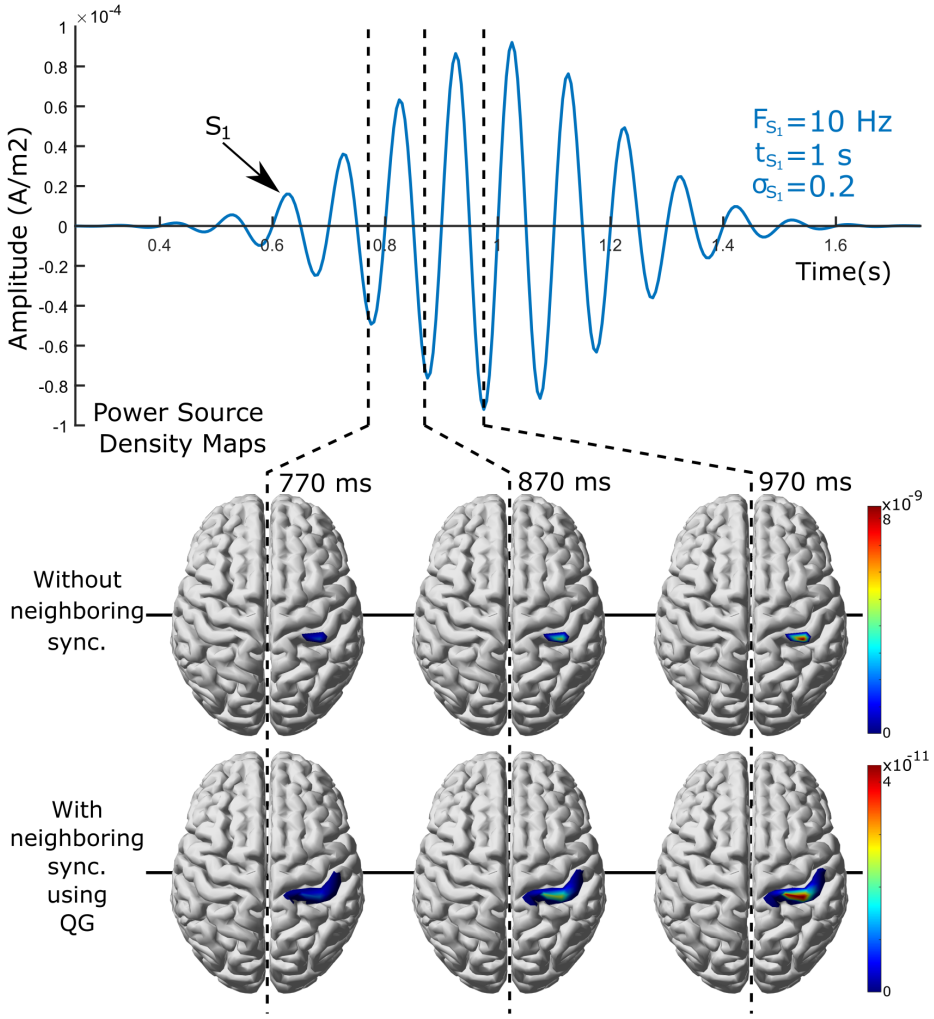

Figure 3.5: Time-course of a single source and its power density maps at three times with and without the neighbor synchronization included.

of the current source m k_i. In a multiple source case, this can be done to make a source dominant over other sources, and to set smaller sources in the background. After the distributed source activity $\boldsymbol{x}$ is obtained, the EEG forward equation (equation 2.2) can be used to simulate the EEG trial $\boldsymbol{y}$, the noise ε can be added to include measurement noise, or ignored for noise-free EEG. The measurement

noise ε can be added by computing the power of each EEG channel, and using its value as reference to generate random or Gaussian noise to add it to the signal. The power of the noise will determine the SNR of the measurements, the SNR ratio in dB can be computed from the following expression:

$$SNR_{dB} = 10log_{10}(\frac{P_{signal}}{P_{noise}}) \tag{3.29}$$

To summarize the simulation framework figure 3.6 presents a multi-source case with two simulated sources, where their power source map and time-courses are shown. The two sources were simulated using different parameters.In addition, the simulated EEG is presented with a SNR of 0dB, and noise-free.

3.3 From Raw EEG Signals to ERPs

The ill-posed characteristic of the inverse problem makes it sensible to input noise, where small changes in the input can largely affect the source distribution map. To attenuate this effect the input should have the best SNR possible. This allows to avoid source disturbances caused by the artifacts presented in the data. Source reconstruction typically uses averaged ERP responses due to the noise reduction during the averaging process. Although single-trial source reconstruction has been previously attempted, it is scarcely reported [179].

This work considers two kinds of inputs for the source reconstruction algorithms: the ERPs of measured data or the synthetic trials generated by using the simulation framework (see section 3.2). Here, the typical pipeline for extracting ERP responses is introduced. First, by introducing the artifact rejection and artifact correction concepts and methods, and second, by presenting the pre-processing steps of the pipeline.

3.3.1 Artifact Correction

Artifact correction refers to the procedures applied to the EEG signals in order to estimate the contributions of the artifacts and subtract them from the signal [62]. Procedures that lie in this category are: filtering and blind source separation (BSS) methods.

- **Filtering**: This is a common pre-processing step in signal-analysis. For EEG signals several configuration of filters can be applied; low-pass, high-pass,

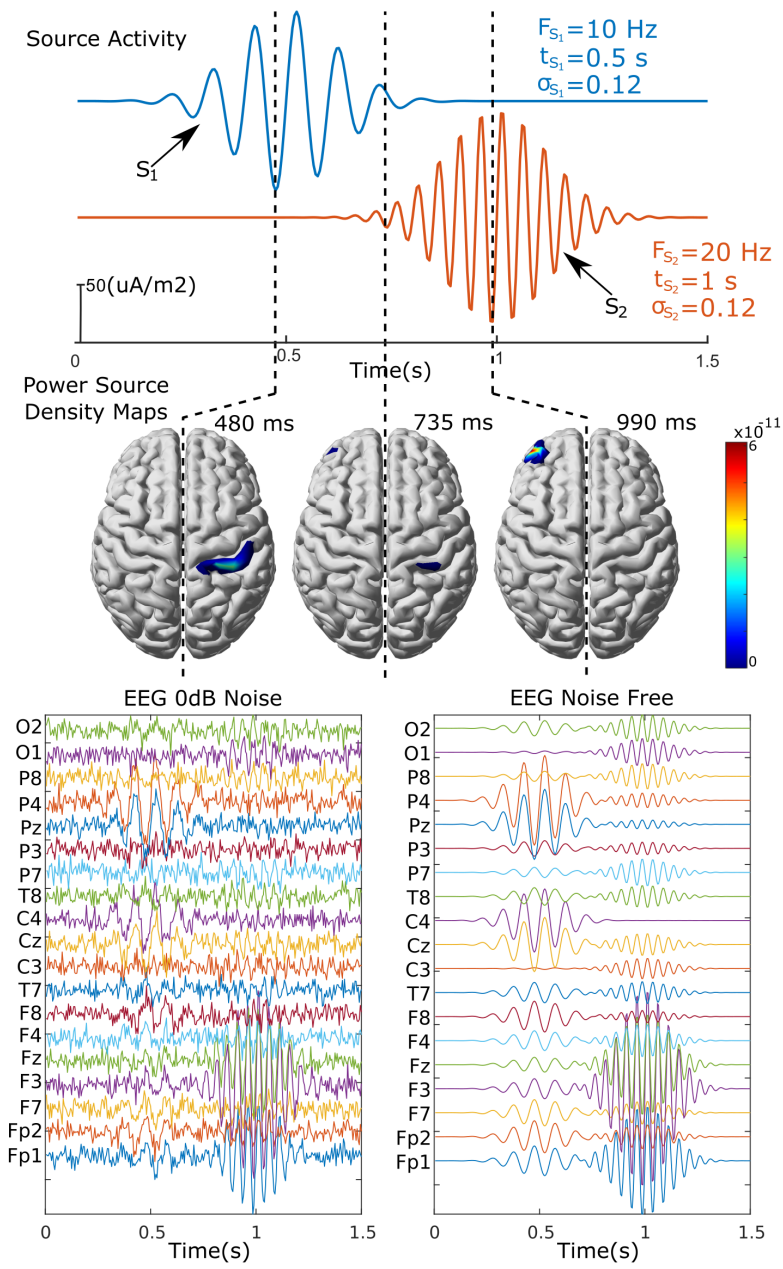

Figure 3.6: Time-courses and power source map of two sources with different weights, simulated EEG noise free and with SNR of 0 db.

band-pass, and notch filters are commonly applied. The filters to apply can be dependent on data, participant, and measurement conditions.

A high-pass filter is used to attenuate the effects of slow drifts produced by the skin potentials. Authors often differ in the value cutoff frequency of the filter. In addition the kind of electrodes used at scalp can influence the selection of this frequency, usually a 0.1 Hz is used when recording with wet electrodes and low-input impedance amplifiers, while higher values might be used with dry electrodes and high-input impedance amplifiers. However, filters above 0.1 Hz can severely distort the ERP waveforms, while filters above 0.5 Hz have been found significant in affecting ERP responses [64].

Low-pass filtering can be applied to the data to attenuate the effect of EMG activity (primarily above 100 Hz). Often the frequency of interest for brain activity is below 40 Hz [43]. However, the application of this filter can be optional and might depend on the data and participants' behavior. e.g, data from participants that move, chew or swallow constantly might require the use of a high-pass filter. Band-pass filtering is equivalent to the combination of a low-pass and a high-pass filter.

Notch filters reject a narrow band of frequencies around a specific cutoff frequency. It is usually applied to remove the power line noise which is well known to appear at 50/60 Hz depending on the network frequency of the recording location.

- **BSS Methods**: These methods approach the artifact correction by separating the data into components that can be related to the brain responses and artifacts, and then reconstruct the data excluding those artifact-related components. Principal component analysis (PCA) and independent component analysis (ICA) are common methods for BSS. In particular, ICA technique has been adopted and used to remove the contribution mostly of EOG artifacts, but also for ECG and power line. Its analysis is based on the scalp voltage distribution (topography) in which the components that have a similar scalp distribution can be separated. The components are assumed to be independent and come from different sources (note that in this context, source is not the current source from neuron populations) therefore

a linear transformation matrix can be estimated to separate the data into components. The components are evaluated (usually by visual inspection) and the data is reconstructed only with the components associated with brain activity, while the components associated with artifacts are rejected. Artifacts with variable topography e.g. specific movement artifacts, and skin potentials, are not clearly separable by ICA [62, 180–182].

Despite its efficacy to remove artifacts, this method should be applied carefully. The use of ICA can introduce error patterns in ERPs [183] and therefore, can affect the results of source localization [184]. It has been found that it can also distort the phase of the waveforms and their spectral properties [185], an important drawback to consider for connectivity analysis. Another drawback of this method is that the selection of the components can be problematic and time consuming. It requires an expert operator or analyst to decide on the components to retain and discard, which is done by analyzing the topography, power spectrum density (PSD) and patterns in the appearance. However, the components vary from participant to participant, and therefore it is often difficult to objectively remove the same kind of components from all participants, which may result in biased conclusions [62].

3.3.2 Artifact Rejection

Artifact rejection refers to the removal of data that contains artifacts and can be done in several ways; by identifying and removing bad channels e.g. channels that contain multiple artifacts, channels that were not properly connected and mostly captured noise. Another common artifact rejection practice is to identify segments of the data that contain large artifacts due to movements and remove them. This is often done by visual inspection.

The use of a threshold is typically applied to identify and reject epochs that contain EOG activity, where the typical value is $\pm 75\mu V$ to $\pm 100\mu V$ [62].

3.3.3 The typical ERP pipeline

The pipeline is presented in figure 3.7, where the steps related to artifact correction are marked in light blue, and the steps related to artifact rejection in light green.

The steps have not been covered in the artifact correction and artifact rejection sections and are explained as follows:

- **Down-sampling**: This is an optional step usually done to reduce the memory requirements for subsequent steps. Here, it is important to consider the Nyquist theorem and to avoid down-sampling to lower values than the double of the higher frequency of interest.

- **Epoching**: The epochs are segments of the EEG that are related to a particular event. They define the time ROI of the ERPs. A baseline correction is recommended. This is done by taking the average of a baseline period and subtracting it to the whole window. Usually a period of 200 ms before the stimuli is used as baseline, which minimizes the effects of changes in voltage offset across time periods and drifts [62].

- **Averaging**: This is the last step of the pipeline that results in the ERP components. This step consists of computing the average between all the epochs aligned with respect to the time-locking event or stimuli. This simple step has a significant effect on the noise level. The single trials record the background activity of the brain that is assumed to be random with positive and negative peaks, and the evoked activity, that is assumed to be time-locked to the event. In the average process all the random background activity is attenuated, while all the time-locked responses are enhanced, resulting in the distinguishable ERPs. Often, a high number of epochs is recommended to obtain clear and distinguishable ERPs. The use of low numbers may affect the noise reduction and therefore the source reconstruction accuracy [62, 72, 186].

3.4 Frequency Decomposition Algorithms

The EEG data contains a mix of signals from the brain and its surroundings, such as eyes, muscles, heart, etc. It is well known that different body processes are presented in the EEG signals with different frequencies, and the activity of the brain itself can also be found in several frequency bands related to a variety of underlying brain processes. Thus, it seems natural to use frequency decomposition

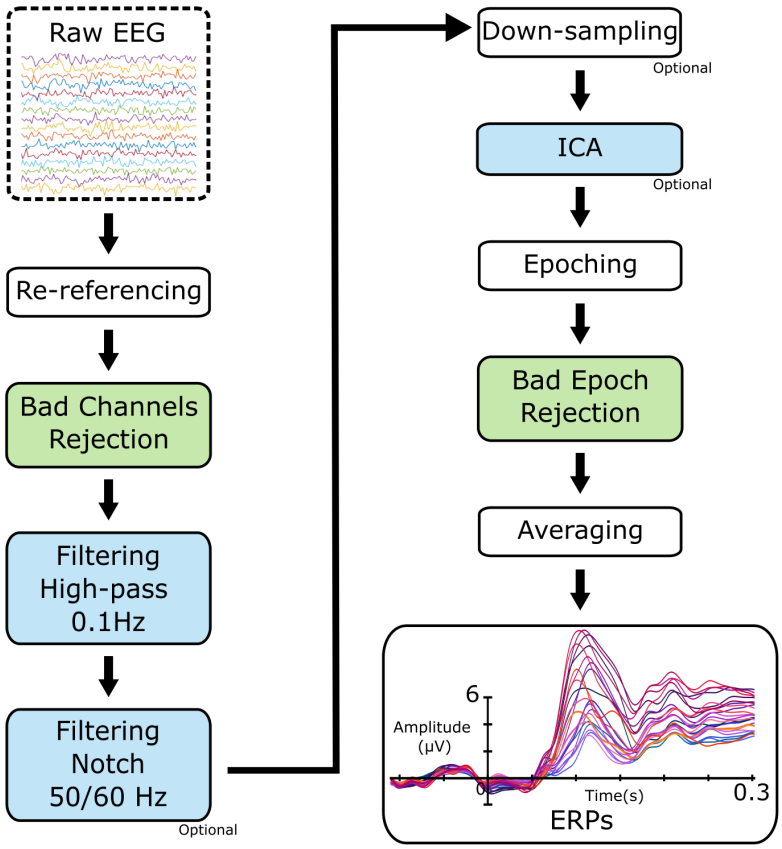

Figure 3.7: Typical pipeline for ERP calculation.

methods to decompose the EEG signals in frequency bands to analyze its content. However, the EEG signals are non-linear and non-stationary signals [18], and methods that can deal with those properties are preferred to decompose the EEG signals in frequency. Empirical mode decomposition (EMD) and its variations have been applied in multiple applications involving EEG signal analysis [187–191] and EEG source reconstruction [178, 192, 193] due to its ability to deal with non-linear and non-stationary signals to decompose the signal in intrinsic mode functions (IMF). This section presents the decomposition methods EMD and the multivariate version MEMD. These methods are further related with chapter 4.

3.4.1 Empirical Mode Decomposition

EMD is an adaptive and data-driven method for analyzing non-stationary and non-linear processes [194, 195]. It decomposes the signals in a set of oscillatory modes or IMFs time series using a sifting process. Briefly, this consists of identifying the local minima and maxima of a time series, creating new time series by interpolating across the local minima and maxima, and subtracting the mean from the original signal. Each IMF must comply with the following definition:

- The numbers of zero-crossing and extrema that are either equal or differ at most by one.
- At any point, there is a symmetry of the upper/lower envelopes with zero mean.

The process of extracting the IMFs from a time-series signal is called sifting. This is a data-driven method that does not involve any *a priori* assumption of the signal and its properties. To exemplify the process and put it into context with EEG data, let's consider the EEG from a single channel $\boldsymbol{y}(t)$ to be decomposed. EMD decomposes the time series of the channel $\boldsymbol{y}(t)$ into a set of k IMFs $\gamma_i(t)$ and a residue $r(t)$:

$$\boldsymbol{y}(t) = \sum_{i=1}^{k} y_i(t) + r(t) \tag{3.30}$$

The sifting process consists of the following steps:

1. Identify all extrema (upper and lower) in $vey(t)$
2. Generate envelopes, lower envelope $e_l(t)$ and upper envelope $e_u(t)$ by interpolating between minima and maxima.
3. Compute the mean envelope $m(t) = \frac{e_l(t)+e_u(t)}{2}$.
4. Compute the residue by extracting the mean envelope to the signal $r(t) = \boldsymbol{y}(t) - m(t)$
5. Evaluate if $r(t)$ fulfills the IMF definition. If so, $\gamma_i(t) = r(t)$, if not, repeat steps 1 to 4.

An example of a decomposed EEG signal using EMD is presented in figure 3.8.

The main drawback of EMD is the mode mixing problem, which represents the fact that oscillatory modes of several close frequencies appear in the same IMF, resulting in an unclear separation. This problem appears mainly when EMD is applied over signals with intermittent behavior and have components with close frequencies [196]. Several variants of EMD have been proposed to attenuate this effect, e.g. ensemble EMD (EEMD) and complete ensemble (CEEMD) methods have been designed to separate components in the presence of intermittency signal properties [197, 198]. Another drawback arises when applying the standard EMD and its variations in multivariate data. Usually, the number of IMF differs across channels and the information of a similar event recorded from different channels can be found in different IMF numbers for each channel (IMF misalignment). Therefore selection of IMF is required in order to extract similar frequency information in multivariate data. To attenuate the mode mixing, and improve the IMF misalignment in multivariate data, the multivariate version MEMD was proposed [199].

3.4.2 Multivariate Empirical Mode Decomposition

The MEMD method aims to address the following standard EMD limitations[200]:

1. Non-uniform signals: standard EMD can not always guarantee the same number of IMFs for each channel.

2. Scale alignment: it is not possible to guarantee that the corresponding scales have the same modes.

3. Constraining the number of IMFs for every channel could compromise time-frequency estimation; it is the nature of IMFs to vary in number.

In addition, univariate EMD can be applied channel-wise if the channels are not strongly coupled. Furthermore it is known that the EEG channels are strongly coupled, in part due to volume conduction problem, and trying to select the same number of IMFs that represent the same event information from different channels can lead to the rejection of valuable data [200]. Multivariate data are characterized by generalized oscillations (joint rotational modes), which must be

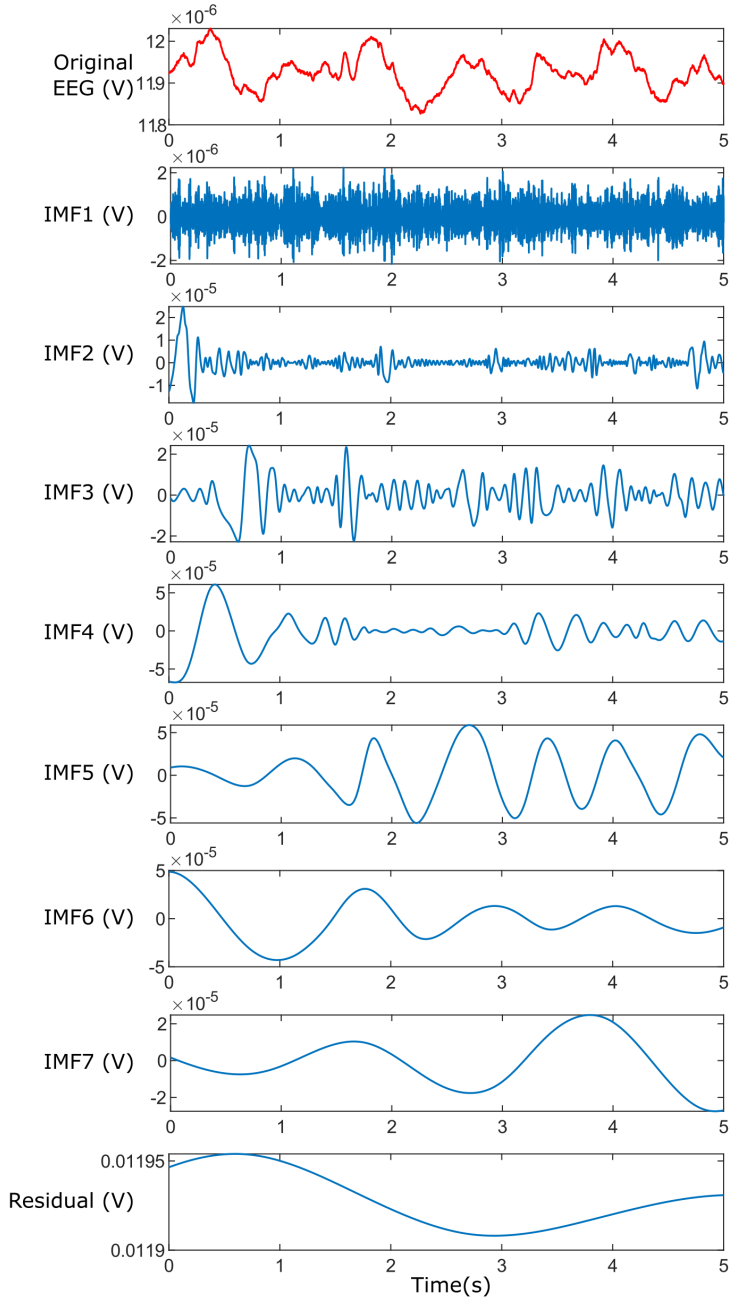

Figure 3.8: EEG signal and the IMFs and residue obtained by EMD.

treated consistently to reach a meaningful estimation of time-frequency properties ([199]).

The signal in EMD is the sum between a slow and a fast oscillation, whereas the signal in the MEMD method is the result of the sum of a slow rotation and fast rotation. In that sense, MEMD can decompose multivariate signals (p-variate) $v(t)$ in *p-variate IMFs* γ_i and a residue $r(t)$:

$$\boldsymbol{y}(t) = \sum_{i=1}^{p} \gamma_i(t) + r(t) \tag{3.31}$$

where c_i represents the joint rotational modes.

EMD computes the local mean by interpolating among local minima and maxima to calculate the mean of the upper and lower envelopes. In contrast, the solution with MEMD proposes a method to generate multiple n-dimensional envelopes, which are computed using the projections of the signal over different directions in n-dimensional space. These projections are then averaged to calculate the local mean [199]. Consider the multivariate data $\boldsymbol{y}(t) = y_1, y_2, ..., y_p$ as a p vector, representing the multivariate signal with p components, and $\boldsymbol{d} = d_{\theta 1}, d_{\theta 2}, ..., d_{\theta p}$ denoting a set of direction vectors along the direction given by the angles of $\boldsymbol{\theta} = \theta_1, \theta_2, ..., \theta_{(p-1)}$ on a $(p-1)$ dimensional sphere. Then the steps of the MEMD algorithm are presented as follows:

1. A *p-point* Hammersley sequence is generated for uniformly sampling a $p-1$-dimensional sphere.

2. Calculate a set of the projections $\boldsymbol{P}_i$ using each one of the vectors of the signal y_i along all the directions of $\boldsymbol{d}$.

3. Identify the time instants $t_{i\theta_i}$ that correspond to the maxima of the set of projections $\boldsymbol{P}_i$ of the signals.

4. Interpolate $[t_{i\theta_i}, \boldsymbol{y}(t_{i\theta_v})]$ to obtain the envelope curves $e_{\theta_i}(t)$.

5. the mean of the p multidimensional envelopes is calculated using:

$$\boldsymbol{m}(t) = \frac{1}{p} \sum_{i=1}^{p} \boldsymbol{e}_{\theta_i}(t) \tag{3.32}$$

6. Extract the "detail" $d(t) = \boldsymbol{y}(t) - m(t)$. If $d(t)$ fulfills the stoppage criterion for a multivariate IMF, apply the above procedure to $\boldsymbol{y}(t) - d(t)$. Otherwise repeat for $d(t)$.

MEMD has several advantages over EMD. One of the most relevant is the alignment of the modes in the same IMFs for each channel (mode alignment). This property favors making use of similar scales in the different channels and by that offering the possibility of direct multi-channel data analysis preserving the common channel properties. Also, the data channels have the same number of scale-aligned IMFs and although mode mixing remains, its impact is reduced. Another important benefit of MEMD is the noise reduction, where it has been found that noise reduction with MEMD is significant against the standard EMD [201, 202], where noise reduction allows for identification of instantaneous frequency at a more accurate level.

After a decomposition of an EEG signal in IMFs, the signals can be easily retrieved by a direct sum of all the components, as the number of samples is preserved. EMD-based methods have this property, in which no time resolution is reduced when decomposing the signal. EMD and MEMD can be used for denoising by removing the IMFs related to noise and reconstructing the signals from the components related to the activity of interest. However, this requires careful selection of the IMFs.

3.5 Relevance Analysis

Relevance analysis is a measure to evaluate the clustering quality of a subset of features based on energy or spectral properties [203, 204]. This concept has been proposed for feature selection in supervised and unsupervised inference problems [203]. In the context of EEG source reconstruction, it has been applied to weight the channels data, giving a higher influence to the most relevant channels and attenuating the influence of the less relevant ones [205]. In this work, the algorithm Power Embedded Q-Alpha Algorithm (Q-α) is applied to compute a weight α for each channel and select a group of N_α relevant channels to perform source reconstruction. The details are presented in chapter 5.

3.5.1 Power Embedded Q-Alpha Algorithm

The objective of this algorithm is to compute a weight α to weight a set of features according to the clustering quality of the data points using the power properties. In the context of EEG signals, to estimate a weight α related to the clustering quality of EEG channels. Consider the EEG data $\boldsymbol{y}$ from N_{ch}, where each one of its rows corresponds to a channel $vey = [y_1^T, y_2^T, ..., \boldsymbol{y}_{N_{ch}}^T]$. The rows are then pre-processed such that each row is centered around zero and its L2 norm $||\boldsymbol{y}_i|| = 1$. Consider $\boldsymbol{A}_\alpha$ to be the affinity matrix of the inner product between data points weighted by α as:

$$\boldsymbol{A}_\alpha = \sum_{i=1}^{n} \alpha_i y_i y_i^T \tag{3.33}$$

Also consider $\boldsymbol{Q} \in \mathbb{R}^{N_t \times kK}$ as an orthonormal matrix, whose columns are the k eigenvectors of $\boldsymbol{A}$ associated with the highest eigenvalues. To compute the channel relevance, the weight α can be calculated by solving the optimization problem presented below:

$$\begin{aligned} \max_{\boldsymbol{Q},\alpha} \quad & (\boldsymbol{Q}^T \boldsymbol{A}_\alpha^T \boldsymbol{A}_\alpha \boldsymbol{Q}) \\ \text{subject to} \quad & \alpha^T \alpha = 1 \end{aligned} \tag{3.34}$$

This optimization can be solved by applying the Power-Embedded Q-α algorithm adapted for EEG channel relevance. It is presented in algorithm 1, where r represents the number of iterations for convergence of the algorithm. This value is often set to $r = 10$ according to the number of iterations suggested in [203].

3.6 Multi-objective Optimization Algorithms

A single-objective optimization refers to the optimization of a cost function $f(x)$ in which the parameters of x are identified, generally to find the global maximum or minimum, which depends if the optimization problem is to minimize or maximize the cost function $f(x)$. In the case of multi-objective optimization problems (MOOP), several cost functions $f_m(x)$ with $i = 1, 2, \ldots, M$ are considered as objectives to minimize or maximize, and there may not exist an unique solution

Algorithm 1 Power-Embedded Q-α algorithm

procedure Q-$\alpha(y)$
  $Q_0 \leftarrow$ random orthonormal matrix
  $r \leftarrow 1$
  while $r \leq 10$ **do**
    $G_{i,j} \leftarrow (y_i^T y_j) y_i^T \boldsymbol{Q}_{r-1} \boldsymbol{Q}_{r-1}^T y_j$
    $\alpha \leftarrow$ the largest eigenvector of G
    $\boldsymbol{A}_\alpha \leftarrow \sum_{i=1}^{N_{ch}} \alpha_i y_i y_i^T$
    $Z \leftarrow \boldsymbol{A}_\alpha \boldsymbol{Q}_{r-1}$
    $\boldsymbol{Q}_r R \leftarrow$ QR decomposition of Z
    $r \leftarrow r + 1$
  end while
  return α
end procedure

that is the best with respect to all the objectives. Typically, there exist a set of solutions that can be superior to the most of the solutions of the search space, this solutions are considered non-dominated solutions and form the well known Pareto-optimal [206].

A generalized mathematical framework for a MOOP problem can be written as [207]:

$$\begin{aligned} &\text{Minimize/Maximize} && f_m(x), && m = 1, 2, ..., M \\ &\text{subject to} \\ & && g_j(x) \geq 0, && j = 1, 2, ..., J \\ & && h_k(x) = 0, && k = 1, 2, ..., K \\ & && x_i^{(L)} \leq x_i \leq x_i^{(U)}, && i = 1, 2, ..., n \end{aligned} \tag{3.35}$$

where $g_j(x)$ and $h_k(x)$ are restriction functions. $x \in \mathbb{R}^n$ is a solution vector with $\mathbf{n}$ decision variables, $\mathbf{x} = x_1, x_2, ..., {x_n}^T$. The last set of constraints $x_i^{(L)} \leq x_i \leq x_i^{(U)}$ establishes a lower $x_i^{(L)}$ and upper $x_i^{(U)}$ bound for the decision variable x_i. The solution in these bounds forms the decision space $\boldsymbol{D}$ [207]. However a MOOP can be formulated with more restrictions or without any. The optimization process consists then in identifying and evaluating multiple feasible

values for x_i to identify the best parameters that minimize/maximize the objective functions; being a feasible solution $x_i \in \boldsymbol{D}$.

Evolutionary algorithms, in particular genetic algorithms (GA), have been extensively used for searching and optimizing the decision variables in multiple engineering applications [208–210]. In this work, the non-dominated sorting genetic algorithm NSGA-II [211] has been proposed for channel selection in source reconstruction problems. This is explained in detail in chapter 6.

3.6.1 The Non-dominated Sorting Genetic Algorithm II

The core of NSGA-II consists of several stages: Population initialization, Fitness calculation, Crossover, Mutation, Survivor selection, and Termination criteria to return the best solutions x_i. The population P consists of a set of solutions x_i, which are possible solutions to the problem, and each chromosome can have as many genes as variables in the problem.

The NSGA algorithms use a non-dominated sorting ranking selection method to identify and evolve the best candidates to maintain stable populations of good and feasible solutions to conform a Pareto-front [206]. NSGA-II includes an elitist approach to compare the current and previous populations that allows to identify the best non-dominated solutions and improve the original version of NSGA [211]. NSGA-II is used to solve certain problems related to computational complexity, as it aims to reduce the computational cost from $O(MN^3)$ to $O(MN^2)$, where N is the size of the population, and M the number of objectives to optimize.

In NSGA-II the performance of the solutions are ranked based on a non-dominated sorting: the half of the population with better performance is used to create the next generations using crossover and mutation procedures. The actual generation finishes when the new population is created and the process is repeated with the next generation until the termination criteria is reached. Figure 3.9 presents an example of the NSGA-II procedure of ranking and rejecting the possible solutions of a population.

3.7 EEG Datasets

Several datasets are analyzed in this work. They are presented and described here: A synthetic multi-source EEG dataset computed using the simulation framework explained in section 3.2, the Multi-modal Faces dataset [212], and the Localize-

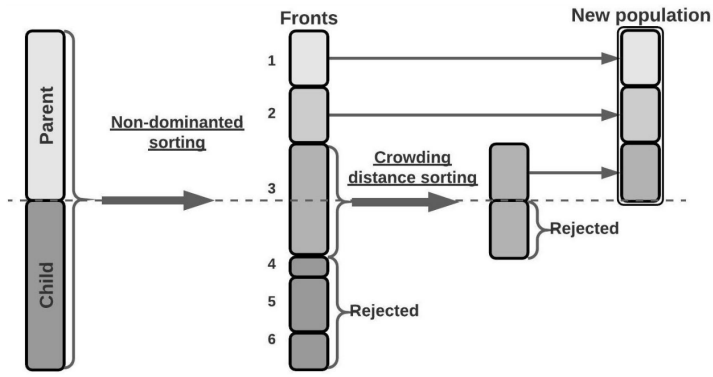

Figure 3.9: Typical ranking NSGA-II procedure. (Adapted from [211]).

MI dataset [213]. They were used in several tests and evaluations presented in chapters 4, 5, and 6.

3.7.1 Synthetic Multi-Source EEG Dataset

A synthetic dataset using the simulation framework in section 3.2 was created in order to provide a ground-truth for source reconstruction accuracy measurements. The multi-source EEG dataset consists of 150 trials of EEG activity that contains six simulated sources with temporal mixing distributed over three brain areas; frontal lobe, sensory-motor cortex, and occipital lobe. This dataset is used in evaluations presented in chapters 5 and 6. Segments of the dataset descriptions are taken from [214, 215].

The sources were time distributed every half second from 0.5 s to 3 s, and the shape of the parameter σ_i in equation 3.26 was set at $\sigma = 0.12$ for all the sources. The time location of the sources and the adjustment of σ allow to have temporal mixing of around 40% in the transitions between source waveforms. In the case of the first and sixth source, the temporal mixing is the half and it occurs only at the second half of the waveform and first half of the waveform, respectively. The parameters for computing the time-courses are presented in table 3.2. An example of the six sources time-courses computed with the parameters of table 3.2 is presented in figure 3.10. For displaying purposes the parameter $a_i = 1$ was used for the figure realization. In the dataset, this parameter is used to produce source-time courses in the range of $\mu A/mm^2$ and is computed using the following

equation:

$$a_i = \frac{l_b + (u_b - l_b) * r_1}{r_2} \tag{3.36}$$

where $u_b = 1$ is an upper boundary, $l_b = 0.7$ a lower boundary, $r_1 = rand(0, 1)$ is a random value between 0 and 1, and $r_2 = 10000$ is a predefined value to approach the units to $\mu A/mm^2$.

s_i	i=1	i=2	i=3	i=4	i=5	i=6
f_i (Hz)	19	10	7	21	12	8
c_i (s)	0.5	1.0	1.5	2	2.5	3.0
sigma_i	0.12					
loc_i	Occipital	Sensory-motor	Frontal	Occipital	Sensory-motor	Frontal
a_i	Equation 3.36					

Table 3.2: Simulation Parameters for the Multi-Source EEG Dataset

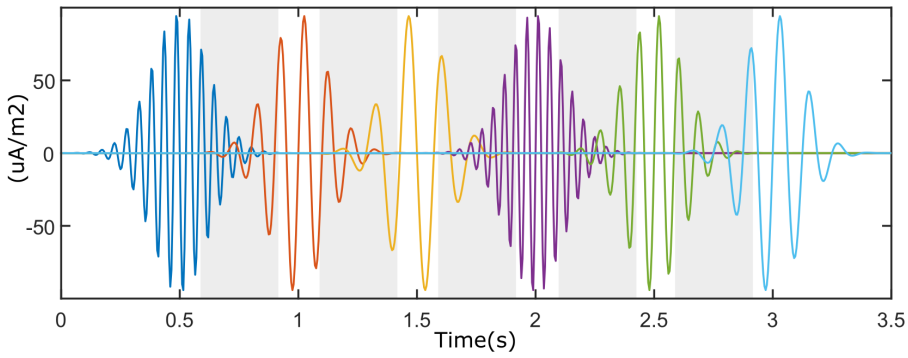

Figure 3.10: Example of a set of six sources time-courses with temporal mixing. The temporal mixing is represented with the lightgray in the boundaries of the sources time-courses. They were computed using the parameters of table 3.2, except for the amplitude factor parameter a_i that was set to $a_i = 1$ for displaying equal amplitude time-courses

The sources were distributed over the brain in three main areas: occipital lobe, sensory-motor cortex, and frontal lobe. Per each area, a set of twelve positions (six

per hemisphere) was predefined, and during the simulation procedure the position was randomly selected from the pre-defined sets. This allowed for the creation of trials with different combinations of sources. Figure 3.11 shows the locations of the pre-defined sources (represented by the blue circles), and the number of times they were selected in the dataset (represented by the diameter of the circles).

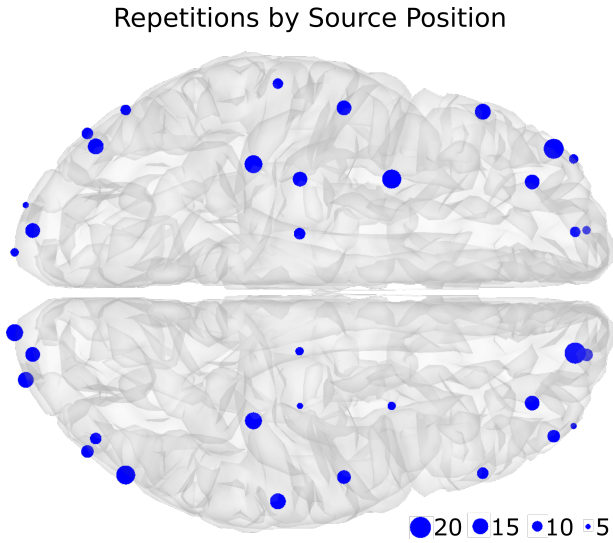

Figure 3.11: Repetition by source position. Blue circles represent where the simulated activity was placed, and their diameter represents the number of times the position was selected in the 150 EEG trials. It can be seen that each area, occipital lobe, sensory-motor cortex, and frontal lobe, has six locations by hemisphere [214].

After computing the source-time courses and the source activity matrix $\boldsymbol{x}$, the equation 2.2 was used to compute the synthetic EEG $\boldsymbol{y}$. The lead-field matrix $\boldsymbol{M}$ for solving the forward equation was based on a FEM forward model called the "New York" head model [216]. It is available at `https://www.parralab.org/nyhead/`.

The lead field matrix of the New York head model was computed using FEM considering the segmentation of six tissues: scalp, skull, air cavities, CSF, gray matter, and white matter. The New York head model was proposed as a standard model to be used in EEG studies, and it is based on a non-linear average of the MRI of 152 adult human brains. The forward model includes a high-resolution lead field matrix relating 75000 sources with 231 channels. It also includes additional

versions with a reduced number of sources of 10000, 5000 and 2000 sources. The model considers 231 electrodes, from which 161 are located on the scalp (based on the 10-10 and 10-5 systems), 2 on the left/right pre auricular point (LPA/RPA), 4 on the neck, and 64 distributed around the face and on the back of the head below Iz channel [216]. Figure 3.12 presents a lateral and top view of the channel and source locations using the model with 10000 sources.

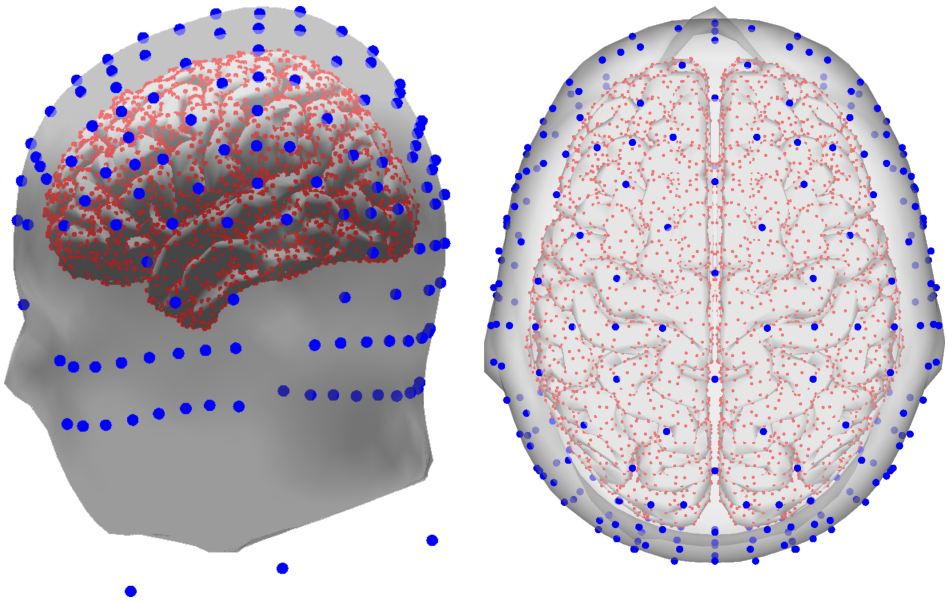

Figure 3.12: New York head model[216] with 10000 sources and 231 channels. Lateral view (left), and top view (right). The blue circles represent the location of the channels over the scalp, face, and neck, while the red circles, the location of the distributed sources on the brain's cortical areas [214].

The model of 10000 sources was used for forward computations to generate the EEG signals and the model of 5000 sources to calculate the inverse solutions. This allows to avoid the effects of the so-called inverse crime [217]. The use of the New York head model[216] was preferred due to the realistic representation using six tissues. In FEM models the influence of including the CSF and the white matter during modeling have been found significant for solving the inverse problem [110]. Using a more detailed model can allow to achieve more accurate source reconstruction results.

After calculating the EEG using equation 2.2, the signals of the channels were corrupted with noise with a SNR of $0dB$ (signal and noise with the same power). Each trial has a duration of $3.5s$, with a sampling frequency of $200Hz$. The dataset with the 150 trials and ground-truth information is freely available at https://github.com/anfesogu/Ground-Truth-EEG-Dataset, and can be used in future studies where a ground-truth for source localization is required.

3.7.2 Multi-modal Faces Dataset

The multi-modal faces is a dataset acquired with multiple modalities: EEG, MEG, and fMRI data, during visual stimulation. The dataset includes 16 participants for whom the stimuli consisted of images projected onto a screen [212]. Three types of stimuli were tested: familiar faces (famous), unfamiliar faces (non-famous), and scrambled faces. This paradigm and dataset has been used in several studies for source reconstruction of evoked responses and multi-modal integration [70, 218–222]

The participants' data were recorded in two separate sessions, one for simultaneous MEG/EEG recording, and one for fMRI with three months between first and second visit. Six runs (sessions) of approximately 10 mins were acquired for each participant, where approximately 300 events were recorded per each face condition. The MRI data were acquired on a 3T system (Siemens 3T TIM TRIO, Siemens, Erlangen, Germany) including T1 weighted structural MRI, and T2 weighted fMRIm where the echo-planar imaging (EPI) volumes were acquired during 9 runs of the same task. The faces sets were different for each participant between the first and second sessions.

The MEG/EEG data were recorded in a light magnetically shielded room using 306 MEG sensors (Elekta Neuromag Vectorview, Helsinki, FI) and a 70 electrode EEG cap (Easycap) with 10-10 system layout. The EEG electrode and MEG sensor locations were digitized to allow for co-registration with MRI data.

The study was conducted in accordance with the Declaration of Helsinki, and approved by the Cambridge University Psychological Ethics Committee. Participants signed an informed consent form and gave separate written consent for their anonymized data to be freely available on the internet [212]. The dataset is available at https://openneuro.org/datasets/ds000117 in brain imaging data structure (BIDS) [223–225], and non-BIDS structure at ftp://ftp.mrc-cbu.

cam.ac.uk/personal/rik.henson/wakemandg_hensonrn.

The multi-modal faces dataset is not a ground-truth as the information of the source activity is not directly recorded, however, a multi-modal integration of fMRI+MEG+EEG procedure[193] can be applied to compute source reconstruction maps that can serve as a ground-truth.

3.7.2.1 Multi-modal Ground-Truth

The multi-modal solution and estimation of the source activity is not provided directly, however, the procedures for the multi-modal integration and scripts are explained in detail in [226]. This allows for the computation of the ground-truth for the dataset to be performed. For this thesis, a ground-truth of the evoked activity was computed for the 16 participants' data, including fMRI, MEG and EEG modalities. In addition a three-layer BEM model was used to compute the multi-modal ground-truth. All the procedures were done using the statistical parametric mapping (SPM) 12 toolbox.

The followed steps for multi-modal integration are briefly summarized here. The procedure started by applying a standard ERP pipeline similar to figure 3.7 to the MEG/EEG data. The data were filtered using a high-band of 0.1Hz, the bad channels were identified and removed from the data. The EEG was re-referenced to the average across channels. The epochs were established between -100 ms to 800 ms related to the stimuli onset, and baseline correction applied using the 100 ms before the stimuli onset. A threshold of $\pm 100 \mu V$ was applied to reject the epochs containing large EOG or EMG activity. Finally the trials were averaged to obtain the ERP responses. An example of the ERP for a participant 3 is shown in figure 3.13

The fMRI processing steps to estimate the blood oxygenation level dependent (BOLD) responses versus the inter-stimulus baseline are summarized as follows: The EPI images were realigned for correcting movement. A normalization and segmentation of the T1 images was performed prior to the co-registration of mean EPI and structural MRI to obtain a set of normalization parameters or warps. In a subsequent step the warps are applied to each one of the EPI volumes to produce new re-sliced images. The images were smoothed using an 8mm isotropic Gaussian kernel. Then a general linear model approach was used to separate stimulus-induced signals from noise. Then the images were contrasted using a F-

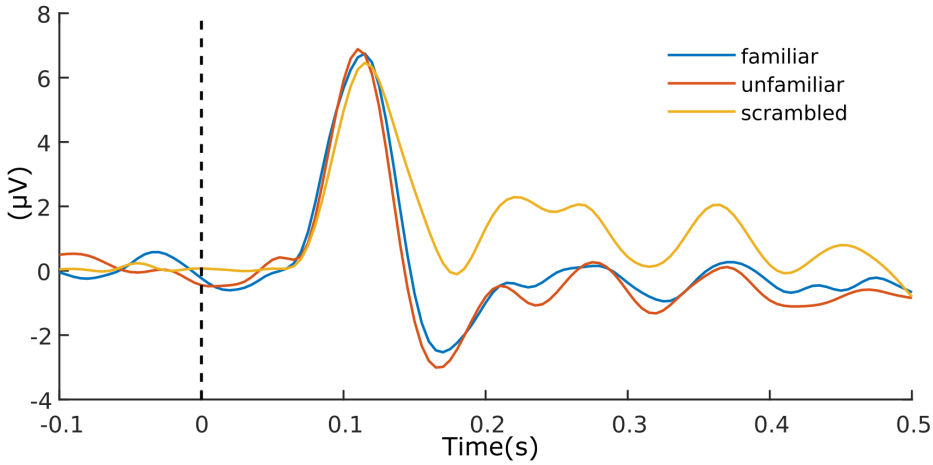

Figure 3.13: ERP average of familiar, unfamiliar and scrambled faces at EEG channel O2 for the subject 3 of the multi-modal faces dataset[212].

contrast, and a set of images with the responses for each participant and condition were retrieved. Finally a group statistics was performed using repeated-measures ANOVA to identify the significant clusters per each condition that served as priors for the source reconstruction using MEG/EEG data.

A head model was created for each participant, the MRI images were segmented and co-registered with the MEG/EEG sensors'/electrodes' locations, and a three-layer BEM model was used to estimate distributed solution space using 4098 sources per hemisphere. For estimating the inverse responses, the MSP algorithm was used, and the significant clusters from fMRI were used as priors, assuming the same set of source priors across subjects. The head model, ERP data, and multi-modal estimation were stored. This ground-truth was used in chapter 4 to perform source reconstruction evaluations.

3.7.3 Localize-MI Dataset

Localize-MI is a dataset of simultaneous human intracerebral stimulation and hdEEG. The dataset is freely available at https://doi.gin.g-node.org/10.12751/g-node.1cc1ae/. This dataset is intended to serve as ground-truth to validate forward modeling and inverse modeling techniques for EEG data. The

dataset consists of electrophysiological and structural data from patients with drug-resistant epilepsy. They were monitored for several days for seizure recording using stereo-electroencephalography (sEEG). sEEG refers to the implantation of electrodes to detect and localize the seizure onset zone during a minimally invasive procedure, typically, multiple multi-contact electrodes of 0.8 mm are stereotactically implanted through small skull holes of around 2.5 mm [227]. This dataset is used in evaluations presented in chapter 6.

During the patient monitoring, it is habitual to use intracortical stimulation to induce seizures and to provide a map of the physiological functions of the implanted sites. This is done by injecting a current pulse between two adjacent electrode leads [213]. This stimulation combined with hdEEG recordings have been use to generate real scalp recordings from currents originating inside the brain, where the locations of the stimulation sides are known. This offers the possibility of using the dataset for benchmarking and validation of forward and inverse solutions. However, in this thesis the dataset is used only for source reconstruction evaluations in chapter 6.

The dataset consists of hdEEG recordings and anonymized MRI of seven participants, with a total of 61 stimulation sessions. All of the participants signed an informed consent form, and the study was approved by the local Ethical Committee of Niguarda Hospital (Milan, Italy). All the studies and evaluations were carried out in accordance with the declaration of Helsinki [213]. The electrical currents for stimulation consisted of single-pulse biphasic currents lasting 0.5 ms with a range between 0.1 to 5 mA. The frequency of the current was 0.5Hz for stimulation with 1 and 5 mA currents, and 1 Hz for other current stimulation. The EEG signals were recorded with a 256 electrode net in a geodesic distribution (Electrical Geodesics, Inc; Oregon, USA) at a 8000 Hz sampling rate. The electrodes' locations and fiducial points were digitized to allow for co-registration with a pre-implant MRI (Achieva 1.5 T, Philips Healthcare).

The dataset was already pre-processed and available in BIDS structure. The data were divided in epochs from -300 to 50 ms related to the onset of the stimulation artifact. They were filtered with a high-pass filter at 0.1 Hz, and notch filter at 50,100,150, and 200 Hz (only for subjects 5 and 7). Baseline correction was applied between -300 to -50 ms. Finally the epochs were averaged and the artifact

ERPs cropped 20 ms around the stimulation event. An example of the artifact ERP and its topography is presented in figure 3.14.

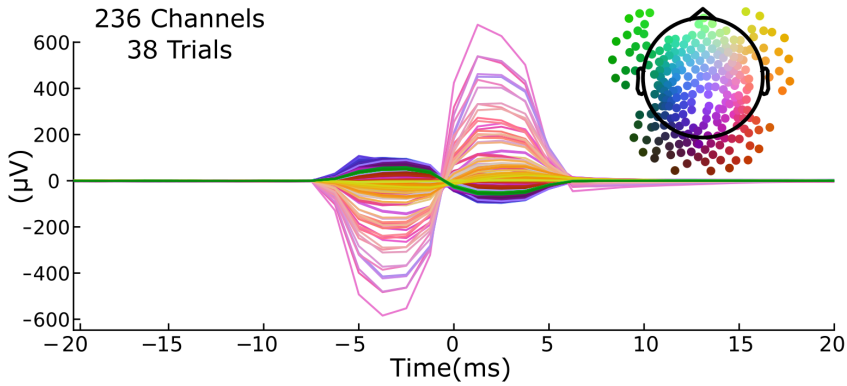

Figure 3.14: Bi-phasic stimulation current ERPs from 236 EEG channels. Subject 1, session 7 of the Localize-Mi dataset[213].

Regarding forward modeling, a head model of each participant was created to be used during source reconstruction. The models were created by processing the individual MRI using Freesurfer[228] for tissue segmentation [229, 230] and MNE-python[231]. The number of sources was defined as 4098 per hemisphere, and the lead field matrix was computed using BEM, considering the conductivities of scalp, skull, and brain as 0.3, 0.006 and $0.3 S/m$ respectively (MNE-python default values).

3.8 Software and Hardware

Multiple software and hardware tools have been used for evaluating the algorithms and methodologies proposed in this work.

In terms of software, several toolbox and functions used for this work were implemented mainly in two software packages: Matlab (The MathWorks, Inc.) version 2016, and python using version 3 [232].

Several toolboxes were used in this work: MNE, which is an open-source python package for analyzing human neurophysiological data [231]. More information about MNE is available at `https://mne.tools/stable/index.html`. SPM is a free Matlab package for the analysis of brain imaging data

sequences [233]. More information about SPM is available at https://www.fil.ion.ucl.ac.uk/spm/. Freesurfer is a software package for the analysis and visualization of structural and functional neuroimaging [228–230]. More information about Freesurfer is available at https://surfer.nmr.mgh.harvard.edu/fswiki/FreeSurferWiki. The source reconstruction algorithms wMNE, sLORETA, MUSIC, RAP-MUSIC and TRAP-MUSIC were implemented as custom functions in Matlab. For the MSP algorithm, SPM version 12 was used to estimate the source activity. Freesurfer was used to process brain structural data of the Localize-MI dataset, while MNE was used to process the Localize-MI EEG dataset. SPM was used to process fMRI, MRI and EEG data from the Multi-modal Faces dataset.

The NGPM software is available at NGPM mathworks [234] and was used for multi-objective optimization with NSGA-II. It was adapted to include source reconstruction. All the tests involving optimization with NSGA-II were carried out on the NTNU IDUN computing cluster [235].

Chapter 4

Low-density EEG Source Reconstruction Based on Frequency Decomposition

This chapter introduces a methodology for extracting the underlying source activity based on frequency decomposition, and outlines the procedure to use it for constraining the source reconstruction algorithms to selected frequency modes. Here, a multiple-channel analysis is performed using MEMD to reduce the mode mixing and provide useful a priori time-frequency information for the reconstruction of neuronal activity using several low-density EEG electrode montages.

This chapter is based on the journal article [177] and mainly addresses the 1st research question.

4.1 Introduction

EEG is an indicator of neural activity and is used to study complex brain dynamic processes. The analysis of EEG signals is challenging in both time and frequency domains, due to the non-linearity introduced by the volume conduction and their non-stationary nature. In addition, the interest information or responses can be hidden in environmental noise and background brain activity. This hidden information can be extracted for the early detection of different disorders using advanced signal processing and analysis techniques [236]. A highly effective

technique to extract the underlying information is the computation of ERPs, in which the average of multiple evoked responses related to the same event is typically applied to obtain clear responses. This analysis is performed in time domain, however, the ERPs can also be decomposed in frequencies to analyze its content [43].

The EEG data, in particular ERPs, are generally used as inputs for computing the source activity, however, the inverse problem associated with the estimation is ill-conditioned [12, 142, 163], therefore, it is highly sensible to input noise, and small variations can generate a large impact in the source estimation. From this, it can be hypothesized that clearer information (less noisy) can attenuate the effect of the ill-condition of the inverse problem and produce more accurate results. To evaluate this hypothesis, frequency-based decomposition methods could be applied to ERP signals to separate them in frequency modes and constraining the estimation to the frequencies they represent.

In recent years, the HHT has been increasingly used for the analysis of EEG signals [237]. Methods based on EMD frequency decomposition are preferred over other frequency decomposition techniques. e.g. wavelet decomposition and linear filters. This is due to its ability to deal with non-linear and non-stationary signals, to maintain the time resolution and preserve the signals' phase. However, the extraction of information for certain applications can be hampered by the mode-mixing problem that appears in the EMD decomposition when frequency components are relatively close or exhibit intermittency. This effect can disturb the physical interpretation of the process, which is normally described by the individual IMFs [197, 198]. Therefore, variations of EMD have been proposed to attenuate this effect and extrapolate this method for the analysis of multivariate signals. MEMD is a method that reduces the mode-mixing problem while allowing for multichannel data analysis [199], and provides several advantages over the standard EMD (Section 3.4.2).

EMD has been applied in multiple applications involving EEG signal analysis. e.g. muscular artifact removal [189], feature extraction for emotion recognition [188], epilepsy detection [190, 191], and subject identification [238, 239] among others. The use of MEMD has been evaluated in multiple EEG signal analysis studies. In [240], the authors presented a method for data analysis based on MEMD

in which they applied a pre-processing step with ICA to calculate and evaluate the energy presented in an EEG recording from quasi-brain-deaths and evaluate their brain activity. [241] proposed a data-driven method for classifying ictal (epileptic activity) and non-ictal EEG signals using the MEMD algorithm. They extracted and selected suitable feature sets to classify neural activity based on a multiscale time-frequency representation of the EEG signals by applying MEMD.

In the context of source reconstruction, MEMD was applied for unmixing the estimated source activity in brain-ROIs [193]. The source estimation was performed using LORETA, and then MEMD was applied over the source time-courses to disentangle the source activity within a brain-ROI. A fusion between MEMD, source reconstruction algorithms, and an unsupervised wavelet eye blink artifact remover was introduced in [242]. The fusion of those methods was applied for the accurate localization of epileptogenic sources in five subjects, the results of which suggest than MEMD can improve source localization when the sLORETA inverse method is applied. However, they did not evaluate the influence of reducing the number of electrodes, and the information about the selection of the MEMD intrinsic mode functions was not provided. In [192] a comparison between EMD and wavelet decomposition was performed, where EMD-based source reconstruction obtained a lower reconstruction error. Multiple variations of EMD (including MEMD) were evaluated in [178] for reconstructing source activity, where the results over a single trial of three simulated sources case and one-subject ERP in hdEEG, resulted in a promising MEMD source reconstruction accuracy.

In this chapter, the application of multivariate time-frequency EEG signal analysis for source reconstruction is presented. MEMD method was applied to decompose the ERPs and to separate the source activity in IMFs. An IMF selection based on entropy was applied to remove the noisier components. MEMD decomposes the signal into several IMFs, in which the information of the underlying brain activity can be separated into frequency bands. MEMD reduces the mode-mixing problem, due to the relation between the information in each channel, making it possible to understand the effect of a stimulus on different regions of the brain. Next, the selected IMFs were used to perform source activity reconstruction. A lower number of electrodes can, in principle, extract and provide

such underlying time-frequency information due to the properties of MEMD and the redundancy of high-density EEG in a given neuro-paradigm. This hypothesis was tested using simulated EEG data and real EEG signals from the multi-modal faces dataset.

4.2 Methodology for Source Reconstruction Based on Frequency Decomposition

A summary of the proposed methodology for frequency decomposition is presented in figure 4.1. The process starts with data pre-processing to obtain the ERP (a typical ERP pipeline is presented in section 3.3.3). Then, a spatial down-sampling by reducing the number of channels can be performed to reduce the computational time for calculating the frequency decomposition with MEMD. However, this step is optional. In the case that spatial down-sampling is applied, it is recommended to down-sample the channels maintaining coverage over the scalp and a symmetry between hemispheres. The effects of using only channels close to the particular region to map have been found to be counterproductive for estimating the source activity of the region [127]. In [127], an evaluation over several channel down-sampling approaches was performed by several sets of electrodes over the occipital lobe to estimate the source activity in that area. It was found that such channel distributions produce distortions in the reconstructed source map.

The data were then decomposed using MEMD. One of the most relevant advantages of using this algorithm is the mode alignment in the channels, which represents that all the channels have the same number of IMFs and the same frequencies can be found in the same IMF indexes for each channel. The mode alignment property helps to make use of similar scales in the different channels and by that also offers the possibility of direct multi-channel data analysis preserving the common channel properties. Another important benefit of MEMD is the significant noise reduction, compared to the standard EMD [201, 202].

After the signals were decomposed in IMFs, their selection was performed. An approach to select the IMFs is to use the entropy of each IMF and to select the n IMFs with lower entropy value among the k number of IMFs [192]. To calculate the entropy of the IMF γ_i the following equation can be applied:

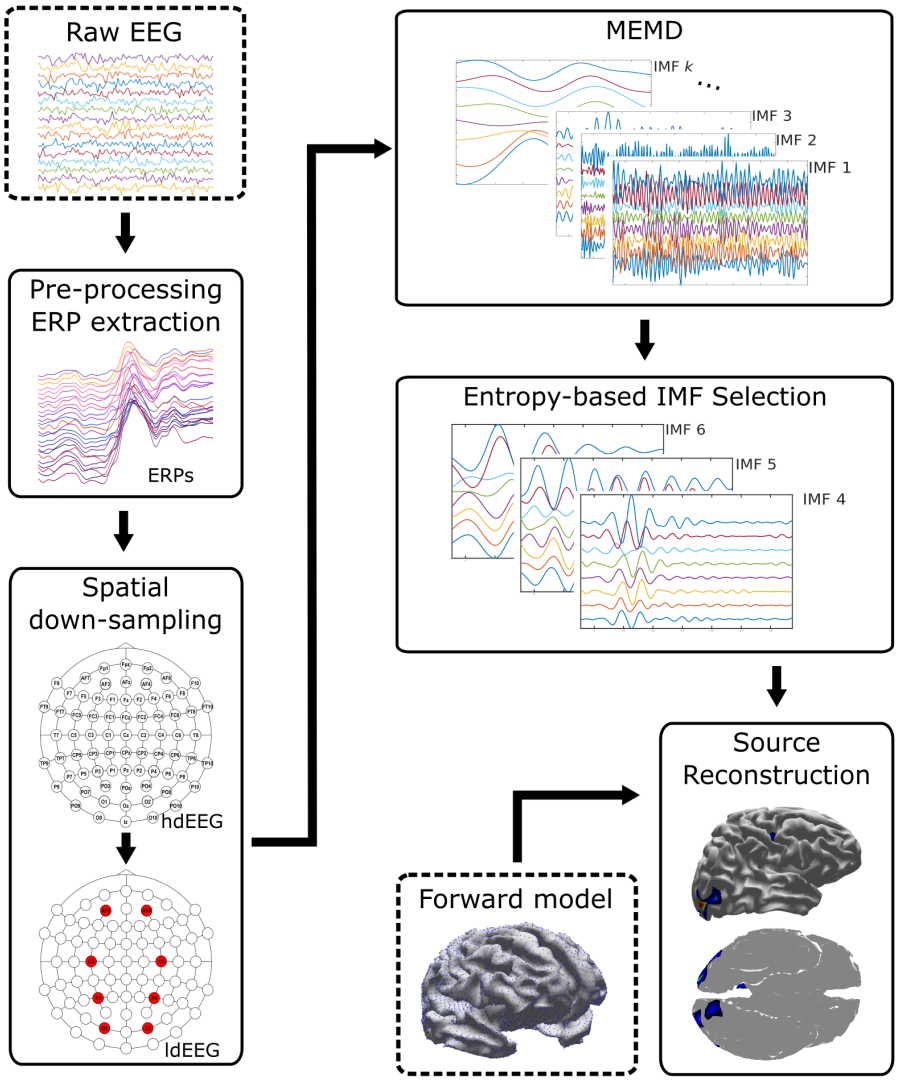

Figure 4.1: Methodology for source reconstruction based on frequency decomposition using MEMD. The dashed squares denote the inputs of the process.

$$e_i = -\|\gamma_i\|_2^2 \log(\|\gamma_i\|_2^2) \tag{4.1}$$

where e_i represents the entropy of each IMF, being the entropy $\boldsymbol{e} = [e_1 \ \ldots \ e_k]$.

A subset O can be created with the n selected IMFs, rejecting the $k - n$ IMFs that do not contain the activity of interest or are related to noise. The subset O can be used to estimate a denoised signal $\tilde{\boldsymbol{y}}$ by:

$$\tilde{\boldsymbol{y}} = \sum_{i \in O} \gamma_i \tag{4.2}$$

The reconstructed signal $\tilde{\boldsymbol{y}}$ using a few IMFs can be used e.g. for feature extraction [191, 243]. In this methodology, the application of MEMD is used to constrain the source reconstruction to the frequencies of selected IMFs that contain information of the underlying source activity. In addition, the IMFs with high levels of noise can be rejected, improving the SNR of the data and favoring more accurate source estimations.

The final step is to apply an inverse algorithm using the reconstructed and denoised EEG from the selected IMFs as inputs. Here, the MSP method was selected to perform source reconstruction, as it maximizes the free energy, resulting in more focal solutions than other reconstruction methods [149, 150]. In addition, previous evaluations performed on ldEEG electrode counts in [244] suggest that MSP performed better than other reconstruction algorithms while using a reduced set of seven electrodes.

4.3 Experimental Framework - Synthetic EEG Signals

To evaluate the methodology proposed, a set of single- and multi-source scenarios were simulated, in which the brain activity ground-truth is known, and which allows for evaluation and comparison with the estimated activity.

The head model used to generate the synthetic EEG signals can be found in at `http://www.fil.ion.ucl.ac.uk/spm/data/mmfaces/` of SPM software. This is a single-subject dataset obtained using the same paradigm reported in [3] and contains EEG, MEG, and fMRI data for one subject. It contains a cortical mesh with 8196 distributed sources, and a lead field matrix $\boldsymbol{M}$ with 128 channels. It was computed using a three-layer BEM, using gray matter, skull, and scalp. To perform multiple evaluations in ldEEG, the number of channels were down-sampled to 32, 16, and 8, trying to maintain an equal distribution and coverage of the brain. This reduction was carried out to analyze the quality of the reconstruction against

the number of measurements. Figure 4.2 presents the distributed sources over the cortical sheet and the position of the down-sampled electrode subsets.

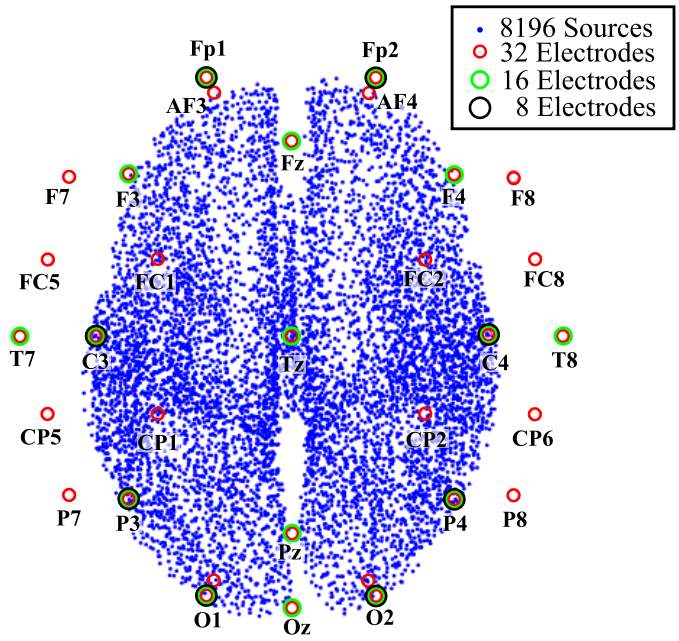

Figure 4.2: Head model and electrode subsets positions for EEG simulation [177].

Multiple EEG signal configurations were evaluated that varies in number of sources, number of channels, and level of noise. Three different numbers of active sources were considered: one, three, and five. For each number of active sources, the synthetic EEG was computed for the 128 channels, and down-sampled to 8, 16 or 32 channel subsets. Two levels of SNR of 10 db and -5 dB were used when including noise in the measurements. The source activity for the single, three, and five active sources cases was simulated at various frequencies and in various instances of time. The source activity was simulated for the time-courses of the active current sources using the windowed sinusoidal equation 3.26, and following the procedure for the simulation framework (section 3.2). The parameters for the simulation are presented in table 4.1, for all the sources a width parameter $\sigma_i = 0.12$ was used.

Single source case					
s_i	i=1				
f_i (Hz)	10				
c_i (s)	1				
loc_i	4000				
Three source case					
s_i	i=1	i=2	i=3		
f_i (Hz)	20	12	4		
c_i (s)	1	3	5		
loc_i	4000	5020	150		
Five source case					
s_i	i=1	i=2	i=3	i=4	i=5
f_i (Hz)	20	15	10	6	2
c_i (s)	1	2	3	4	5
loc_i	4000	5020	150	8100	2200

Table 4.1: Simulation Parameters for the single, three, and five source cases

This parameters of the simulation framework were used to simulate single and multiple active sources cases to evaluate the performance of MEMD in terms of its ability to separate source activity in the frequency domain, and to reduce the mode-mixing generated in the process of obtaining the IMFs. Thus, simulated EEG activity was obtained for the multiple cases that were spatially and temporally located at different points. Source frequencies (f_i) in the range of 2 to 20 Hz were tested and the temporal localization c_i of sources was in the range of 1 to 5 s.

After the simulation of the source activity the equation 3.27 was used to compute the synthetic EEG $\boldsymbol{y}$. Then, noise was added to the EEG signals, leaving the signals with two SNR of 10 dB and -5 dB. Three configurations were considered for the measurements: 32, 16, or 8 EEG channels. A reduced lead field matrix was used for each synthetic EEG for each number of channels to perform the inverse computations. An example of the EEG signals that resulted from the simulation is presented in figure 4.3.

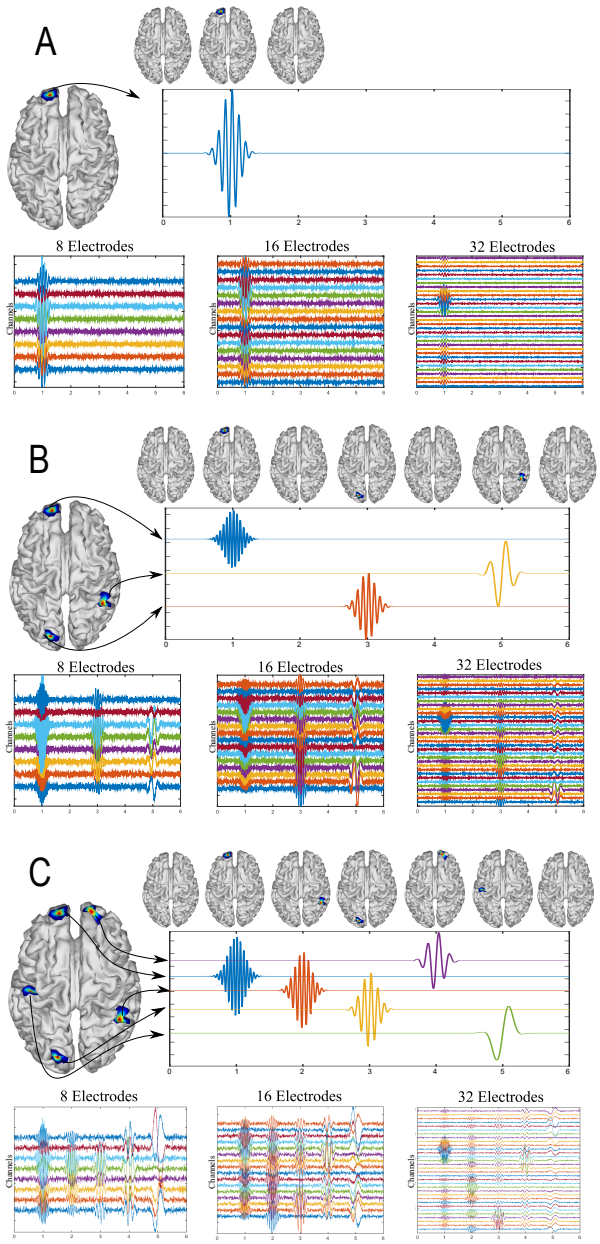

Figure 4.3: Simulated activity for one source **(A)** using 10Hz and 32, 16, or 8 EEG channels. Simulated activity for three sources **(B)** using 4, 12, and 20Hz windowed sinusoidal activity and 32, 16, or 8 EEG channels. Simulated activity for five sources **(C)** using 2, 6, 10, 15, and 20Hz windowed sinusoidal activity and 32, 16, or 8 EEG channels [177].

Source reconstruction was performed in two ways: first, using MSP directly from the synthetic EEG without any pre-processing step, here referred to as raw-MSP, and second, using the proposed methodology by applying MEMD prior to MSP, referred to as MEMD-MSP, in which the main IMFs were selected according to the entropy function in equation 4.1, for which those IMFs which presented the highest entropy were used to recalculate the EEG. Finally, the reconstructions were compared using the WM (section 3.1.4.4) to obtain a spatial accuracy measurement.

4.4 Experimental Framework- Multi-modal Faces Dataset

The multi-modal faces dataset was used to evaluate the extraction of the underlying activity using MEMD decomposition. The details of the dataset and the multimodal ground-truth extraction are presented in section 3.7.2. In this dataset each subject has their individual forward model and their ground-truth activity. The individual lead field matrix was used to solve the inverse problem and the ground-truth activity was used to compare the solutions. Similar to the simulation case, the solutions were obtained using the ERPs as inputs for MSP (raw-MSP) and obtained with the MEMD-MSP methodology, using the *a priori* extracted information as inputs for the MSP.

The dataset contains the ERPs of familiar faces, unfamiliar, and scrambled, where the N170 component has been found significant when differentiating the faces from the scrambled images [212, 219]. Here the ERPs around 170 ms were considered for the experiments with scrambled and familiar faces. In addition, a spatial down-sampling similar to the simulated case was performed, by down-sampling from 70 channels to 32, 16, and 8. To evaluate the performance of the source reconstruction with MSP using one or several IMFs from MEMD and to compare the results with those for MSP without MEMD decompostion, the activity around the N170 component was considered. This was done by establishing a time-ROI, as in [220]. The window was defined between 100 and 220 ms. The comparison process applied to the multi-modal faces dataset is summarized in figure 4.4.

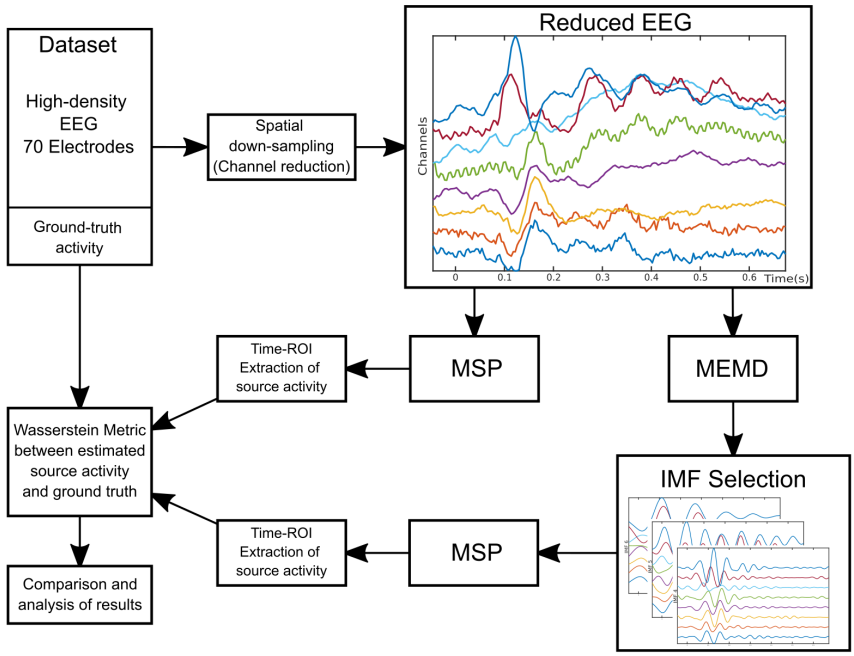

Figure 4.4: Block diagram of the evaluation and processing steps applied to the multi-modal faces dataset [177].

Channels were selected from the hdEEG according to the number of electrodes to be evaluated. The down-sampling data were directly processed by MSP to obtain the so-called raw-MSP inverse solution. In addition, the reduced channel data were also processed using MEMD and one or several IMFs were selected to obtain the inverse solution with MSP, to obtain the so-called MEMD-MSP. Finally, the WM was used to compare both reconstructions, raw-MSP and MEMD-MSP, against the ground-truth to evaluate the spatial accuracy of the solutions. The lead field matrix was reduced according to the position of the electrodes following a similar procedure as that used for the synthetic EEG signals, the channels selected to maintain as much as possible their equal spatial distribution over the scalp. The 8196 distributed sources of one of the subjects, the electrode down-sampling layouts for 32, 16, and 8 channels, and their positions are shown related to the sources in figure 4.5.

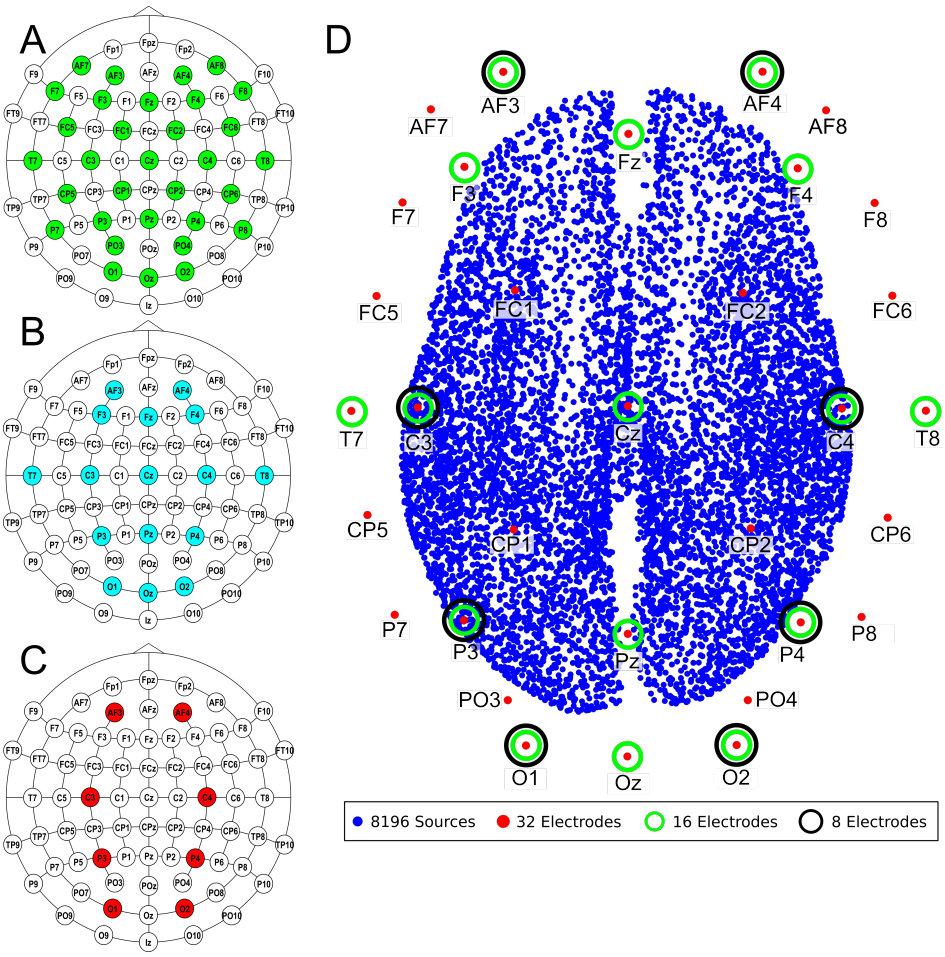

Figure 4.5: Layout according to the 10-10 system for 70 electrodes and the electrode down-sampling performed for **(A)** 32, **(B)** 16, and **(C)** 8 electrodes.**(D)** The 8196 distributed sources and the positions of electrodes [177].

4.5 Results

4.5.1 Synthetic EEG Signals

The synthetic EEG signals were generated and processed for the multiple source configurations of single, three, and five active sources. An example of the application of MEMD for the reconstruction case of a single source with 10Hz and 8 EEG channels is shown in figure 4.6. Following MEMD, IMF2 showed only noise

activity with no identifiable source activity, whereas IMF3 unmixed the source activity, which was clearly identifiable, with no underlying noise. In addition, the reconstruction of the source activity by raw-MSP split the source activity into two sources, where only one had an acceptable location. However, the main activity, represented in red, was mislocated in a lateral position the frontal lobe, with an important distance from the original source at the pre-frontal cortex. This explains the higher WM of 6.23 obtained with raw-MSP. In contrast, a WM value of 1.26 was obtained using MEMD-MSP and the main activity in the source map was correctly located. Although spurious activity appeared at the same position as that found with raw-MSP, its value was attenuated. However, it is remarkable that the value obtained using MEMD-MSP was lower than raw-MSP and the main activity was accurately located.

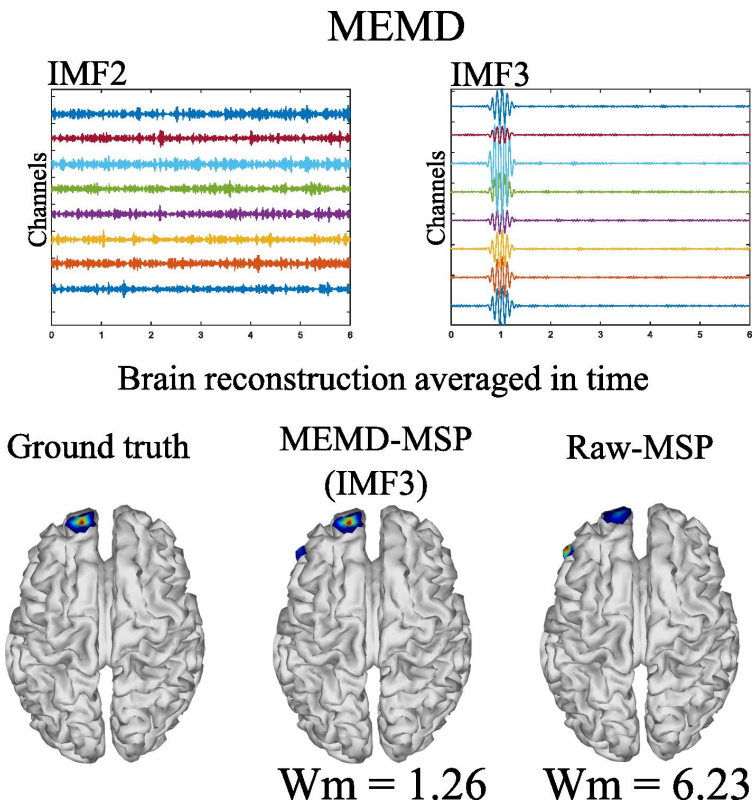

Figure 4.6: MEMD for one source with 10 Hz sinusoidal windowed activity and 8 EEG channels [177].

MEMD was able to separate from the noisy signal the frequency activity for the single source case. This effect was also observed for the three and five active sources. In addition, for the multiple source cases, no mode-mixing was presented in the extracted IMFs, as can be seen in figure 4.7 at left, for the three source case. This case was also evaluated with univariate EMD to provide a comparison and the mode-mixing effects. When using univariate EMD, the mode-mixing at IMF2 and IMF3 can be seen. As a consequence, the source reconstruction was clearly affected by its effects, which become evident in the EMD-MSP reconstruction (figure 4.7 at right bottom) by the higher WM value due to the error in the location of sources and the ghost activity.

The main IMFs decomposed by MEMD over 16 EEG channels, and the resulting brain reconstruction for the three source case is shown in figure 4.7. The decomposition using MEMD clearly split the activity into three IMFs as follows: the activity at 20 Hz is shown in IMF2, the activity at 12 Hz in IMF4, and the activity at 4 Hz in IMF6. There was no mode-mixing in the MEMD decomposition. In addition, the MEMD-MSP achieved a WM of 10.14, which is substantially less than the 15.57 value achieved using raw-MSP. Moreover, the MEMD-MSP reconstruction correctly identified the position of the three simulated sources, even if some spurious activity also appeared. In contrast, in the raw-MSP reconstruction, the position of the second source, located in the left hemisphere of the visual cortex, was incorrectly assigned and spurious activity appeared in various areas, with even higher intensity than the main source, shown by the higher WM values obtained.

The spatial and temporal evolution of the neural activity for the ground-truth and the reconstructions using MEMD-MSP and raw-MSP are shown in figure 4.8 for the three source case reconstructed using the information from 16 EEG channels. The neural activity reconstruction obtained by the MEMD-MSP offered a better WM than that obtained from the raw-MPS in terms of the WM for each source. The time evolution of the neural activity for the MEMD was obtained by mixing the resulting brain mapping for IMF2, IMF4, and IMF6 of the MEMD, as the activity corresponding to each source was clearly divided between the selected IMFs.

A similar evaluation of the spatio-temporal evolution to the sources was

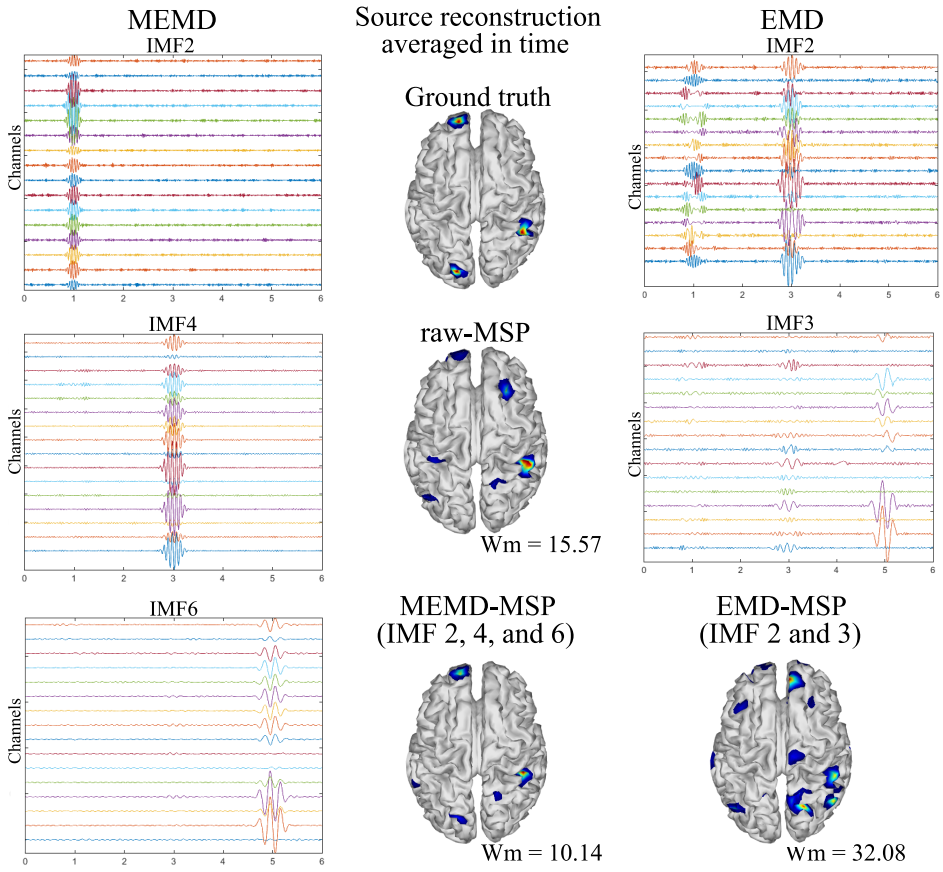

Figure 4.7: Ground-truth activity, MEMD-MSP reconstruction, EMD-MSP reconstruction, and raw-MSP reconstruction (center) [177]. The source reconstruction was performed using 16 EEG channels. For the depicted MEMD-MSP reconstruction, IMFs 2, 4, and 6 (left) were added to rebuild the EEG. For the depicted EMD-MSP reconstruction, IMFs 2 and 3 were used (right).

obtained with the five source case, which is presented in figure 4.9. In it, the five active sources were reconstructed using the down-sampled subset of 32 EEG channels and were analyzed. In this analysis, MEMD-MSP outperformed raw-MSP, with the reconstructed neural activity by raw-MSP showing a lower spatial accuracy in almost all the sources. Raw-MSP gave a lower WM value than MEMD-MSP for only the third source at t_3. However, the raw-MSP reconstruction contained several spurious activities for this source. In addition,

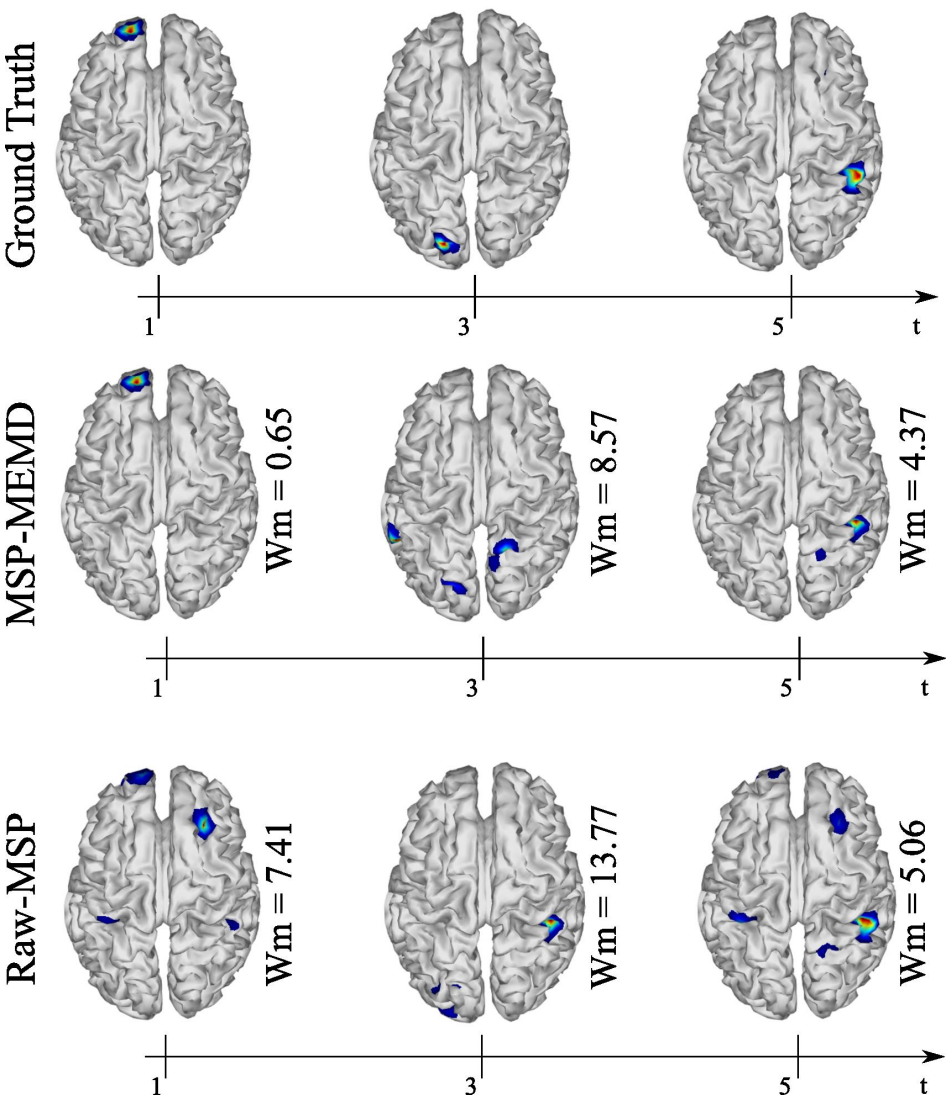

Figure 4.8: Ground truth, MEMD-MSP and raw-MSP neural activity mapping considering the evolution in time for three sources at time $t_1 = 1$, $t_2 = 3$, and $t_3 = 5$ seconds with 16 EEG channels [177].

it is possible to observe the effects of anterior and posterior sources in the other source reconstructions. In contrast, these effects were reduced when MEMD decomposition was applied, for which only attenuated activity from the third source is visible in the fourth reconstructed source. Furthermore, the WM values

were smaller than those for raw-MSP for almost all sources. Such a reduction of spurious activity and the attenuation of effects from other sources appeared when the EEG signals were decomposed into IMFs, and is arguably due to the rejection of noisy information in the IMF selection process and the attenuation of mode-mixing effects by MEMD.

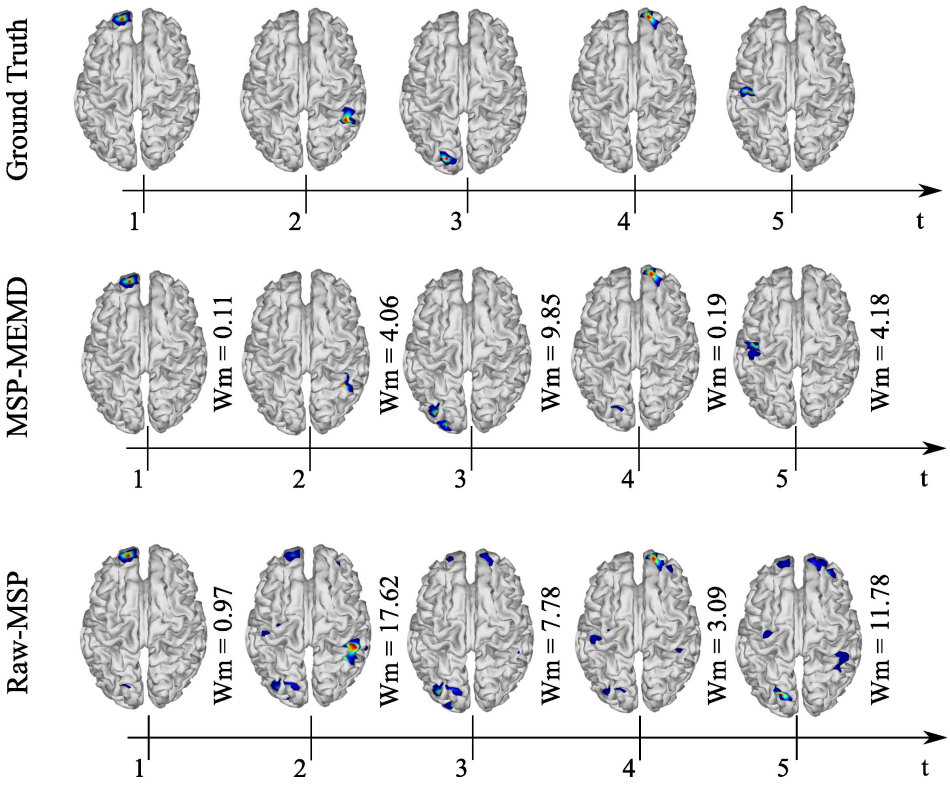

Figure 4.9: Ground truth, MEMD-MSP, and raw-MSP neural activity mapping considering the evolution in time for five sources at time $t = 1$, $t = 2$, $t = 3$, $t = 4$, and $t = 5$ seconds with 32 EEG channels [177].

To perform a quantitative evaluation of the performance of MEMD-MSP and raw-MSP, a comparison was performed for the mean across trials of source reconstruction performance for the three sources case. The performance for each one of the sources at the time instants $t = 1$, $t = 3$, and $t = 5$ seconds with 32, 16, and 8 electrodes was analyzed. The results of this evaluation are presented in figure 4.10. In general, the effects of the electrode down-sampling are visible by the

higher inaccuracy of raw-MSP than MEMD-MSP for eight channels. These results suggest that brain reconstruction with MEMD-MSP can still be performed without affecting the accuracy by reducing the number of EEG channels by a factor of two. Although the WM index increases when spatial down-sampling, its slope is small and the reconstruction quality can be considered reasonable. In contrast, the raw-MSP reconstruction showed an exponential increase in the WM value when spatial down-sampling was performed. In several cases the inclusion of the MEMD step improved significantly the performance of the source reconstruction, specially with a lower number of electrodes. With 32 electrodes, no significant difference was found. This fact can be explained by the MSP estimation itself, due to the fact that when the estimations are made using a higher number of electrodes, the noise estimation in the EEG made by MSP become feasible and accurate, resulting in similar WM values between MEMD-MSP and raw-MSP. However, when the number of electrodes is reduced, the MSP method accuracy decreases significantly, which effect is attenuated by the pre-processing step by MEMD. These significant differences were obtained by performing two-sided pairwise t-tests with an alpha level of $p < 0.05$ using Bonferroni adjustment for multiple comparisons in the software IBM SPSS Statistics for Windows, version 24 (IBM Corp., Armonk, N.Y., USA).

In general, the results for the synthetic EEG signals suggest that the use of the information extracted by MEMD improves the MSP source reconstruction, alleviating its ill-condition. In all analyzed cases, MEMD-MSP attenuated the appearance of spurious activity and the proposed methodology with the MEMD-MSP approach retained spatial accuracy despite the electrode spatial down-sampling. In addition, according to the reconstruction shown in figure 4.8 for the three sources case and figure 4.9 for the five sources case, it is remarkable that with MEMD-MSP the reconstructions seem cleaner of ghost sources, localizing the source in the same place or with a close location to the place where the original activity was simulated. In contrast, in the reconstructions made by raw-MSP, the existence of ghost sources remains due to the influence of the sources that have occurred before and after the analyzed source, an effect that is clearly attenuated due to the extraction of the underlying source activity by MEMD.

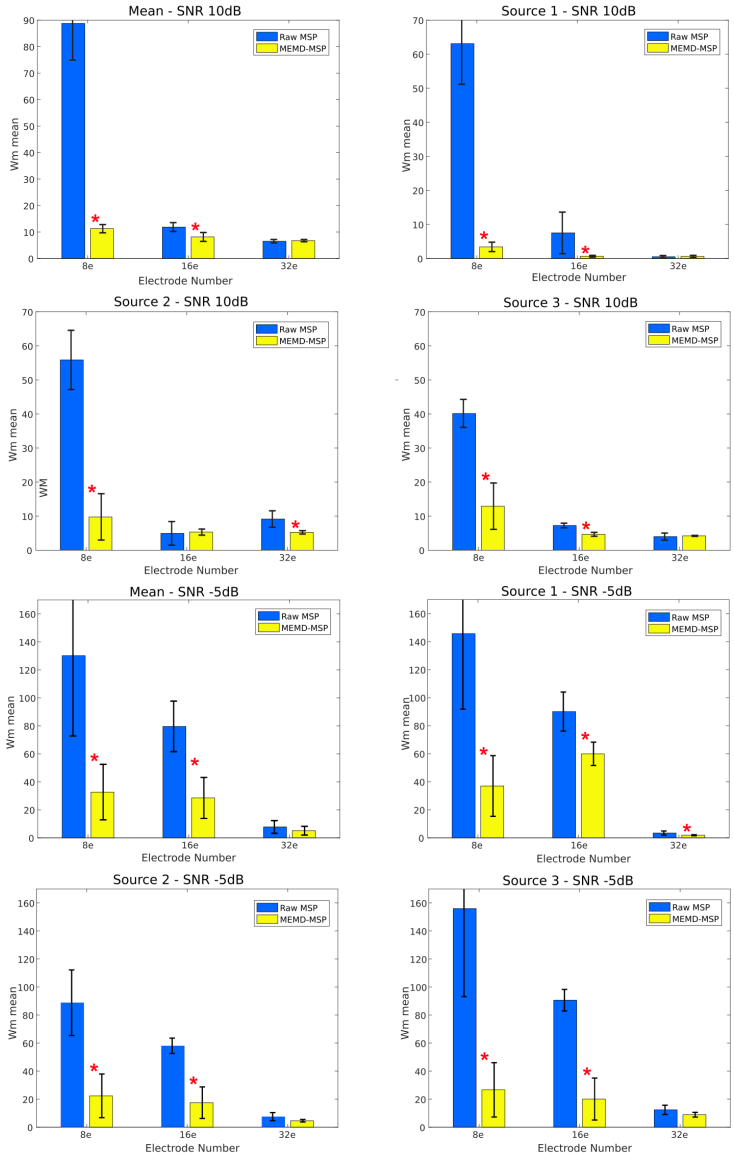

Figure 4.10: Mean WM and standard deviation of the reconstruction considering two levels of noise 10dB and -5dB and three levels of electrode resolution 8, 16, and 32 [177]. The WM was calculated in each time-ROI around the simulated sources at times 1s, 3s, and 5s. *Significant value $p<0.001$.

4.5.2 Multi-modal EEG Dataset

Following the methodology described in figure 4.4 the ERP data were decomposed using MEMD prior to the reconstruction of the source activity. The source estimation solutions obtained using MSP for MEMD and directly from the ERP signals were compared to the ground-truth activity for each individual. A general vision of the results over the dataset is presented in figure 4.11. In it, the general mean across all subjects and conditions of the WM index is presented with its standard deviation. When comparing the raw-MSP and MEMD-MSP estimations with the ground-truth activity, the results are discriminated by the number of channels used. Electrode down-sampling directly affected the quality of the source reconstruction, for which the solutions with MEMD-MSP had a lower WM mean and a lower standard deviation than those with raw-MSP in all the cases. The inaccuracy of raw-MSP increased as the number of electrodes was reduced with a steep slope. In contrast, MEMD-MSP retained a constant quality index when the brain mapping was performed with 32 or 16 electrodes, and increased slightly when 8 electrodes were used. However, with 8 electrodes, MEMD-MSP reached a WM value and standard deviation similar to that obtained with raw-MSP with 32 electrodes, for which there was no significant difference between raw-MSP using 32 electrodes and MEMD-MSP using eight electrodes when a two-sided pairwise t-test was applied using an alpha value of $p < 0.05$.

Figure 4.12 presents the labeled WM indexes according to the condition of the EEG signals, familiar faces or scrambled faces, and the number of channels used to perform the inverse solutions to provide another vision of the results. The mean WM value was slightly higher for scrambled faces with eight electrodes with MEMD-MSP than that obtained with raw-MSP with 32 electrodes. However, raw-MSP with 32 electrodes obtained a lower WM value for familiar faces (24.43% less) than MEMD-MSP with 8 electrodes. However, MEMD-MSP outperformed raw-MSP in all the cases for comparisons between the same condition and the same number of electrodes.

The improvement of the results by applying the MEMD can be explained by the separation of IMFs, as shown in figure 4.13, in which the 8 electrode EEG signals are presented together with their IMF4 EEG reconstruction obtained by MEMD. The figure depicts how the main information of the ERPs is extracted around

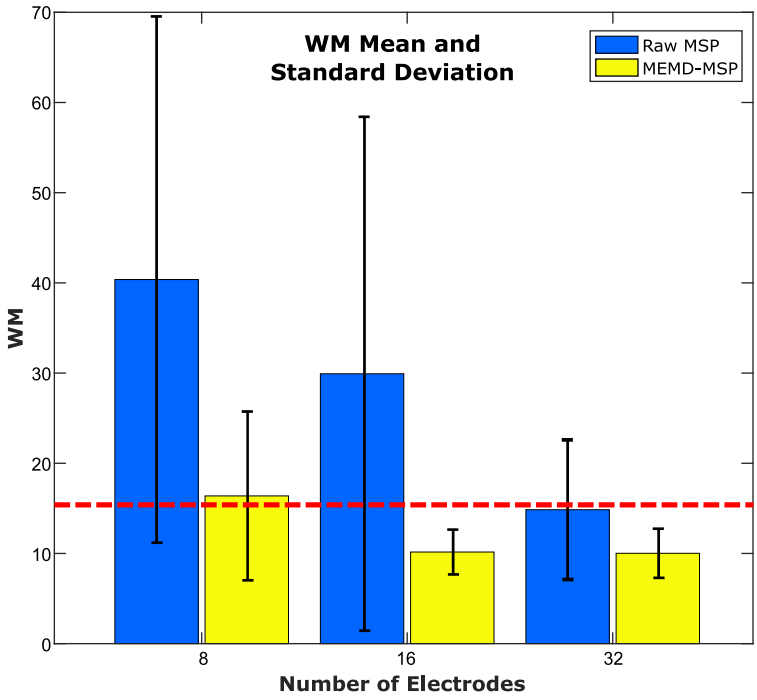

Figure 4.11: Mean WM and standard deviation according to the number of electrodes for 16 subjects [177] . The red line points out the similar error obtained between raw-MSP with 32 electrodes and MEMD-MSP with 8 electrodes, even when the electrode number with MEMD-MSP was lower than raw-MSP.

the established time-ROI, where the sparse temporal and frequency information provided by the IMF is sufficient to obtain better source localization of the activity than by using all the components of the EEG signal.

The location of the neural activity in the brain is shown in figure 4.14. Its activity was found in the visual cortex and the fusiform gyrus, by [212] and [220] using a multi-modal technique involving EEG+MEG+fMRI. The figure provides the ground-truth activity and the brain mapping reconstruction with 8, 16, and 32 electrodes with raw-MSP and MEMD-MSP.

The reconstructions using MEMD-MSP showed a small variation between the different numbers of electrodes involved during source reconstruction (figure 4.14). In contrast, the localization of the reconstructed sources varied without pre-processing the data in the raw-MSP, according to the number of electrodes.

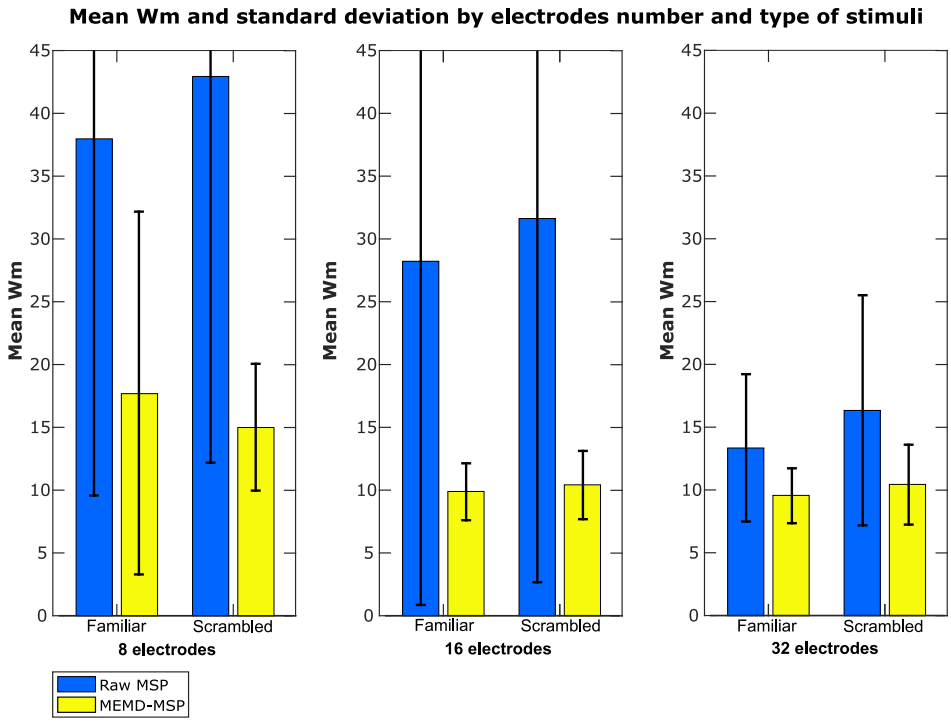

Figure 4.12: Mean WM and standard deviation according to the number of electrodes used in the reconstruction and the type of stimuli presented [177].

Moreover, these solutions showed activity in different brain areas, whereas the MEMD method focused solely on the visual cortex and fusiform gyrus, which are directly involved during the visual face stimulus. Therefore, the use of certain IMFs provided by MEMD resulted in consistent accurate localization of the neural activity and an attenuation of background activity, represented by the lower WM values.

4.6 Discussion

It is well known that the brain can exhibit activity at frequencies between 0.5Hz for Delta waves to 45Hz for Gamma waves (section 2.1.4). The use of time-frequency decomposition methods for EEG signals is generally applied to study brain processes associated with activity at certain frequencies and changes in brain wave oscillations during a number of experimental situations e.g. ERP

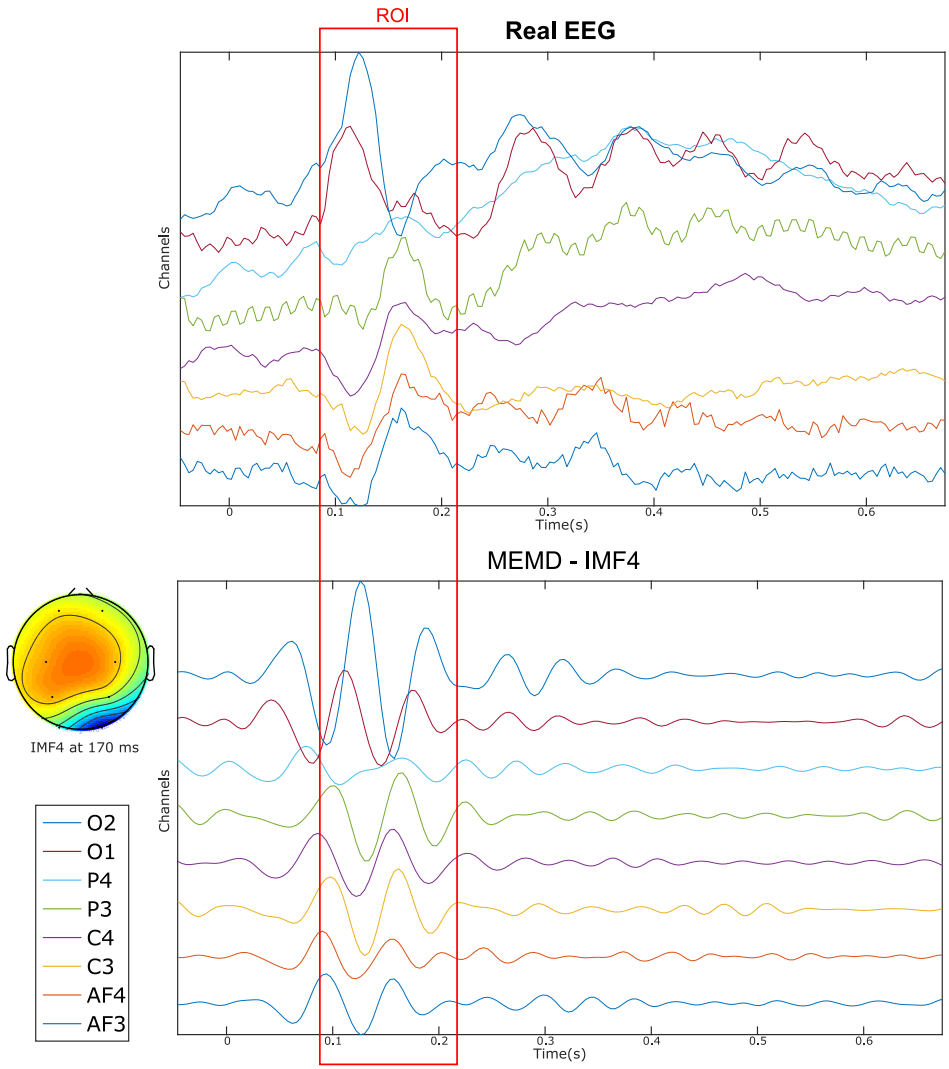

Figure 4.13: Eight-channel real EEG (Top) and the IMF4 component by MEMD (Bottom) [177]. The topographic plot at 170 ms of the IMF4 represents the activation of the occipital region after the stimuli presentation.

studies. EMD is a method that has shown the ability to separate signals using time-frequency decomposition in various contexts. However, EEG signals are challenging due to the frequency proximity of the source activity. Thus, EMD solutions are generally hampered by mode-mixing during IMF decomposition.

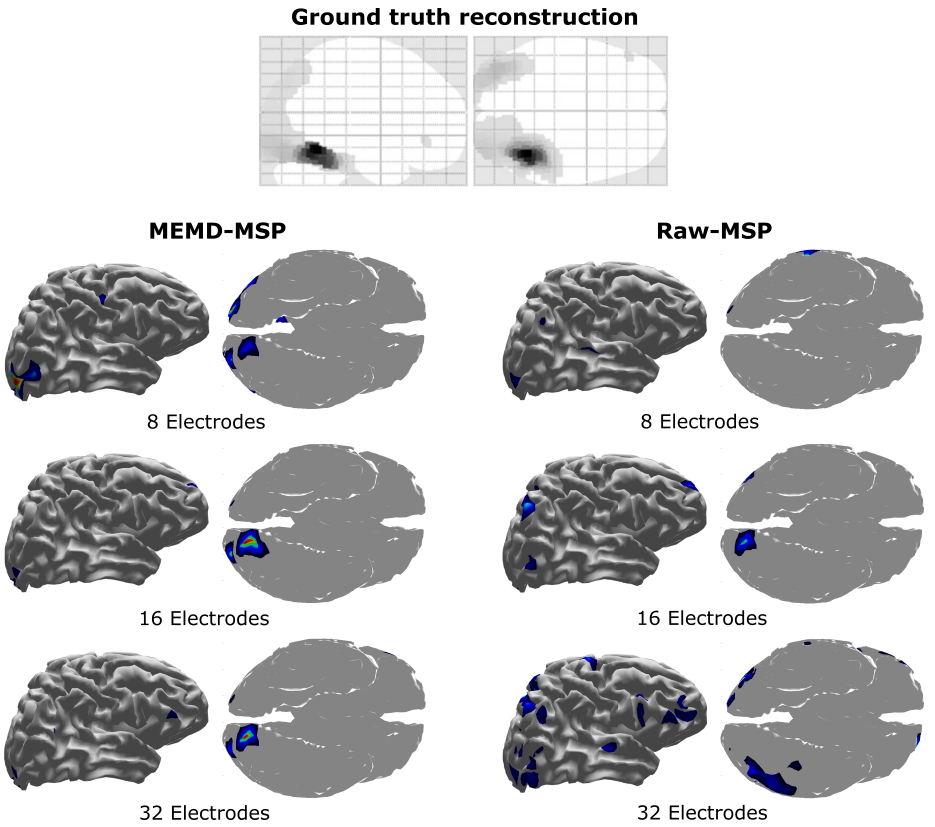

Figure 4.14: Source activity reconstruction using a multi-modal technique involving EEG+MEG+fMRI [177]. (Left) Brain activity reconstruction using MEMD-MSP with 8, 16, and 32 electrodes. (Right) Brain activity reconstruction using raw-MSP with 8, 16, and 32 electrodes.

MEMD attenuates such effects when sources exhibit close frequency, as shown by [178].

Here, this study investigated the MEMD decomposition combined with the source reconstruction algorithm MSP to evaluate the effects of MEMD as a pre-processing step during the calculation of inverse problem solutions and to examine their performance for three different electrode counts: 32, 16, and 8 channels. The solutions obtained with MEMD-MSP were compared to those obtained by raw-MSP for synthetic EEG signals, for which three scenarios of source activity were tested: one active source, three active sources, and five active sources, which were

simulated at frequencies from 2 to 20 Hz. The solutions were also compared using a real dataset of EEG signals from 16 subjects who participated in a behavioral study of face perception, as reported by [3].

The use of a pre-processing step with MEMD improves the accuracy of source reconstruction by MSP for all the evaluations. The results for synthetic and real EEG data showed that the quality of the solutions obtained by MEMD-MSP remained stable when 16 or 32 electrodes were used, and decreased slightly only when using 8 channels. The reconstructions using MEMD-MSP with 8 channels achieved similar values as raw-MSP with 32 channels for simulated sources (figure 4.10) and for real data (figure 4.12), for which no significant differences were found between the reconstructions. Moreover, the proposed methodology involving the decomposition stage with MEMD and using selected information during the source reconstruction process clearly makes it feasible to perform this process using low-density electrode counts, for which the small number of electrodes and sparse information of IMFs from MEMD are sufficient to retain the accuracy of the source reconstruction and reduce the effects of noise in the inverse problem calculation. Besides, this accuracy retention is favored by the mode alignment, and it allows to obtain the same frequency mode in the same IMF for each channel of the original signal. This property allowed this study to separate the noise in the first IMFs and after this, the other modes were decomposed in aligned form. This could be useful when designing an automatic algorithm to choose the IMFs with the relevant modes.

The performed temporal evaluation was focused on time-ROIs defined by time windows around the appearance of sources in the synthetic EEG signals test and around the evoked activity for the real dataset. In general, the reconstructions with MEMD-MSP showed a clear attenuation of the background activity (figures 4.7, 4.8, 4.9, and 4.14). This effect can be explained by the frequency decomposition and attenuation of mode-mixing resulting from MEMD, in which the analysis of the frequency information of the EEG channels allows MSP to focus on the source activity presented in the selected IMFs (figures 4.7, and 4.13), resulting in solutions with a lower WM index for the combination of methods.

In conclusion, the proposed methodology shows that adding a *priori* time-frequency information as an input to the MSP source reconstruction algorithm

makes it possible to obtain better solutions, even when information from only a reduced number of electrodes is used. MEMD should allow extraction of the main time-frequency information of sources that are hidden within the channels' data, and then it can be used to obtain an reconstruction with spatial reconstruction accuracy comparable to that obtained using the same MSP method with a high number of electrodes and without any prior decomposition. Moreover, source activity is clearly separable in the MEMD-MSP solutions, resulting in an unmixing effect in the source space. The application of MEMD with other methods and the unmixed activity for brain connectivity should be studied in future studies. Here, it is considered that the proposed methodology can be applied for source activity reconstruction studies using ldEEG. In addition, due to the temporal accuracy showed by the MEMD-MSP, this method can be considered suitable to study brain connectivity at source levels.

Recently, in [245], a new method of time-frequency decomposition for multivariate signal called multivariate variational mode decomposition (MVMD) was presented. This method as the MEMD decomposes the signal in intrinsic mode functions while keeping the mode-alignment property. In [245] the MVMD was applied to EEG signals showing robustness to noise. Such characteristics can be considered to be useful for source reconstruction applications as the MEMD. Here the strong impact that the proposed methodology has on the source reconstruction is demonstrated. Due to its intrinsic properties multivariate time-frequency decomposition methods based on mode decomposition are an important tool for unmixing source activity and their impact should be studied further in future works.

Chapter 5

Low-density EEG Source Reconstruction Based on Partial Brain Models and Relevance-based Channel Selection

This chapter introduces a methodology to apply source reconstruction constraining the solution to a brain-ROI by intervening the forward model, and using a section of the brain denominated partial brain model (PBM), that is related to the brain activity of interest. This is done to alleviate the ill-possedness of the inverse solution, by reducing the number of unknowns to estimate. In addition, the relevance-based selection is also introduced and applied to identify ldEEG subsets of channels that can be used for source estimation while maintaining a hdEEG reconstruction accuracy. The relevance-based selection of channels is compared with multiple electrode layouts that lie in both, hdEEG and ldEEG categories. The evaluations presented here are performed on the synthetic EEG dataset presented in section 3.7.1.

This chapter is based on the articles [215] and [246], and mainly addresses the 2^{nd} research question.

5.1 Introduction

The inverse problem that requires to be solved for estimating the source activity is well known to be ill-posed, where the number of *knowns*, EEG channels, is much less than the number of *unknowns* [12]. In addition, the spatial resolution of EEG ≈10 mm is the lowest compared to other brain imaging techniques like fMRI, PET, CT, and MEG [161] and section 2.4.5. In source reconstruction it has been established that to obtain reliable reconstructions and control the ill-possedness of the EEG inverse problem, hdEEG is required. It has been proven to be the most accurate option to perform source reconstruction and localize the activity sources [24, 25, 247]. In contrast, recent studies have suggested that source reconstruction can be performed with ldEEG [159, 160]. Considering this, a methodology to reduce the number of unknowns to alleviate the ill-posed problem and select a reduced set of channels in the ldEEG category is introduced. It consists of estimating the source activity of a particular brain region by using the model of a section of the brain called PMB, and applying frequency constraining and relevance-based channel selection to perform source reconstruction in ldEEG settings.

A few studies have shown the possibility of performing source reconstruction methods using a small number of electrodes. e.g. in [244]. The authors proposed and evaluated the use of 7 electrodes to map the activity of the whole brain using several brain mapping methods, obtaining a localization accuracy around 15 mm using MSP. In [248], a low-density approach to BCI was presented, in which the occipital activity was mapped using MSP and a PBM of the occipital region, obtaining an accuracy around 23 mm in the location of the source with four electrodes. However the selection of channels was based on local electrodes and the PBM was briefly formulated. To alleviate ill-possedness, in [249] an approach to reduce the number of unknowns was presented with the objective to perform faster computations that can be used in BCI. The alleviation was performed by computing a reduced lead field matrix that groups the sources of the Broadmann areas, leaving one source per area. By using this approach functional areas could be mapped. The authors obtained localization error values below 18 mm while using hdEEG sets. A similar approach of dividing the cortex using the Broadmann areas as functional zones and grouping the sources into the areas

was presented in [250], In this, multiple numbers of electrodes were used, 19, 33 and 71, obtaining errors below 22 mm, where the best result was around 5 mm with the hdEEG set. However, the number of channels in studies involving ldEEG were selected based on spatial down-sampling by maintaining coverage and local electrodes close to the ROI. In here, the selection of channels by relevance criteria is introduced, where multiple tests and evaluations were performed to evaluate the source reconstruction accuracy of relevance-based selected channels and multiple layouts in hdEEG and ldEEG.

Two evaluations were performed using separate experimental frameworks used in publications [215] and [246]. The first experimental framework related to [215] is focused on the evaluation of the proposed methodology combining: PBM, frequency constraining and relevance-based channel selection. The second experimental framework related to [246] is intended to evaluate relevance-based channel selection by comparing source reconstruction results of selected channels with hdEEG montages, standard positioning systems in hdEED and ldEEG, and down-sampled versions based on coverage in ldEEG category.

5.2 Partial Brain Model Formulation

Consider the problem of EEG generation for a time instant given by the forward EEG equation in 2.2. This model can be rewritten by considering two subsets of brain activity $\boldsymbol{x}$ as follows:

$$\boldsymbol{y} = \begin{bmatrix} \boldsymbol{M}_1 & \boldsymbol{M}_2 \end{bmatrix} \begin{bmatrix} \boldsymbol{x}_1 \\ \boldsymbol{x}_2 \end{bmatrix} + \boldsymbol{\epsilon} \tag{5.1}$$

where $\boldsymbol{M}_1$ and $\boldsymbol{x}_1$ is the leadfield matrix and its corresponding neural activity for a specific brain-ROI or target zone, and $\boldsymbol{M}_2$ and $\boldsymbol{x}_2$ the lead field matrix and its corresponding neural activity of the remaining brain. It can be seen that the equation 5.1 can be rewritten as:

$$\boldsymbol{y} = \boldsymbol{M}_1\boldsymbol{x}_1 + \boldsymbol{\eta} \tag{5.2}$$

where $\boldsymbol{\eta}$ is a vector that holds the noise and the activity in the part of the brain related to $\boldsymbol{M}_2$ and $\boldsymbol{x}_2$. In addition, if the vector $\boldsymbol{x}_2$ is close to zero (which means

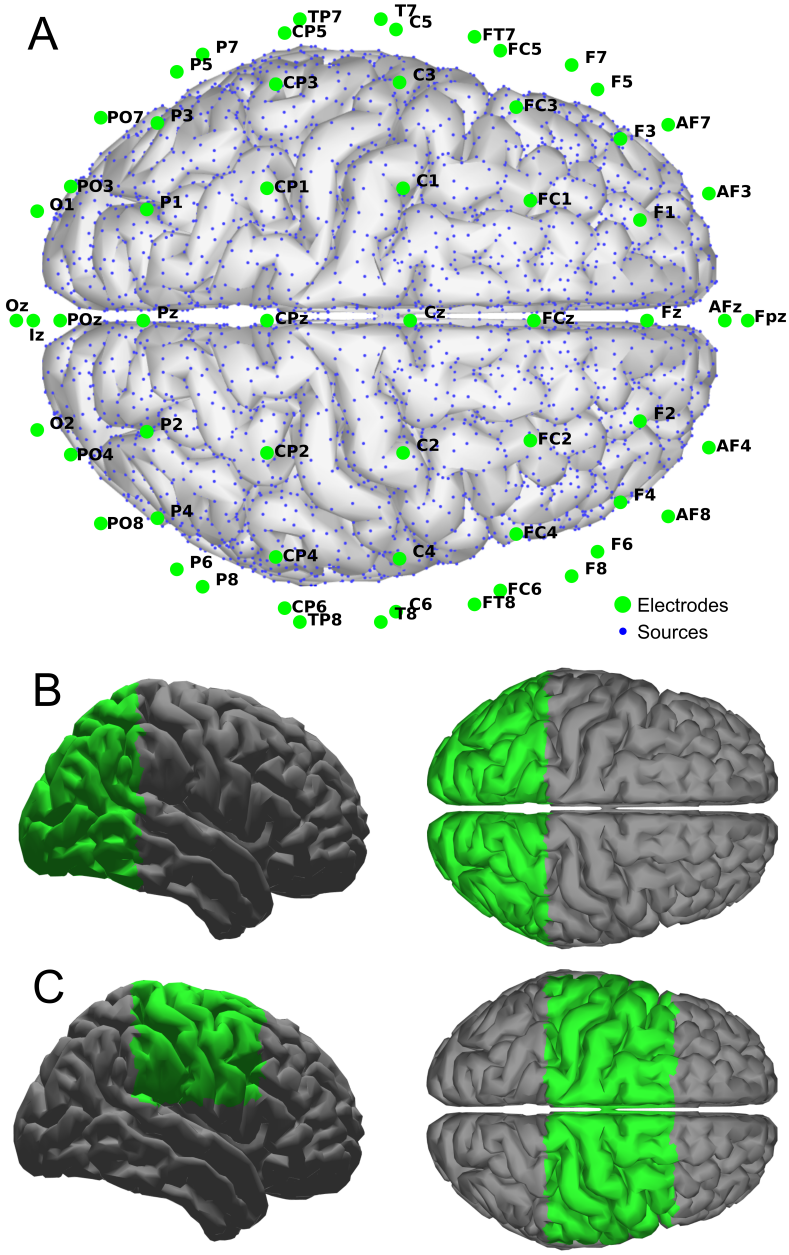

Figure 5.1: **(A)** New York head model[216] with 60 electrodes and 10016 sources, 10K model, **(B)** brain section for occipital cortex area PBM, OC model, and **(C)** brain section for the sensory-motor cortex area PBM, MC model [215].

that the neural activity outside the target zone is closed to zero), the following approximation can be performed:

$$\boldsymbol{y} \approx \boldsymbol{M}_1 \boldsymbol{x}_1 + \boldsymbol{\epsilon} \tag{5.3}$$

By using an approximated model as described in equation 5.3 the inverse problem for $\hat{\boldsymbol{x}}_1$ can be solved. However, the activity outside the target zone could affect the estimation because all recorded activity by the electrodes will be projected in the target zone. Therefore, an additional stage to reduce the effect of $\boldsymbol{M}_2 \boldsymbol{x}_2$ over $\boldsymbol{y}$ can be added before performing the inverse problem, by considering that the source in the target zone appears in a known frequency, then, the EEG e.g. by applying MEMD decomposition or band-pass filtering; leading to an attenuation of the activity outside the region of interest. In addition, by assuming that the electrodes mostly record activity in the neighbor spaces around it, a reduction in the number of electrodes can be made as:

$$\boldsymbol{y}_r \approx \boldsymbol{M}_{1r} \boldsymbol{x}_{1r} + \boldsymbol{\epsilon}_r \tag{5.4}$$

where the resulting estimation of $\boldsymbol{x}_{1r}$ is an approximation of $\boldsymbol{x}_1$ obtained by using a reduced number of channels.

A PBM is a section of the brain based on a specific brain-ROI and it is generated from a complete brain model. To exemplify this, the New York head model [216] is considered. It is based on the computation of a FEM over a non-linear average of 152 individual MRI (ICBM152 v2009) from the International Consortium for Brain Mapping [251]. Detailed information of this model is presented in section 3.7.1. In here, the model and lead field matrix of 10016 source was considered, and an electrode down-sampling was performed to reduce from 231 electrodes in 10-5 to 60 positions of the 10-10 international system. This model is presented in figure 5.1A. In this chapter, this model is referred as the 10K model and is used to compare the performance of a hdEEG montage with the PBM with ldEEG. Two PBMs were generated from the occipital cortex area, referred to the OC model, and the sensory motor cortex areas referred to the MC model. Both cortex sections of the PBMs are presented in figure 5.1. The number of distributed sources for PBM is 3054 for the OC model and 2162 for the MC model.

5.3 Channel Selection Based on Relevance

Here, relevance analysis [203] is proposed as an approach to select the N_α most relevant EEG channels to be used for source reconstruction. The input for this analysis is the ERP data $\boldsymbol{y}$ to be reconstructed. Then, the relevance value $\alpha_{N_{ch}}$ for each channel is calculated using the Standard Power-Embedded Q-α algorithm (Q-α algorithm details are presented in section 3.5). Then the N_α channels with the highest α value are selected to obtain a reduced EEG $\boldsymbol{y}_{N_\alpha}$.

5.4 Methodology for Source Reconstruction Based on Partial Brain Models and Relevance-based Channel Selection

A summary of the proposed methodology is presented in figure 5.2. The methodology has two main branches, the first one related to the processing and selection of EEG channels, and a second one related to the model reduction and estimation of the PBM. For the first branch, the input is the ERP data $\boldsymbol{y}$. Then, the ERP can be filtered or decomposed e.g. using band-pass filtering or using MEMD as in the chapter 4 methodology. This process is referred to here as frequency constraining. Independently of the selected frequency analysis to filter the signals, the filtered EEG $\hat{\boldsymbol{y}}$ can constrain the solution in particular frequencies, e.g. the signals can be decomposed in frequency bands related to brain rhythms. In a subsequent step, the filtered $\hat{\boldsymbol{y}}$ is used for relevance-based channel selection. In this step, the complete epoch of the ERP can be evaluated or a particular time-ROI can be defined for applying the channel selection. The relevance α is computed by the $Q-\alpha$ algorithm for each channel, and a subset of selected channels N_α is used for source reconstruction.

In the case of the second branch of the methodology, the input is the the head model including the lead field matrix $\boldsymbol{M}$ and the 3D locations of the distributed sources. This model is then reduced, by considering only the sources associated of a Brain-ROI. This can be done by cortical parcellation including atlases to differentiate the brain regions [252–254] when forward modeling or directly by dissecting the 3D cortex mesh. Then the reduced model and the selected channel branches are joined in the source reconstruction process.

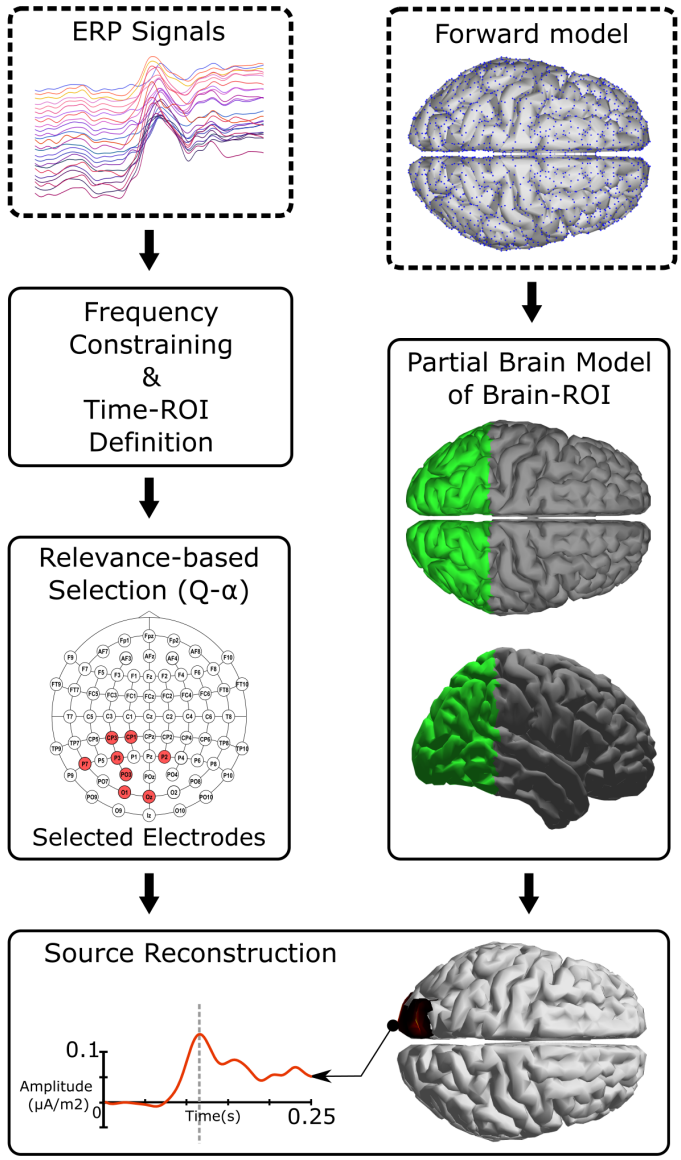

Figure 5.2: Methodology for source reconstruction using PBM and $Q - \alpha$ relevance-based channel selection. The dashed squares represent the inputs of the methodology.

5.5 Experimental Framework - PBM and Relevance-Based Channel Selection

The experimental framework and evaluation procedure is summarized in figure 5.3. To evaluate the performance of the proposed methodology a two-source

dataset was generated. The procedure started with the generation of 400 trials of simulated EEG activity using the simulation framework 3.2, five levels of noise are considered in the dataset: 0, 5, 10, 15, and 20 dB, 80 trials per level. Each trial has two simulated sources overlapping between 37.5% and 40%. The parameters of simulation are presented in table 5.1.

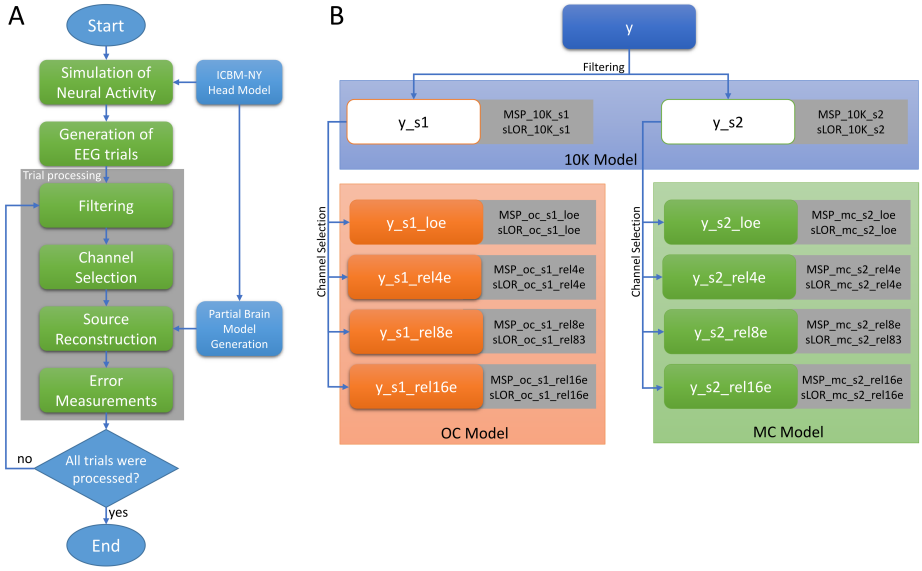

Figure 5.3: **(A)** Flowchart of the followed pipeline, after the trial generation, the procedure is applied per trial (gray square). **(B)** Source reconstruction tree, gray squares contain the name of the reconstruction using the EEG signal at left, the region in blue indicates the use of the 10K model, orange for the OC model, and green for the MC model [215].

The first source was simulated in the occipital areas, while the second source was simulated in the sensory-motor cortex areas, with a frequency simulating a source in the range of mu rhythm. The positions were randomly selected between a set of pre-defined positions distributed on the corresponding regions. The pre-defined set of positions has six locations, three in each hemisphere. The positions were: 3727, 8735, 2734, 7742, 3461, and 8469 for the source s_1 at occipital areas and 3837, 8845, 2284, 7292, 2271, and 7279 for the source s_2 at motor cortex areas. An example of the simulated activity is shown in figure 5.4. It shows the location of the simulated sources at the center of activity and the time courses of the sources

s_i	i=1	i=2
f_i (Hz)	20	10
c_i (s)	0.3	0.8
\sigma_i	0.12	
loc_i	Occipital	Sensory-Motor
a_i	Equation 3.36	Equation 3.36

Table 5.1: Simulation Parameters for PBM and Q-α evaluation

during the simulated trial. In addition, the EEG related to the simulated activity is presented with the channel names.

Each EEG trial was filtered by using high order FIR band-pass filters. The cutoff frequencies were set up at 19 and 21 Hz for the first source, and for the second source were at 9 and 11 Hz. The filters were applied in both directions of time to prevent losing information. As the output of the filter stage, two filtered sets of EEG signals were obtained $\boldsymbol{y}_{s_1}$ and $\boldsymbol{y}_{s_2}$ for the respective simulated source.

After filtering, several EEG reductions were calculated. Here, two criteria were applied to select the electrodes. The first criteria is related with the proposed methodology, by using Q-α method, three levels of relevance based on the 4, 8 and 16 most relevant channels were applied. This results in $\boldsymbol{y}_{s_1\_rel4e}$ and $\boldsymbol{y}_{s_2\_rel4e}$ by the first level of relevance with 4 electrodes, $\boldsymbol{y}_{s_1\_rel8e}$ and $\boldsymbol{y}_{s_2\_rel8e}$ by the second level of relevance with 8 electrodes, and $\boldsymbol{y}_{s_1\_rel16e}$ and $\boldsymbol{y}_{s_2\_rel16e}$ by the third level of relevance with 16 electrodes. A second criteria based on local electrodes was applied. In it a configuration of 8 electrodes around the target zone is selected maintaining an equal number of electrodes across both brain hemispheres. This results in a set of channels $\boldsymbol{y}_{s_1\_loe}$ and $\boldsymbol{y}_{s_2\_loe}$. Those configurations are shown in figure 5.5 for the OC and MC PBMs.

Two methods were applied for source reconstruction: sLORETA and MSP. Multiple source reconstructions were evaluated for each one of the 400 trials, using combinations of channel selection, model, and filtering. They are summarized in figure 5.3B, where a diagram with the name of each EEG configuration and the respective reconstructions is presented. The localization error was used as

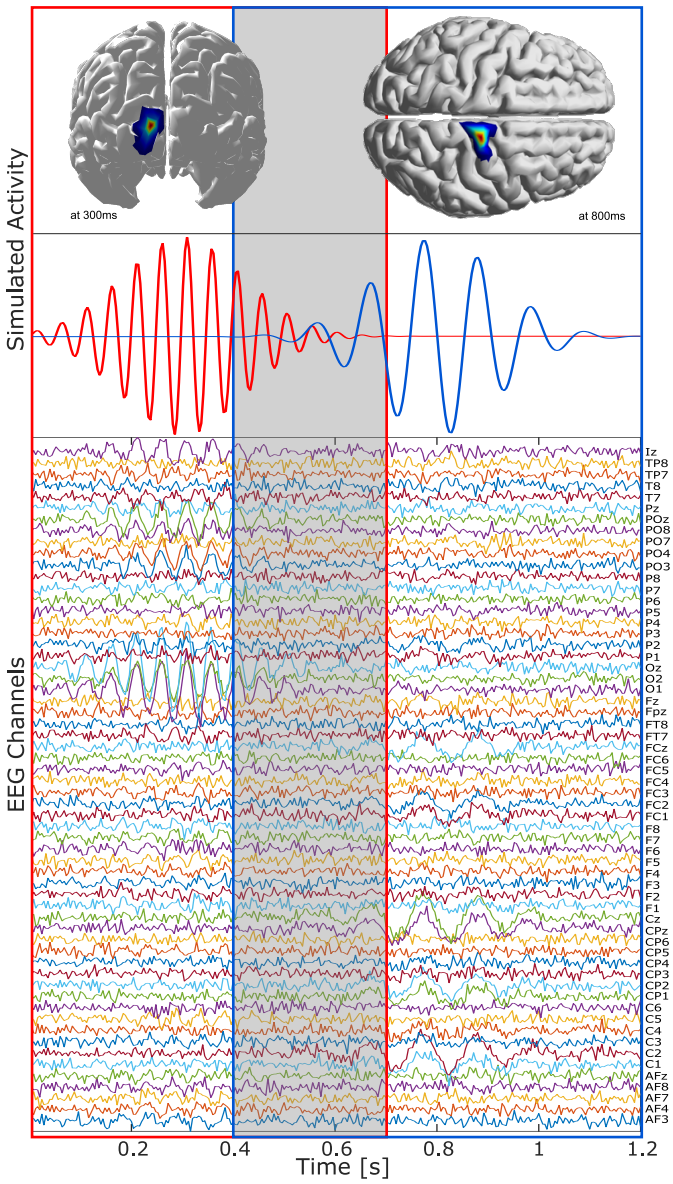

Figure 5.4: (Top) Example of source activity, source activity one simulated between 0-0.7s at 20Hz in the occipital area (red), source activity two simulated between 0.4-1.2s at 12Hz in the motor cortex (blue). (Bottom) EEG and channel information . The overlap between the source activity one and two is around 37.5% to 42% (marked in the gray area) [215].

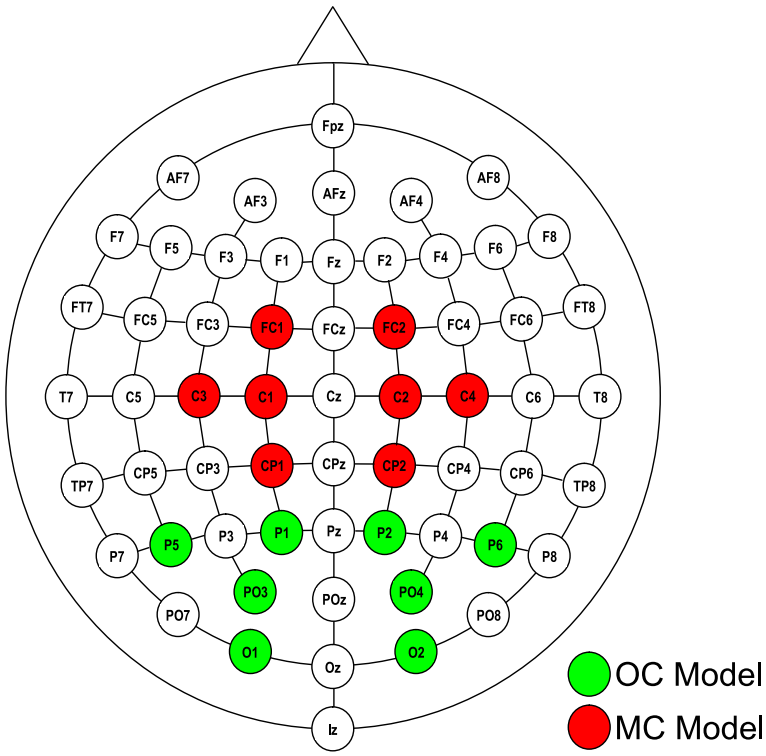

Figure 5.5: Electrode layout and selected local electrodes, local electrodes for OC model (green), and local electrodes for MC model (red) [215].

performance measurement. Here the location of the source with the highest power was selected as the main source location. This estimated location was then compared with the original simulated position using the equation 3.22. In addition, to provide a view of the effects of filtering over the channel selection and source reconstruction, the same reconstructions were calculated removing the filtering stage from the procedure, making $\boldsymbol{y}_{s_1}$ and $\boldsymbol{y}_{s_2}$ equal to $\boldsymbol{y}$.

5.6 Results PBM and Relevance-Based Channel Selection

The results of the proposed methodology are presented in figure 5.6 and table 5.2. The mean localization error across the 400 trials is presented for both cases, when applying the complete procedure including filtering and without applying it. It

can be seen that when the filter stage is not applied (figure 5.6A), the sources were mixed and the relevance criteria tended to select the channels related to the same source. In the case of source s_1, it presents a higher power than source s_2, therefore it was reconstructed with higher accuracy than s_2. The accuracy obtained without filtering for source s_2 shows that the inverse methods projected the s_1 in the MC model, which explains the high mean localization error of the methods using the full set of electrodes.

Analyzing the results of the hdEEG count with the full 10K model. It obtained the best localization error for the first source s_1 by using sLORETA for both, when filtering 1.1 mm and without filtering 3.2 mm. For the MSP, there was a notable increasing of the localization error, it increased from 4.2 mm with filtering, to 24.4 mm without filtering. For the second source s_2 sLORETA and MSP did not obtained the best localization error, both obtained a value >10mm, with 13.8 mm and 15.9 mm, respectively. In addition, both had a significant increase in the localization error when removing the filtering stage. sLORETA increased to 109,6 mm, and MSP to 91.1 mm, being those values the worse performance for s_2 without filtering.

Regarding the reconstructions using the proposed methodology, the relevance-based channel selection obtained more stable values, than the hdEEG with 10K model. The localization error also increased when removing the filtering stage, however, the slope was less notable. For source s_1 using the complete methodology including the frequency constraining, the selected channels with PBM and sLORETA obtained a value <8.2 mm, with 8.1, 5.5, and 4.6 mm for 4, 8, and 16 channels respectively, and with MSP <20.5 mm, with 20.4, 12.6, and 9.1 mm for 4, 8, and 16 channels respectively. For source s_2, the selected channels with PBM and sLORETA obtained a value <9.3 mm, with 9.2, 7.1, and 6.4 mm for 4, 8, and 16 channels respectively, and with MSP <16.2 mm, with 15.2, 16.1, and 13.6 mm for 4, 8, and 16 channels respectively.

The local electrodes criteria presented a stable value for the reconstruction even if the filtering stage was not applied. For the source s_1 with PBM, the mean localization error was between 15 to 20 mm, and for source s_2 and MC model, between 11 to 22 mm. In general, when used the PBM with relevance-based channel selection, the localization error remained below 10 mm for the sLORETA method, and below 21 mm for the MSP reconstructions.

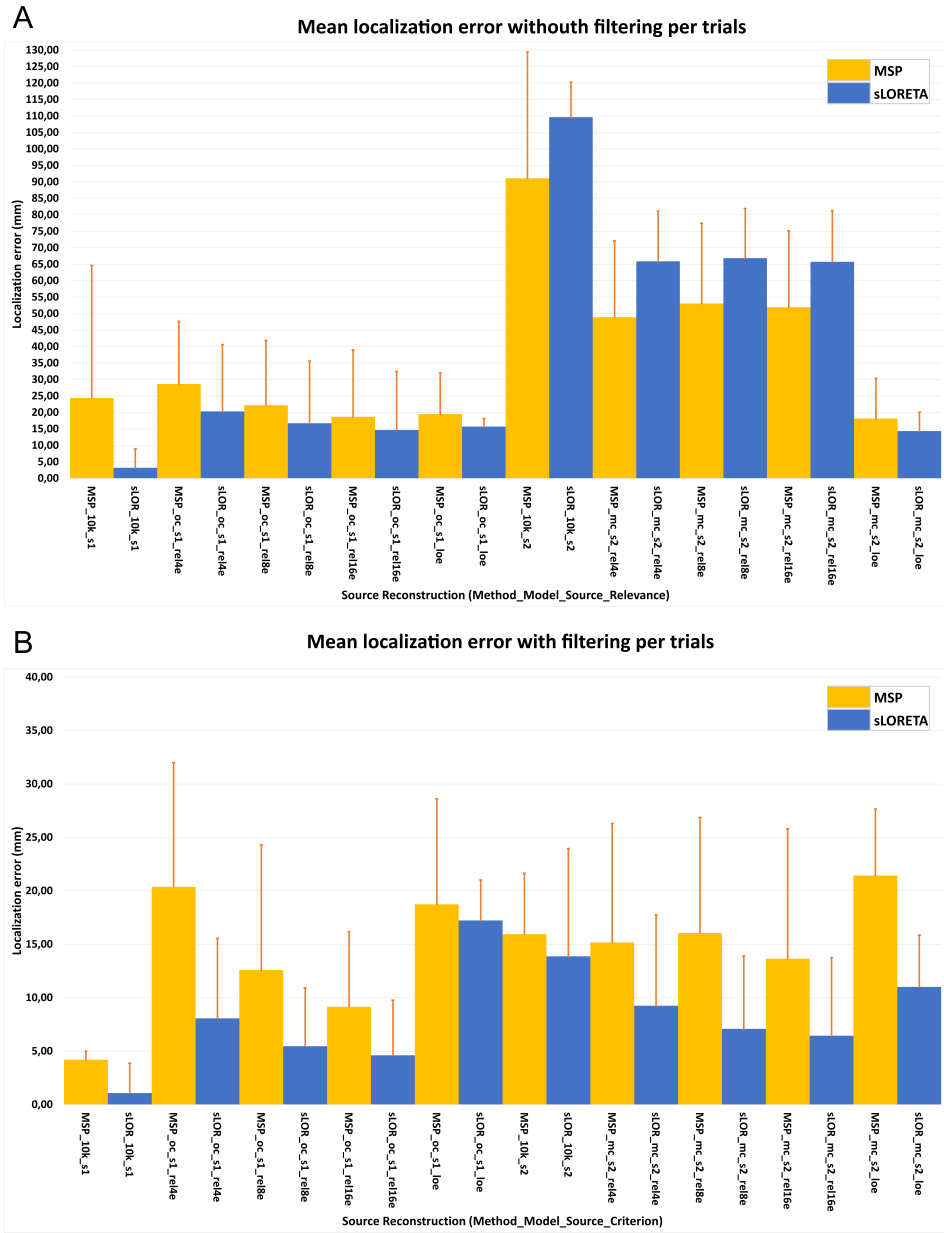

Figure 5.6: Mean error localization, without applying the filter stage **(A)**, and following the complete procedure with the frequency constraining stage using linear filters **(B)** [215].

					Non-Filtered Data		Filtered Data	
Method	**Head Model**	**Source**	**Channel Selection Criteria**	**Number of Electrodes**	**Mean Localization Error (mm)**	**SD**	**Mean Localization Error (mm)**	**SD**
MSP	10K	S1	-	60	24.41	40.22	4.19	0.82
sLORETA	10K	S1	-	60	3.22	5.70	1.08	2.79
MSP	OC	S1	Relevance	4	28.67	18.97	20.37	11.63
sLORETA	OC	S1	Relevance	4	20.33	20.26	8.07	7.48
MSP	OC	S1	Relevance	8	22.19	19.69	12.58	11.72
sLORETA	OC	S1	Relevance	8	16.74	18.86	5.46	5.46
MSP	OC	S1	Relevance	16	18.68	20.29	9.14	7.02
sLORETA	OC	S1	Relevance	16	14.67	17.74	4.61	5.17
MSP	OC	S1	Local	8	19.47	12.54	18.73	9.89
sLORETA	OC	S1	Local	8	15.70	2.44	17.23	3.79
MSP	10K	S2	-	60	91.09	38.32	15.94	5.71
sLORETA	10K	S2	-	60	109.66	10.61	13.87	10.08
MSP	MC	S2	Relevance	4	48.90	23.16	15.17	11.13
sLORETA	MC	S2	Relevance	4	65.88	15.25	9.24	8.51
MSP	MC	S2	Relevance	8	53.09	24.39	16.05	10.82
sLORETA	MC	S2	Relevance	8	66.83	15.07	7.09	6.82
MSP	MC	S2	Relevance	16	51.93	23.19	13.64	12.17
sLORETA	MC	S2	Relevance	16	65.71	15.61	6.44	7.30
MSP	MC	S2	Local	8	18.14	12.27	21.44	6.22
sLORETA	MC	S2	Local	8	14.34	5.71	11.01	4.85

Table 5.2: Mean error localization without applying the filter stage, and following the complete procedure including the filtering stage [215].

sLORETA with the proposed methodology obtained stable results with a localization error below 10mm even with 4 selected channels, in several cases the error level was lower than values obtained with the same method and MSP with hdEEG montage. Comparing to [150], the levels of error of MSP obtained a similar error value around 5 mm when using the 60 electrodes for source s_1. Regardless of the use of the filtering stage, it is notable that with the proposed methodology was achieved a mean localization error around 7 mm using 8 channels with sLORETA and 16 mm with MSP, and slightly less with 16 electrodes, around 6 mm with sLORETA and 14 mm with MSP.

To offer an overview of the computation time required to perform source reconstruction with the PBMs and the full model, the mean and standard deviation of the computation times over the 400 trials is presented in table 5.3 for the two

source reconstruction methods with the 10K model and the PBMs.

	10K Model		OC Model		MC Model	
Method	Time (ms)	std (ms)	Time (ms)	std (ms)	Time (ms)	std (ms)
MSP	405,02	44,50	265,88	36,12	224,52	28,31
sLOR	47,03	1,90	12,22	0,92	7,36	0,69

Table 5.3: Mean and standard deviation of computation times for source reconstruction over the 400 trials using the 10K model and the PBMs.

5.7 Experimental Framework - Relevance-based Channel Selection

The synthetic dataset presented in section 3.7.1 is used here to perform multiples evaluations using the ground-truth to compare the source reconstruction performance using relevance-based channel selection with multiple hdEEG and ldEEG electrode layouts. The dataset consists of EEG data of 150 trials with six underlying sources with temporal mixing, the data contains the signals recorded by 231 electrode positions, of which 161 are located on the scalp according to the 10-5 system, and 70 electrodes distributed between neck and face. Before applying channel selection, a time-ROI for the first three sources of the dataset was defined, 250 to 750 ms for the first source s_1, 750 to 1250 ms for the second source s_2, and 1250 to 1750 ms for the third source s_3. Then, the channel selection based on relevance was applied to select the $N_\alpha = 2$ and $N_\alpha = 3$ most relevant channels per each source time-ROI. Therefore, the total number of electrodes per EEG used during source reconstruction for $N_\alpha = 2$ was 6 channels, and for $N_\alpha = 3$ was 9 channels. They are referred to as $Rel - 6E$ and $Rel - 9E$, respectively. Figure 5.7 summarizes the selection process and presents the time-ROI times for each source.

To compare the performance of source reconstruction using relevance-based channel selection, multiple layouts based on coverage and standard systems were considered. The first electrode layout considered is based on the 161 scalp electrodes of the model, referred to as $HD - 161E$. Two subsets of 19 and 62 electrodes were considered based on the 10-20 and 10-10 standard electrode distribution, referred to as $LD - 19E(10-20)$ and $HD - 62E(10-10)$, respectively. Four more subsets of electrodes were selected based on coverage criteria, one lies

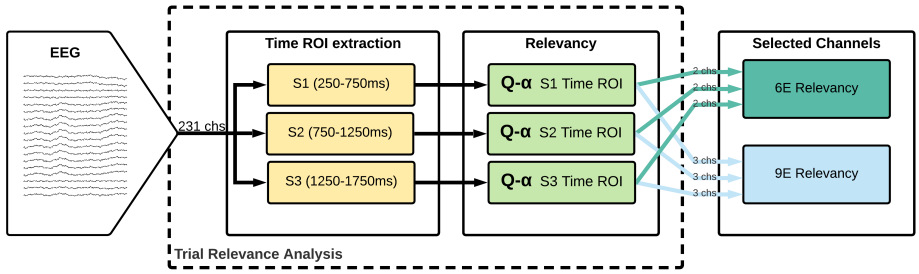

Figure 5.7: Relevance-based channel selection procedure for selecting the 6 and 9 most relevant channels per each EEG trial [246].

in the category of high-density with 128 channels and is referred to as $HD-128E$; the other three are considered low-density, with electrode numbers of 32, 16, and 8, and were selected by electrode down-sampling, trying to keep an equal coverage of the head. They are referred to as $LD-32E$, $LD-16E$, and $LD-8E$. Figure 5.8 shows the different standard-based and coverage-based layouts.

The evaluation procedure is presented in figure 5.9. The inputs are the ground-truth synthetic dataset and the forward model. Each one of the 150 trials were processed separately. The channels were selected according to the three criteria: coverage-based, standard-based, and relevance-based. The selected channels were considered during inverse solution and processed with wMNE, sLORETA, and MSP source reconstruction algorithms, and with MUSIC and TRAP-MUSIC source localization algorithms. After performing the inverse computing, the localization error for each of the three sources was calculated by using the localization error equation 3.22 between the ground-truth P_x and the estimated $P_{\hat{x}}$ location. Then, the localization error was averaged between the three sources to provide a single value for the error of localization. The number of trials in which the localization error with relevance selection was equal or lower than with coverage or with standard-based layouts was proposed to measure at what extent of trials the relevance selection produced equal or better accuracy compared to the other criteria. This is to referred as the Accuracy Comparison index. The time course of the sources reconstructed with wMNE, sLORETA, and MSP with relevance-based channel selection $Rel-6E$, $Rel-9E$ were extracted and compared to the time courses reconstructed with the denser electrode layout $HD-161E$. To compare

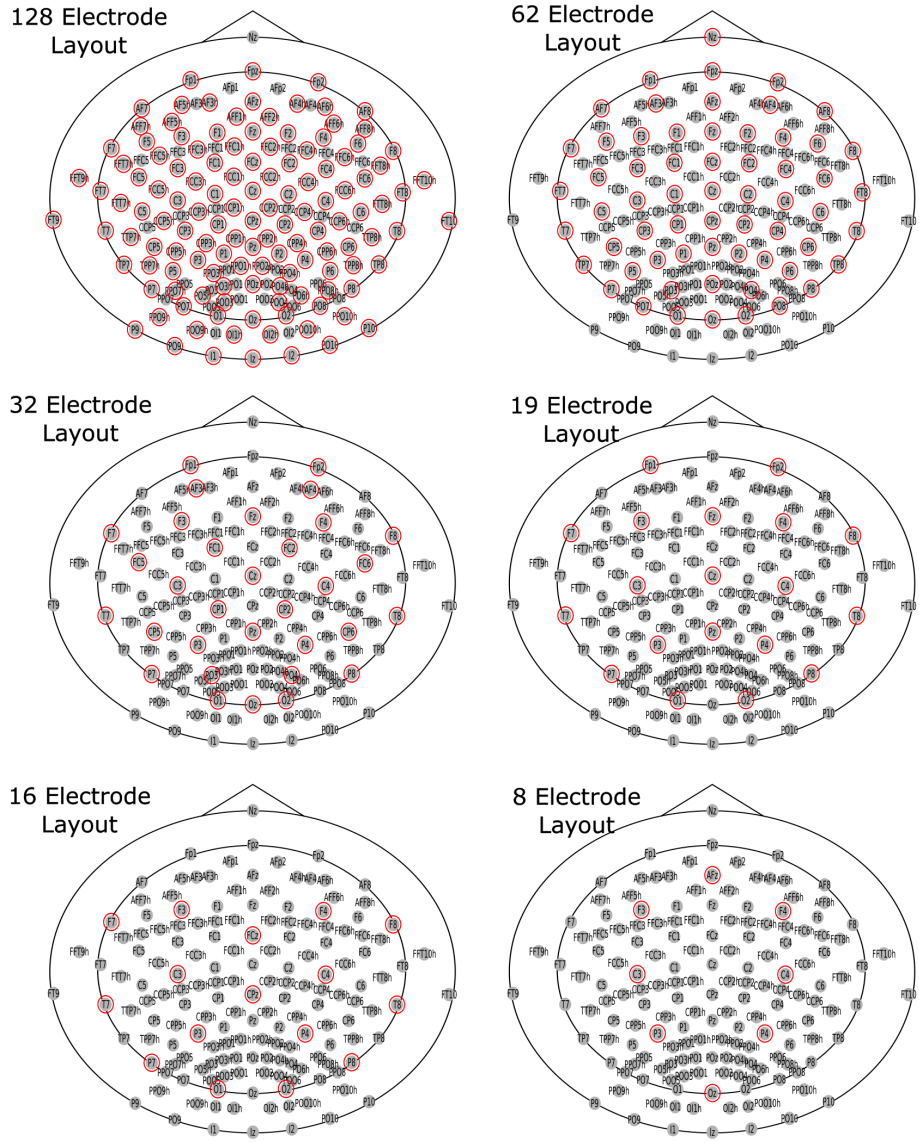

Figure 5.8: Standard-based (top row) and coverage-based (middle and bottom rows) electrode Layouts [246]. The selected electrodes for each layout are marked with a red circle over the 161 scalp electrodes available in the New York Head[216].

them, the Pearson correlation coefficient was used, computed using equation 3.25.

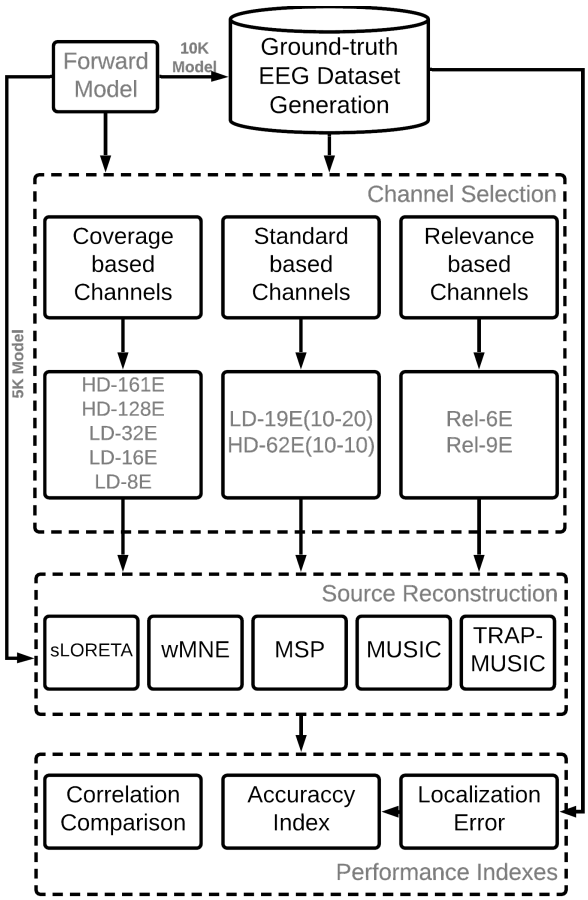

Figure 5.9: Summary of the evaluation procedure of multiple electrode layouts and channel selection [246].

5.8 Results - Relevance-based Channel Selection

The mean and standard deviation of the localization error for the 150 trials is shown in figure 5.10. The electrode layouts on the x-axis were organized according to the number of electrodes they consider, except the $Rel-6E$ and $Rel-9E$ that were located first on the left side. The best accuracy was obtained when using the highest number of electrodes with the $HD-161E$ layout when considering all the scalp electrodes of the forward model. In contrast, the worst accuracy was obtained when using the $LD-8E$ layout. A trend can be seen in the localization error, as

the number of electrodes is being reduced, the localization accuracy decreases. However, the trend is abruptly interrupted when considering the results of the channels selected with the relevance criteria.

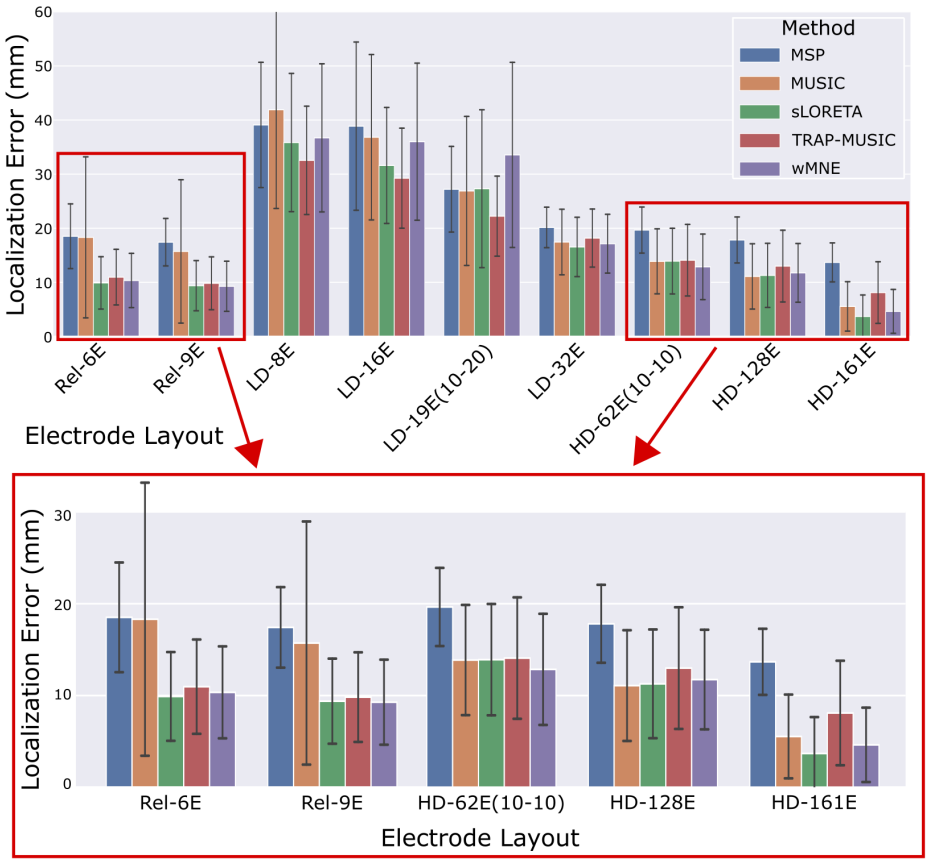

Figure 5.10: Localization error of the multiple electrode layouts combined with each of the source reconstruction algorithms. (Adapted from [246]).

The localization error of the relevance selection $Rel-6E$ and $Rel-9E$ are comparable to the $HD-128E$ test. Particularly the methods wMNE, sLORETA, and TRAP-MUSIC, for the relevance cases offer a slightly better localization error mean with similar standard deviation as with the $HD-128E$. Here, it is remarkable that for the same methods, $Rel-9E$ kept the mean localization error below 10mm, a result that was achieved only with all the electrodes $HD-161$ case. The case of the

MSP method presented a similar behavior with $Rel - 9E$ compared to $HD - 128E$, and the MSP accuracy with $Rel - 9E$ was slightly lower than with $HD - 128E$. In contrast, the MUSIC method was highly affected by the reduction in the number of electrodes. It is a generalized effect for this particular algorithm, regardless of whether the channels were selected with relevance or not; as the number of electrodes is reduced the standard deviation increases.

Table 5.4. offers the accuracy comparison indexes when considering the percentage of trials that obtained equal or better localization error with relevance criteria $Rel - 6E$ and $Rel - 9E$, than the other layouts based on standard and coverage criteria. It is remarkable that for methods sLOR, wMNE, and TRAP-MUSIC, $Rel - 9E$ obtained an index between 61% and 68% when compared to $HD - 128E$ and between 67% and 73% when compared to $HD - 62E(10 - 10)$, especially considering that $Rel - 9E$ has 119 and 51 fewer channels than $HD - 128E$, and $HD - 62E$ respectively. In the case of $Rel - 6E$ the results are also noticeable, it uses 122 fewer channels than $HD - 128E$ and 55 less than $HD - 62E(10 - 10)$, and it obtained indexes between 59% and 64% when compared to $HD - 128E$ and between 63% and 71% when compared to $HD - 62E(10 - 10)$.

To compare the reconstructed time courses of the estimated source activity, the Pearson correlation coefficient was computed between the reconstructions using $Rel - 6E$ and $Rel - 9E$ and the denser electrode layouts of $HD - 161E$ and $HD - 128E$. The comparison was done for the reconstructions with the methods that obtained the lowest localization error, sLORETA, and wMNE. The results of the comparison between the aforementioned sets of channels are presented in figure 5.11. It can be seen that the correlation in all the cases was more than 98% and particularly for the comparisons with $Rel - 9E$, the correlation values were higher than 99%.

To offer an overview of the relevance-based selected channels the number of times that the channels were repeatedly chosen by the two relevance criteria are presented in figure 5.12. For relevance analysis, the 231 channel positions of the forward model were considered, including 70 locations on the face and neck, however, none of the selected channels were in those areas. It is important to note that the selected channels across trials were distributed between both hemispheres, in which a particular position in the right hemisphere and its equivalent at the

Method	Channel Layout	Rel 6E	Rel 9E	Method	Channel Layout	Rel 6E	Rel 9E
sLOR	LD-8E	0,96	0,97	MUSIC	LD-8E	0,82	0,88
	LD-16E	0,95	0,95		LD-16E	0,83	0,89
	LD-19E	0,91	0,92		LD-19E	0,75	0,79
	LD-32E	0,77	0,85		LD-32E	0,62	0,68
	HD-62E	0,71	0,73		HD-62E	0,47	0,55
	HD-128E	0,59	0,61		HD-128E	0,42	0,47
	HD-161E	0,11	0,11		HD-161E	0,13	0,15
WMN	LD-8E	0,97	0,97	TRAP-MUSIC	LD-8E	0,96	0,97
	LD-16E	0,95	0,97		LD-16E	0,96	0,95
	LD-19E	0,93	0,94		LD-19E	0,89	0,87
	LD-32E	0,79	0,84		LD-32E	0,81	0,88
	HD-62E	0,63	0,67		HD-62E	0,65	0,69
	HD-128E	0,62	0,68		HD-128E	0,64	0,63
	HD-161E	0,19	0,21		HD-161E	0,32	0,41
MSP	LD-8E	0,91	0,97				
	LD-16E	0,90	0,94				
	LD-19E	0,75	0,80				
	LD-32E	0,67	0,70				
	HD-62E	0,57	0,64				
	HD-128E	0,49	0,53				
	HD-161E	0,21	0,22				

Table 5.4: Accuracy Comparison Index, which presents the percentage of trials that obtained equal or better localization error when comparing the relevance criteria $Rel - 6E$ and $Rel - 9E$ with other electrode configurations [246].

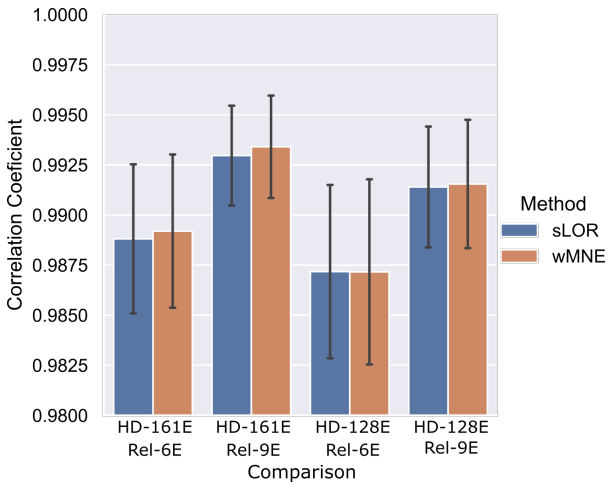

Figure 5.11: Source time courses correlation coefficient between high-density layouts and relevance-based channel selection [246].

left hemisphere obtained similar repetition values. The small differences can be explained by the location of the simulated sources which were selected randomly from a pre-set of sources for each brain area, equally distributed between both hemispheres.

5.9 Discussion

The PBM approach works by alleviating the number of unknowns of the inverse problem, and constrains the solution to a reduced area of the brain. Applying the proposed methodology by extracting the information in frequency, and selecting relevant electrodes, the activity in the PBM can be unmixed from other non target regions, and accurately reconstructed. The reconstruction performance was measured in terms of localization error, and based on the accuracy of the results obtained herein, using PBM in the proposed methodology can reconstruct the source activity using ldEEG number of channels, being remarkable that only with 8 and 16 channels a precision below 10 mm was obtained with sLORETA and 20 mm with MSP, see figure 5.6.

The use of PBM constrains the source reconstruction to find a solution in a pre-defined space, which will make it prone to error when the source of interest originates from other areas. For this reason, the application of PBM should be

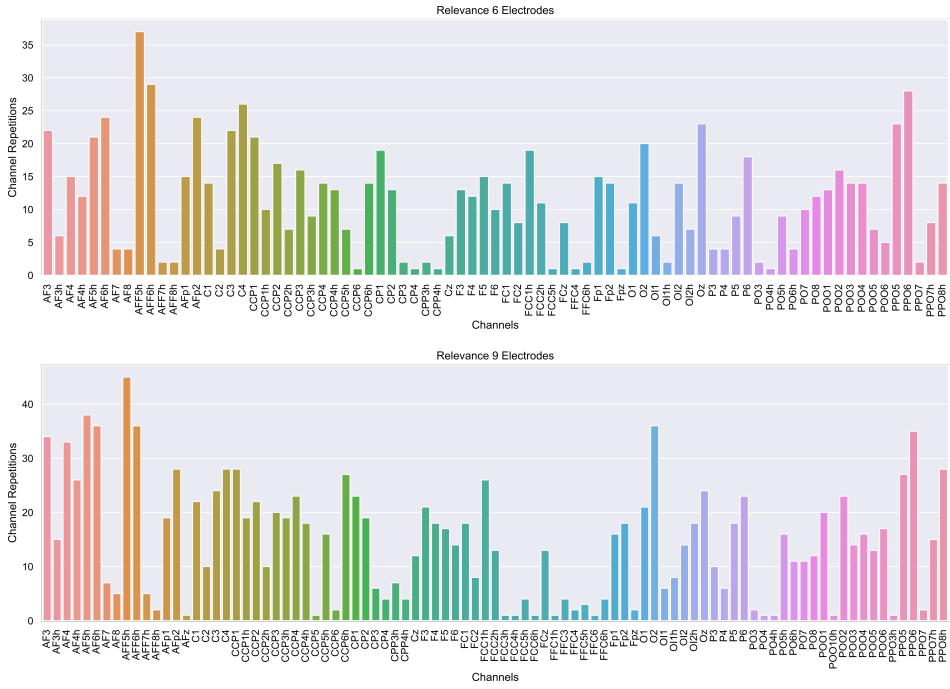

Figure 5.12: Channel repetition for relevance-based selection [246].

restricted to applications in which the area of interest that will be activated is well known, e.g, in some visual evoked potentials (VEP) experiments, in which the interest is to know how the visual cortex areas respond to certain stimuli [5, 255], or in motor imaginary tasks where it is well known that the motor cortex is activated [256, 257].

Regarding the comparisons with the proposed methodology with the local electrodes criteria, the localization error was higher with the local electrodes. In [127] an evaluation using local electrodes for source reconstruction was performed, showing that the local electrodes contribute to false localization of sources. However, there the full model was considered. Here, the local electrodes showed an average performance, as shown in figure 5.6 and table 5.2, the mean error was kept below 22 mm regardless of the use of filters to isolate the sources. This method could be applied in settings in which a high quantity of electrodes is not available, however, a careful analysis of the source maps should be done to evaluate the apparition of ghost sources.

The methodology proposed here was evaluated using linear filtering for frequency constraining with the intention to focus on the PBM to source activity reconstruction. However, it has been demonstrated in chapter 4 and previous studies [177, 178, 193] that the use of advanced techniques for frequency decomposition like MEMD can offer a solution for unmixing the source activity and improving the source reconstruction solutions.

The method Q-α was used to select relevant channels, where it was demonstrated that a subset of selected channels, with a sparser number far from hdEEG, can reconstruct a set of sources in the brain with comparable quality as a high-density number of channels, as shown in figures 3.22 and 5.10. The reconstruction quality obtained with relevance-based channel selection can be comparable to using a set of 128 channels, and better than 62 channels in terms of the localization error as shown in figure 5.10. Moreover, in terms of the time-courses similarity, the high level of correlation obtained between the reconstruction with the relevant channels and the densest coverage-based as presented in figure 5.11. This supports the hypothesis that ldEEG using relevance-based channel selection can be comparable with high-density to reconstruct a particular brain activity.

The location of the selected channels was found on scalp, with any of the selected electrodes positioned on the neck or face. This is in line with the results presented in [158], where the face and neck electrodes were not found significant to contribute to the localization accuracy.

In this chapter, a formal definition of the PBM was introduced. Multiple evaluations showed the capability to reconstruct the source activity of a brain-ROI using a reduced model of the regions. In addition the combination with relevance-based channel selection allowed this study to find subsets of channels in ldEEG and accurately localize the multiple sources in the two evaluations performed.

The proposed relevance-based channel selection for source reconstruction remains to be verified over real signals. Further studies on multiple recording paradigms and analysis of different brain activity responses should be done in order to validate the proposed selection over a more realistic scenario. However, the presented framework for source and EEG simulation in this study simulates signals with similarities to ERPs, as can be seen in figure 6.2. In addition, considering

that the level of noise added to the signals had equal power than the signal, the trial data simulated here can be regarded as having a similar SNR to typical ERP signals.

Chapter 6

Low-density EEG Source Reconstruction based on Optimal Channel Selection

This chapter introduces an automated methodology for minimizing the number of channels and to identify ldEEG subsets to perform source reconstruction while maintaining a high reconstruction accuracy, equal to or better than hdEEG electrode counts. The number of channels and the accuracy are optimized using a multi-objective approach. This optimization is performed by the NSGA-II algorithm, by identifying ldEEG channel subsets that contribute to obtain a hdEEG accuracy level. Multiple validation test over synthetic and real signals are performed using the synthetic EEG dataset and the localize-MI dataset presented in sections 3.7.1 and 3.7.3, respectively.

This chapter is based on article [214] and mainly addresses the 3rd research question.

6.1 Introduction

Estimation of the brain source activity using EEG depends on several factors to be accurately performed, with the number and location of electrodes at scalp being one of the most important. It is generally accepted that increasing the number of electrodes yields more precise localization [22, 23, 25]. The number of electrodes

has evolved towards high-density numbers with the introduction of the standard 10-10 positioning system [81, 258] introducing up to 70 locations, and with the introduction of the 10-5 system [83] the number was elevated to 345 locations for scalp coverage. While the 10-10 system was accepted as a standard by the ACNS and the IFCN [82, 259], the 10-5 system was not accepted by either of them [260]. In section 2.4.4 the evolution and influence of the number of electrodes for source reconstruction is presented in more detail.

In [261] an extensive investigation of the validity of the 10-20, 10-10 and 10-5 systems as relative head-surface-based positioning systems was performed. There it was argued that even though the 10-20 system has not been conceived to support localization of brain sources, its high-density extensions into the 10-10 and 10-5 systems have mainly provided increased electrode density proven to be effective in brain source localization [169]. The high-density extensions of the 10-20 system logically inherit its electrode positioning principle, which was not conceived to improve the accuracy of brain source localization algorithms. Although it is sufficiently proven that these extensions are effective in increasing the accuracy of brain source localization, it remains to be seen to what extent these high-density systems require all the electrode positions for attaining that. Even though the use of hdEEG systems has resulted in improved spatial resolution in source localization, practical use has come at a cost [260, 261]. Increasing electrode number decreases localization error but this improvement plateaus at some point[24]. This has been revealed by examining the relationship between localization error and the number of electrodes for the particular case of partial epilepsy in pediatric patients [24].

Here, an automated methodology for channel selection based on the contribution of the electrode locations to accuracy is presented. The methodology uses information from electrode locations on multiple systems and electrode configurations, e.g. the systems inherent to the 10-5, 10-10, 10-20 and/or geodesics systems, to select the optimal number of electrodes and their locations to solve the problem of EEG source localization for single and multiple sources. This optimization is performed using multi-objective optimization, to minimize the number of electrodes while minimizing the localization error obtained. The optimization is based on the NSGA-II algorithm [211]. The algorithm,

combined with EEG source reconstruction algorithms, searches for combinations of electrodes for solving the EEG inverse problem that minimizes the localization error while using the lowest number of channels possible. Considering C as the number of channels, exploring all the combinations of electrodes in order to find the optimal solution means solving the inverse problem 2^C times for a single source case, and $S(2^C)$ for S multiple sources. These numbers will exponentially grow when increasing the number of channels, significantly increasing the computational efforts, e.g. in the case of 128 electrodes, it is required to solve the inverse problem $3.4x10^{38}$ times to evaluate all the possible electrode combinations. In contrast, the NSGA-II aims to reduce the computational cost on average to $O*(P^2)$, where O is the number of objectives, in this case $s+1$, and P the population size [211].NSGA algorithms have been successfully applied in multiple fields for optimization and feature selection, like facial expression recognition [262] and telecommunications [263]. This algorithm has been applied to EEG channel selection for classification of motor imagery [264]. Moreover, the algorithm has proven to be effective in identifying low-density EEG subsets that maximize classification accuracy while reducing the number of EEG channels required for epileptic seizure classification [191] and subject identification [238]. Channel selection based on other optimization algorithms have been previously explored with genetic algorithms for classification of alcoholics in [265], and for motor imagery in [266, 267], and using harmony search algorithm for alcoholism screening and detection [268].

In this chapter, the methodology for channel selection based on contribution to source reconstruction accuracy is evaluated in a step-by-step manner, by first evaluating a simulation-based source reconstruction problem for one single source and for multiple sources, using the synthetic dataset presented in section 3.7.1. In a second phase, it is examined how effective the methodology is in accurately detecting the stimulation site from intra-cerebral stereotactically implanted electrodes, based on the Localize-MI dataset, presented in detail in section 3.7.3. Three widely used source reconstruction algorithms, wMNE, sLORETA, and MSP, were combined with the NSGA-II algorithm, to evaluate the effect of optimally reducing the number of electrodes.

6.2 Automated Methodology for Channel Selection Based on Genetic Algorithm Multi-objective Optimization

The proposed methodology is presented in figure 6.1. It combines a source reconstruction algorithm and NSGA-II to find electrode subsets with the minimum number of channels that maximize the localization accuracy, attempting to retain the highest possible source localization accuracy. The general structure of the automated methodology can be summarized by a loop of four blocks: NSGA-II, Weighting, Source Reconstruction, and Performance indexes, where the outputs of NSGA-II are a set of best channel combinations and a set of all evaluated candidates.

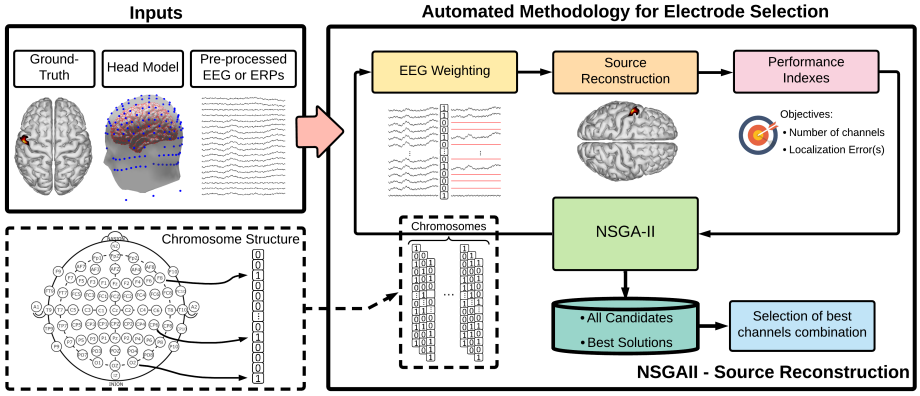

Figure 6.1: Flowchart of the proposed automated methodology for channel selection based on contribution to source reconstruction accuracy [214].

The central block of NSGA-II consists of several stages: Population initialization, Fitness calculation, Crossover, Mutation, Survivor selection, and Termination criteria to return the best solutions. The population consists of a set of chromosomes, which are possible solutions to the problem, and each chromosome can have as many genes as variables in the problem. In this case, each gene represents an EEG channel, and the chromosome contains as many genes as the number of EEG channels in the registered EEG $\boldsymbol{y}$. A representation of the chromosome structure representing the electrode combination is presented

at the bottom left of figure 6.1. The NSGA-II initializes with a population of P chromosomes with random binary values. Then, in the weighting block, the gene values are used to weight the EEG by a dot multiplication between the EEG and the chromosome to compute the weighted EEG $\boldsymbol{y_w} = \boldsymbol{y} \cdot chromosome$. As a result of this mathematical operation, the channels with a gene value of one keep their value, while information of the channels with a gene value of zero is discarded.

The number of objectives O is defined as $O = \boldsymbol{s} + 1$. Where, the algorithm considers a fixed objective to minimize **the number of EEG channels** used to localize single or multiple sources. The subsequent objectives are to minimize **the localization error** of the number of sources $\boldsymbol{s}$ desired to localize, with a separate objective per each source. NSGA uses a non-dominated sorting ranking selection method to emphasize good candidates and a niche method to maintain stable sub-populations of good points (Pareto-front).

The weighted EEG $\boldsymbol{y_w}$ is used in the source reconstruction block for calculating the source activity and estimating the location of each source. In each weighted EEG $\boldsymbol{y_w}$ the non-selected channels are converted to a temporal data series with zero value, therefore, the inverse solution is calculated using all the electrodes available in the head conduction model, but the information contained in the non-used electrodes is discarded during source estimation. The use of all electrodes is preferred to avoid increasing the ill-posedness of the inverse problem when using a subset of the volume conduction matrix and to avoid using computational resources for re-calculating the volume conduction for each candidate combination.

In the performance indexes block, the number of channels extracted from each chromosome and the localization errors per each source are computed by comparing the estimated position with a ground-truth. The performance indexes return to the NSGA-II block that applies the non-dominated sorting, the half of the population with better performance is used to create the next generations using crossover and mutation procedures. The actual generation finishes when the new population is created and the process is repeated with the next generation until the termination criteria is reached. A number of maximum generations was used as criteria to stop the algorithm. Finally, from all sets of chromosomes, the best combination per each number of channels is extracted to create a pseudo-Pareto front. In the case of the multiple sources, the pseudo-Pareto front is generated

from the mean of the localization error between all the sources

6.3 Experimental Framework - Synthetic Dataset

The synthetic EEG dataset is presented in section 3.7.1. It consists of 150 trials of multiple source activity for 231 electrodes, from which 161 are located on the scalp (based on the 10-10 and 10-5 systems), and the others are distributed between LPA, RPA, neck and face. Only the first three sources of the dataset have been considered for the evaluation tests. An example of the time course of the simulated sources and their location is shown in figure 6.2

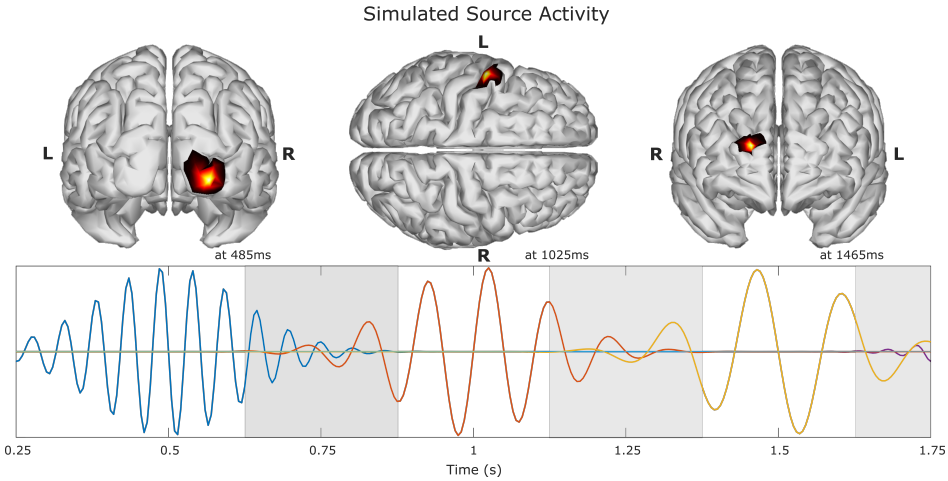

Figure 6.2: Example of simulated source activity [214]. Source s_1 time course is depicted in blue color, source s_2 in orange, source s_3 in yellow, and the remaining activity from s_4 in purple. The locations of the first three sources are depicted on top, where the time was chosen where the maximum amplitude value for each source took place. The light gray areas depict the time sections where there are temporal mixing between sources.

Two tests over the synthetic dataset are proposed, where the objective is to investigate to what extent the quality of the source reconstruction of hdEEG, measured in terms of source location error, can be maintained while using a set of reduced number of channels that were selected by the proposed methodology. The first test was based on source reconstruction for one source, referred to as a single-source test. This test was performed by setting two minimizing objectives for the optimization: the localization error of the single source and the number of

channels. The first source s_1 of the synthetic dataset was considered for testing, the epoch was set between 250 to 750 ms, including a section of overlapping with the next source s_2.

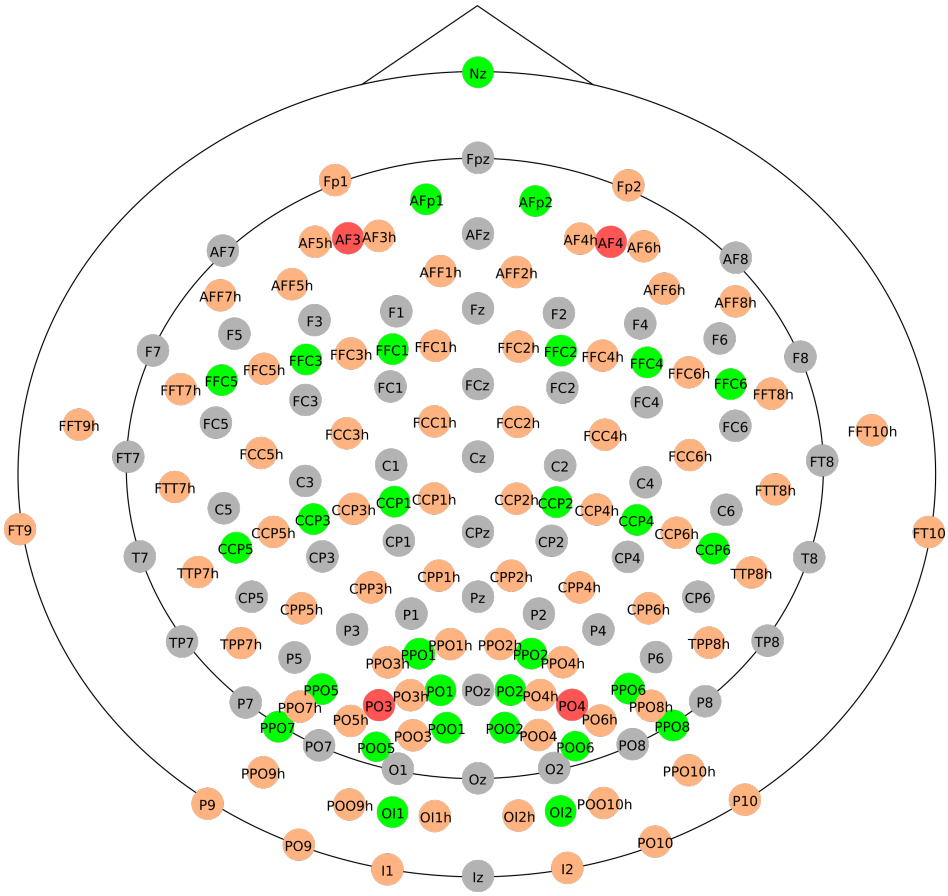

Figure 6.3: Location and names of the 161 scalp electrodes included in the New York head model[216]. Red and gray circles represent the subset of 60 electrodes, and orange and gray circles represent the subset of 128 [214].

A second test was performed considering the first three sources of the synthetic dataset s_1, s_2, and s_3. This is referred to as the multiple-source test. In this test, the epoch definition was set between 250 to 1750 ms, and four minimization objectives were set for the optimization algorithm: the individual localization error of each source and the number of channels. To evaluate the approach over a different

number of electrodes, the multiple-source test was performed over the full set of 231 electrodes. This is referred to as multiple-source test 231e (161 electrodes at scalp, of those 73 are located in positions of the standard 10-10 system and 88 located in positions of the standard 10-5 system, the other electrodes are placed in the neck and face areas (figure 3.12)). A second number of electrodes was considered by constraining the search space for the optimization algorithm to 128 scalp electrodes, of which 64 channels were selected from the standard 10-10 and 64 channels from the standard 10-5. This is referred to as multiple-source test 128e. Finally a third number of electrodes was considered by constraining the search space of the NSGA-II to 60 electrodes, all of them located in standard 10-10 positions. This test is referred to as multiple-source test 60e. Figure 6.3 shows the 161 positions of the scalp electrodes of the New York head model, and the subsets configuration for 128 and 60 electrodes.

6.4 Experimental Framework - Localize-MI Dataset

To test the methodology over real EEG signals the Localize-MI dataset presented in section 3.7.3 was used. It consist of recordings from 256 scalp locations using a geodesic electrode system of seven participants, while they were stimulated with a single-pulse biphasic current by implanted electrodes. This was used as the stimulation position is known and the dataset serves as ground-truth for evaluating inverse solutions. The dataset includes 61 sessions of stimulation, and in each session the stimulation took place in the location. Therefore, the epochs for each session were averaged and cropped 20 ms around the stimulation artifact. For this case, the dataset was processed as a single source case, by setting two minimizing objectives for the optimization algorithm: the localization error of the artifact source and the number of channels. This test is referred to as the Localize-MI test.

6.5 Test Structure

The procedure during all tests started by defining the electrodes to be considered. Only in the multiple-source tests did the electrode number vary according to the test (when constraining to 128 or 60 electrode positions); in the single-source test all the electrodes were considered. In the case of the Localize-MI test, the

electrodes that were marked as bad were removed when calculating the forward model, no attempt to clean or interpolate channels was carried out. The number of electrodes to use defines the length of the chromosome for the optimization. After setting the number of electrodes, the number of objectives was defined, and the EEG of each trial (in the case of the synthetic data) or the ERP of the session (in the case of the Localize-MI dataset) were transferred to the algorithm. In the next step, the population size and the maximum number of generations were set. Their values were determined experimentally and set as 100 and 400 respectively. Finally, the algorithm for source reconstruction was defined, and the algorithm could start processing data by combining the NSGA-II with sLORETA, wMNE and MSP in separated runs respectively.

Each trial or ERP was processed by the algorithm at least three times, each time with a different source reconstruction algorithm. During a run, the algorithm evaluated 40000 combinations of electrodes while trying to minimize the objectives. When the run finalized, a output file with the combinations and performance indexes of all generations and chromosomes was generated. From this, the performance of the best combination per each number of channels can be extracted to create the pseudo-Pareto front. Finally an accuracy index was computed for comparing the reconstructions from the optimized set of channels versus all the channels available. The accuracy index represents the percentage of trials or ERPs that obtained equal or lower localization error with a given number of electrodes when comparing the accuracy when using all the electrodes for the same trial or ERP.

6.6 Results

6.6.1 Single-source test - Synthetic EEG Dataset

The pseudo-Pareto front from the single-source test and localization error with all the electrodes are presented in figure 6.4. The accuracy obtained with the optimized combinations of channels presents a stable value for the localization error when using combinations with five or more channels, independently of the source reconstruction method applied. An inflection point can be seen in the pseudo-Pareto front when reducing from 5 to 4 channels. It is also evident when looking at the values presented in table 6.1, where the results from the

optimization with 2 to 16 channels and the results with all the electrodes are summarized. The accuracy index of the optimized combinations of channels was extracted by quantifying the percentage of trials with a given number of channels that obtained equal or lower localization error than when using all the electrodes for the same trial. The accuracy index for the single source test exhibits a relatively stable behavior from 16 to 5 channels, but it has a decrease of more than two perceptual points when reducing from 5 to 4 channels. Its value continues decreasing substantially while reducing the channels, coinciding with the increasing of the localization error and the standard deviation.

When analyzing the results presented in figure 6.4 and table 6.1 in a more detailed level, it can be seen that with a combination of 4 or more channels, more than 92% of accuracy index was obtained for sLORETA and wMNE, indicating that at least 138 over 150 trials obtained equal or lower accuracy than when using all the electrodes. In the case of MSP it presents a lower accuracy index than the other methods, with a stable value around 88%, and when considering combinations with 4 or more channels at least 127 of 150 trials were equal or better than the reconstructions with all electrodes.

6.6.2 Multiple-source test

The pseudo-Pareto Front for the multiple-source test with the different electrode configurations are shown in figure 6.5. The multiple test had four optimization objectives. To facilitate the visualization of the results, the pseudo-Pareto front was obtained from the mean localization error across the 150 trials, where the localization error is the average of the individual localization error for each one of the three sources. Table 6.2 presents the localization error, standard deviation and accuracy index for the multiple-source tests for a selected number of channels and with all electrodes.

The results for all electrodes in the three tests show a tendency of increasing the localization error when using a lower number of electrodes (figure 6.5 right column). When localizing the sources, the mean between 60 and 128 channels presents a similar value in each method, with the solution with 60 channels being less accurate. In contrast, the difference is notorious when increasing from 128 to 231 channels, and it is more evident for sLORETA and wMNE methods. In the pseudo-Pareto's fronts of the proposed methodology, the same tendency as with

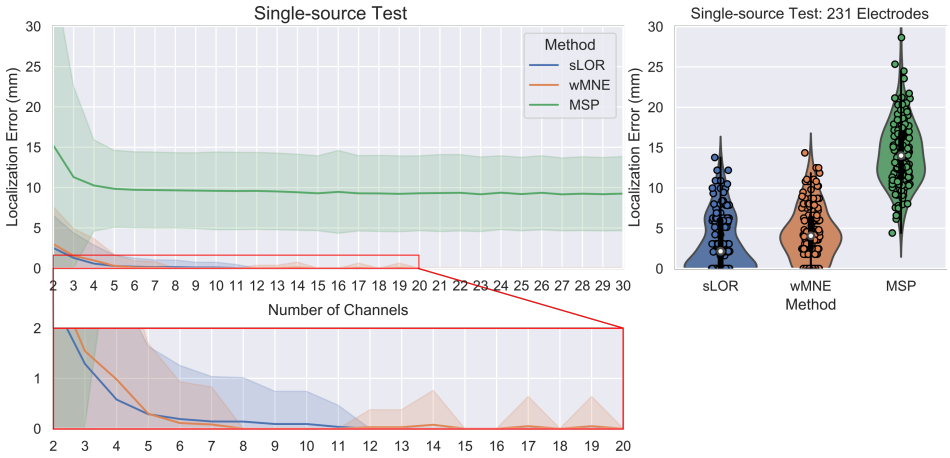

Figure 6.4: Results for the single-source test [214]. The pseudo-Pareto fronts relating the number of channels and the localization error by each source reconstruction method are presented at left. The lines represent the mean localization error across the 150 trials and their respective colored bands represent their standard deviation. The mean localization errors across the trials and the standard deviation obtained by using all the electrodes available (231) by each method are presented at right.

all electrodes can be observed. In them, the localization error was more accurate when using the full set of 231 channels, and when restricting the search space to 128 and 60 channels, the localization error increased. However, when comparing the solutions for the test with 128 and 231 channels, there is not a considerable difference between the solutions, but the obtained localization error values were lower for sLORETA and wMNE in the multiple-source test with 231 electrodes.

When analyzing the values of table 6.2, it can be seen that for the multiple-source tests of 60e and 128e, the proposed methodology obtained a lower mean localization error when considering optimized combinations with 4 or more electrodes than with the 60e and 128e subsets. In the case of the multiple-source test 231e, the proposed methodology obtained lower errors than with all the 231 channels, when using optimized combinations of eight or more channels. Regarding the accuracy index, in the multiple-source test 231e, for the optimized combinations with 16 electrodes, in 145 of 150 trials the proposed methodology obtained equal or lower accuracy than the full set of electrodes. The accuracy

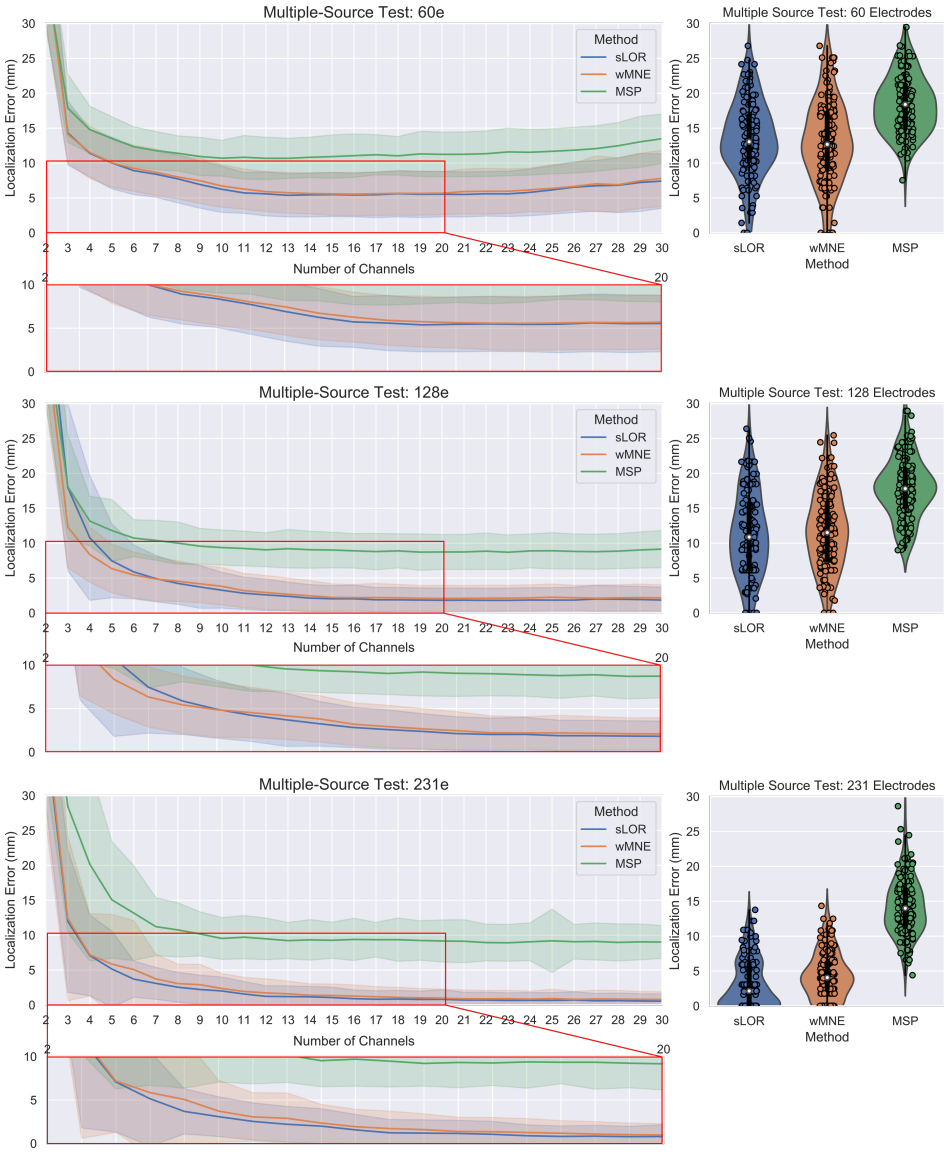

Figure 6.5: The pseudo-Pareto fronts for the multiple-source test with the different constrained number of channels are shown at left [214]. They relate to the number of channels vs the average between the three sources localization error. The lines represent the mean of the localization error* of the three sources across the 150 trials, and the colored bands the standard deviation. The mean localization error* across the trials and the standard deviation obtained by using the subsets of 60 and 128 electrodes, and the full set of 231 electrodes for the three sources are presented at right. *The mean localization error is computed using the average error between the three sources and then the average of this value across the 150 trials.

Method	Chs	Mean Loc. Error	SD	Acc. Index	Method	Chs	Mean Loc. Error	SD	Acc. Index	Method	Chs	Mean Loc. Error	SD	Acc. Index
sLOR	2	2.5	4.0	66.7	wMNE	2	3.0	4.6	76.7	MSP	2	15.3	21.3	71.3
	3	1.3	3.1	82.7		3	1.5	3.3	89.3		3	11.3	11.2	80.0
	4	0.6	2.3	92.0		4	1.0	2.7	93.3		4	10.3	5.6	84.7
	5	0.3	1.3	95.3		5	0.3	1.4	96.0		5	9.8	4.8	88.0
	6	0.2	1.1	96.7		6	0.1	0.8	98.0		6	9.7	4.7	88.0
	7	0.1	0.9	97.3		7	0.1	0.7	98.7		7	9.7	4.7	87.3
	8	0.1	0.9	97.3		8	0.0	0.0	100.0		8	9.7	4.7	88.7
	9	0.1	0.6	98.0		9	0.0	0.0	100.0		9	9.6	4.7	88.0
	10	0.1	0.6	98.0		10	0.0	0.0	100.0		10	9.6	4.8	88.0
	11	0.0	0.4	99.3		11	0.0	0.0	100.0		11	9.6	4.8	88.7
	12	0.0	0.0	100.0		12	0.0	0.3	99.3		12	9.6	4.7	88.7
	13	0.0	0.0	100.0		13	0.0	0.3	99.3		13	9.5	4.7	88.7
	14	0.0	0.0	100.0		14	0.1	0.7	99.3		14	9.4	4.7	89.3
	15	0.0	0.0	100.0		15	0.0	0.0	100.0		15	9.3	4.6	89.3
	16	0.0	0.0	100.0		16	0.0	0.0	100.0		16	9.5	5.1	88.7
	All	0.0	0.0	-		All	1.6	3.8	-		All	11.8	6.2	-

Table 6.1: Summary of the localization error obtained with the optimized combinations of channels, from 2 to 16, and with the full set of 231 electrodes [214]. The accuracy index represents the percentage of trials with the given number of channels that obtained equal or lower localization error than when using all the electrodes for the same trial.

index reduces as the number of channels decreases. At the point of 8 electrodes the accuracy index presents a value of 58% (87 of 150 trials), however, despite the relative low accuracy index, the mean across the trials was lower than with the full set.

Examples of the position of the true and estimated source locations and the selected channels are show in figure 6.6. This shows the optimized combinations with 4 and 8 electrodes for one trial of the dataset, and the resulting combinations were obtained from the multiple-source test 231e results for each source reconstruction method. In the combinations of 4 channels, it can be observed that the channels selected are located close to the true source location, where the mean localization errors were 5.3, 4.7, and 14, 5 mm, for sLORETA, wMNE, and MSP, respectively. In addition, when observing the combination of 8 channels, the selected electrodes were located not only close to the source location, but also in intermediate positions between the sources that were relatively close. In contrast, for the sources that were more separated, there was not

Method	Chs	Mean Loc. Error	SD	Index (%)	Method	Chs	Mean Loc. Error	SD	Index (%)	Method	Chs	Mean Loc. Error	SD	Index (%)
sLOR Test 60e	4	11.40	3.38	65.33	wMNE Test 60e	4	11.53	3.75	58.00	MSP Test 60e	4	14.79	3.36	74.00
	6	8.91	3.43	84.67		6	9.25	3.30	74.67		6	12.34	2.85	90.67
	8	7.73	3.42	91.33		8	8.01	3.15	84.67		8	11.40	2.49	97.33
	10	6.25	3.31	98.00		10	6.72	3.05	92.00		10	10.70	2.56	98.67
	12	5.59	3.16	98.67		12	5.90	2.85	96.00		12	10.68	3.02	98.00
	14	5.45	3.15	98.67		14	5.64	2.91	96.67		14	10.83	2.88	98.00
	16	5.44	3.12	99.33		16	5.55	3.08	98.67		16	11.07	3.10	97.33
	All	13.56	5.25	-		All	13.06	5.77	-		All	18.98	5.07	-
sLOR Test 128e	4	10.75	8.92	55.33	wMNE Test 128e	4	8.35	3.96	69.33	MSP Test 128e	4	13.16	3.54	74.67
	6	5.87	3.84	79.33		6	5.43	3.30	87.33		6	10.72	2.64	94.00
	8	4.23	3.00	87.33		8	4.54	2.90	90.00		8	10.00	3.03	96.67
	10	3.26	2.56	94.00		10	3.82	2.67	96.00		10	9.37	2.51	97.33
	12	2.58	2.25	95.33		12	2.92	2.43	97.33		12	9.04	2.43	96.67
	14	2.13	1.94	98.00		14	2.46	2.18	99.33		14	9.06	2.66	98.00
	16	2.03	1.96	99.33		16	2.20	1.87	100		16	8.90	2.47	98.00
	All	11.28	5.93	-		All	11.74	5.43	-		All	17.82	4.25	-
sLOR Test 231e	4	7.08	5.75	20.00	wMNE Test 231e	4	7.18	5.87	24.00	MSP Test 231e	4	20.15	13.81	29.33
	6	3.69	2.59	44.00		6	5.06	6.99	47.33		6	13.15	6.76	56.00
	8	2.54	2.13	58.00		8	3.06	2.78	60.67		8	10.74	3.87	74.00
	10	2.00	2.00	71.33		10	2.35	2.14	66.67		10	9.53	2.99	82.00
	12	1.23	1.53	88.00		12	1.72	2.00	76.00		12	9.47	2.97	81.33
	14	1.16	1.49	90.00		14	1.38	1.64	82.00		14	9.32	2.90	84.00
	16	0.90	1.26	96.67		16	1.26	1.60	82.67		16	9.39	3.02	86.00
	All	3.17	3.52	-		All	4.43	3.28	-		All	14.19	4.01	-

Table 6.2: Multiple-sources test results [214].

selected any channel between them. The mean localization errors for the eight channel combinations were 2.4, 4.2, and 4, 5 mm, for sLORETA, wMNE, and MSP, respectively. This suggests that the proposed methodology selected not only the channels that contained the most information from a single source, but also the channels that contained shared information from multiple sources.

Regarding the effects of the estimated waveform for each source, the standardized time courses of the sources estimated with 231 channels, and with the optimized sets of 4 and 8 channels for the one trial, are presented in figure 6.7. The sources' waveform are highly similar, independently of the number of channels, however, the reconstructions were noisier when using the optimized sets than with the full set of electrodes. For the same trial, the time courses of the pseudo-Pareto channel combinations were compared against the time course using the 231 channels. The relative error and Pearson correlation coefficient were

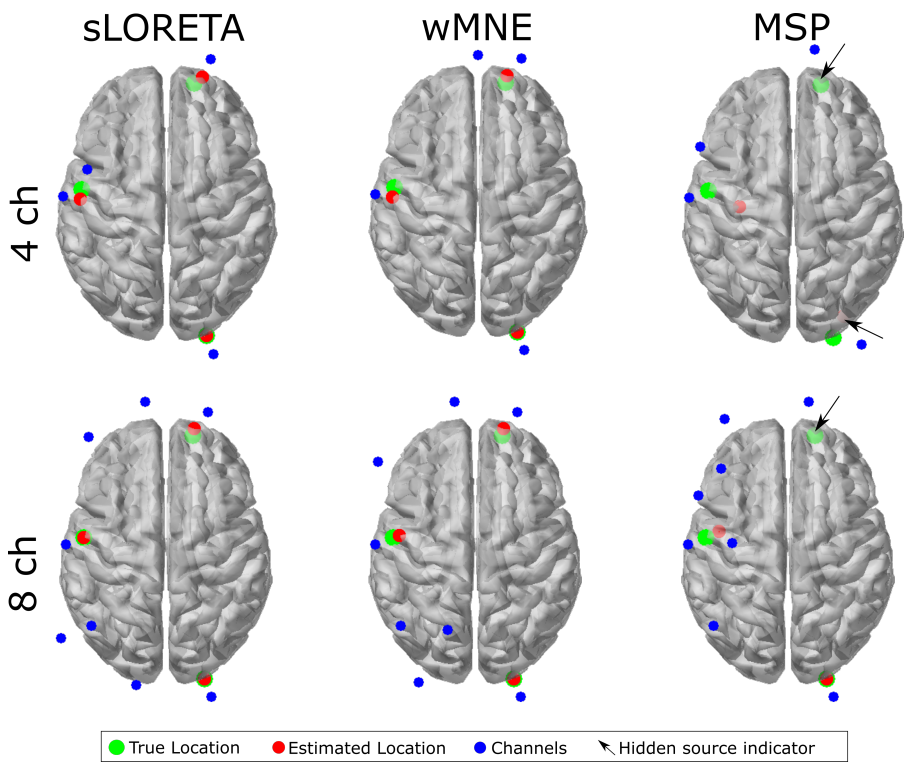

Figure 6.6: Optimized combinations and source localization for one trial during the multiple-source test 231e [214]. The mean localization errors with 4 channels were 5.3, 4.7, and 14, 5 mm, and with eight channels were 2.4, 4.2, and 4, 5 mm, for sLORETA, wMNE, and MSP, respectively. The hidden source indicator is intended to point where there is a source that can not be seen from the top view.

calculated for each source, each number of channels from 3 to 30, and for each reconstruction algorithm. It values are presented in figure 6.8. It was found that the source time courses estimated with the optimized combinations and the full set had more than a 97% correlation when considering 5 or more channels, obtaining a relative error lower than 0.25. When considering optimized combinations with more electrodes, the difference became smaller. The level of correlation with 16 channels or more is around 99%, independently of the source reconstruction method.

Table 6.3 presents the mean computation times required to obtain the reconstruction of the three sources over the 150 trials, and its standard deviation.

It can be seen that the computation time for sLORETA and wMNE methods is much lower than in MSP, in addition, their computational time are below 100 ms.

Method	Time (ms)	std (ms)
MSP	1841.95	155.94
sLOR	63.46	1.16
wMNE	50.11	1.07

Table 6.3: Mean and standard deviation of computation times for source reconstruction over the 150 trials

6.6.3 Localize-MI test

The ERPs for the 61 sessions were processed by the proposed methodology with each one of the source reconstruction algorithms. During processing, the channels marked as bad channels were not taken into account, neither in the optimization nor in the calculation of the values with "all channels". The number of channels varied according to the number of channels labeled as good. The average number of good channels among the 61 sessions was 210 channels (sd = 23). In the worst case 162/256 and in the best case, 246/256 channels were considered during the optimization process. Therefore, the number of channels used varied between sessions, and the term "all channels" refers here to all channels labeled as good channels. The pseudo-Pareto front resulting from processing each one of the ERPs and the values with all channels are presented in figure 6.9. A similar tendency than in the previous tests can be observed, in which the optimized combinations obtained a lower localization error than with all the electrodes. In contrast to previous tests, there is not an exponential trend when considering the fewest number of channels, instead, a more linear behavior can be observed, where the localization error and standard deviation increases as the number of channels decreases.

Table 6.4 presents the summary of the localization error, standard deviation and accuracy index for the Localize-MI test for the pseudo-Pareto combinations from 2 to 16 channels. The accuracy index shows that more than 70% of the ERPs were located with the same or higher accuracy than with all the electrodes when using 8 or more electrodes, and more than 60% when using 4. It is noticeable that

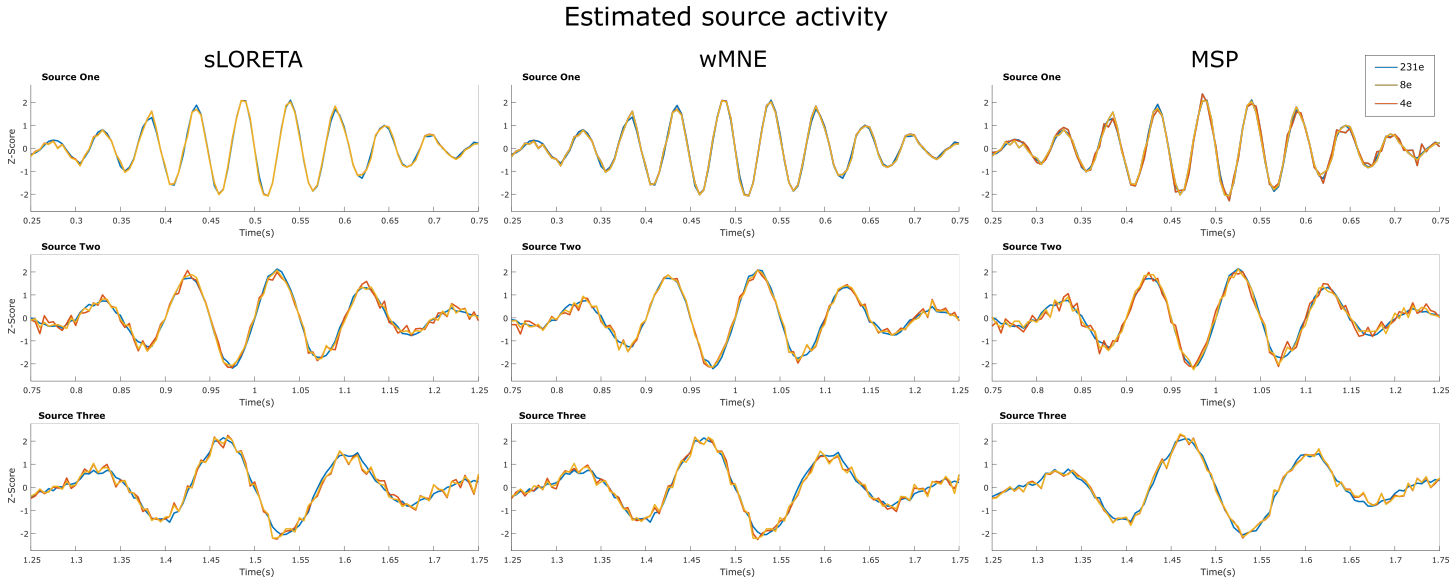

Figure 6.7: Example of the estimated time courses of the three sources with the full set of 231 channels, and with the optimized combinations with 4 and 8 channels for one trial [214].

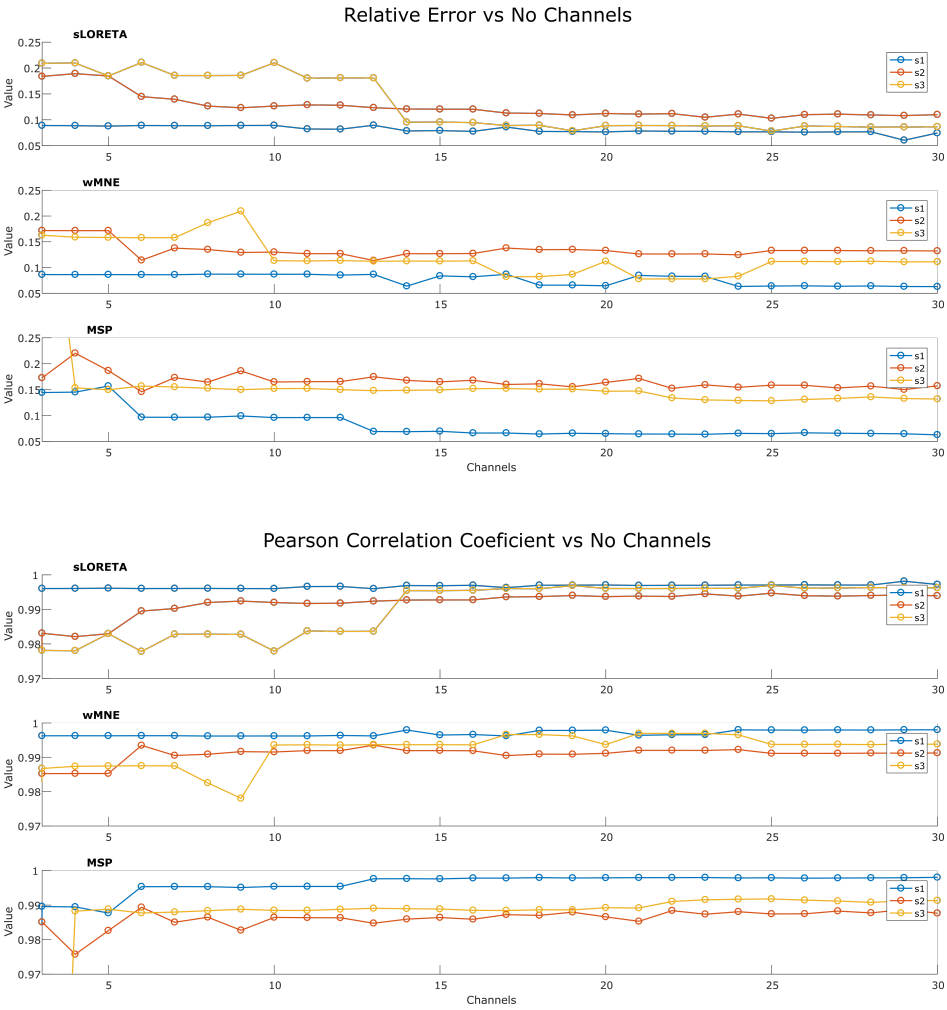

Figure 6.8: Relative error and Pearson correlation coefficient for each source, comparing the pseudo-Pareto combinations with the full set of 231 channels [214].

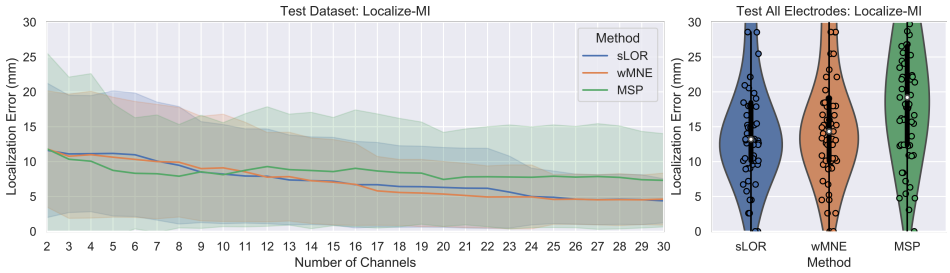

Figure 6.9: Results for the Localize-MI test. The pseudo-Pareto fronts relating to the number of channels and the localization error by each source reconstruction method are presented at left [214]. The lines represent the mean localization error across the 61 sessions and their respective colored bands represent their standard deviation. The mean localization errors across the trials and the standard deviation obtained by using all the electrodes available (all channels labeled as good) by each method are presented at right.

Method	Chs	Mean Loc. Error	SD	Index (%)	Method	Chs	Mean Loc. Error	SD	Index (%)	Method	Chs	Mean Loc. Error	SD	Index (%)
sLOR	2	11.62	9.57	63.93	wMNE	2	11.82	8.27	65.57	MSP	2	11.83	13.58	40.98
	3	11.10	8.34	63.93		3	10.77	8.83	65.57		3	10.34	11.64	50.82
	4	11.14	8.25	63.93		4	10.99	9.01	65.57		4	10.06	12.41	60.66
	5	11.17	8.90	63.93		5	10.63	8.53	67.21		5	8.74	9.45	70.49
	6	10.98	8.78	63.93		6	10.31	8.24	68.85		6	8.32	7.90	72.13
	7	10.07	8.40	68.85		7	10.00	8.13	68.85		7	8.26	8.35	78.69
	8	9.47	8.35	73.77		8	9.91	7.79	70.49		8	7.91	7.35	81.97
	9	8.49	7.18	73.77		9	9.00	7.44	73.77		9	8.54	8.04	80.33
	10	8.21	7.05	73.77		10	9.11	7.63	73.77		10	8.13	7.39	83.61
	11	7.94	6.70	73.77		11	8.53	7.06	75.41		11	8.75	8.04	78.69
	12	7.89	6.74	73.77		12	7.77	6.35	77.05		12	9.29	8.50	83.61
	13	7.37	6.39	73.77		13	7.84	6.31	75.41		13	8.85	7.89	83.61
	14	7.27	6.23	75.41		14	7.25	6.08	78.69		14	8.72	8.27	88.52
	15	7.18	6.24	75.41		15	7.05	6.06	78.69		15	8.57	7.70	85.25
	16	6.69	6.16	77.05		16	6.74	5.83	80.33		16	9.04	8.30	85.25
	All	15.12	8.88	-		All	15.89	8.94	-		All	19.83	9.61	-

Table 6.4: Localize-MI test results [214].

with the optimized subset of 2 channels, the mean localization error was lower than with all channels. In addition, the accuracy index values were 63.93%(39/61) , 65.57%(40/61) , and 40.98%(25/61) for sLORETA, wMNE and MSP respectively, with a marginal difference in the standard deviation for sLORETA and wMNE, when compared to the deviation obtained with all electrodes.

6.7 Discussion

The minimum number of electrodes required for modeling a single source is defined by the number of parameters to describe it: the localization based on three location coordinates (x,y,z) and the orientation based on three strength components in each coordinate axis [16]. However, in distributed models based on FEM and BEM modeling, the orientation can be assumed as fixed throughout the activation period of the source, where often it is assumed to be normal to the cortical surface. Therefore the number of parameters and electrodes required can be reduced. In the single-source test, the results shown in figure 6.4 suggest that 4 or 5 channels (where is located the inflection point of the pesudo-Pareto's front) are enough to estimate the source parameters with a satisfying localization accuracy when compared to a set of hdEEG. These results are also supported by the values shown in table 6.4, where the mean localization error was lower with these number of channels than when using all available electrodes.

Previously, it was discussed that a plateau behavior was observed in the localization error when increasing the number of electrodes [24]. This plateau can also be observed in the pseudo-Pareto front for all the tests performed here (figures 6.4, 6.5 and 6.9), where adding channels to the subset did not continue decreasing the localization error. However, the plateau did not remain flat until reaching the full number of electrodes. At some point adding channels started to increase the localization error. This effect is possible to see in the pseudo-Pareto front of the multiple-source test constrained to 60 channels, where at around 23 channels the error starts increasing notably. This effect is presented because the optimization algorithm was set to identify electrode combinations with the lowest number of electrodes and the lowest localization error possible for each source; during the optimization process, the algorithm does not find the optimal for each number of electrodes, rather, it evaluates a given number and as it finds combinations with a lower number, it keeps the search in that direction. At the end, most of the combinations evaluated lay in the first third of the total electrode number. This effect was also present in the other test but for a higher number of electrodes, figure 6.10 shows the pseudo-Pareto front for the multiple-source test with 231 electrodes, showing the number of channels from 2 to 130 to exemplify this effect.

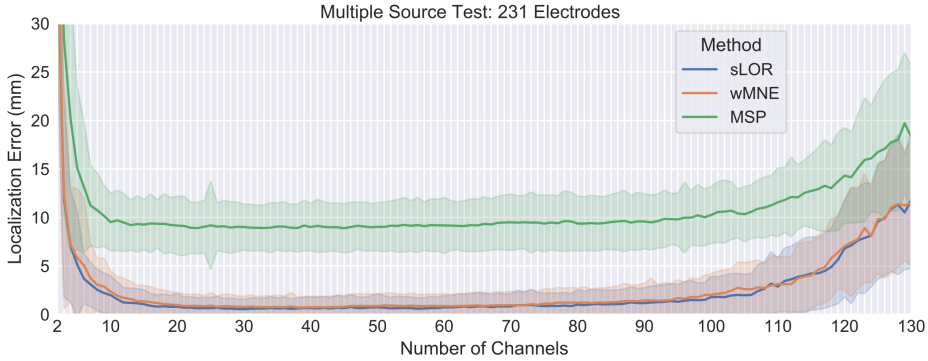

Figure 6.10: The pseudo-Pareto front for the multiple-source test with 231 electrodes [214].

The results of the multiple-test with 231, 128, and 60 channels offer evidence of the general effect of using a lower number of channels, where the localization error achieved the lower values when using 231 channels in both, without optimization when using all channels, and with optimization for the subset of channels. Considering this, when constraining the search to use less electrode positions, as in the tests with 128 and 60 channels, it was possible to observe an evident increment in the localization error with and without optimization (figure 6.5). This accuracy behavior supports the proposition that intermediate positions between electrodes in the 10-10 system adopted by the 10-5 electrode layout play an important role. As there are more channels, the probability of recording closer to the source of interest increases, resulting in a more accurate estimation. Moreover, the results are in line with the widely accepted concept of a higher number of channels leading to a higher localization accuracy, which has been previously demonstrated and discussed [24, 25].

What is new in the results presented here is that an optimized subset of electrodes can attain similar or better localization accuracy than when using all electrodes in a hdEEG setting (extensions of the 10-20), as shown in tables 6.1, 6.2 for a simulated dataset, and in 6.4 for the Localize-MI dataset. At first it can appear counter-intuitive that a reduced number of electrodes can attain such levels of accuracy. However, it should be cautiously noted that not any subset of channels can attain that accuracy. Through the combination of methods proposed in our

methodology, it was possible to find combinations of channels for a particular brain source/s configuration that attained values of localization error equal to or better than with hdEEG.

In conclusion, the different tests performed in this study offer multiple views of the channel optimization effects for source reconstruction in which multiple and single source cases were analyzed. Overall, the proposed methodology was able to optimize the localization error and the number of channels, by finding a subset of channels with few electrodes that attained equal or similar localization accuracy than hdEEG. In both cases, when analyzing the Localize-MI and the synthetic EEG datasets, the sources have different localization, which allowed us to evaluate the methodology over different brain regions and source configurations. Additionally, the proposed methodology was tested on several electrode systems (10-20, 10-10, 10-5, and geodesic) and considering different head modeling methods (FEM and BEM). Independently of the variations, our proposal was able to find combinations of channels with few channels that offer equal or better localization accuracy, demonstrating the feasibility of using low-density optimized electrode combinations to localize single and multiple sources.

Chapter 7

Conclusions and Future Work

This chapter summarizes the findings presented in this thesis, and offers an overview of the research questions in section 1.2

7.1 Findings Summary

A diagram summarizing the contributions of the thesis is presented in figure 7.1.

7.1.1 Extraction of underlying information using frequency decomposition

Chapter 4 presented a methodology for extracting frequency information to improve source reconstruction accuracy in ldEEG. The alleviation of the ill-condition characteristic of the inverse problem was performed by improving the SNR using frequency decomposition with MEMD. This was discussed in chapter 4 and in the article related to the thesis [177]. The use of MEMD to extract the underlying information of the source activity hidden in the EEG signals contributed to improving the reconstruction accuracy for ldEEG settings.

It was shown that the use of selected IMFs decomposed by MEMD allowed capturing of the underlying structure of source activity presented in the recordings, resulting in an improvement of spatial accuracy when comparing the solutions without pre-processing the EEG data with MEMD. As shown in figure 4.10 for synthetic data, the use of MEMD decomposition contributed to obtaining a significant difference in the reconstruction accuracy and maintaining a low reconstruction error when using ldEEG electrode counts of 16 and 8 channels.

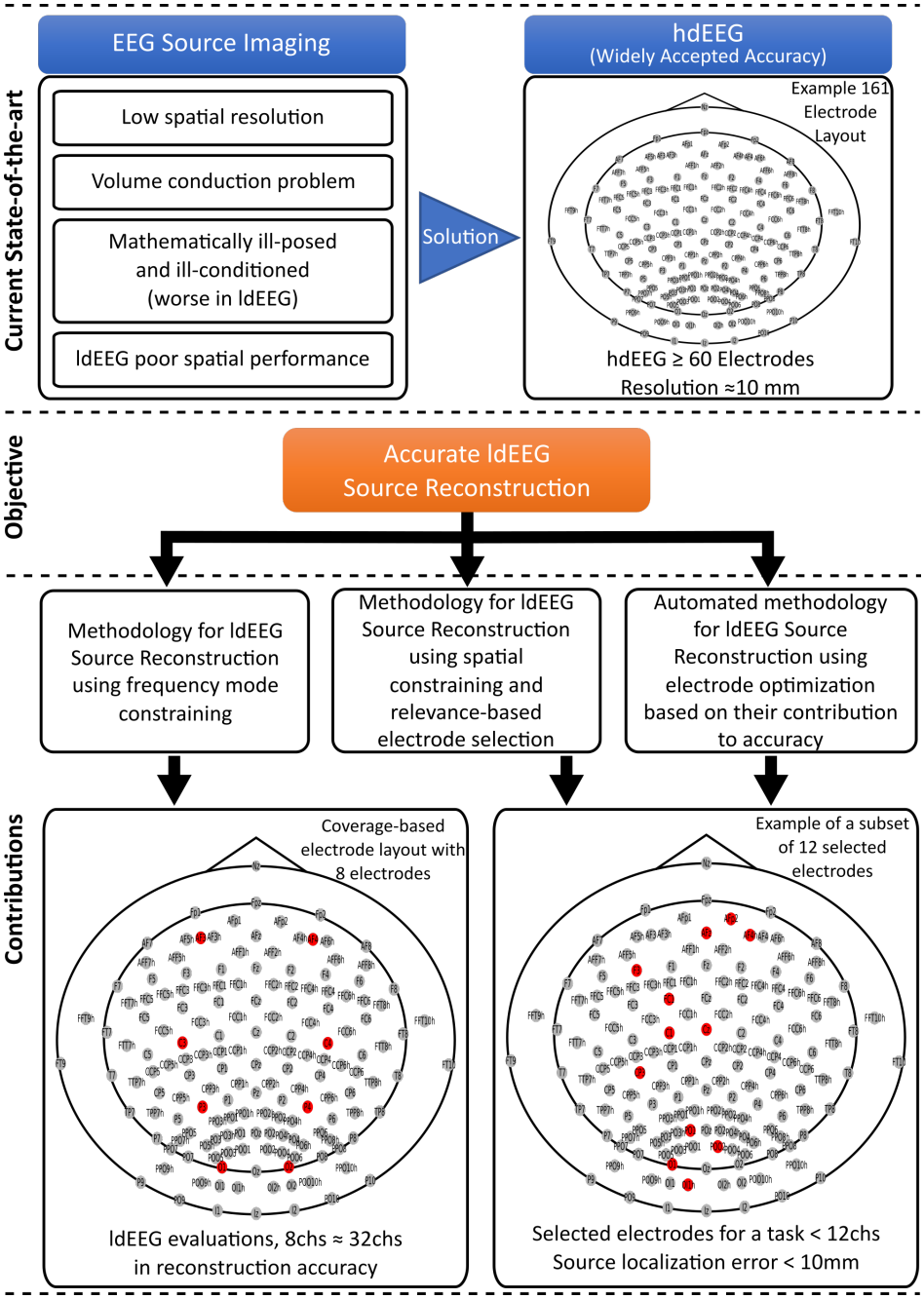

Figure 7.1: Summary of the thesis contributions

This was confirmed with the multi-modal dataset in figure 4.11, where the reconstruction accuracy of 32 channels with MSP was retained with MEMD-MSP using considering only 8 electrode positions.

The frequency decomposition and attenuation of mode-mixing resulting from MEMD had a positive impact over the source reconstruction accuracy. As the inverse method is constrained on the selected IMFs the solutions were more accurate and cleaner using MEMD-MSP than raw-MSP (figures 4.7, 4.8, 4.9, and 4.14), obtaining MEMD-MSP lower reconstruction errors.

7.1.2 Partial brain models and relevance-based channel selection

Chapter 5 presented a methodology involving reduced models of target brain regions or PBM as a technique to reduce the number of unknowns for the inverse problem. This, combined with relevance-based channel selection, allowed to obtain source localization errors typically seen in hdEEG but using ldEEG electrode counts.

The PBM approach allowed to constrain the solution to a particular brain region by reducing the number of unknowns of the inverse problem. The benefits of this approach were seen when using selected channels using relevance-based criteria and local electrodes. As shown in figure 5.6 and table 5.2, when using PBM and relevance-based selection it was possible to obtain reconstruction errors below 10 mm even with selected ldEEG electrode counts of 4, 8, and 16 electrodes, similar to hdEEG using 60 channels. In addition, when combining PBM with local electrodes, it was possible to obtain reconstruction errors below 20 mm.

The relevance selection based on Q-α method demonstrated that applying channel selection for source reconstruction can maintain a high level of spatial accuracy. As presented in figure 5.10 using ldEEG electrode counts of 6 and 9 channels selected by relevance criteria obtained source reconstruction errors similar to a hdEEG system with 128 channels and better than with 62 channels. In addition, even with such a smaller number of channels, the localization error was maintained below 10 mm, showing that the use of ldEEG can obtain high localization accuracy with selected channels. Moreover, the time courses were accurately extracted, and the selected ldEEG did not compromise the temporal accuracy as presented in figure 5.11, a high level of correlation was obtained between the reconstruction with selected channels and the densest coverage-

based.

7.1.3 Optimization-based channel selection

An automated methodology for channel selection was presented in chapter 6. In this, the number of electrodes and the localization error for single and multiple source cases were optimized using the NSGA-II algorithm combined with source reconstruction.

The optimization-based methodology was able to identify subsets of electrodes that lay in the category of ldEEG that retained the hdEEG source reconstruction accuracy. The experimental results show that optimal subsets with 6 electrodes can obtain an equal or better accuracy than hdEEG, with more that 200 channels, for a single source case. This happened when reconstructing a particular brain activity in more than 88% of the cases, for synthetic signals (table 6.1); and 63%, for real signals (table 6.4), and in more than 88% and 73% of the cases when considering optimal combinations with 8 channels for synthetic and real signals, respectively. For a multiple-source case of three sources (table 6.2), it was found that optimized combinations of 8, 12 and 16 electrodes attained an equal or better accuracy than hdEEG with 231 electrodes in at least 58%, 76%, and 82% of the cases respectively. Additionally, for such electrode numbers, a lower mean error and standard deviation than with 231 electrodes were obtained.

The pseudo-Pareto fronts obtained from the multiple optimizations showed that there are multiple ldEEG channel combinations that obtained a lower mean localization error, with electrode numbers much lower than high-density numbers. In multiple cases electrode counts with 6 to 12 electrodes exhibited a lower mean with similar standard deviation, as shown in figures 6.4, 6.5, and 6.9. In addition, when comparing the time-source reconstruction using the selected electrode counts with the densest electrode array, it was found that the signals obtained a high correlation over 97% as presented in figure 6.8, demonstrating that the time courses were marginally affected by the channel reduction.

7.2 Final Conclusions and Remarks

The proposed methodologies presented and the results discussed in chapters 4, 5, and 6 demonstrate the feasibility of using ldEEG to perform accurate source reconstruction. Three different approaches were presented, evaluated over

multiple EEG signals (synthetic and real), and the results discussed. From them, two approaches for channel selection for source reconstruction were introduced, based on relevance analysis and based the optimization of the electrode number and reconstruction accuracy.

In particular, the optimization-based approach for electrode selection can enable systematic searches of electrode subsets for any given source or combination of sources that can estimate the source/s location/s. Also, the accuracy of different high-density electrode configurations widely used today can be compared and benchmarked for any given source scenario. In ldEEG systems, it can be used for evaluating the source localization capabilities of multiple consumer-grade and wearable EEG systems that proliferate nowadays [269], to verify to what extent they can be used, and to determine the potential brain source activity they can monitor. The outcome of this research is envisioned as a powerful enabler of flexible wearable EEG systems that can offer source imaging capabilities with same accuracy as hdEEG to ldEEG systems in clinical and non-clinical settings. Also, as a platform to validate and benchmark existing wearables and any other type of EEG systems.

Multiple BCI systems are based on brain activity and responses of a particular region or area of the brain e.g. classification of SSVEP, or motor imaginary movements. Several works have studied the applicability, feasibility of source reconstruction in BCI classification [270, 271] and have been applied over motor imaginary tasks [103, 107, 272] reporting an increase in the classification accuracy for source-based approaches over the traditional sensor-based methods. The use of the source space has been poorly exploited in BCI systems, partially due to the uncertainty of source reconstruction when recording with non-hdEEG systems. As presented here, a selected configuration of electrodes can favor the development of source-centered BCI systems with a sparse number of electrodes that can surpass actual systems in accuracy, portability and comfort.

Simplifying the number of electrodes by implementing the approaches presented can be beneficial for applications and systems based on a sparse number of channels in medical and non-medical fields. Nowadays, there are an important number of devices with EEG recording capabilities with less than 32 electrodes, and especially in the clinical setting systems with 21 electrodes based on the standard

10-20 are still the gold standard for multiple analysis [82]. For those systems, the electrodes can be selected to estimate the activity of an area of interest; as demonstrated, the sources retrieved when using a selected subset presented a high level of correlation with the signals obtained with the full set of electrodes (figures 5.11 6.7), therefore, the source time-courses can be used for further analysis and feature extraction.

The use of a low number of electrodes, inherently, reduces the preparation time, and increases the portability of the EEG systems. The implementation of the proposed methodology can increase the flexibility of brain source reconstruction in multiple studies. For example, in mobile brain/body imaging (MoBI) there is a need to offer flexibility and ease the acquisition of brain data [273] in order to perform studies in natural environments for the participants, like while exercising or working [274]. The proposed methodologies also have potential applications in clinical settings in which it is required to monitor the activity of a specific area of the brain. The electrodes required to map a particular region of the brain related to a disease can be identified with the proposed approaches and placed in a patient, then, the estimated time-course can be analyzed, i.g. for detecting the start of a seizure in epileptic patients, or monitoring the changes in the brain activation over time.

The use of individual head models can be seen as a particular limitation to extend the applicability of the proposed methodologies. In multiple applications, especially the non-medical, there is no anatomical information available that allows to estimate a subject-specific model. However, in such cases, it is recommended to use template precise models and to apply a warping process using head landmarks and electrode positions [111]. After warping the model and co-registering with the electrodes, the forward model can be computed and used during source reconstruction.

It is important to consider that the selected electrodes based on optimization or relevance criteria are important for the basis of the particular source activity in which the analysis is applied. It must not be mis-interpreted that a selected set of electrodes can be used for mapping all the cortical regions. In such cases, to estimate a generalized activity over the brain, hdEEG is proven to be effective regardless of the area of brain activity. It is also important to note that multiple

channels that were repeatedly selected were located in positions out of standards 10-10, and 10-20, which supports the idea that multiple locations in non-standard positions contribute to improving the reconstruction quality, unfortunately, these positions are generally available only in denser layouts and EEG caps. However, the use of head models including intermediate positions can be combined with the physical adjustment of the positions of the electrodes of a system to the relevant selected ones, in order to monitor a particular brain activity.

The aim of this study is not to discourage the use of hdEEG systems, it is rather to offer alternative techniques to select and reduce the number of electrodes for source reconstruction while maintaining the localization accuracy of hdEEG systems. In several situations where for practical reasons high-density systems are not an option, ldEEG solutions designed based on the methodologies proposed can favor portability and reduce the volume of data while achieving the same quality as hdEEG systems. These traits can enable the development of much needed of portable EEG tools for medical diagnosis and non-medical applications.

7.3 Future Work

MEMD was proven to improve the source reconstruction accuracy by constraining the solution to selected frequency modes extracted over the EEG signals. MEMD is a time-frequency decomposition method based on a data-driven approach that does not use any particular assumption of the time course of the signals, and that does not influence the signal to adopt a particular shape. As the decomposed signals maintain their original frequency properties, MEMD should be evaluated in further studies to analyze the connectivity of brain regions of constrained solutions, and to evaluate the effects of ldEEG in connectivity analysis.

The use of frequency decomposition methods can improve source reconstruction by providing unmixed frequency activity. Here the MEMD was selected due to the mode-mixing attenuation and the mode-alignment of the IMFs in multivariate analysis. However, new decomposition methods as MVDM [245] and multivariate Fourier decomposition method (MFDM) [275] can also be applied over multivariate data to extract frequency components that contain underlying source activity. Those approaches have shown advantages over MEMD. In particular MVMD has been found to show advantages in noise robustness and

mode separation [245], and MFDM improves the mode-mixing [275]. Although, multiple authors have applied them for feature extraction and time-frequency decomposition [276–279], those methods remain to be evaluated over source reconstruction.

As mentioned in the conclusions, multiple BCI systems are based on the brain activity and responses of a particular region or area of the brain, and several studies have demonstrated the advantages of using a source space-based approach over electrode space [103, 107, 270–272]. It remains to be verified for those applications whether the use of selected ldEEG electrode counts for source reconstruction can be applied in the BCI domain. Future studies could focus on evaluating to what extent the optimal selection of channels for source reconstruction with ldEEG can impact the feature extraction from the estimated source activity, as well as the classification accuracy. In BCI the computation times required for source reconstruction must be added to the typical procedures of feature extraction and classification. In that regard, the results of tables 5.3 and 6.3 suggest that the methodologies proposed in chapters 5 and 6 are computationally feasible for BCI implementation and general online applications, in particular when using the algorithms based on minimum norm.

One of the most relevant applications of EEG source imaging is the detection of epileptogenic zones in drug-resistant focal epilepsy, in particular during pre-surgical stages [87, 280–282]. In future, studies should be performed on this task. As the localization accuracy is the focus, selected electrodes can be be studied to verify if reduced electrode numbers can locate the foci and/or monitor an affected area.

The methodologies presented in this thesis were evaluated over synthetic and real signals in most of the cases. In particular, the methodology of PBM and relevance-based channel selection was only evaluated on synthetic signals using the presented simulation framework for creating multi-source EEG signals 3.2. Although multiple tests were performed providing ldEEG and hdEEG comparisons, further studies should include the evaluation of real signals.

EEG connectivity analysis is a growing topic nowadays, as it offers the possibility to measure and quantify the interaction of brain regions during multiple tasks [27]. The study of brain connectivity is proven to be useful for neuromarker

identification of different brain conditions and processes [283–285]. Even though sensor-based connectivity is possible, the EEG volume conduction problem poses several challenges for the analysis and interpretation of results. In contrast, the source reconstructed maps offer more localized and unmixed information that is used to perform clearer connectivity analysis that offer a better interpretation of the connectivity between regions [28, 102]. However, this analysis on the source space is limited to the use of hdEEG. As demonstrated here, ldEEG can achieve a hdEEG localization accuracy for a particular brain activity or constrained to brain-ROI. It remains to be determined as to what extent source connectivity can be applied over a few regions of the brain, and provide meaningful results of the interaction of limited regions. The use of ldEEG for tracing subcortical activation using co-registration with fMRI and creating new models that based on connectivity and afferent region activation, could illuminate by inference, the subcortical region activation.

Here was demonstrated that multiple channels non-included in standard 10-10 and 10-20 systems also can contribute to improve the source reconstruction quality. However, those electrode positions are only available in denser layouts (10-5) and EEG caps, and they are generally not considered in ldEEG and wearable systems. Therefore, it remains to be verified how intermediate positions not considered in the typical positioning systems can contribute to source reconstruction. Moreover, a flexible system that allows re-positioning electrodes should be considered. Opposite to dipole fitting, instead of a dipole moving in the forward model, electrodes that search for optimal locations on the scalp for best capturing the underlying source activity remain to be studied. Although this can add challenges for noise handling and might require more complex models, they might contribute to the development of more accurate and personalized systems for source activity monitoring.

References

[1] Hans Berger. Über das Elektrenkephalogramm des Menschen. *Archiv für Psychiatrie und Nervenkrankheiten 1929 87:1*, 87(1):527–570, dec 1929.

[2] Wolfgang Klimesch. Eeg alpha and theta oscillations reflect cognitive and memory performance: a review and analysis. *Brain Research Reviews*, 29:169–195, 4 1999.

[3] R N Henson, Y Goshen-Gottstein, T Ganel, L J Otten, A Quayle, and M D Rugg. Electrophysiological and haemodynamic correlates of face perception, recognition and priming. *Cerebral Cortex*, 13:793–805, 7 2003.

[4] Mohammad Soleymani, Sadjad Asghari-Esfeden, Yun Fu, and Maja Pantic. Analysis of eeg signals and facial expressions for continuous emotion detection. *IEEE Transactions on Affective Computing*, 7:17–28, 1 2016.

[5] Kenneth Vilhelmsen, Seth B. Agyei, F. R.(Ruud) van der Weel, and Audrey L.H. van der Meer. A high-density eeg study of differentiation between two speeds and directions of simulated optic flow in adults and infants. *Psychophysiology*, 56, 1 2019.

[6] Ching Chang Kuo, Don M. Tucker, Phan Luu, Kevin Jenson, Jeffrey J. Tsai, Jeffrey G. Ojemann, and Mark D. Holmes. Eeg source imaging of epileptic activity at seizure onset. *Epilepsy Research*, 146:160–171, 10 2018.

[7] Samantha J. Broyd, Charmaine Demanuele, Stefan Debener, Suzannah K. Helps, Christopher J. James, and Edmund J.S. Sonuga-Barke. Default-mode brain dysfunction in mental disorders: A systematic review. *Neuroscience and Biobehavioral Reviews*, 33:279–296, 3 2009.

[8] Jaeseung Jeong. Eeg dynamics in patients with alzheimer's disease. *Clinical Neurophysiology*, 115:1490–1505, 7 2004.

[9] Jonathan R. Wolpaw, Niels Birbaumer, William J. Heetderks, Dennis J. McFarland, P. Hunter Peckham, Gerwin Schalk, Emanuel Donchin, Louis A. Quatrano, Charles J. Robinson, and Theresa M. Vaughan. Brain-computer interface technology: A review of the first international meeting. *IEEE Transactions on Rehabilitation Engineering*, 8:164–173, 6 2000.

[10] F. Lotte, L. Bougrain, A. Cichocki, M. Clerc, M. Congedo, A. Rakotomamonjy, and F. Yger. A review of classification algorithms for eeg-based brain-computer interfaces: A 10 year update. *Journal of Neural Engineering*, 15, 4 2018.

[11] Christoph M. Michel and Micah M. Murray. Towards the utilization of eeg as a brain imaging tool. *NeuroImage*, 61:371–385, 6 2012.

[12] Roberta Grech, Tracey Cassar, Joseph Muscat, Kenneth P Camilleri, Simon G Fabri, Michalis Zervakis, Petros Xanthopoulos, Vangelis Sakkalis, and Bart Vanrumste. Review on solving the inverse problem in eeg source analysis. *Journal of NeuroEngineering and Rehabilitation*, 5, 2008.

[13] Christoph M. Michel and Denis Brunet. Eeg source imaging: A practical review of the analysis steps. *Frontiers in Neurology*, 10:325, 4 2019.

[14] P.L. Nunez and R. Srinivasan. *Electric Fields of the Brain: The neurophysics of EEG*. Oxford University Press, 2006.

[15] Paul L. Nunez, Ramesh Srinivasan, Andrew F. Westdorp, Ranjith S. Wijesinghe, Don M. Tucker, Richard B. Silberstein, and Peter J. Cadusch. Eeg coherency: I: statistics, reference electrode, volume conduction, laplacians, cortical imaging, and interpretation at multiple scales. *Electroencephalography and Clinical Neurophysiology*, 103:499–515, 11 1997.

[16] PhD Riitta Hari, MD and PhD Aina Puce. *MEG-EEG Primer*. Oxford University Press, Oxford, UK, 03 2017.

[17] Risto J. Ilmoniemi and Jukka Sarvas. Brain signals: Physics and mathematics of meg and eeg. *Brain Signals*, 8 2019.

[18] Sanei Saeid. *Brain Signals, Their Generation, Acquisition and Properties*. John Wiley & Sons, Ltd, 2013.

[19] Hans Hallez, Bart Vanrumste, Roberta Grech, Joseph Muscat, Wim De Clercq, Anneleen Vergult, Yves D'Asseler, Kenneth P. Camilleri, Simon G. Fabri, Sabine Van Huffel, and Ignace Lemahieu. Review on solving the forward problem in eeg source analysis. *Journal of NeuroEngineering and Rehabilitation*, 4, 2007.

[20] Uwe Schmitt, Alfred K. Louis, Felix Darvas, Helmut Buchner, and Manfred Fuchs. Numerical aspects of spatio-temporal current density reconstruction from eeg-/meg-data. *IEEE Transactions on Medical Imaging*, 20:314–324, 2001.

[21] Ramesh Srinivasan, William R. Winter, and Paul L. Nunez. Source analysis of eeg oscillations using high-resolution eeg and meg. *Progress in Brain Research*, 159:29–42, 1 2006.

[22] Goran Lantz, R. Grave de Peralta, L. Spinelli, M. Seeck, and C. M. Michel. Epileptic source localization with high density eeg: How many electrodes are needed? *Clinical Neurophysiology*, 114:63–69, 1 2003.

[23] Verena Brodbeck, Laurent Spinelli, Agustina M. Lascano, Michael Wissmeier, Maria Isabel Vargas, Serge Vulliemoz, Claudio Pollo, Karl Schaller, Christoph M. Michel, and Margitta Seeck. Electroencephalographic source imaging: A prospective study of 152 operated epileptic patients. *Brain*, 134:2887–2897, 10 2011.

[24] Abbas Sohrabpour, Yunfeng Lu, Pongkiat Kankirawatana, Jeffrey Blount, Hyunmi Kim, and Bin He. Effect of eeg electrode number on epileptic source localization in pediatric patients. *Clinical Neurophysiology*, 126:472–480, 3 2015.

[25] Jasmine Song, Colin Davey, Catherine Poulsen, Phan Luu, Sergei Turovets, Erik Anderson, Kai Li, and Don Tucker. Eeg source localization: Sensor density and head surface coverage. *Journal of Neuroscience Methods*, 256:9–21, 12 2015.

[26] John G. Samuelsson, Noam Peled, Fahimeh Mamashli, Jyrki Ahveninen, and Matti S.

Hämäläinen. Spatial fidelity of meg/eeg source estimates: A general evaluation approach. *NeuroImage*, 224:117430, 1 2021.

[27] Mahmoud Hassan and Fabrice Wendling. Electroencephalography source connectivity: Aiming for high resolution of brain networks in time and space. *IEEE Signal Processing Magazine*, 35:81–96, 5 2018.

[28] Elham Barzegaran and Maria G. Knyazeva. Functional connectivity analysis in eeg source space: The choice of method. *PLOS ONE*, 12:e0181105, 7 2017.

[29] William Bosl, Adrienne Tierney, Helen Tager-Flusberg, and Charles Nelson. Eeg complexity as a biomarker for autism spectrum disorder risk. *BMC Medicine*, 9:1–16, 2 2011.

[30] Maeike Zijlmans, Premysl Jiruska, Rina Zelmann, Frans S.S. Leijten, John G.R. Jefferys, and Jean Gotman. High-frequency oscillations as a new biomarker in epilepsy. *Annals of Neurology*, 71:169–178, 2 2012.

[31] M. Bear, B. Connors, and M.A. Paradiso. *Neuroscience: Exploring the Brain, Enhanced Edition: Exploring the Brain, Enhanced Edition*. Jones & Bartlett Learning, 2020.

[32] Anthony A. Mercadante and Prasanna Tadi. *Neuroanatomy, Gray Matter*. StatPearls Publishing, 2021.

[33] Lennart Heimer. *The Human Brain and Spinal Cord*. Springer-Verlag, New York, USA, 1983.

[34] D.P. Pelvig, H. Pakkenberg, A.K. Stark, and B. Pakkenberg. Neocortical glial cell numbers in human brains. *Neurobiology of Aging*, 29(11):1754–1762, 2008.

[35] Suzana Herculano-Houzel. The human brain in numbers: a linearly scaled-up primate brain. *Frontiers in Human Neuroscience*, 3, 2009.

[36] Paul Johns. Neurons and glial cells. *Clinical Neuroscience*, pages 61–69, 1 2014.

[37] Gyorgy Buzsaki, Costas A. Anastassiou, and Christof Koch. The origin of extracellular fields and currents — eeg, ecog, lfp and spikes. *Nature Reviews Neuroscience 2012 13:6*, 13:407–420, 5 2012.

[38] Risto J. Ilmoniemi and Jukka Sarvas. *Brain Signals: Physics and Mathematics of MEG and EEG*. The MIT Press, 05 2019.

[39] Seward B. Rutkove. Introduction to volume conduction. *The Clinical Neurophysiology Primer*, pages 43–53, 2007.

[40] Akke Bakker, Brianne Smith, Philip Ainslie, and Kurt Smith. Near-infrared spectroscopy. *Applied Aspects of Ultrasonography in Humans*, 4 2012.

[41] David Gutiérrez, Arye Nehorai, and Carlos H. Muravchik. Estimating brain conductivities and dipole source signals with eeg arrays. *IEEE Transactions on Biomedical Engineering*, 51:2113–2122, 12 2004.

[42] Jeffrey W Britton, Lauren C Frey, Jennifer L Hopp, Pearce Korb, Mohamad Z Koubeissi, William E Lievens, Elia M Pestana-Knight, and EK Louis St. *Electroencephalography (EEG): An introductory text and atlas of normal and abnormal findings in adults, children, and infants*. American Epilepsy Society, Chicago, 2016.

[43] Mike X Cohen. *Analyzing Neural Time Series Data: Theory and Practice*. The MIT Press, 01 2014.

[44] Priyanka A. Abhang, Bharti W. Gawali, and Suresh C. Mehrotra. Introduction to eeg- and

speech-based emotion recognition. *Introduction to EEG- and Speech-Based Emotion Recognition*, pages 1–187, 3 2016.

[45] José Luis Cantero and Mercedes Atienza. Alpha burst activity during human REM sleep: descriptive study and functional hypotheses. *Clinical neurophysiology*, 111(5):909–915, 2000.

[46] J.L. O'Leary. Hans berger on the electroencephalogram of man. the fourteen original reports on the human electroencephalogram. translated from the german and edited by pierre gloor. *Science*, 168:562–563, 1970.

[47] Juri D. Kropotov. *Quantitative EEG, Event-Related Potentials and Neurotherapy*. Elsevier Inc., 2009.

[48] Juri D. Kropotov. Chapter 2.3 - beta and gamma rhythms. In Juri D. Kropotov, editor, *Functional Neuromarkers for Psychiatry*, pages 107–119. Academic Press, San Diego, 2016.

[49] Priyanka A. Abhang, Bharti W. Gawali, and Suresh C. Mehrotra. Chapter 3 - technical aspects of brain rhythms and speech parameters. In Priyanka A. Abhang, Bharti W. Gawali, and Suresh C. Mehrotra, editors, *Introduction to EEG- and Speech-Based Emotion Recognition*, pages 51–79. Academic Press, 2016.

[50] G. Pfurtscheller and F. H. Lopes Da Silva. Event-related eeg/meg synchronization and desynchronization: basic principles. *Clinical Neurophysiology*, 110:1842–1857, 11 1999.

[51] Greg Worrell and Jean Gotman. High-frequency oscillations and other electrophysiological biomarkers of epilepsy: clinical studies. *Biomarkers in medicine*, 5(5):557–566, 2011.

[52] Juri D. Kropotov. Chapter 2.2 - alpha rhythms. In Juri D. Kropotov, editor, *Functional Neuromarkers for Psychiatry*, pages 89–105. Academic Press, San Diego, 2016.

[53] Richard Caton. Electrical Currents of the Brain. *The Chicago Journal of Nervous & Mental Disease*, 2(4):610, 1875.

[54] Hans Berger and Pierre Gloor. Hans berger on electroencephalography. *http://dx.doi.org/10.1080/00029238.1969.11080728*, 9:1–8, 3 1969.

[55] D L Keene, S Whiting, and E C Ventureyra. Electrocorticography. *Epileptic disorders : international epilepsy journal with videotape*, 2(1):57–63, mar 2000.

[56] Nitish V. Thakor. Translating the brain-machine interface. *Science Translational Medicine*, 5, 11 2013.

[57] Jay L. Shils, Ryan Kochanski, Alireza Borghei, and Sepehr Sani. Neurophysiological monitoring during neurosurgery for movement disorders. *Neurophysiology in Neurosurgery*, pages 473–497, 2020.

[58] Erwin Habibzadeh Tonekabony Shad, Marta Molinas, and Trond Ytterdal. Impedance and noise of passive and active dry eeg electrodes: A review. *IEEE Sensors Journal*, 20:14565–14577, 12 2020.

[59] M. A. Lopez-Gordo, D. Sanchez Morillo, and F. Pelayo Valle. Dry eeg electrodes. *Sensors (Basel, Switzerland)*, 14:12847, 7 2014.

[60] Selenia di Fronso, Patrique Fiedler, Gabriella Tamburro, Jens Haueisen, Maurizio Bertollo, and Silvia Comani. Dry eeg in sports sciences: A fast and reliable tool to assess individual alpha peak frequency changes induced by physical effort. *Frontiers in Neuroscience*, 13:982, 9 2019.

[61] Pablo F. Diez, Vicente Mut, Eric Laciar, and Enrique Avila. A comparison of monopolar and bipolar EEG recordings for SSVEP detection. *2010 Annual International Conference of the IEEE Engineering in Medicine and Biology Society, EMBC'10*, pages 5803–5806, 2010.

[62] Steven J. Luck. *An Introduction to the Event-Related Potential Technique*. The MIT Press, 2015.

[63] Dezhong Yao, Yun Qin, Shiang Hu, Li Dong, Maria L. Bringas Vega, and Pedro A. Valdés Sosa. Which reference should we use for eeg and erp practice? *Brain Topography*, 32:530–549, 7 2019.

[64] Emily S. Kappenman and Steven J. Luck. The effects of electrode impedance on data quality and statistical significance in erp recordings. *Psychophysiology*, 47:888–904, 9 2010.

[65] Steven J. Luck, Geoffrey F. Woodman, and Edward K. Vogel. Event-related potential studies of attention. *Trends in Cognitive Sciences*, 4:432–440, 11 2000.

[66] Albert Kok. Event-related-potential (erp) reflections of mental resources: A review and synthesis. *Biological Psychology*, 45:19–56, 3 1997.

[67] Martin Eimer and Amanda Holmes. Event-related brain potential correlates of emotional face processing. *Neuropsychologia*, 45:15–31, 2007.

[68] Yurena Morera, Maartje van der Meij, Manuel de Vega, and Horacio A. Barber. Are sensory-motor relationships encoded ad hoc or by default?: An erp study. *Frontiers in Psychology*, 10, 2019.

[69] Kenneth Vilhelmsen, F. R. Van Der Weel, and Audrey L.H. Van Der Meer. A high-density eeg study of differences between three high speeds of simulated forward motion from optic flow in adult participants. *Frontiers in Systems Neuroscience*, 9:146, 10 2015.

[70] Richard N. Henson, Elias Mouchlianitis, and Karl J. Friston. Meg and eeg data fusion: Simultaneous localisation of face-evoked responses. *NeuroImage*, 47:581–589, 8 2009.

[71] Jonathan R. Folstein and Cyma Van Petten. Influence of cognitive control and mismatch on the n2 component of the erp: A review. *Psychophysiology*, 45:152–170, 1 2008.

[72] Geoffrey F. Woodman. A brief introduction to the use of event-related potentials in studies of perception and attention. *Attention, Perception, & Psychophysics 2010 72:8*, 72:2031–2046, 2010.

[73] John Polich. Updating P300: an integrative theory of P3a and P3b. *Clinical neurophysiology*, 118(10):2128–2148, 2007.

[74] IFCN. The ten twenty electrode system: International federation of societies for electroencephalography and clinical neurophysiology. *American Journal of EEG Technology*, 1(1):13–19, 1961.

[75] Herbert Jasper. Report of the committee on methods of clinical examination in electroencephalography. *Electroencephalography Clinical Neurophysiology*, 10:370–375, 1958.

[76] G. H. Klem, H. O. Lüders, H. H. Jasper, and C. Elger. The ten-twenty electrode system of the international federation. the international federation of clinical neurophysiology. *Electroencephalography and Clinical neurophysiology. Supplement*, 52:3–6, 1 1999.

[77] M. R. Nuwer, G. Comi, R. Emerson, A. Fuglsang-Frederiksen, J. M. Guérit, H. Hinrichs, A. Ikeda, F. J. Luccas, and P. Rappelsberger. Ifcn standards for digital recording of clinical eeg. *Electroencephalography and Clinical Neurophysiology*, 106:259–261, 3 1998.

[78] American Electroencephalographic Society. Guideline thirteen: Guidelines for standard electrode position nomenclature. *Journal of Clinical Neurophysiology*, 11(1):111–3, 1994.

[79] G. E. Chatrian, E. Lettich, and P. L. Nelson. Ten percent electrode system for topographic studies of spontaneous and evoked eeg activities. *American Journal of EEG Technology*, 25:83–92, 1985.

[80] Marc R Nuwer. Recording electrode site nomenclature. *Journal of Clinical Neurophysiology*, 4:121–134, 4 1987.

[81] G. E. Chatrian, E. Lettich, and P. L. Nelson. Improved nomenclature for the '10%' electrode system. *American Journal of EEG Technology*, 28(3):161–163, 1988.

[82] Margitta Seeck, Laurent Koessler, Thomas Bast, Frans Leijten, Christoph Michel, Christoph Baumgartner, Bin He, and Sándor Beniczky. The standardized EEG electrode array of the IFCN, oct 2017.

[83] Robert Oostenveld and Peter Praamstra. The five percent electrode system for high-resolution EEG and ERP measurements. *Clinical Neurophysiology*, 112(4):713–719, apr 2001.

[84] Electrical Geodesics. Geodesic Sensor Net Technical Manual. Technical report, Electrical Geodesics, Inc, 2007.

[85] Christoph M. Michel, Göran Lantz, Laurent Spinelli, Rolando Grave De Peralta, Theodor Landis, and Margitta Seeck. 128-channel eeg source imaging in epilepsy: Clinical yield and localization precision. *Journal of Clinical Neurophysiology*, 21:71–83, 2004.

[86] Francesca Sperli, Laurent Spinelli, Margitta Seeck, Mary Kurian, Christoph M. Michel, and Göran Lantz. Eeg source imaging in pediatric epilepsy surgery: A new perspective in presurgical workup. *Epilepsia*, 47:981–990, 6 2006.

[87] Sándor Beniczky, Ivana Rosenzweig, Michael Scherg, Todor Jordanov, Benjamin Lanfer, Göran Lantz, and Pål Gunnar Larsson. Ictal eeg source imaging in presurgical evaluation: High agreement between analysis methods. *Seizure*, 43:1–5, 12 2016.

[88] Pierre Mégevand, Laurent Spinelli, Mélanie Genetti, Verena Brodbeck, Shahan Momjian, Karl Schaller, Christoph M Michel, Serge Vulliemoz, and Margitta Seeck. Electric source imaging of interictal activity accurately localises the seizure onset zone. *Journal of Neurology, Neurosurgery & Psychiatry*, 85:38–43, 1 2014.

[89] Claudio Babiloni, Emanuele Cassetta, Giuliano Binetti, Mario Tombini, Claudio Del Percio, Florinda Ferreri, Raffaele Ferri, Giovanni Frisoni, Bartolo Lanuzza, Flavio Nobili, Laura Parisi, Guido Rodriguez, Leonardo Frigerio, Mariella Gurzì, Annapaola Prestia, Fabrizio Vernieri, Fabrizio Eusebi, and Paolo M. Rossini. Resting eeg sources correlate with attentional span in mild cognitive impairment and alzheimer's disease. *European Journal of Neuroscience*, 25:3742–3757, 6 2007.

[90] C. Huang, L. O. Wahlund, T. Dierks, P. Julin, B. Winblad, and V. Jelic. Discrimination of alzheimer's disease and mild cognitive impairment by equivalent eeg sources: a cross-sectional and longitudinal study. *Clinical Neurophysiology*, 111:1961–1967, 11 2000.

[91] Thinh Nguyen, Thomas Potter, Trac Nguyen, Christof Karmonik, Robert Grossman, and Yingchun Zhang. Eeg source imaging guided by spatiotemporal specific fmri: Toward an understanding of dynamic cognitive processes. *Neural Plasticity*, 2016, 2016.

[92] Stephanie Morand, Gregor Thut, Rolando Grave De Peralta, Stephanie Clarke, Asaid Khateb, Theodor Landis, and Christoph M. Michel. Electrophysiological evidence for fast visual processing through the human koniocellular pathway when stimuli move. *Cerebral cortex (New York, N.Y. : 1991)*, 10:817–825, 2000.

[93] Gregor Thut, Claude Alain Hauert, Stéphanie Morand, Margitta Seeck, Theodor Landis, and Christoph Michel. Evidence for interhemispheric motor-level transfer in a simple reaction time task: an eeg study. *Experimental Brain Research 1999 128:1*, 128:256–261, 1999.

[94] Christoph M. Michel, Gregor Thut, Stéphanie Morand, Asaid Khateb, Alan J. Pegna, Rolando Grave de Peralta, Sara Gonzalez, Margitta Seeck, and Theodor Landis. Electric source imaging of human brain functions. *Brain Research Reviews*, 36:108–118, 10 2001.

[95] Asaid Khateb, Alan J. Pegna, Christoph M. Michel, Michaël Mouthon, and Jean Marie Annoni. Semantic relatedness and first-second language effects in the bilingual brain: a brain mapping study*. *Bilingualism: Language and Cognition*, 19:311–330, 2016.

[96] Bérangère Thirioux, Manuel R. Mercier, Gérard Jorland, Alain Berthoz, and Olaf Blanke. Mental imagery of self-location during spontaneous and active self–other interactions: An electrical neuroimaging study. *Journal of Neuroscience*, 30:7202–7214, 5 2010.

[97] Karl J. Friston. Functional and effective connectivity in neuroimaging: A synthesis. *Human Brain Mapping*, 2:56–78, 1 1994.

[98] Jan Mathijs Schoffelen and Joachim Gross. Source connectivity analysis with meg and eeg. *Human Brain Mapping*, 30:1857–1865, 6 2009.

[99] Andrew Zalesky, Luca Cocchi, Alex Fornito, Micah M. Murray, and Ed Bullmore. Connectivity differences in brain networks. *NeuroImage*, 60:1055–1062, 4 2012.

[100] Bin He, Laura Astolfi, Pedro Antonio Valdes-Sosa, Daniele Marinazzo, Satu O. Palva, Christian George Benar, Christoph M. Michel, and Thomas Koenig. Electrophysiological brain connectivity: Theory and implementation. *IEEE Transactions on Biomedical Engineering*, 66:2115–2137, 7 2019.

[101] Tim R. Mullen, Christian A.E. Kothe, Yu Mike Chi, Alejandro Ojeda, Trevor Kerth, Scott Makeig, Tzyy Ping Jung, and Gert Cauwenberghs. Real-time neuroimaging and cognitive monitoring using wearable dry eeg. *IEEE Transactions on Biomedical Engineering*, 62:2553–2567, 11 2015.

[102] Margherita Lai, Matteo Demuru, Arjan Hillebrand, and Matteo Fraschini. A comparison between scalp- and source-reconstructed eeg networks. *Scientific Reports*, 8:1–8, 12 2018.

[103] Bradley J. Edelman, Bryan Baxter, and Bin He. Eeg source imaging enhances the decoding of complex right-hand motor imagery tasks. *IEEE Transactions on Biomedical Engineering*, 63:4–14, 1 2016.

[104] Radu Ranta, Steven Le Cam, Gundars Bergmanis-Korats, Sebastien Rimbert, and Laurent Bougrain. On source space resolution in eeg brain imaging for motor imagery. *International IEEE/EMBS Conference on Neural Engineering, NER*, 2019-March:1025–1029, 5 2019.

[105] Mustafa Yazici, Mustafa Ulutas, and Mukadder Okuyan. A comprehensive sloreta study on the contribution of cortical somatomotor regions to motor imagery. *Brain Sciences 2019, Vol. 9, Page 372*, 9:372, 12 2019.

[106] David Sabbagh, Pierre Ablin, Gaël Varoquaux, Alexandre Gramfort, and Denis A. Engemann. Predictive regression modeling with meg/eeg: from source power to signals and cognitive states. *NeuroImage*, 222:116893, 11 2020.

[107] Ming Ai Li, Yi Fan Wang, Song Min Jia, Yan Jun Sun, and Jin Fu Yang. Decoding of motor imagery eeg based on brain source estimation. *Neurocomputing*, 339:182–193, 4 2019.

[108] Ming ai Li, Yu xin Dong, Yan jun Sun, Jin fu Yang, and Li juan Duan. Subject-based dipole selection for decoding motor imagery tasks. *Neurocomputing*, 402:195–208, 8 2020.

[109] Helmut Buchner, Till D. Waberski, Manfred Fuchs, Hans Aloys Wischmann, Michael Wagner, and Ralf Drenckhahn. Comparison of realistically shaped boundary-element and spherical head models in source localization of early somatosensory evoked potentials. *Brain Topography 1995 8:2*, 8:137–143, 12 1995.

[110] Johannes Vorwerk, Jae Hyun Cho, Stefan Rampp, Hajo Hamer, Thomas R. Knösche, and Carsten H. Wolters. A guideline for head volume conductor modeling in eeg and meg. *NeuroImage*, 100:590–607, 10 2014.

[111] Zeynep Akalin Acar and Scott Makeig. Effects of forward model errors on eeg source localization. *Brain Topography 2013 26:3*, 26:378–396, 1 2013.

[112] S. P. Van Den Broek, F. Reinders, M. Donderwinkel, and M. J. Peters. Volume conduction effects in eeg and meg. *Electroencephalography and Clinical Neurophysiology*, 106:522–534, 6 1998.

[113] Patrick Berg and Michael Scherg. A fast method for forward computation of multiple-shell spherical head models. *Electroencephalography and Clinical Neurophysiology*, 90(1):58–64, 1 1994.

[114] Manfred Fuchs, Jörn Kastner, Michael Wagner, Susan Hawes, and John S. Ebersole. A standardized boundary element method volume conductor model. *Clinical Neurophysiology*, 113(5):702–712, 5 2002.

[115] J. Vorwerk, C. Engwer, S. Pursiainen, and C. H. Wolters. A mixed finite element method to solve the eeg forward problem. *IEEE Transactions on Medical Imaging*, 36:930–941, 4 2017.

[116] Ernesto Cuartas Morales, Carlos D. Acosta-Medina, German Castellanos-Dominguez, and Dante Mantini. A finite-difference solution for the eeg forward problem in inhomogeneous anisotropic media. *Brain Topography*, 32:229–239, 3 2019.

[117] Gildas Marin, Christophe Guerin, Sylvain Baillet, Line Garnero, and Gérard Meunier. Influence of skull anisotropy for the forward and inverse problem in EEG: Simulation studies using FEM on realistic head models. *Human Brain Mapping*, 6(4):250–269, 1 1998.

[118] Federica Vatta, Fabio Meneghini, Fabrizio Esposito, Stefano Mininel, and Francesco Di Salle. Realistic and spherical head modeling for EEG forward problem solution: A comparative cortex-based analysis. *Computational Intelligence and Neuroscience*, 2010, 2010.

[119] Bradley J. Roth, David Ko, Irene R. Von Albertini-Carletti, David Scaffidi, and Susumu Sato. Dipole localization in patients with epilepsy using the realistically shaped head model. *Electroencephalography and Clinical Neurophysiology*, 102:159–166, 1997.

[120] Lyubomir Zagorchev, Matthias Brueck, Nick Flaschner, Fabian Wenzel, Damon Hyde, Arne Ewald, and Jurriaan Peters. Patient-specific sensor registration for electrical source imaging

using a deformable head model. *IEEE Transactions on Biomedical Engineering*, 68:267–275, 1 2021.

[121] Deepak Khosla, Manuel Don, and Betty Kwong. Spatial mislocalization of eeg electrodes - effects on accuracy of dipole estimation. *Clinical Neurophysiology*, 110:261–271, 2 1999.

[122] Yohan Céspedes-Villar, Juan David Martinez-Vargas, and G. Castellanos-Dominguez. Influence of Patient-Specific Head Modeling on EEG Source Imaging. *Computational and Mathematical Methods in Medicine*, 2020, 2020.

[123] C. D. Geisler and G. L. Gerstein. The surface EEG in relation to its sources. *Electroencephalography and Clinical Neurophysiology*, 13(6):927–934, dec 1961.

[124] Michel R. Schneider. A multistage process for computing virtual dipolar sources of eeg discharges from surface information. *IEEE Transactions on Biomedical Engineering*, BME-19:1–12, 1972.

[125] Jean Daunizeau, Jérémie Mattout, Diego Clonda, Bernard Goulard, Habib Benali, and Jean Marc Lina. Bayesian spatio-temporal approach for eeg source reconstruction: Conciliating ecd and distributed models. *IEEE Transactions on Biomedical Engineering*, 53:503–516, 3 2006.

[126] Zoltan J. Koles. Trends in eeg source localization. *Electroencephalography and Clinical Neurophysiology*, 106:127–137, 2 1998.

[127] Christoph M. Michel, Micah M. Murray, Göran Lantz, Sara Gonzalez, Laurent Spinelli, and Rolando Grave De Peralta. Eeg source imaging. *Clinical Neurophysiology*, 115:2195–2222, 10 2004.

[128] Michael Scherg and Detlev Von Cramon. Evoked dipole source potentials of the human auditory cortex. *Electroencephalography and Clinical Neurophysiology/Evoked Potentials Section*, 65:344–360, 9 1986.

[129] Bin He, Abbas Sohrabpour, Emery Brown, and Zhongming Liu. Electrophysiological source imaging: A noninvasive window to brain dynamics. *https://doi.org/10.1146/annurev-bioeng-062117-120853*, 20:171–196, 6 2018.

[130] Jun Yao and Julius P.A. Dewald. Evaluation of different cortical source localization methods using simulated and experimental eeg data. *NeuroImage*, 25:369–382, 4 2005.

[131] Lei Ding and Han Yuan. Inverse source imaging methods in recovering distributed brain sources. *Biomedical Engineering Letters 2012 2:1*, 2:2–7, 3 2012.

[132] Munsif Ali Jatoi, Nidal Kamel, Aamir Saeed Malik, Ibrahima Faye, and Tahamina Begum. A survey of methods used for source localization using eeg signals. *Biomedical Signal Processing and Control*, 11:42–52, 5 2014.

[133] Shiva Asadzadeh, Tohid Yousefi Rezaii, Soosan Beheshti, Azra Delpak, and Saeed Meshgini. A systematic review of eeg source localization techniques and their applications on diagnosis of brain abnormalities. *Journal of Neuroscience Methods*, 339:108740, 6 2020.

[134] Chamandeep Kaur, Preeti Singh, Amandeep Bisht, Garima Joshi, and Sunil Agrawal. Recent developments in spatio-temporal eeg source reconstruction techniques. *Wireless Personal Communications*, 122:1531–1558, 1 2022.

[135] E. Giraldo-Suarez, J. D. Martinez-Vargas, and G. Castellanos-Dominguez. Reconstruction

of neural activity from eeg data using dynamic spatiotemporal constraints. *International Journal of Neural Systems*, 26:1650026, 2016.

[136] Gilbert. Strang. *Linear algebra and its applications*. Thomson, Brooks/Cole, 2006.

[137] Christian Hansen. *Rank Deficient and Discrete Ill Posed Problems*. SIAM Monographs on Mathematical Modeling and Computation, Lyngby, 1998.

[138] Kazufumi Ito and Bangti Jin. *Inverse Problems Tikhonov Theory and Algorithms*. WORLD SCIENTIFIC, 2015.

[139] M. S. Hämäläinen and R. J. Ilmoniemi. Interpreting magnetic fields of the brain: minimum norm estimates. *Medical & Biological Engineering & Computing*, 32(1):35–42, Jan 1994.

[140] Manfred Fuchs, Michael Wagner, Thomas Köhler, and Hans Aloys Wischmann. Linear and nonlinear current density reconstructions, 1999.

[141] Sunao Iwaki and Shoogo Ueno. Weighted minimum-norm source estimation of magnetoencephalography utilizing the temporal information of the measured data. *Journal of Applied Physics*, 83(11):6441, oct 1998.

[142] R D Pascual-Marqui, C.M. Michel, and D Lehmann. Low resolution electromagnetic tomography: a new method for localizing electrical activity in the brain. *International Journal of Psychophysiology*, 18(1):49–65, 1994.

[143] Anders M. Dale, Arthur K. Liu, Bruce R. Fischl, Randy L. Buckner, John W. Belliveau, Jeffrey D. Lewine, and Eric Halgren. Dynamic statistical parametric mapping: Combining fmri and meg for high-resolution imaging of cortical activity. *Neuron*, 26:55–67, 4 2000.

[144] Anett Seeland, Mario M. Krell, Sirko Straube, and Elsa A. Kirchner. Empirical comparison of distributed source localization methods for single-trial detection of movement preparation. *Frontiers in Human Neuroscience*, 12:340, 9 2018.

[145] Mayrim Vega-Hernández, Eduardo Martínez-Montes, José M. Sánchez-Bornot, Agustín Lage-Castellanos, and Pedro A. Valdés-Sosa. Penalized least squares methods for solving the eeg inverse problem. *Statistica Sinica*, 18(4):1535–1551, 2008.

[146] Lei Ding and Bin He. Sparse source imaging in electroencephalography with accurate field modeling. *Human Brain Mapping*, 29:1053–1067, 9 2008.

[147] Todor Jordanov, Karsten Hoechstetter, Patrick Berg, Isabella Paul-Jordanov, and Michael Scherg. Clara: classical loreta analysis recursively applied. 2014.

[148] José David and López Hincapié. MEG/EEG brain imaging based on Bayesian algorithms for ill-posed inverse problems. *Ph.D. Thesis - Universidad Nacional de Colombia*, 2012.

[149] Karl Friston, Lee Harrison, Jean Daunizeau, Stefan Kiebel, Christophe Phillips, Nelson Trujillo-Barreto, Richard Henson, Guillaume Flandin, and Jérémie Mattout. Multiple sparse priors for the M/EEG inverse problem. *NeuroImage*, 39(3):1104–1120, 2008.

[150] J. D. López, V. Litvak, J. J. Espinosa, K. Friston, and G. R. Barnes. Algorithmic procedures for Bayesian MEG/EEG source reconstruction in SPM. *NeuroImage*, 84:476–487, jan 2014.

[151] Munsif Ali Jatoi, Nidal Kamel, and José D. López. Multiple sparse priors technique with optimized patches for brain source localization. *International Journal of Imaging Systems and Technology*, 30(1):154–167, mar 2020.

[152] Nelson J. Trujillo-Barreto, Eduardo Aubert-Vázquez, and Pedro A. Valdés-Sosa. Bayesian

model averaging in eeg/meg imaging. *NeuroImage*, 21:1300–1319, 4 2004.

[153] John C. Mosher and Richard M. Leahy. Recursive MUSIC: A framework for EEG and MEG source localization. *IEEE Transactions on Biomedical Engineering*, 45(11):1342–1354, nov 1998.

[154] Niko Mäkelä, Matti Stenroos, Jukka Sarvas, and Risto J. Ilmoniemi. Truncated RAP-MUSIC (TRAP-MUSIC) for MEG and EEG source localization. *NeuroImage*, 167:73–83, feb 2018.

[155] Don M. Tucker. Spatial sampling of head electrical fields: the geodesic sensor net. *Electroencephalography and Clinical Neurophysiology*, 87(3):154–163, 9 1993.

[156] Nikolas Williams, Genevieve M McArthur, and Nicholas A Badcock. 10 years of epoc: A scoping review of emotiv's portable eeg device. *BioRxiv*, 2020.

[157] Ramesh Srinivasan, Don M. Tucker, and Michael Murias. Estimating the spatial nyquist of the human eeg. *Behavior Research Methods, Instruments, & Computers 1998 30:1*, 30:8–19, 1998.

[158] Bernd J. Vorderwülbecke, Margherita Carboni, Sebastien Tourbier, Denis Brunet, Martin Seeber, Laurent Spinelli, Margitta Seeck, and Serge Vulliemoz. High-density electric source imaging of interictal epileptic discharges: How many electrodes and which time point? *Clinical Neurophysiology*, 131:2795–2803, 12 2020.

[159] Bernd J. Vorderwülbecke, Amir G. Baroumand, Laurent Spinelli, Margitta Seeck, Pieter van Mierlo, and Serge Vulliémoz. Automated interictal source localisation based on high-density eeg. *Seizure*, 92:244–251, 11 2021.

[160] Amir G. Baroumand, Pieter van Mierlo, Gregor Strobbe, Lars H. Pinborg, Martin Fabricius, Guido Rubboli, Anne Mette Leffers, Peter Uldall, Bo Jespersen, Jannick Brennum, Otto Mølby Henriksen, and Sándor Beniczky. Automated eeg source imaging: A retrospective, blinded clinical validation study. *Clinical Neurophysiology*, 129:2403–2410, 11 2018.

[161] Sanjay P. Singh. Magnetoencephalography: Basic principles. *Annals of Indian Academy of Neurology*, 17:107, 2014.

[162] Cheryl A Olman and Essa Yacoub. High-field fmri for human applications: An overview of spatial resolution and signal specificity. *The Open Neuroimaging Journal*, 5:74–89, 11 2011.

[163] Matti S. Hämäläinen and R. J. Ilmoniemi. *Interpreting measured magnetic fields of the brain: Estimates of current distributions.* University of Helsinki, 1984.

[164] Manfred Fuchs, Michael Wagner, and Hans Aloys Wischmann. Generalized minimum norm least squares reconstruction algorithms. *ISBET Newsletter*, 5(5):8–11, 1994.

[165] Roberto D Pascual-Marqui, M. Esslen, K. Kochi, and D. Lehmann. Functional imaging with low-resolution brain electromagnetic tomography (LORETA): a review. *Methods and findings in experimental and clinical pharmacology*, 24 Suppl C:91–95, 2002.

[166] Olaf Hauk. Keep it simple: A case for using classical minimum norm estimation in the analysis of EEG and MEG data. *NeuroImage*, 21(4):1612–1621, 2004.

[167] Evangelos Galaris, Ioannis Gallos, Ivan Myatchin, Lieven Lagae, and Constantinos Siettos. Electroencephalography source localization analysis in epileptic children during a visual working-memory task. *International Journal for Numerical Methods in Biomedical Engineering*, 36:e3404, 12 2020.

[168] Roberto D Pascual-Marqui. Reply to comments made by R. Grave De Peralta Menendez and S.L. Gozalez Adino. *International Journal of Bioelectromagnetism*, 1(2):1–10, 1999.

[169] R. D. Pascual-Marqui. Standardized low-resolution brain electromagnetic tomography (sLORETA): Technical details. *Methods and Findings in Experimental and Clinical Pharmacology*, 24(SUPPL. D):5–12, 2002.

[170] L. M. Harrison, W. Penny, J. Ashburner, N. Trujillo-Barreto, and K. J. Friston. Diffusion-based spatial priors for imaging. *NeuroImage*, 38:677–695, 12 2007.

[171] Karl Friston, Jérémie Mattout, Nelson Trujillo-Barreto, John Ashburner, and Will Penny. Variational free energy and the laplace approximation. *NeuroImage*, 34:220–234, 1 2007.

[172] Yossi Rubner, Carlo Tomasi, and Leonidas J. Guibas. Metric for distributions with applications to image databases. *Proceedings of the IEEE International Conference on Computer Vision*, pages 59–66, 1998.

[173] Yossi Rubner, Carlo Tomasi, and Leonidas J. Guibas. The earth mover's distance as a metric for image retrieval. *International Journal of Computer Vision 2000 40:2*, 40:99–121, 11 2000.

[174] Stefan Haufe, Vadim V. Nikulin, Andreas Ziehe, Klaus Robert Müller, and Guido Nolte. Combining sparsity and rotational invariance in eeg/meg source reconstruction. *NeuroImage*, 42:726–738, 8 2008.

[175] Felix Lucka, Sampsa Pursiainen, Martin Burger, and Carsten H. Wolters. Hierarchical bayesian inference for the eeg inverse problem using realistic fe head models: Depth localization and source separation for focal primary currents. *NeuroImage*, 61:1364–1382, 7 2012.

[176] Sebastián Castaño-Candamil, Johannes Höhne, Juan David Martínez-Vargas, Xing Wei An, German Castellanos-Domínguez, and Stefan Haufe. Solving the eeg inverse problem based on space–time–frequency structured sparsity constraints. *NeuroImage*, 118:598–612, 9 2015.

[177] Andres Soler, Pablo A. Muñoz-Gutiérrez, Maximiliano Bueno-López, Eduardo Giraldo, and Marta Molinas. Low-Density EEG for Neural Activity Reconstruction Using Multivariate Empirical Mode Decomposition. *Frontiers in Neuroscience*, 14:175, feb 2020.

[178] Pablo Andrés Muñoz-Gutiérrez, Eduardo Giraldo, Maximiliano Bueno-López, and Marta Molinas. Localization of active brain sources from eeg signals using empirical mode decomposition: a comparative study. *Frontiers in Integrative Neuroscience*, 12, 11 2018.

[179] Quentin Noirhomme, Richard I. Kitney, and Benoît Macq. Single-trial eeg source reconstruction for brain-computer interface. *IEEE Transactions on Biomedical Engineering*, 55:1592–1601, 5 2008.

[180] Scott Makeig, Anthony Bell, Tzyy-Ping Jung, and Terrence J Sejnowski. Independent component analysis of electroencephalographic data. In D. Touretzky, M. C. Mozer, and M. Hasselmo, editors, *Advances in Neural Information Processing Systems*, volume 8. MIT Press, 1995.

[181] James V. Stone. *Independent Component Analysis: A Tutorial Introduction.* The MIT Press, 09 2004.

[182] Nathan Kutz. *Data-driven modeling and scientific computation.* Oxford University Press, 2013.

[183] Guofa Shou and Lei Ding. Detection of eeg spatial-spectral-temporal signatures of errors: a comparative study of ica-based and channel-based methods. *Brain topography*, 28:47–61, 1 2015.

[184] Giovanni Pellegrino, Min Xu, Abdulla Alkuwaiti, Manuel Porras-Bettancourt, Ghada Abbas,

Jean Marc Lina, Christophe Grova, and Eliane Kobayashi. Effects of independent component analysis on magnetoencephalography source localization in pre-surgical frontal lobe epilepsy patients. *Frontiers in Neurology*, 11:479, 6 2020.

[185] R Thatcher, EP Soler, DM North, and G Otte. Independent components analysis artifact correction distorts eeg phase in artifact free segments. *Journal of Neurology and Neurobiology*, 6:1592–1601, 9 2020.

[186] Geoffrey F Woodman and Steven J Luck. Serial deployment of attention during visual search., 2003.

[187] Maximiliano Bueno-López, Marta Molinas, and Geir Kulia. Understanding instantaneous frequency detection: A discussion of hilbert-huang transform versus wavelet transform. *International conference on Time Series 2017*, 2017.

[188] Ahmet Mert and Aydin Akan. Emotion recognition from eeg signals by using multivariate empirical mode decomposition. *Pattern Analysis and Applications*, 21:81–89, 2 2018.

[189] Xun Chen, Xueyuan Xu, Aiping Liu, Martin J. McKeown, and Z. Jane Wang. The use of multivariate emd and cca for denoising muscle artifacts from few-channel eeg recordings. *IEEE Transactions on Instrumentation and Measurement*, 67:359–370, 2 2018.

[190] Wei Zeng, Mengqing Li, Chengzhi Yuan, Qinghui Wang, Fenglin Liu, and Ying Wang. Classification of focal and non focal eeg signals using empirical mode decomposition (emd), phase space reconstruction (psr) and neural networks. *Artificial Intelligence Review*, 52:625–647, 4 2019.

[191] Luis Alfredo Moctezuma and Marta Molinas. Eeg channel-selection method for epileptic-seizure classification based on multi-objective optimization. *Frontiers in Neuroscience*, 14:593, 6 2020.

[192] Maximiliano Bueno-López, Pablo A Munoz-Gutierrez, Eduardo Giraldo, and Marta Molinas. Electroencephalographic Source Localization based on Enhanced Empirical Mode Decomposition. *IAENG International Journal of Computer Science*, 45:228–236, 2019.

[193] Sofie Therese Hansen, Apit Hemakom, Mads Gylling Safeldt, Lærke Karen Krohne, Kristoffer Hougaard Madsen, Hartwig R. Siebner, Danilo P. Mandic, and Lars Kai Hansen. Unmixing oscillatory brain activity by EEG source localization and empirical mode decomposition. *Computational Intelligence and Neuroscience*, 2019, 2019.

[194] Norden E. Huang, Zheng Shen, Steven R. Long, Manli C. Wu, Hsing H. Shih, Quanan Zheng, Nai-Chyuan Yen, Chi Chao Tung, and Henry H. Liu. The empirical mode decomposition and the hilbert spectrum for nonlinear and non-stationary time series analysis. *Proceedings of the Royal Society of London. Series A: Mathematical, Physical and Engineering Sciences*, 454(1971):903–995, 1998.

[195] Norden E Huang and Samuel S P Shen. *Hilbert-Huang Transform and Its Applications*. WORLD SCIENTIFIC, 2005.

[196] Gabriel Rilling and Patrick Flandrin. One or two frequencies? the empirical mode decomposition answers. *IEEE Transactions on Signal Processing*, 56(1):85–95, 2008.

[197] ZHAOHUA Wu and NORDEN E. HUANG. Ensemble empirical mode decomposition: A noise-assisted data analysis method. *Advances in Adaptive Data Analysis*, 01(01):1–41, 2009.

[198] María E. Torres, Marcelo A. Colominas, Gastón Schlotthauer, and Patrick Flandrin. A complete ensemble empirical mode decomposition with adaptive noise. *ICASSP, IEEE International Conference on Acoustics, Speech and Signal Processing - Proceedings*, pages 4144–4147, 2011.

[199] N. Rehman and D. P. Mandic. Multivariate empirical mode decomposition. *Proceedings of the Royal Society A: Mathematical, Physical and Engineering Sciences*, 466(2117):1291–1302, may 2010.

[200] Danilo P. Mandic, Naveed Ur Rehman, Zhaohua Wu, and Norden E. Huang. Empirical mode decomposition-based time-frequency analysis of multivariate signals: The power of adaptive data analysis. *IEEE Signal Processing Magazine*, 30(6):74–86, 2013.

[201] Y. Miao and J. Cao. Comparison of emd, memd and 2t-emd by analyzing standard artificial signals and eeg. In *2017 International Joint Conference on Neural Networks (IJCNN)*, volume 1, pages 1367–1371, May 2017.

[202] Naveed Rehman, Cheolsoo Park, Norden E. Huang, and Danilo Mandic. Emd via memd: Multivariate noise-aided computation of standard emd. *Advances in Adaptive Data Analysis*, 05(02):1350007, 2013.

[203] Lior Wolf and Annon Shashua. Feature Selection for Unsupervised and Supervised Inference: The Emergence of Sparsity in a Weight-Based Approach * Amnon Shashua. *Journal of Machine Learning Research*, 6:1855–1887, 2005.

[204] Lior Wolf and Annon Shashua. Feature selection for unsupervised and supervised inference: The emergence of sparsity in a weighted-based approach. In *Proceedings of the IEEE International Conference on Computer Vision*, volume 1, pages 378–384, 2003.

[205] E. Giraldo, D. Peluffo-Ordoñez, and G. Castellanos-Dominguez. Weighted Time Series Analysis for Electroencephalographic Source Localization. *DYNA Universidad Nacional de Colombia*, 79:64–70, 2012.

[206] Nidamarthi Srinivas and Kalyanmoy Deb. Muiltiobjective optimization using nondominated sorting in genetic algorithms. *Evolutionary computation*, 2(3):221–248, 1994.

[207] Kalyanmoy Deb. *Multi-objective optimization using evolutionary algorithms*, volume 16. John Wiley & Sons, 2001.

[208] R. T. Marler and J. S. Arora. Survey of multi-objective optimization methods for engineering. *Structural and Multidisciplinary Optimization 2004 26:6*, 26:369–395, 3 2004.

[209] D. A. Van Veldhuizen and G. B. Lamont. Multiobjective evolutionary algorithms: Analyzing the state-of-the-art. *Evolutionary Computation*, 8:125–147, 6 2000.

[210] Tinkle Chugh, Karthik Sindhya, Jussi Hakanen, and Kaisa Miettinen. A survey on handling computationally expensive multiobjective optimization problems with evolutionary algorithms. *Soft Computing*, 23(9):3137–3166, 2019.

[211] Kalyanmoy Deb, Amrit Pratap, Sameer Agarwal, and T. Meyarivan. A fast and elitist multiobjective genetic algorithm: NSGA-II. *IEEE Transactions on Evolutionary Computation*, 6(2):182–197, 4 2002.

[212] Daniel G. Wakeman and Richard N. Henson. A multi-subject, multi-modal human neuroimaging dataset. *Scientific Data 2015 2:1*, 2:1–10, 1 2015.

[213] Ezequiel Mikulan, Simone Russo, Sara Parmigiani, Simone Sarasso, Flavia Maria Zauli,

Annalisa Rubino, Pietro Avanzini, Anna Cattani, Alberto Sorrentino, Steve Gibbs, Francesco Cardinale, Ivana Sartori, Lino Nobili, Marcello Massimini, and Andrea Pigorini. Simultaneous human intracerebral stimulation and HD-EEG, ground-truth for source localization methods. *Scientific Data*, 7(1):1–8, 12 2020.

[214] A. Soler, L. Moctezuma, E. Giraldo, and M. Molinas. Automated methodology for optimal selection of minimum electrode subsets for accurate eeg source estimation based on genetic algorithm optimization. *bioRxiv*, 2021.

[215] Andres Soler, Eduardo Giraldo, and Marta Molinas. Low-density EEG for Source Activity Reconstruction using Partial Brain Models. In *Proceedings of the 13th International Joint Conference on Biomedical Engineering Systems and Technologies*, pages 54–63. SCITEPRESS - Science and Technology Publications, 2020.

[216] Yu Huang, Lucas C. Parra, and Stefan Haufe. The New York Head—A precise standardized volume conductor model for EEG source localization and tES targeting. *NeuroImage*, 140:150–162, 10 2016.

[217] David Colton and Rainer Kress. *Inverse Acoustic and Electromagnetic Scattering Theory*. Springer, 4 edition, 2019.

[218] Karl Friston, Richard Henson, Christophe Phillips, and Jérémie Mattout. Bayesian estimation of evoked and induced responses. *Human Brain Mapping*, 27(9):722–735, 2006.

[219] R. N. Henson, J. Mattout, K. D. Singh, G. R. Barnes, A. Hillebrand, and K. Friston. Population-level inferences for distributed MEG source localization under multiple constraints: Application to face-evoked fields. *NeuroImage*, 38(3):422–438, 2007.

[220] Richard N. Henson, Daniel G. Wakeman, Vladimir Litvak, and Karl J. Friston. A Parametric Empirical Bayesian Framework for the EEG/MEG Inverse Problem: Generative Models for Multi-Subject and Multi-Modal Integration. *Frontiers in Human Neuroscience*, 5(August):1–16, 2011.

[221] A. Gramfort, D. Strohmeier, J. Haueisen, M.S. Hamalainen, and M. Kowalski. Time-frequency mixed-norm estimates: Sparse m/eeg imaging with non-stationary source activations. *NeuroImage*, 70(0):410 – 422, 2013.

[222] Makoto Fukushima, Okito Yamashita, Thomas R. Knösche, and Masa aki Sato. MEG source reconstruction based on identification of directed source interactions on whole-brain anatomical networks. *NeuroImage*, 105:408–427, 2015.

[223] Krzysztof J. Gorgolewski, Tibor Auer, Vince D. Calhoun, R. Cameron Craddock, Samir Das, Eugene P. Duff, Guillaume Flandin, Satrajit S. Ghosh, Tristan Glatard, Yaroslav O. Halchenko, Daniel A. Handwerker, Michael Hanke, David Keator, Xiangrui Li, Zachary Michael, Camille Maumet, B. Nolan Nichols, Thomas E. Nichols, John Pellman, Jean Baptiste Poline, Ariel Rokem, Gunnar Schaefer, Vanessa Sochat, William Triplett, Jessica A. Turner, Gaël Varoquaux, and Russell A. Poldrack. The brain imaging data structure, a format for organizing and describing outputs of neuroimaging experiments. *Scientific Data 2016 3:1*, 3:1–9, 6 2016.

[224] Guiomar Niso, Krzysztof J. Gorgolewski, Elizabeth Bock, Teon L. Brooks, Guillaume Flandin, Alexandre Gramfort, Richard N. Henson, Mainak Jas, Vladimir Litvak, Jeremy T. Moreau, Robert Oostenveld, Jan Mathijs Schoffelen, Francois Tadel, Joseph Wexler, and Sylvain Baillet.

Meg-bids, the brain imaging data structure extended to magnetoencephalography. *Scientific Data 2018 5:1*, 5:1–5, 6 2018.

[225] Cyril R. Pernet, Stefan Appelhoff, Krzysztof J. Gorgolewski, Guillaume Flandin, Christophe Phillips, Arnaud Delorme, and Robert Oostenveld. Eeg-bids, an extension to the brain imaging data structure for electroencephalography. *Scientific Data 2019 6:1*, 6:1–5, 6 2019.

[226] Richard N. Henson, Hunar Abdulrahman, Guillaume Flandin, and Vladimir Litvak. Multimodal integration of m/eeg and f/mri data in spm12. *Frontiers in Neuroscience*, 13:300, 2019.

[227] Guangye Li, Shize Jiang, Meng Wang, Zehan Wu, Peter Brunner, Gerwin Schalk, Liang Chen, and Dingguo Zhang. Seegview: A toolbox for localization and visualization of stereo-electroencephalography (seeg) electrodes. *Proceedings - 2018 IEEE International Conference on Systems, Man, and Cybernetics, SMC 2018*, pages 67–70, 1 2019.

[228] Bruce Fischl. FreeSurfer. *NeuroImage*, 62(2):774–781, 8 2012.

[229] Anders M. Dale, Bruce Fischl, and Martin I. Sereno. Cortical surface-based analysis: I. segmentation and surface reconstruction. *NeuroImage*, 9:179–194, 2 1999.

[230] Bruce Fischl, Martin I. Sereno, and Anders M. Dale. Cortical surface-based analysis: Ii: Inflation, flattening, and a surface-based coordinate system. *NeuroImage*, 9:195–207, 2 1999.

[231] Alexandre Gramfort, Martin Luessi, Eric Larson, Denis A. Engemann, Daniel Strohmeier, Christian Brodbeck, Roman Goj, Mainak Jas, Teon Brooks, Lauri Parkkonen, and Matti Hämäläinen. Meg and eeg data analysis with mne-python. *Frontiers in Neuroscience*, 0:267, 2013.

[232] Guido Van Rossum and Fred L. Drake. *Python 3 Reference Manual*. CreateSpace, Scotts Valley, CA, 2009.

[233] William Penny, Karl Friston, John Ashburner, Stefan Kiebel, and Thomas Nichols. Statistical parametric mapping: The analysis of functional brain images. *Statistical Parametric Mapping: The Analysis of Functional Brain Images*, 2007.

[234] Lin Song. NGPM a NSGA-II Program in Matlab v1.4. *MATLAB Central File Exchange*, 2011.

[235] Magnus Själander, Magnus Jahre, Gunnar Tufte, and Nico Reissmann. {EPIC}: An Energy-Efficient, High-Performance {GPGPU} Computing Research Infrastructure, 2019.

[236] D. Puthankattil Subha, Paul K. Joseph, Rajendra Acharya U, and Choo Min Lim. EEG signal analysis: A survey. *Journal of Medical Systems*, 34(2):195–212, Apr 2010.

[237] Maximiliano Bueno-López, Pablo A. Muñoz-Gutiérrez, Eduardo Giraldo, and Marta Molinas. Analysis of epileptic activity based on brain mapping of eeg adaptive time-frequency decomposition. In *Brain Informatics*, pages 319–328, Cham, 2018. Springer International Publishing.

[238] Luis Alfredo Moctezuma and Marta Molinas. Multi-objective optimization for eeG channel selection and accurate intruder detection in an eeG-based subject identification system. *Scientific Reports*, 10(1):1–12, 2020.

[239] Luis Alfredo Moctezuma, Alejandro A Torres-García, Luis Villaseñor-Pineda, and Maya Carrillo. Subjects identification using EEG-recorded imagined speech. *Expert Systems with Applications*, 118:201–208, 2019.

[240] Y. Yin, J. Cao, and T. Tanaka. EEG energy analysis based on memd with ica pre-processing. In *Proceedings of The 2012 Asia Pacific Signal and Information Processing Association Annual Summit and Conference*, pages 1–5, Dec 2012.

[241] Asmat Zahra, Nadia Kanwal, Naveed ur Rehman, Shoaib Ehsan, and Klaus D. McDonald-Maier. Seizure detection from eeg signals using multivariate empirical mode decomposition. *Computers in Biology and Medicine*, 88:132 – 141, 2017.

[242] P. Khosropanah, A. Rahman Ramli, K. S. Lim, M. Hamiruce Marhaban, A. Ahmedov, and S. Jong-Mo. Fused multivariate empirical mode decomposition (memd) and inverse solution method for eeg source localization. *Biomedical Engineering / Biomedizinische Technik*, 63(4):467–479, Jul 2018.

[243] Luis Alfredo Moctezuma and Marta Molinas. EEG-based Subjects Identification based on Biometrics of Imagined Speech using EMD. In *International Conference on Brain Informatics*, pages 458–467. Springer, 2018.

[244] Munsif Ali Jatoi and Nidal Kamel. Brain source localization using reduced eeg sensors. *Signal, Image and Video Processing*, 12(8):1447–1454, Nov 2018.

[245] N. Rehman and H. Aftab. Multivariate variational mode decomposition. *IEEE Transactions on Signal Processing*, 67(23):6039–6052, 2019.

[246] Andres Soler, Eduardo Giraldo, Lars Lundheim, and Marta Molinas. Relevance-based channel selection for eeg source reconstruction: An approach to identify low-density channel subsets. *Proceedings of the 15th International Joint Conference on Biomedical Engineering Systems and Technologies*, pages 174–183, 2022.

[247] James W. Phillips, Richard M. Leahy, John C. Mosher, and Bijan Timsari. Imaging neural activity using MEG and EEG. *IEEE Engineering in Medicine and Biology Magazine*, 16(3):34–42, may 1997.

[248] Andres Soler, Eduardo Giraldo, and Marta Molinas. Partial brain model for real-time classification of rgb visual stimuli: A brain mapping approach to bci. *8th Graz Brain Computer Interface Conference*, 2019.

[249] L. Duque-Munoz, F. Vargas, and J. D. Lopez. Simplified eeg inverse solution for bci real-time implementation. *Proceedings of the Annual International Conference of the IEEE Engineering in Medicine and Biology Society, EMBS*, 2016-October:4051–4054, 10 2016.

[250] Sajib Saha, Yakov Nesterets, Rajib Rana, Murat Tahtali, Frank de Hoog, and Timur Gureyev. Eeg source localization using a sparsity prior based on brodmann areas. *International Journal of Imaging Systems and Technology*, 27:333–344, 12 2017.

[251] VS Fonov, AC Evans, RC McKinstry, CR Almli, and DL Collins. Unbiased nonlinear average age-appropriate brain templates from birth to adulthood. *NeuroImage*, 47:S102, jul 2009.

[252] Bruce Fischl, André van der Kouwe, Christophe Destrieux, Eric Halgren, Florent Ségonne, David H Salat, Evelina Busa, Larry J Seidman, Jill Goldstein, David Kennedy, Verne Caviness, Nikos Makris, Bruce Rosen, and Anders M Dale. Automatically parcellating the human cerebral cortex. *Cortex*, 14:11–22, 2004.

[253] Rahul S. Desikan, Florent Ségonne, Bruce Fischl, Brian T. Quinn, Bradford C. Dickerson, Deborah Blacker, Randy L. Buckner, Anders M. Dale, R. Paul Maguire, Bradley T. Hyman,

Marilyn S. Albert, and Ronald J. Killiany. An automated labeling system for subdividing the human cerebral cortex on mri scans into gyral based regions of interest. *NeuroImage*, 31:968–980, 7 2006.

[254] Christophe Destrieux, Bruce Fischl, Anders Dale, and Eric Halgren. Automatic parcellation of human cortical gyri and sulci using standard anatomical nomenclature. *NeuroImage*, 53:1–15, 10 2010.

[255] Audrey L.H. Van Der Meer, Monica Svantesson, and F. R.Ruud Van Der Weel. Longitudinal study of looming in infants with high-density EEG. *Developmental Neuroscience*, 34(6):488–501, mar 2013.

[256] Hana Burianová, Lars Marstaller, Paul Sowman, Graciela Tesan, Anina N. Rich, Mark Williams, Greg Savage, and Blake W. Johnson. Multimodal functional imaging of motor imagery using a novel paradigm. *NeuroImage*, 2013.

[257] Zhaoyang Qiu, Brendan Z. Allison, Jing Jin, Yu Zhang, Xingyu Wang, Wei Li, and Andrzej Cichocki. Optimized motor imagery paradigm based on imagining Chinese characters writing movement. *IEEE Transactions on Neural Systems and Rehabilitation Engineering*, 25(7):1009–1017, jul 2017.

[258] Gian-Emilio Chatrian, Ettore Lettich, and Paula L. Nelson. Modified Nomenclature for the "10%" Electrode System. *Journal of Clinical Neurophysiology*, 5(2):183–186, 1988.

[259] Saurabh R. Sinha, Lucy Sullivan, Dragos Sabau, Daniel San-Juan, Keith E. Dombrowski, Jonathan J. Halford, Abeer J. Hani, Frank W. Drislane, and Mark M. Stecker. American Clinical Neurophysiology Society Guideline 1: Minimum Technical Requirements for Performing Clinical Electroencephalography. *Journal of Clinical Neurophysiology*, 33(4):303–307, 8 2016.

[260] Jayant N. Acharya, Abeer Hani, Janna Cheek, Partha Thirumala, and Tammy N. Tsuchida. American Clinical Neurophysiology Society Guideline 2: Guidelines for Standard Electrode Position Nomenclature. *Journal of Clinical Neurophysiology*, 33(4):308–311, 8 2016.

[261] Valer Jurcak, Daisuke Tsuzuki, and Ippeita Dan. 10/20, 10/10, and 10/5 systems revisited: Their validity as relative head-surface-based positioning systems. *NeuroImage*, 34(4):1600–1611, 2 2007.

[262] Sally M. Stoyell, Janina Wilmskoetter, Mary Ann Dobrota, Dhinakaran M. Chinappen, Leonardo Bonilha, Mark Mintz, Benjamin H. Brinkmann, Susan T. Herman, Jurriaan M. Peters, Serge Vulliemoz, Margitta Seeck, Matti S. Hämäläinen, and Catherine J. Chu. High-Density EEG in Current Clinical Practice and Opportunities for the Future. *Journal of clinical neurophysiology : official publication of the American Electroencephalographic Society*, 38(2):112–123, 3 2021.

[263] Bingquan Huang, B. Buckley, and T. M. Kechadi. Multi-objective feature selection by using NSGA-II for customer churn prediction in telecommunications. *Expert Systems with Applications*, 37(5):3638–3646, 5 2010.

[264] Chea Yau Kee, S. G. Ponnambalam, and Chu Kiong Loo. Multi-objective genetic algorithm as channel selection method for P300 and motor imagery data set. *Neurocomputing*, 161:120–131, 8 2015.

[265] Ramaswamy Palaniappan, Paramesran Raveendran, and Sigeru Omatu. Vep optimal channel

selection using genetic algorithm for neural network classification of alcoholics. *IEEE Transactions on Neural Networks*, 13:486–491, 3 2002.

[266] Lin He, Youpan Hu, Yuanqing Li, and Daoli Li. Channel selection by rayleigh coefficient maximization based genetic algorithm for classifying single-trial motor imagery eeg. *Neurocomputing*, 121:423–433, 12 2013.

[267] Jianhua Yang, Harsimrat Singh, Evor L. Hines, Friederike Schlaghecken, Daciana D. Iliescu, Mark S. Leeson, and Nigel G. Stocks. Channel selection and classification of electroencephalogram signals: An artificial neural network and genetic algorithm-based approach. *Artificial Intelligence in Medicine*, 55:117–126, 6 2012.

[268] Sandeep Bavkar, Brijesh Iyer, and Shankar Deosarkar. Optimal eeg channels selection for alcoholism screening using emd domain statistical features and harmony search algorithm. *Biocybernetics and Biomedical Engineering*, 41:83–96, 1 2021.

[269] Phattarapong Sawangjai, Supanida Hompoonsup, Pitshaporn Leelaarporn, Supavit Kongwudhikunakorn, and Theerawit Wilaiprasitporn. Consumer Grade EEG Measuring Sensors as Research Tools: A Review. *IEEE Sensors Journal*, 20(8):3996–4024, 4 2020.

[270] Minkyu Ahn, Jun Hee Hong, and Sung Chan Jun. Feasibility of approaches combining sensor and source features in brain–computer interface. *Journal of Neuroscience Methods*, 204(1):168–178, 2 2012.

[271] Jussi T Lindgren. As above, so below? Towards understanding inverse models in BCI. *Journal of Neural Engineering*, 15(1):012001, dec 2017.

[272] Fabien Lotte, Anatole Lécuyer, and Bruno Arnaldi. FuRIA: An inverse solution based feature extraction algorithm using fuzzy set theory for brain-computer interfaces. *IEEE Transactions on Signal Processing*, 57(8):3253–3263, 2009.

[273] Alex Lau-Zhu, Michael P.H. Lau, and Gráinne McLoughlin. Mobile EEG in research on neurodevelopmental disorders: Opportunities and challenges. *Developmental Cognitive Neuroscience*, 36:100635, apr 2019.

[274] Ranjana K Mehta and Raja Parasuraman. Neuroergonomics: a review of applications to physical and cognitive work. *Frontiers in Human Neuroscience*, 0(DEC):889, 12 2013.

[275] Pushpendra Singh, Shiv Dutt Joshi, Rakesh Kumar Patney, and Kaushik Saha. The fourier decomposition method for nonlinear and non-stationary time series analysis. *Proceedings of the Royal Society A: Mathematical, Physical and Engineering Sciences*, 473, 3 2017.

[276] V. Padhmashree and Abhijit Bhattacharyya. Human emotion recognition based on time–frequency analysis of multivariate eeg signal. *Knowledge-Based Systems*, 238:107867, 2 2022.

[277] Muhammad Tariq Sadiq, Xiaojun Yu, Zhaohui Yuan, Muhammad Zulkifal Aziz, Naveed ur Rehman, Weiping Ding, and Gaoxi Xiao. Motor imagery bci classification based on multivariate variational mode decomposition. *IEEE Transactions on Emerging Topics in Computational Intelligence*, 2022.

[278] Vipin Gupta and Ram Bilas Pachori. Fbdm based time-frequency representation for sleep stages classification using eeg signals. *Biomedical Signal Processing and Control*, 64:102265, 2 2021.

[279] Virender Kumar Mehla, Amit Singhal, Pushpendra Singh, and Ram Bilas Pachori. An efficient method for identification of epileptic seizures from eeg signals using fourier analysis. *Physical and Engineering Sciences in Medicine*, 44:443–456, 6 2021.

[280] Amir G. Baroumand, Anca A. Arbune, Gregor Strobbe, Vincent Keereman, Lars H. Pinborg, Martin Fabricius, Guido Rubboli, Camilla Gøbel Madsen, Bo Jespersen, Jannick Brennum, Otto Mølby Henriksen, Pieter van Mierlo, and Sándor Beniczky. Automated ictal eeg source imaging: A retrospective, blinded clinical validation study. *Clinical Neurophysiology*, 4 2021.

[281] Evelina Iachim, Simone Vespa, Amir G. Baroumand, Venethia Danthine, Pascal Vrielynck, Marianne de Tourtchaninoff, Alexane Fierain, Jose Geraldo Ribeiro Vaz, Christian Raftopoulos, Susana Ferrao Santos, Pieter van Mierlo, and Riëm El Tahry. Automated electrical source imaging with scalp eeg to define the insular irritative zone: Comparison with simultaneous intracranial eeg. *Clinical Neurophysiology*, 132:2965–2978, 12 2021.

[282] Mette Thrane Foged, Terje Martens, Lars H. Pinborg, Nizar Hamrouni, Minna Litman, Guido Rubboli, Anne Mette Leffers, Philippe Ryvlin, Bo Jespersen, Olaf B. Paulson, Martin Fabricius, and Sándor Beniczky. Diagnostic added value of electrical source imaging in presurgical evaluation of patients with epilepsy: A prospective study. *Clinical Neurophysiology*, 131:324–329, 1 2020.

[283] Bin He, Lin Yang, Christopher Wilke, and Han Yuan. Electrophysiological imaging of brain activity and connectivity-challenges and opportunities. *IEEE Transactions on Biomedical Engineering*, 58:1918–1931, 7 2011.

[284] M. Hassan, L. Chaton, P. Benquet, A. Delval, C. Leroy, L. Plomhause, A. J.H. Moonen, A. A. Duits, A. F.G. Leentjens, V. van Kranen-Mastenbroek, L. Defebvre, P. Derambure, F. Wendling, and K. Dujardin. Functional connectivity disruptions correlate with cognitive phenotypes in parkinson's disease. *NeuroImage: Clinical*, 14:591–601, 1 2017.

[285] Michela Pievani, Willem de Haan, Tao Wu, William W. Seeley, and Giovanni B. Frisoni. Functional network disruption in the degenerative dementias. *The Lancet Neurology*, 10:829–843, 9 2011.

ISBN 978-82-326-5845-9 (printed ver.)
ISBN 978-82-326-5909-8 (electronic ver.)
ISSN 1503-8181 (printed ver.)
ISSN 2703-8084 (online ver.)

NTNU

Norwegian University of
Science and Technology